

論文 / 著書情報
Article / Book Information

| | |
|-------------------|--|
| 題目(和文) | 遷移金属基カルコゲナイド超伝導体・半導体に関する研究 |
| Title(English) | Study on Transition Metal-Based Chalcogenide Superconductors and Semiconductors |
| 著者(和文) | 半沢幸太 |
| Author(English) | Kota Hanzawa |
| 出典(和文) | 学位:博士(工学), 学位授与機関:東京工業大学, 報告番号:甲第11146号, 授与年月日:2019年3月26日, 学位の種別:課程博士, 審査員:平松 秀典,細野 秀雄,神谷 利夫,大場 史康,一杉 太郎 |
| Citation(English) | Degree:Doctor (Engineering), Conferring organization: Tokyo Institute of Technology, Report number:甲第11146号, Conferred date:2019/3/26, Degree Type:Course doctor, Examiner:,,,, |
| 学位種別(和文) | 博士論文 |
| Type(English) | Doctoral Thesis |

Study on Transition Metal-Based Chalcogenide
Superconductors and Semiconductors

Kota Hanzawa

2018

Department of Materials Science and Engineering

School of Materials and Chemical Technology

Tokyo Institute of Technology

Contents

| | |
|---|----|
| Chapter 1. General Introduction | 7 |
| 1.1. Background of Present Study | 7 |
| 1.1.1. Transition metal-based chalcogenides | 7 |
| 1.1.2. Relationship between structural distortion and electronic structure..... | 16 |
| 1.2. Objective of Present Study | 19 |
| References | 23 |
| | |
| Chapter 2. Fabrication of Insulator-Like FeSe Thin Films and Determination of the Origin | 48 |
| 2.1. Strategy on Enhancement of T_c in Fe-Based Superconductors | 48 |
| 2.2. Experimental Procedure | 50 |
| 2.2.1. MBE Growth of FeSe thin films | 50 |
| 2.2.2. Structural and compositional analyses | 50 |
| 2.2.3. Electronic transport and Hall effect measurements | 52 |
| 2.2.4. Observation of electronic structure using ARPES..... | 52 |
| 2.3. Results and Discussion | 53 |
| 2.3.1. Phase diagram of FeSe grown on STO (001)..... | 53 |
| 2.3.2. Fabrication of FeSe epitaxial films with different chemical compositions | 54 |
| 2.3.3. Effects of lattice strain on FeSe films..... | 57 |
| 2.3.4. Chemical composition dependence of insulator-like electronic transport properties in strained FeSe..... | 60 |
| 2.3.5. Electronic structure of insulator-like FeSe films..... | 62 |
| 2.3.6. Potential barrier for percolation conduction..... | 64 |
| 2.3.7. Origin of the insulator-like behavior | 66 |
| 2.4. Conclusion | 66 |
| References | 67 |

| | |
|---|----|
| Chapter 3. Stability of FeSe Epitaxial Films against Air Exposure | 85 |
| 3.1. Importance of Surface Stability for Electric Field-Induced Carrier Doping..... | 85 |
| 3.2. Experimental Procedure | 86 |
| 3.2.1. Fabrication of FeSe epitaxial films and the EDLTs..... | 86 |
| 3.2.2. Structure and surface analyses of FeSe films..... | 87 |
| 3.2.3. Chemical composition analysis of FeSe surface..... | 88 |
| 3.3. Results and Discussion..... | 88 |
| 3.3.1. Generation of nano-sized particular structures at film surface by air exposure..... | 88 |
| 3.3.2. Investigation of origin of nano-sized particular structures..... | 90 |
| 3.3.3. EDLT using air-exposed FeSe channel layer..... | 91 |
| 3.3.4. Long-time stability of epitaxial FeSe film preserved in Ar..... | 92 |
| 4.4. Conclusion..... | 93 |
| References | 93 |

| | |
|--|-----|
| Chapter 4. Electric Field-Induced Superconducting Transition of Insulator-like FeSe Thin Film at 35 K | 100 |
| 4.1. EDLT for Electrostatic Carrier Doping | 100 |
| 4.2. Experimental Procedure | 101 |
| 4.2.1. Epitaxial thin film growth of ~10 nm thick FeSe..... | 101 |
| 4.2.2. Structure analysis of FeSe thin film | 102 |
| 4.2.3. In-situ fabrication of EDLT using FeSe as a channel..... | 102 |
| 4.2.4. Electronic transport measurements of FeSe-EDLT..... | 103 |
| 4.3. Results and Discussion..... | 103 |
| 4.3.1. FeSe epitaxial thin film exhibiting insulator-like electric behavior | 103 |
| 4.3.2. Device properties of EDLT using an insulator-like FeSe channel | 104 |
| 4.3.3. Electric field-induced superconductivity at 35 K..... | 105 |
| 4.3.4. Accumulated carrier density in superconducting FeSe-EDLT | 106 |
| 4.3.5. Discussion: origin of the high- T_c superconductivity..... | 107 |
| 4.4. Conclusion..... | 108 |
| References | 109 |

Chapter 5. Carrier Density Dependence of T_c in FeSe-EDLT

| | |
|--|-----|
| under Electric Field | 120 |
| 5.1. FeSe-Related EDLTs..... | 120 |
| 5.2. Experimental Procedure | 120 |
| 5.2.1. Preparation of three different FeSe epitaxial thin films | 120 |
| 5.2.2. Analyses of structure parameters and chemical compositions | 121 |
| 5.2.3. Evaluation of electronic transport properties of three different FeSe-EDLTs..... | 121 |
| 5.3. Results and Discussion | 122 |
| 5.3.1. Three kinds of FeSe epitaxial thin films..... | 122 |
| 5.3.2. Electronic transport properties of three FeSe-EDLTs..... | 124 |
| 5.3.3. Discussion: origin of difference of T_c among three FeSe-EDLTs | 125 |
| 5.4. Conclusion | 127 |
| References | 127 |

Chapter 6. Fabrication of Metastable Tetragonal FeS Heteroepitaxial

| | |
|--|-----|
| Thin Film and the EDLT | 134 |
| 6.1. Tetragonal FeS | 134 |
| 6.2. Experimental Procedure | 135 |
| 6.2.1. Synthesis of polycrystalline hexagonal FeS bulk targets | 135 |
| 6.2.2. PLD growth of tetragonal FeS epitaxial films..... | 135 |
| 6.2.3. Analyses of structure and chemical composition | 136 |
| 6.2.4. STEM measurements of tetragonal FeS epitaxial film..... | 136 |
| 6.2.4. Electronic transport measurements of epitaxial tetragonal FeS and the EDLT | 137 |
| 6.3. Results and Discussion | 137 |
| 6.3.1. Stabilization of metastable tetragonal FeS phase via thin film growth process..... | 137 |
| 6.3.2. Fabrication of tetragonal epitaxial FeS thin film..... | 139 |
| 6.3.3. Structure parameters of tetragonal FeS on various substrates..... | 140 |
| 6.3.4. Microstructure analysis of epitaxial tetragonal FeS on CaF_2 | 141 |
| 6.3.5. Electric transport of tetragonal FeS films..... | 142 |
| 6.3.6. Electric transport of tetragonal FeS-EDLT under electric field..... | 143 |

| | |
|----------------------|-----|
| 6.4. Conclusion..... | 144 |
| References | 145 |

Chapter 7. Chemical Design of Green Emitting Semiconductors:

| | |
|--|------------|
| Perovskite-Type Sulfide SrHfS₃..... | 154 |
| 7.1. Design of Highly Efficient Light-Emitting Semiconductors..... | 154 |
| 7.2. Computational and Experimental Procedures | 156 |
| 7.2.1. Theoretical calculations..... | 156 |
| 7.2.2. Polycrystalline sample preparation | 157 |
| 7.2.3. Structure analysis | 157 |
| 7.2.4. Optical properties | 158 |
| 7.2.5. Electronic transport properties | 158 |
| 7.3. Results | 158 |
| 7.3.1. Electronic structures of <i>AEeTMS</i> ₃ | 158 |
| 7.3.2. SrHfS ₃ with an appropriate band gap for green-light emission..... | 161 |
| 7.3.3. <i>n</i> - and <i>p</i> -type carrier conduction of SrHfS ₃ | 162 |
| 7.3.4. Intense green luminescence of SrHfS ₃ | 164 |
| 7.4. Conclusion..... | 165 |
| References | 166 |

Chapter 8. Heteroepitaxial Growth of Perovskite-Sulfide Semiconductor

| | |
|---|------------|
| <i>AEHfS</i>₃ (<i>AE</i> = Sr and Ba)..... | 179 |
| 8.1. Motivation for Fabrication of <i>AEHfS</i> ₃ Epitaxial Thin Film..... | 179 |
| 8.2. Experimental Procedure | 180 |
| 8.2.1. PLD growth of <i>AEHfS</i> ₃ epitaxial thin films..... | 180 |
| 8.2.2. Structure parameter analysis | 180 |
| 8.2.3. Optical measurements | 181 |
| 8.2.4. Auger electron spectroscopy | 181 |
| 8.3. Results and Discussion..... | 181 |
| 8.3.1. Epitaxial growth of SrHfS ₃ thin film..... | 181 |
| 8.3.2. Intense orange PL of bulk BaHfS ₃ | 184 |
| 8.3.3. Epitaxial growth of single phase BaHfS ₃ thin film..... | 185 |

| | |
|---|------------|
| 8.4. Conclusion..... | 187 |
| References | 188 |
| Chapter 9. General Conclusion..... | 196 |
| Acknowledgments..... | 200 |
| Publication List..... | 202 |
| Papers included in this thesis..... | 202 |
| Other papers..... | 203 |
| Presentation List..... | 204 |
| International Presentations | 204 |
| Domestic Presentations..... | 206 |
| Awards..... | 208 |
| Biography..... | 208 |
| Education..... | 208 |

Chapter 1. General Introduction

1.1. Background of Present Study

1.1.1. Transition metal-based chalcogenides

In transition metal oxides/chalcogenides, transition metal (*TM*) cation and oxygen (*O*)/chalcogen (*Ch*: S, Se, and Te) anion play important roles to exhibit their physical properties and/or to stabilize their crystal structures. *TMs* are elements, ranging from the third to twelfth rows with principal quantum numbers of three, four, or five. **Figure 1-1a** shows a periodic table of elements. The *TMs* are categorized into three groups. The first group is composed of post transition metals (*pTM*) belonging to the eleventh and twelfth rows, Zn, Cu, Cd, and Hg. Their usual valence states in *pTM-O/Ch* are $nd^{10}ms^0$, such as Zn^{2+} and Cu^{1+} ; i.e., fully filled *d*-orbitals and unoccupied *s*-orbitals. The second group contains *TMs* ranging between the fifth and tenth rows, for instance Mo, Fe, and Ni. Because they have partially occupied *d*-orbitals, they are called nd^l *TM*. This last group is comprised of unoccupied nd^0 -orbitals, which is called early transition metals (*eTM*). Lanthanoids, Sc, Y, and elements in the fourth row belong to this group.

Because *TMs* in the different groups possess different valence states with each other, the preferred coordination number is also different, resulting in the formation of different preferred crystal structures. Furthermore, the different electro-negativities of each *TM* affect their electronic structures. The energy levels of *d*-orbitals elevate from *pTM*, nd^l *TM*, to *eTM* in terms of vacuum level (**Fig. 1-1b**). Therefore, this variation of electronic structure contributes to the physical properties, such as the band gap (E_g), carrier polarity, and effective mass. Moreover, the difference of electron localization at *TM* cations affects electron-electron correlation and electron trapping.

1.1.1.1. *pTM-based oxides*

Electric conductive functionalities of *pTM*-based oxides have been well investigated, especially for their superconducting and semiconducting properties. The most well-known compounds would be Cu-based oxide superconductors, which are also called cuprates.

Superconductivity was first observed in 1911 for cooled Hg that exhibited completely zero resistance at 4.2 K [1]. Since the discovery of the first superconductor, many new superconductors have been discovered and a lot of theoretical approaches have been proposed to reveal the origins of superconductivity. The superconductors found so far can be categorized into four types: metal superconductors obeying the BCS theory proposed by Bardeen, Cooper, and Schrieffer [2]; organic superconductors [3–5]; cuprates; and Fe-based superconductors. Some of the discovered representative superconductors are displayed together with the T_c and their year of discovery in **Fig. 1-2**. Superconductivity appears when electron-electron interaction overcomes electron-electron Coulomb repulsion, suggesting that the mediation of the interaction and low surrounding thermal energy to avoid thermal decomposition are necessary. BCS theory tells us that superconductivity is induced by phonon-mediated formation of electron-electron coupling [2]. The highest T_c at ambient pressure is 39 K in MgB₂ among BCS-type superconductors [6]. Recently, under pressure higher than ~180 GPa, it was reported that H₃S exhibits extremely high- T_c superconductivity at > 200 K, which is the highest T_c among all superconductors [7].

However, the highest T_c system at ambient pressure is cuprates. The earliest cuprate high- T_c superconductor to be discovered is (La, Ba)₂CuO₄ with T_c of 20 K in 1986 [8]. After this report, a lot of new cuprate superconductors were found; the highest T_c among cuprates is 133 K observed in HgBa₂Ca₂Cu₃O_x [9]. Because BCS theory cannot explain their high T_c , origin of superconductivity in cuprates is different from BCS-type superconductors, which should be strongly related to spin fluctuation [10, 11]. **Figures 1-3** and **1-4** display common

features of cuprates, which possess a CuO_2 superconducting plane and a strong electron-electron correlation in the undoped parent phase, indicating that Cu is essential for the appearance of this superconductivity.

Like cuprates, the idea to use Cu for electric conduction has been developed in *pTM*-based oxide semiconductors. In 1997, a chemical design concept was proposed to realize the wide gap *p*-type semiconductor [12]. For realization of *p*-type doping, it should be essential that energy levels of valence band maximum (VBM) locates around a typical doping limit (-6 eV for VBM from vacuum level) [13]; i.e., a shallow energy level from the vacuum level is preferred for *p*-type conduction. **Fig. 1-5** shows the concept of utilizing the chemical bonding of hybridized shallow Cu $3d$ - and deep O $2p$ -orbitals for VBM. So far, many *p*-type semiconductors have been discovered; e.g., CuAlO_2 [14] and SrCu_2O_2 [15].

In contrast to the *p*-type semiconductors, *n*-type doping requires energy levels of conduction band minimum (CBM) located around the typical doping limit (~ -4 eV for CBM from vacuum level) [13]; i.e., deep CBM is appropriate for *n*-type doping. Because the energy levels of *s*-orbitals of *pTM* is generally deep from the vacuum level, *pTM*-based oxides other than Cu tend to exhibit a *n*-type conduction, where CBM and VBM are mainly composed of *pTM* *s*-orbitals and O *p*-orbitals. Although the *n*-type *pTM*-based oxides e.g., $\text{InGaZn}_5\text{O}_8$ and ZnO , have high electron mobilities (80 $\text{cm}^2/\text{V}\cdot\text{s}$ for $\text{InGaZn}_5\text{O}_8$ [16] and 440 $\text{cm}^2/\text{V}\cdot\text{s}$ for ZnO [17]), they have a critical issue; in the *pTM* oxides, *p*-type doping is very difficult due to the intrinsically deep energy level of O *p*-orbitals [18]. Therefore, a *p*- and *n*-type conductive wide-gap *pTM*-oxide semiconductor is hard to design.

This study focuses on *TM-Chs* from the viewpoint of the ionic radii and ionicity of *Chs*. Functionalities of *TM-Chs* are veiled compared with *TM*-oxides due to their typically lower symmetry crystal structures originating from large ionic radii of *Chs*, contributing to make the thin film growth hard. However, the weaker ionicities of *Chs* than O should lead to an

advantageous electronic structure for electronic conduction, where p -orbitals of Chs locating a shallower energy level than that of O contributes to p -type dopability, and the resultant formation of wide band width results in a sharp band dispersion; i.e., small hole effective mass is expected.

1.1.1.2. pTM -based chalcogenides

Generally, pTM -based chalcogenide is a semiconductor using the empty s -orbital and/or occupied pTM d -orbital for carrier conduction like the oxides. The functional semiconductors have been studied for practical applications, such as light emitting semiconductor [19–21], photoresistor, cathode for Li-ion battery, absorber for photovoltaic cell [22–24], and transparent conductor [25–127].

II-VI group semiconductors, binary $ZnCh$ and $CdCh$, form zinc blend-type $P6_3/mc$ (No. 186) and wurtzite-type $F\bar{4}3m$ (No. 216) crystal structures. The CBM and VBM consist of antibonding and bonding states between Zn/Cd and Ch [28] locating at same k point. **Table 1-1** summarizes the band gap (E_g) and mobilities for electron and hole. Both of $ZnCh$ and $CdCh$ become both n - and p -type semiconductor by chemical doping; e.g., N^{3-} doping at Se^{2-} -site in $ZnSe$ contributes to p -type conduction [29], whereas n -type doping is achieved through the substitution of Zn^{2+} with Ga^{3+} or Al^{3+} [30].

Even though II-VI semiconductors utilize a bonding state between cation and anion for p -type conduction, $CuInCh_2$, $CuGaCh_2$, and $LnCuOCh$ utilize Cu $3d$ -orbital. The VBM and CBM are mainly composed of Cu $3d$ - and In/Ga s -orbitals [31, 32]. In a $Ch = Se$ case, by introducing excess Se and In, $CuInSe_2$ exhibits p - and n -type conduction [33], respectively. Moreover, owing to the suitable E_g tuned from 1.0 ($CuInSe_2$) to 1.7 eV ($CuGaSe_2$) [34] via replacement of In with Ga, as well as small effective mass [33], they are used for absorber of photovoltaic application [35]. However, because the widest E_g is as narrow as 1.7 eV,

much wider E_g cannot be obtained.

$LnCuOCh$ has a ZrCuSiAs-type tetragonal crystal structure (space group: $P4/nmm$), where LnO layer and $CuCh_4$ tetrahedra layer alternatively stacking for a vertical direction of the layers are regarded as a natural superlattice [36]. The electronic structure is composed of empty Cu 4s-orbital and hybridized filled Ch 3p- and Cu 3d-orbitals, which form CBM and VBM, respectively [37, 38]. By replacing La or S with larger Ln or Ch ion, the direct band gap decreases; e.g., in a case of Se substituted LaCuOS, the E_g changes from 3.2 eV (LaCuOS) to 2.8 eV (LaCuOSe) [37, 39]. In this system, due to the shallow hybridized Cu 3d- and Ch 3p-orbitals, the energy level of VBM is also shallow with respect to vacuum level [40], leading to p -type conduction by Mg^{2+} doping [25, 39, 41]. The E_g and hole mobility are summarized in **Table 1-2**. Because of the high anisotropy of the layered crystal structure, the exciton exists at a temperature much higher than room temperature (thermal energy at room temperature is ~ 26 meV); the exciton binding energy is ~ 50 meV (LaCuOS [42, 43]). The epitaxial thin films were fabricated [42, 44–46] and, subsequently, the pn -heterojunction shown in **Fig. 1-6** was constructed with a n -type oxide-semiconductor [47]. Consequently, excitonic blue electroluminescence was successfully detected at room temperature.

Even though the pTM -based chalcogenides have a lot of notable functionalities, they have suffered from the influence of defects [48] due to a variable valence state of pTM and the low coordination number. Thus, $nd^l TM$ and eTM -based chalcogenides have been the focus of scientific attention and many interesting functionalities have been discovered.

1.1.1.3. $nd^l TM$ -based chalcogenides

In compounds based on TM with nd^l valence state and Ch anion, electron is not completely supplied to anion and remains in d -orbitals. Band theory proposes that when l is an odd number, $nd^l TM-Ch$ is metal; i.e., Fermi level intersects bands. However, due to the strong electron localization of the d -orbitals originating from electron-electron Coulomb

repulsion and/or electron-*TM* interaction, electron cannot transfer freely in some cases. This results in the appearance of the Mott insulator, where unusual physical properties emerge, such as giant magnet resistance and high critical temperature (T_c) superconductivity. Moreover, the remaining electron spin contributes to long range magnetic ordering, such as ferromagnetism and antiferromagnetism.

In early 2008, a new family of superconductors, the Fe-based superconductor, was discovered. The first reported compound is LaFePO with $T_c = 5$ K [49]. Then, in an analogous compound, LaFeAsO, high- T_c superconductivity was observed at 26 K through electron doping via substitution of O^{2-} with F^{1-} [50]. This discovery activated exploration of other Fe-based superconductors [51–53], leading to the discovery of some of the Fe-based superconductor families displayed in **Fig. 1-7**, with SmFeAsO as the highest T_c of 55 K among Fe-based superconductors [54]. Hence, the Fe-based superconductors are the second highest T_c system at ambient pressure.

In 2009, the simplest Fe-based superconductor, FeSe, was discovered [55]. The T_c of polycrystalline FeSe is as low as 8 K, but FeCh exhibits unique features [56, 57]. **Figure 1-8** summarizes the crystal structures of tetragonal FeCh, the competing phases and the derivatives. Unlike other FeAs-based superconductors, superconducting FeCh has an anti-PbO-type tetragonal crystal structure with space group of $P4/nmm$ (No. 129) composed only of edge-shared FeCh₄ layers without any insertion layer; on the other hand, hexagonal FeCh is not a superconductor (space group: $P6\bar{2}c$ (No. 190) or $P6_3/mmc$ (No. 194)). In FeSe and FeTe, the most thermodynamically stable structure is the tetragonal at ambient pressure and temperature [58]. However, referring to the binary phase diagram of Fe and S [58], the thermodynamically stable phase of FeS is hexagonal. Because the tetragonal FeS is obtained via unconventional synthesis processes, such as the hydro-thermal method [59] and de-

intercalation of K from $\text{KFe}_{2-x}\text{S}_2$ [60], the tetragonal FeS phase is metastable.

The tetragonal FeS and FeSe exhibit superconductivity at 5 K [59] and 8 K [55], respectively; while FeTe is not a superconductor but an antiferromagnetic metal with Néel temperature (T_N) of 64 K [61, 62]. **Figure 1-8** represents their multiband-metallic electronic structures composed of Fe 3*d*-orbitals [63, 64], in which an electron-like band crosses the Fermi surface at M point; whereas a hole-like band intersects it at Γ point. The order parameters of the superconductivity were determined as *s*-wave symmetry with/without sign reversal [65, 66], suggesting that the pairing mechanism of Cooper pairs should be spin or orbital fluctuation like LaFeAsO [67, 68].

The T_c of Fe*Ch* increases by chemical isovalent substitution, intercalation, application of external pressure, strain introduced during thin film growth, and fabrication of the monolayer. Because the ionic radius of S is the smallest among *Chs*; while that of Te is the largest, substitution of e.g., Se with isovalent S or Te varies the lattice parameters without any carrier injection formally. **Figures 1-10–1-12** show the relationship between substituted atomic ratio and the T_c ; in a S-substitution case, the T_c increases up to 15 K ($x = 0.2$) [69] and in $\text{FeSe}_{1-x}\text{Te}_x$, T_c reaches 23 K [70] or 15 K at $x = 0.5$ [69, 71].

In intercalated $A\text{Fe}_{2-x}\text{Ch}_2$ ($A =$ alkali metal [72, 73], alkali-earth metal [74], $\text{Li}_{1-x}\text{Fe}_x(\text{OH})$ [75, 76], and organic molecular [77–79]), A that placed between the Fe*Ch* layers expands distance of Fe*Ch* layers and indirectly supplies carrier into Fe*Ch* layers, leading to the enhancement of the T_c (~ 45 K in $\text{NaFe}_{2-x}\text{Se}_2$ [74]). **Table 1-3** summarizes the T_c . It should be noted that the intercalation also alters the Fermi surface, where the hole-like band disappears at Fermi level in the intercalated Fe*Ch* [80], irrespective of multiband electronic structure of pristine Fe*Ch*. This would suggest that electron doping of Fe*Ch* is one of the more promising paths to obtain high T_c , because the vanishment of the hole band should correspond to the increase of the Fermi level; i.e., electron number increases, like monolayer

FeSe that exhibits the highest among FeCh-related superconductors [81].

The monolayer is the most extreme two-dimensional case (see **Fig. 1-13**). This exhibits unusual properties that are not observed in the two-layer thick case [82]; i.e., even though their monolayer thick FeChs have remarkable features, the features appear only in the monolayer thick. The monolayer thick FeSe was prepared by an atomically controlled deposition on oxide-perovskite substrate [83] and exhibited extremely high- T_c of > 77 K [84], irrespective of the relatively low T_c of the bulk [55].

Up to here, FeCh is introduced with respect to the functionalities. The analogous compound FeCh₂ does not exhibit superconductivity but a remarkable optical property. TM-dichalcogenides (TMCh₂) are roughly classified into two groups; pyrite-type cubic structure of $Pa\bar{3}$ (No. 205) or layered structure of $P6_3/mmc$ (No. 194) with octahedral (1T) and trigonal prismatic (2H or 3R) local structures [85]. TMCh₂, employing the former e.g., Mo of TM, tends to form the layered structure; whereas that using the latter forms the cubic structure, e.g., Ni.

FeS₂ has the pyrite cubic structure. The VBM of is composed of t_{2g} -orbital of Fe 3d-orbital and the CBM is constituted by Fe e_g - and S 3p-orbitals [85, 86]. **Figure 1-14** is a summary of the absorption coefficients in some semiconductors. Because the absorption coefficient of FeS₂ is as high as $\sim 5 \times 10^6 \text{ cm}^{-1}$ [87], irrespective of the indirect band gap ($E_g = 1.13 \text{ eV}$ [88]), FeS₂ has been studied for an absorber of photovoltaic application. Next, NiS₂ is a Mott insulator [89], with long range antiferromagnetic ordering ($T_N = 40 \text{ K}$) [90]. By suppression of the electron correlation via e.g., isovalent Se-doping in **Fig. 1-15**, the Mott insulator phase gradually vanishes, and then a paramagnetic metal phase appears [91, 92].

In contrast to TMCh₂ with the pyrite structure, many layered TMCh₂, such as NbSe₂, TaS₂, and MoCh₂, exhibit superconductivity induced by external pressure [93, 94] and electrostatic carrier doping [95]. The T_c is typically lower than 10 K, which would indicate that Fe or

Cu is a promising element for the achievement of a high- T_c superconductor among *TM*-based compounds. For the layered *TMCh₂* (e.g., *MoCh₂* and *WCh₂*), not only superconductivity, but also semiconductor properties are investigated. Because the E_g is attributed to the crystal-field splitting of *d*-orbitals, it is generally narrow and indirect (1.23 eV for *MoS₂* [96]). However, it changes to direct-type by controlling the dimensionality. **Figure 1-16** represents the thickness dependence of band structure in *MoS₂*. The primitive band structure is an indirect-type and does not exhibit efficient luminescence. However, the electronic structure of *MoS₂* changes to direct band gap by decreasing the thickness down to monolayer thick and exhibits intense luminescence [97].

1.1.1.4. *eTM-based chalcogenides*

eTM-dichalcogenides (*eTMCh₂*), such as *HfS₂*, *ZrS₂*, and *HfSe₂*, are semiconductors with narrow band gaps. The mobilities summarized in **Fig. 1-17** are very high; e.g., electron mobility in *HfS₂* is as high as 2000 cm²/V·s [98], representing the potential for high performance electronic devices. However, the band gaps of these compounds are dominated by the effect of a crystal field, so that they cannot have wider gaps than ~2 eV [99]. This contributes to the limitation of variety for materials application fields.

Y₂O₂S and *La₂O₂S* are an insulator with indirect-type wide band gap [100] of 6.77 eV [101] and 4.35 eV [102]. The electronic structures are constituted mainly by Y/La 4/5*d*- and S 3*p*-orbitals that form very shallow CBM and do relatively shallow VBM [103]. The compounds are parent phases of phosphor with *RE* doping (*RE* = e.g., Sm³⁺ [104], Eu³⁺ [105], Tb³⁺ [106], Yb³⁺ [107]), owing to the primitive wide bad gap and defect tolerance. By employing suitable dopants and tuning the concentrations, the luminescence light color is controlled from red for Eu³⁺ to green for Yb³⁺ and Er³⁺. Owing to the wide band gap and energy levels of CBM formed by *eTM d*-orbitals, it is hard to dope and activate carriers in *Y₂O₂S* and *La₂O₂S*.

To produce semiconductors utilizing *eTM* *d*-orbital, a novel chemical design concept was proposed in **Fig. 1-18**, where a non-bonding state was introduced. This appears in specific high symmetry crystal structures and forms a deeper energy level of CBM [108]. It is also one of the aims that a high defect tolerance should be expected by employing *eTM* as a cation due to the stable and high valence states, such as + 4 of Zr and Hf, which lead to a high coordination number of *eTM* cation and then suppresses the formation of the cation vacancy. According to the concept, electronic transport properties of ZrOS [109] and LaSeF [110] are investigated. The CBM is composed of deep nonbonding state of Zr 4*d*-orbital; while the VBM is composed of antibonding state between cation and anion. Even though ZrOS has a direct band gap of ~ 2.5 eV, the band-edge transition is forbidden; i.e., efficient luminescence is not obtained. The *n*- and *p*-type carrier polarities are validated experimentally. Furthermore, the research indirectly demonstrated not only the effectiveness of the use of the nonbonding state for a semiconductor but also a defect tolerance of *eTM*-based compounds, owing to a great carrier controllability.

1.1.2. Relationship between structural distortion and electronic structure

In the above section, the functionalities of *TM*-based chalcogenides are reviewed with respect to the valence states of each *TM*. This section mentions how crystal structural distortion affects the electronic structure in *TM*-based oxides and chalcogenides. The distortion can be introduced through e.g., applying external pressure, chemical pressure by alternation of constituent ion with others having different ionic radii, and strain by fabrication of heteroepitaxial thin films, as well as vary, such as atomic positions in the solids and the mass density. This contributes to the stimulation of e.g., structure phase transition, change in the overlap of the wave functions of elemental atoms, and the enhancement of carrier density.

1.1.2.1. External pressure

Through the application of external pressure, the crystal lattice of solids is compressed isotropically and three dimensionally, and then distorted. Because this generally contributes to a reduction of the lattice volume with keeping the mass; i.e., increase of the mass density, this change leads to an increase in the number of carriers in each unit cell, so that carrier doping occurs. With a further increase in applied pressure, the solid cannot maintain the structure and consequently takes more stable structure. The external pressure is applied for superconductors. Cuprates have the highest T_c among all superconductors at ambient pressure, as explained in previous section. The T_c is enhanced by the application of external pressure; e.g., **Fig. 1-19** shows T_c of $\text{HgBa}_2\text{Ca}_2\text{Cu}_3\text{O}_x$ enhanced up to 164 K under high pressure of 31 GPa [111]. This dramatic enhancement of T_c also occurs in *TM*-based chalcogenides. **Figure 1-20** summarizes T_c in FeSe under external pressure [112]. Although FeSe exhibits superconductivity at $T_c = 8\text{K}$ [55], the T_c increases to 37 K at 8.9 GPa. These results should indicate that the distortion induced by external pressure effectively tunes the electronic structure, especially the Fermi level.

1.1.2.2 Chemical pressure

Next, chemical pressure is introduced by internal change in the solid. The trigger is an alternation of constituent elements with others possessing different ionic radii through chemical substitution. The increase in the chemical pressure contributes to the stimulation of distortion in the crystal lattice and the resultant structure phase transition, where other crystal structures are stabilized because the total energy of the other structure becomes lower than that of the primitive structure due to the introduced distortion.

Perovskite-type structure, which is identified by the octahedral local structure, has many derivatives induced by the distortion, where the highest symmetry structure is cubic with space group of $Pm\bar{3}m$. SrTiO_3 is one of the *TM*-based cubic perovskite-oxides. The CBM

and VBM are composed of Ti $3d$ -orbitals and O $2p$ -orbitals, which attribute to nonbonding states of Ti $3d$ -orbitals and O $2p$ -orbitals, as will be explained in detail in **Chapter 7**. Because the energy level of CBM should be suitable for n -type doping, SrTiO₃ exhibits electric conduction by e.g., Nb⁵⁺ doping of Ti⁴⁺-site; while the p -type conduction is challenging due to the intrinsic deep energy level of O $2p$ -orbital.

It is well known that the derivatives (i.e., superstructure) of cubic perovskite is stimulated by the tilting of B cation–C anion–B cation bond angle (i.e., distortion) in ABC₃, where A and B are metal cations and C is an anion [113]. The relationship of space groups is depicted in **Figs. 1-21** and **1-22**. Here, the tilting is dominated by the ionic radii of constituents, which is described by using the tolerance factor (t); $t = (d_A + d_C) / [\sqrt{2} \times (d_B + d_C)]$, where d_A , d_B , and d_C denote ionic radii of A cation, B cation, and C anion [114]. In case of $t \approx 1$, the compound generally forms a cubic perovskite structure; while in case that t is far from 1, a derivative superstructure is stabilized. By the stabilization of the superstructure, the electronic structure also changes. Longer-periodic superstructure in real space forms shorter-periodic Brillouin Zone in reciprocal space. This formed small Brillouin Zone leads to band folding, as will be explained in **Chapter 7**. This suggests that bands at specific a k point transfer to the other point via formation of the superstructure. Even though cubic TM -oxide perovskites generally have an indirect band gap; e.g., SrTiO₃ ($E_g = 3.25$ eV), appropriately introduced distortion results in the formation of a suitable superstructure for the band folding and subsequent changes in the electronic structure to direct band gap. CdSnO₃ have an orthorhombic structure with space group of $Pnma$ that is regarded as $\sqrt{2} \times 2 \times \sqrt{2}$ superstructure extended from the cubic cell. **Figure 1-23** is its calculated band structure, where the superstructure results in band folding and resultant direct band gap [115].

Since this has been studied in perovskite-oxides, this should be able to extend also to TM -based chalcogenides. Moreover, Ch employed as a C anion has an advantage compared with

O to effectively introduce the distortion owing to the larger ionic radius.

1.1.2.3. Epitaxial strain by thin film growth

When a material is heteroepitaxially grown on a substrate, the in-plane lattice of the deposited material is attracted by that of the substrate. Consequently, epitaxial strain is introduced into the deposited material, where the largeness of the introduced strain strongly reflects lattice mismatch between the substrate and the deposited material. Since this strain is generally anisotropic; e.g., when an in-plane lattice shrinks, the out-of-plane lattice expands, the anisotropic change in the lattice leads to changes in distance between each atom in the structure and the volume, representing a variation of overlap of the wave functions of atoms and carrier density. Because the overlap is related to electron localization at an atom and electron transfer between atoms, electron correlation should vary; for instance, metal-insulator transition is stimulated by the application of epitaxial strain. In some perovskite-oxides such as LaTiO_3 , LaVO_3 , NdNiO_3 , and SrIrO_3 [116–118], a metallic or insulating electric property was obtained by altering the single crystal substrate, as seen in **Fig. 1-24**. This suggests that an epitaxial strain would change the electronic structure; i.e., electron correlation. In *TM*-chalcogenides, a similar change in electronic structure should be expected to appear, if it is possible to fabricate the epitaxial thin film and effectively introduce the strain. Hence, the appropriate electronic structure would be designed for electric conductive functionalities through the introduction of these structural distortion into *TM-Chs*.

1.2. Objective of Present Study

As the research targets of the present study, the superconductor and the light-emitting *n*- and *p*-type semiconductor constituted by nd^1 *TM*- and *eTM*-based chalcogenides are selected because they have critical issues, as follows.

As explained in **1.1.1.**, T_c of *FeCh* can be enhanced up to > 77 K by fabricating the monolayer. However, it has still been low compared to cuprates, although they have a similar

electronic phase diagram for doping (**Figs. 1-4** for cuprates and **1-25** for Fe-based superconductors). Hence, exploration of novel FeCh-based superconductors and/or the establishment of a concept for enhancement of the T_c in existing FeCh-based superconductors are necessary.

On the other hand, light-emitting semiconductors are key components in practical optoelectronic devices, such as light-emitting diodes (LEDs), laser diodes, and solar cells. Although light-emitting technologies have been widely applicable, there is a strong demand for next-generation new materials to exhibit higher performance in terms of light brightness, quantum efficiency, and color accuracy [119]. Currently, GaN- and GaAs-based IIIb-Vb semiconductors have been employed commercially for light-emitting devices. However, they have a serious issue. **Figure 1-26** summarizes the external quantum efficiency in GaN- and GaAs-based LEDs, as a function of emission wavelength. The emission quantum efficiency drastically decreases in a wavelength region around green and yellow, i.e., it decreases from $\sim 70 - 80\%$ in the red- and blue-light regions to $\sim 15\%$ in the green region (~ 530 nm) or $\sim 20\%$ in the yellow region (~ 570 nm) [120, 121]. This fact is called the ‘green gap problem’ and represents that there is no green-light source bright enough to realize the next-generation optoelectronic devices. Therefore, it is necessary to explore new semiconductor materials with a high quantum efficiency of the emission in the green wavelength region ($E_g = 2.18-2.50$ eV, $\lambda = 495-570$ nm) and n - and p -type dopability. As seen in 1.1.1., some eTM - and nd^l TM -based chalcogenides have noteworthy electronic transport properties, while the optical properties are not suitable for efficient green emission due to band gaps that are narrower than the green wavelength in TM -dichalcogenides and forbidden transition in ZrOS. Thus, a novel concept for the exploration of green-emitting semiconductors along with n - and p -type dopabilities is strongly required.

In **1.1.1.**, the notable characteristics of eTM - and nd^l TM -based chalcogenides and the

relationship between change in electronic structure and structural distortion, such as strain, as well as chemical pressure, are reviewed. According to the review, the required electric conductive functionalities should be designed by using change in electronic structure induced by distortion for *TM*-based chalcogenides and actualized appropriate carrier doping. Thus, the objective of this study is to design electronic conductive functionalities in *TM*-based chalcogenides based on an electronic structure tuned by structural distortion and to experimentally validate the effectiveness of the design concepts by performing carrier doping.

To realize high- T_c superconductivity and efficient light emission of *n*- and *p*-types semiconductor, two individual concepts are proposed.

i) Concept for the superconductor is to dope high density electrons of *FeCh*-based compounds with strong electron-electron correlation stimulated by epitaxial strain for inducement of high- T_c superconductivity.

ii) The light-emitting semiconductors are designed in *eTM*-based chalcogenides with strategies for *n*- and *p*-type conduction based on dopings using nonbonding states of CBM and VBM, and for realizing direct band gaps based on band folding derived from the construction of superstructure stimulated by distortion of chemical pressure. (**Fig. 1-27**).

This thesis is summarized into nine chapters as follow;

Chapter 1 provides the background of this study and gives its objectives.

Chapter 2 describes epitaxial thin film growth of strained FeSe exhibiting insulator-like

electric transport property and unveils the origin of the insulator-like behavior.

Chapter 3 describes the influence of surface degradation of the FeSe channel layer on electronic transport properties of FeSe-EDLT under an electric field.

Chapter 4 validates the effectiveness of the concept to induce high- T_c superconductivity using a strongly electron-correlated $FeCh$ -based parent, FeSe, and performing electrostatic electron doping via using EDLT structure.

Chapter 5 proposes key factors to induce high- T_c superconductivity stimulated in an FeSe-EDLT with respect to the thin film growth condition and accumulated electron density.

Chapter 6 describes the heteroepitaxial growth of metastable tetragonal FeS and evaluation of the electronic transport properties with/without electrostatic carrier doping.

Chapter 7 designed green emitting n - and p -type semiconductor based on nonbonding state and band folding derived from distortion, and experimentally validates the optical and electronic transport properties of perovskite-type chalcogenide, $SrHfS_3$.

Chapter 8 describes heteroepitaxial thin film growth of $AEHfS_3$ ($AE = Sr$ and Ba) and the characterization of the optical properties.

Chapter 9 summarizes this study.

References

1. H. Kamerling Onnes, *Akad. Van Wet. Amst.*, **14**, 113 (1911).
2. J. Bardeen, L. N. Cooper, and J. R. Schrieffer, *Phys. Rev.*, **108**, 1175 (1957).
3. D. Jérôme, A. Mazaud, M. Ribault, and K. Bechgaard, *J. Phys. Lett.*, **41**, 95–98 (1980).
4. A. F. Hebard, M. J. Rosseinsky, R. C. Haddon, D. W. Murphy, S. H. Glarum, T. T. M. Palstra, A. P. Ramirez, and A. R. Kortan, *Nature*, **350**, 600–601 (1991).
5. K. Tanigaki, T. W. Ebbsen, S. Saito, J. Mizuki, J. S. Tsai, Y. Kudo, and S. Kuroshima, *Nature*, **352**, 222–223 (1991).
6. J. Nagamats, N. Nakagawa, T. Muranaka, Y. Zenitani, and J. Akimitsu, *Nature*, **410**, 63–64 (2001).
7. A. P. Drozdov, M. I. Eremets, I. A. Troyan, V. Ksenofontov, and S. I. Shylin, *Nature*, **525**, 73–76 (2015).
8. J. G. Bednorz and K. A. Müller, *Z. Für Phys. B Condens. Matter.*, **64**, 189–193 (1986).
9. A. Schilling, M. Cantoni, J. D. Guo, and H. R. Ott, *Nature*, **363**, 56–58 (1993).
10. D. J. Scalapino, *Phys. Rep.*, **250**, 329–365 (1995).
11. D. J. Scalapino, *Rev. Mod. Phys.*, **84**, 1383 (2012).
12. H. Yanagi, H. Kawazoe, A. Kudo, M. Yasukawa, and H. Hosono, *J. Electroceram.*, **4**, 407–414 (2000).
13. H. Hosono, *Jpn. J. Appl. Phys.*, **52**, 090001 (2013).
14. H. Kawazoe, M. Yasukawa, H. Hyodo, M. Kurita, H. Yanagi, and H. Hosono, *Nature*, **389**, 939–942 (1997).
15. A. Kudo, H. Yanagi, H. Hosono, and H. Kawazoe, *Appl. Phys. Lett.*, **73**, 220 (1998).
16. K. Nomura, H. Ohta, K. Ueda, T. Kamiya, M. Hirano, and H. Hosono, *Science*, **300**, 1269–1272 (2003).
17. A. Tsukazaki, A. Ohtomo, and M. Kawasaki, *Appl. Phys. Lett.*, **88**, 152106 (2006).

18. A. Tsukazaki, A. Ohtomo, T. Onuma, M. Ohtani, T. Makino, M. Sumiya, K. Ohtani, S. F. Chichibu, S. Fuke, Y. Segawa, H. Ohno, H. Koinuma, and M. Kawasaki, *Nat. Mater.*, **4**, 42–46 (2005).
19. H. Jeon, J. Ding, A. V. Nurmikko, W. Xie, M. Kobayashi, and R. L. Gunshor, *Appl. Phys. Lett.*, **60**, 892 (1992).
20. W. Xie, D. C. Grillo, R. L. Gunshor, M. Kobayashi, H. Jeon, J. Ding, A. V. Nurmikko, G. C. Hua, and N. Otsuka, *Appl. Phys. Lett.*, **60**, 1999 (1992).
21. J. Lee, V. C. Sundar, J. R. Heine, M. G. Bawendi, and K. F. Jensen, *Adv. Mater.*, **12**, 1102–1105 (2000).
22. X. Wu, *Solar Energy*, **77**, 803–814 (2004).
23. Y. Wu, C. Wadia, W. Ma, B. Sadtler, and A. P. Alivisatos, *Nano Lett.*, **8**, 2551–2555 (2008).
24. P. Jackson, D. Hariskos, E. Lotter, S. Paetel, R. Wuerz, R. Menner, W. Wischmann, and M. Powalla, *Prog. Photovolt: Res. Appl.*, **19**, 894–897 (2011).
25. K. Ueda, S. Inoue, S. Hirose, H. Kawazoe, and H. Hosono, *Appl. Phys. Lett.*, **77**, 2701 (2000).
26. M.-L. Liu, F.-Q. Huang, L.-D. Chen, Y.-M. Wang, Y.-H. Wang, G.-F. Li, and Q. Zhang, *Appl. Phys. Lett.*, **90**, 072109 (2007).
27. A. M. Diamond, L. Corbellini, K. R. Balasubramaniam, S. Chen, S. Wang, T. S. Matthews, L.-W. Wang, R. Ramesh, and J. W. Ager, *Phys. Status Solidi. A*, **209**, 2101–2107 (2012).
28. J. E. Bernard and A. Zunger, *Phys. Rev. B*, **36**, 3199 (1987).
29. D. J. Chadi, *J. Cryst. Growth*, **138**, 295–300 (1994).
30. I. Suemune, K. Yamada, H. Masato, T. Kanda, Y. Kan and M. Yamanishi, *Jpn. J. Appl. Phys.*, **27**, L2195–L2198 (1988).

31. S. B. Zhang, S.-H. Wei, A. Zunger, and H. Katayama-Yoshida, *Phys. Rev. B*, **57**, 9642 (1998).
32. J. Srour, M. Badawi, F. El Haj Hassan, and A. V. Postnikov, *Phys. Status Solidi. A*, **253**, 1472–1475 (2016).
33. T. Irie, S. Endo, and S. Kimura, *Jpn. J. Appl. Phys.*, **18**, 1303–1310 (1979).
34. S. Siebentritt, *Thin Solid Films*, **403–404**, 1– 8 (2002).
35. P. Reinhard, A. Chirilă, P. Blösch, F. Pianezzi, S. Nishiwaki, S. Buecheler, and A. N. Tiwari, *IEEE J. Photovolt.*, **3**, 572–580 (2013).
36. H. Kamioka, H. Hiramatsu, K. Hayashi, M. Hirano, and H. Hosono, *J. Photochem. Photobiol. A Chem.*, **166**, 141–147 (2004).
37. K. Ueda, K. Takafuji, H. Yanagi, T. Kamiya, H. Hosono, H. Hiramatsu, M. Hirano, and N. Hamada, *J. Appl. Phys.*, **102**, 113714 (2007).
38. S. Inoue, K. Ueda, H. Hosono, and N. Hamada, *Phys. Rev. B*, **64**, 245211 (2001).
39. K. Ueda and H. Hosono, *J. Appl. Phys.*, **91**, 4768 (2002).
40. K. Ueda, H. Hosono, and N. Hamada, *J. Appl. Phys.*, **98**, 043506 (2005).
41. K. Ueda, K. Takafuji, H. Hiramatsu, H. Ohta, T. Kamiya, M. Hirano, and H. Hosono, *Chem. Mater.*, **15**, 3692–3695 (2003).
42. H. Hiramatsu, K. Ueda, K. Takafuji, H. Ohta, M. Hirano, T. Kamiya, and H. Hosono, *J. Appl. Phys.*, **94**, 5805 (2003).
43. H. Hiramatsu, K. Ueda, H. Ohta, M. Hirano, T. Kamiya, and H. Hosono, *Appl. Phys. Lett.*, **82**, 1048 (2003).
44. H. Hiramatsu, T. Kamiya, T. Tohei, E. Ikenaga, T. Mizoguchi, Y. Ikuhara, K. Kobayashi, and H. Hosono, *J. Am. Chem. Soc.*, **132**, 15060–15067 (2010).
45. H. Hiramatsu, H. Kamioka, K. Ueda, M. Hirano, and H. Hosono, *J. Ceram. Soc. Jpn.*, **113**, 10–16 (2005).

46. H. Hiramatsu, K. Ueda, T. Kamiya, H. Ohta, M. Hirano, and H. Hosono, *J. Phys. Chem. B*, **108**, 17344–17351 (2004).
47. H. Hiramatsu, K. Ueda, H. Ohta, T. Kamiya, M. Hirano, and H. Hosono, *Appl. Phys. Lett.*, **87**, 211107 (2005).
48. D. B. Laks, C. G. Van de Walle, G. F. Neumark, and S. T. Pantelides, *Phys. Rev. Lett.*, **66**, 648 (1991).
49. Y. Kamihara, H. Hiramatsu, M. Hirano, R. Kawamura, H. Yanagi, T. Kamiya, and H. Hosono, *J. Am. Chem. Soc.*, **128**, 10012–10013 (2006).
50. Y. Kamihara, T. Watanabe, M. Hirano, and H. Hosono, *J. Am. Chem. Soc.*, **130**, 3296–3297 (2008).
51. H. Hosono and K. Kuroki, *Physica C*, **514**, 399–422 (2015).
52. H. Hosono, A. Yamamoto, H. Hiramatsu, Y. Ma, *Materials Today*, **21**, 278–302 (2018).
53. G. R. Stewart, *Rev. Mod. Phys.*, **83**, 1589 (2011).
54. Z.-A. Ren, W. Lu, J. Yang, W. Yi, X.-L. Shen, C. Zheng, G.-C. Che, X.-L. Dong, L.-L. Sun, F. Zhou, and Z.-X. Zhao, *Chin. Phys. Lett.*, **25**, 2215 (2008).
55. F.-C. Hsu, J.-Y. Luo, K.-W. Yeh, T.-K. Chen, T.-W. Huang, P. M. Wu, Y.-C. Lee, Y.-L. Huang, Y.-Y. Chu, D.-C. Yan, and M.-K. Wu, *Proc. Natl. Acad. Sci. USA.*, **105**, 14262–14264 (2008).
56. Y. Mizuguchi and Y. Takano, *J. Phys. Soc. Jpn.*, **79**, 102001 (2010).
57. M.-K. Wu, M.-J. Wang, and K.-W. Yeh, *Sci. Technol. Adv. Mater.*, **14**, 014402 (2013).
58. T. B. Massalski and H. Okamoto, *Binary Alloy Phase Diagrams* 2nd edition, Ohio: ASM International (1990).
59. X. Lai, H. Zhang, Y. Wang, X. Wang, X. Zhang, J. Lin, and F. Huang, *J. Am. Chem. Soc.*, **137**, 10148–10151 (2015).
60. C. K. H. Borg, X. Zhou, C. Eckberg, D. J. Campbell, S. R. Saha, J. Paglione, and E. E.

- Rodriguez, *Phys. Rev. B*, **93**, 094522 (2016).
61. I. A. Zaliznyak, Z. Xu, J. M. Tranquada, G. Gu, A. M. Tsvelik, and M. B. Stone, *Phys. Rev. Lett.*, **107**, 216403 (2011).
 62. Y. Xiao, Y. Su, C. M. N. Kumar, C. Ritter, R. Mittal, S. Price, J. Perbon and Th. Brückel, *Eur. Phys. J. B*, **82**, 113–121 (2011).
 63. M. Suzuki, R. Arita, and H. Ikeda, *Phys. Rev. B*, **92**, 085116 (2015).
 64. A. Subedi, L. Zhang, D. J. Singh, and M. H. Du, *Phys. Rev. B*, **78**, 134514 (2008).
 65. T. Hanaguri, S. Niitaka, K. Kuroki, and H. Takagi, *Science*, **328**, 474–476 (2010).
 66. Q. Fan, W. H. Zhang, X. Liu, Y. J. Yan, M. Q. Ren, R. Peng, H. C. Xu, B. P. Xie, J. P. Hu, T. Zhang, and D. L. Feng, *Nat. Phys.*, **11**, 946–952 (2015).
 67. I. I. Mazin, D. J. Singh, M. D. Johannes, and M. H. Du, *Phys. Rev. Lett.*, **101**, 057003 (2008).
 68. H. Kontani and S. Onari, *Phys. Rev. Lett.*, **104**, 157001 (2010).
 69. Y. Mizuguchi, F. Tomioka, S. Tsuda, T. Yamaguchi, and Y. Takano, *J. Phys. Soc. Jpn.*, **78**, 074712 (2009).
 70. Y. Imai, Y. Sawada, F. Nabeshima, and A. Maeda, *Proc. Natl. Acad. Sci. USA.*, **112**, 1937–1940 (2015).
 71. K.-W. Yeh, T.-W. Huang, Y.-L. Huang, T.-K. Chen, F.-C. Hsu, P. M. Wu, Y.-C. Lee, Y.-Y. Chu, C.-L. Chen, J.-Y. Luo, D.-C. Yan, and M.-K. Wu, *Euro. Phys. Lett.*, **84**, 37002 (2008).
 72. J. Guo, S. Jin, G. Wang, S. Wang, K. Zhu, T. Zhou, M. He, and X. Chen, *Phys. Rev. B*, **82**, 180520(R) (2010).
 73. F. Ye, S. Chi, Wei Bao, X. F. Wang, J. J. Ying, X. H. Chen, H. D. Wang, C. H. Dong, and M. Fang, *Phys. Rev. Lett.*, **107**, 137003 (2011).
 74. T. P. Ying, X. L. Chen, G. Wang, S. F. Jin, T. T. Zhou, X. F. Lai, H. Zhang, and W. Y.

- Wang, *Sci. Rep.*, **2**, 426 (2012).
75. U. Pachmayr, F. Nitsche, H. Luetkens, S. Kamusella, F. Brückner, R. Sarkar, H.-H. Klauss, and D. Johrendt, *Angew. Chem. Int. Ed.*, **54**, 293–297 (2015).
76. X. F. Lu, N. Z. Wang, H. Wu, Y. P. Wu, D. Zhao, X. Z. Zeng, X. G. Luo, T. Wu, W. Bao, G. H. Zhang, F. Q. Huang, Q. Z. Huang, and X. H. Chen, *Nat. Mater.*, **14**, 325–329 (2015).
77. M. Burrard-Lucas, D. G. Free, S. J. Sedlmaier, J. D. Wright, S. J. Cassidy, Y. Hara, A. J. Corkett, T. Lancaster, P. J. Baker, S. J. Blundell, and S. J. Clarke, *Nat. Mater.*, **12**, 15–19 (2013).
78. A. Krzton-Maziopa, E. V. Pomjakushina¹, V. Y. Pomjakushin, F. von Rohr, A. Schilling, and K. Conder, *J. Phys.: Condens. Matter.*, **24**, 382202 (2012).
79. T. Hatakeda, T. Noji, T. Kawamata, M. Kato, and Y. Koike, *J. Phys. Soc. Jpn.*, **82**, 123705 (2013).
80. L. Zhao, A. Liang, D. Yuan, Y. Hu, D. Liu, J. Huang, S. He, B. Shen, Y. Xu, X. Liu, L. Yu, G. Liu, H. Zhou, Y. Huang, X. Dong, F. Zhou, K. Liu, Z. Lu, Z. Zhao, C. Chen, Z. Xu, and X. J. Zhou, *Nat. Commun.*, **7**, 10608 (2016).
81. Z. Wang, C. Liu, Y. Liu, and J. Wang, *J. Phys.: Condens. Matter.*, **29**, 153001 (2017).
82. S. Tan, Y. Zhang, M. Xia, Z. Ye, F. Chen, X. Xie, R. Peng, D. Xu, Q. Fan, H. Xu, J. Jiang, T. Zhang, X. Lai, T. Xiang, J. Hu, B. Xie, and D. Feng, *Nat. Mater.* **12**, 634–640 (2013).
83. Q. Y. Wang, Z. Li, W.-H. Zhang, Z.-C. Zhang, J.-S. Zhang, W. Li, H. Ding, Y.-B. Ou, P. Deng, K. Chang, J. Wen, C.-L. Song, K. He, J.-F. Jia, S.-H. Ji, Y.-Y. Wang, L.-L. Wang, X. Chen, X.-C. Ma, and Q.-K. Xue, *Chin. Phys. Lett.*, **29**, 037402 (2012).
84. J.-F. Ge, Z.-L. Liu, C. Liu, C.-L. Gao, D. Qian, Q.-K. Xue, Y. Liu, and J.-F. Jia, *Nat Mater.*, **14** 285–289 (2015).

85. J. Hu, Y. Zhang, M. Law, and R. Wu, *J. Am. Chem. Soc.*, **134**, 13216–13219 (2012).
86. P. Lazic, R. Armiento, F. W. Herbert, R. Chakraborty, R. Sun, M. K. Y. Chan, K. Hartman, T. Buonassisi, B. Yildiz and G. Ceder, *J. Phys.: Condens. Matter.*, **25**, 465801 (2013).
87. P. P. Altermatt, T. Kieseewetter, K. Ellmer, and H. Tributsch, *Sol. Energy Mater. Sol. Cells*, **71**, 181–195 (2002).
88. I. J. Ferrer, D. M. Nevskaja, C. de las Heras, C. Sánchez, *Solid State Commun.*, **74**, 913–916 (1990).
89. J. A. Wilson and A. D. Yoffe, *Adv. Phys.*, **18**, 193–335 (1969).
90. S. Ogawa, *J. Appl. Phys.*, **50**, 2308 (1979).
91. J. A. Wilson and G. D. Pitt, *Philos. Mag.*, **23**, 1297–1310 (1971).
92. X. Yao, J. M. Honig, T. Hogan, C. Kannewurf, and J. Spalek, *Phys. Rev. B*, **54**, 17469 (1996).
93. B. Sipos, A. F. Kusmartseva, A. Akrap, H. Berger, L. Forró, and E. Tutiš, *Nature Mater.*, **7**, 960–965 (2008).
94. R. A. Klemm, *Physica C*, **514**, 86–94 (2015).
95. Y. Yu, F. Yang, X. F. Lu, Y. J. Yan, Y.-H. Cho, L. Ma, X. Niu, S. Kim, Y.-W. Son, D. Feng, S. Li, S.-W. Cheong, X. H. Chen, and Y. Zhang, *Nat. Nanotechnol.*, **10**, 270–276 (2015).
96. K. Kobayashi and J. Yamauchi, *Phys. Rev. B*, **51**, 17085 (1995).
97. A. Splendiani, L. Sun, Y. Zhang, T. Li, J. Kim, C.-Y. Chim, G. Galli, and F. Wang, *Nano Lett.*, **10**, 1271–1275 (2010).
98. T. Kanazawa, T. Amemiya, A. Ishikawa, V. Upadhyaya, K. Tsuruta, T. Tanaka, and Y. Miyamoto, *Sci. Rep.*, **6**, 22277 (2016).
99. X. Duan, C. Wang, A. Pan, R. Yu, and X. Duan, *Chem. Soc. Rev.*, **44**, 8859–8876 (2015)
100. M. Mikami and S. Nakamura, *J. Alloys Compd.*, **408–412**, 687–692 (2006).

101. M. Itoh and T. Inabe, *Phys. Rev. B*, **68**, 035107 (2003).
102. Q. Dai, H. Song, M. Wang, X. Bai, B. Dong, R. Qin, X. Qu, and H. Zhang, *J. Phys. Chem. C*, **112**, 19399–19404 (2008).
103. R. Vali, *Comput. Mater. Sci.*, **37**, 300–305 (2006).
104. B. Lei, Y. Liu, G. Tang, Z. Ye, C. Shi, *Mater. Chem. Phys.*, **87**, 227–232 (2004).
105. X. Wang, Z. Zhang, Z. Tang, Y. Lin, *Mater. Chem. Phys.*, **80**, 1–5 (2003).
106. Z. Liu, X. Sun, S. Xu, J. Lian, X. Li, Z. Xiu, Q. Li, D. Huo, and J.-G. Li, *J. Phys. Chem. C*, **112**, 2353–2358 (2008).
107. G. A. Kumar, M. Pokhrel, A. Martinez, R. C. Dennis, I. L. Villegas, and D. K. Sardar, *J. Alloys Compd.*, **513**, 559–565 (2012).
108. H. Mizoguchi, T. Kamiya, S. Matsuishi, and H. Hosono, *Nat. Commun.*, **2**, 470 (2011).
109. T. Arai, S. Iimura, J. Kim, Y. Toda, S. Ueda, and H. Hosono, *J. Am. Chem. Soc.*, **139**, 17175–17180 (2017).
110. T. Arai, S. Iimura, and H. Hosono, *Chem. Mater.*, **30**, 597–601 (2018).
111. L. Gao *et al.*, *Phys. Rev. B*, **50**, 4260 (1994).
112. S. Medvedev, T. M. McQueen, I. A. Troyan, T. Palasyuk, M. I. Eremets, R. J. Cava, S. Naghavi, F. Casper, V. Ksenofontov, G. Wortmann, and C. Felser, *Nature Mater.*, **8**, 630–633 (2009).
113. M. W. Lufaso and P. M. Woodward, *Acta Crystallogr. Sect. B-Struct. Sci.*, **57**, 725–738 (2001).
114. V. M. Goldschmidt, *Naturwissenschaften*, **14**, 477–485 (1926).
115. H. Mizoguchi, H. W. Eng, and P. M. Woodward, *Inorg. Chem.*, **43**, 1667–1680 (2004).
116. A. Biswas, K.-S. Kim, and Y. H. Jeong, *J. Appl. Phys.*, **116**, 213704 (2014).
117. C. He, T. D. Sanders, M. T. Gray, F. J. Wong, V. V. Mehta, and Y. Suzuki, *Phys. Rev. B*, **86**, 081401(R) (2012).

118. M. K. Stewart, J. Liu, M. Kareev, J. Chakhalian, and D. N. Basov, *Phys. Rev. Lett.*, **107**, 176401 (2011).
119. J. Y. Tsao, M. H. Crawford, M. E. Coltrin, A. J. Fischer, D. D. Koleske, G. S. Subramania, G. T. Wang, J. J. Wierer, and R. F. Karliceck Jr. *Adv. Opt. Mater.*, **2**, 809–836 (2014).
120. K. P. O'Donnell, M. Auf der Maur, A. D. Carlo, K. Lorenz, and the SORBET consortium, *Phys. Status Solidi RRL.*, **6**, 49–52 (2012).
121. M. Auf der Maur, A. Pecchia, G. Penazzi, W. Rodrigues, and A. D. Carlo, *Phys. Rev. Lett.*, **116**, 027401 (2016).
122. N. Barišić, M. K. Chan, Y. Li, G. Yu, X. Zhao, M. Dressel, A. Smontara, and M. Greven, *Proc. Natl. Acad. Sci. USA.*, **110**, 12235–12240 (2013).
123. H. Hosono, K. Tanabe, E. Takayama-Muromachi, H. Kageyama, S. Yamanaka, H. Kumakura, M. Nohara, H. Hiramatsu, and S. Fujitsu, *Sci. Technol. Adv. Mater.*, **16**, 033503 (2015).
124. A. Yamamoto, N. Takeshita, C. Terakura, and Y. Tokura, *Nat. Commun.*, **6**, 8990 (2015).
125. R. H. Mitchell, *Perovskites Modern and Ancient*, *Almaz Press Inc.* (2002).
126. M. W. Lufaso and P. M. Woodward, *Acta Cryst. B*, **57**, 725–738 (2001).
127. M. Neupane, P. Richard, Y.-M. Xu, K. Nakayama, T. Sato, T. Takahashi, A. V. Federov, G. Xu, X. Dai, Z. Fang, Z. Wang, G.-F. Chen, N.-L. Wang, H.-H. Wen, and H. Ding, *Phys. Rev. B*, **83**, 094522 (2011).

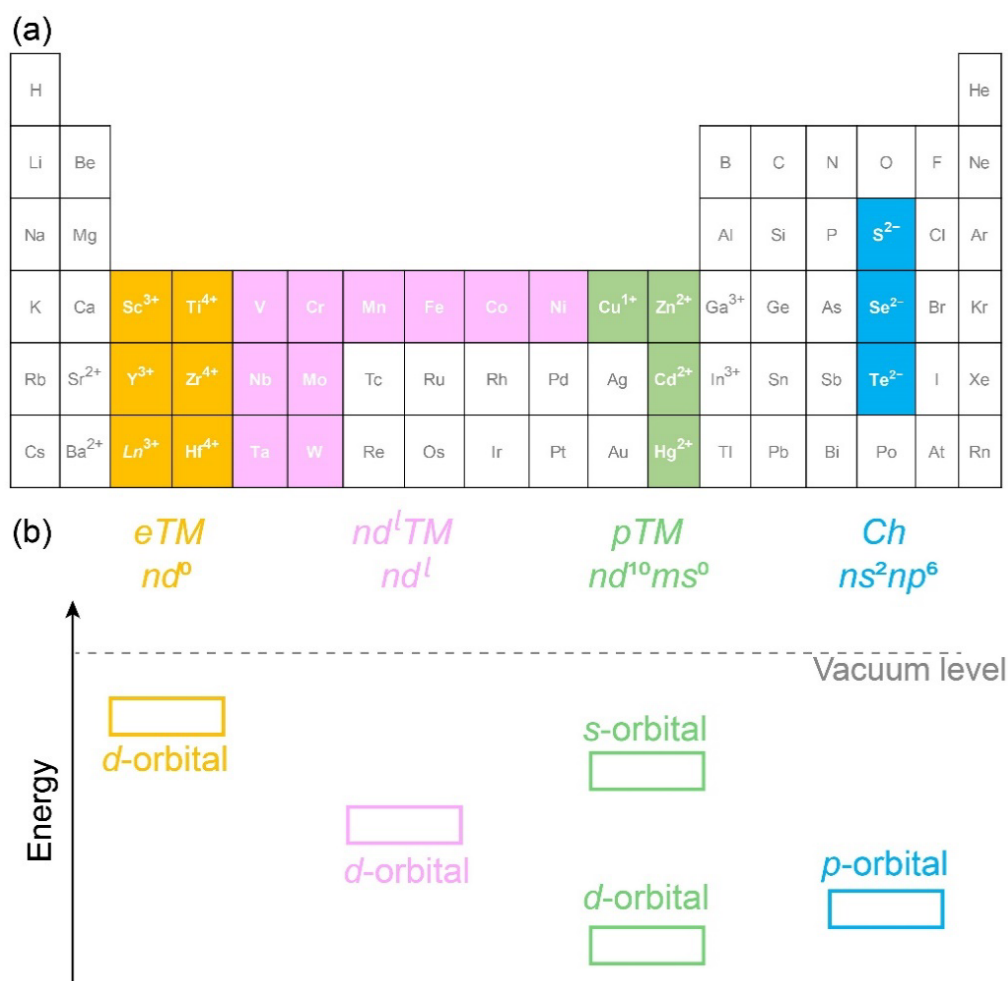


Figure 1-1. (a) Periodic table of elements. Orange, red, green, and blue colored elements are *e*TM, *nd^l* TM, *p*TM, and *Ch*, respectively. (b) Schematic energy diagram of orbitals.

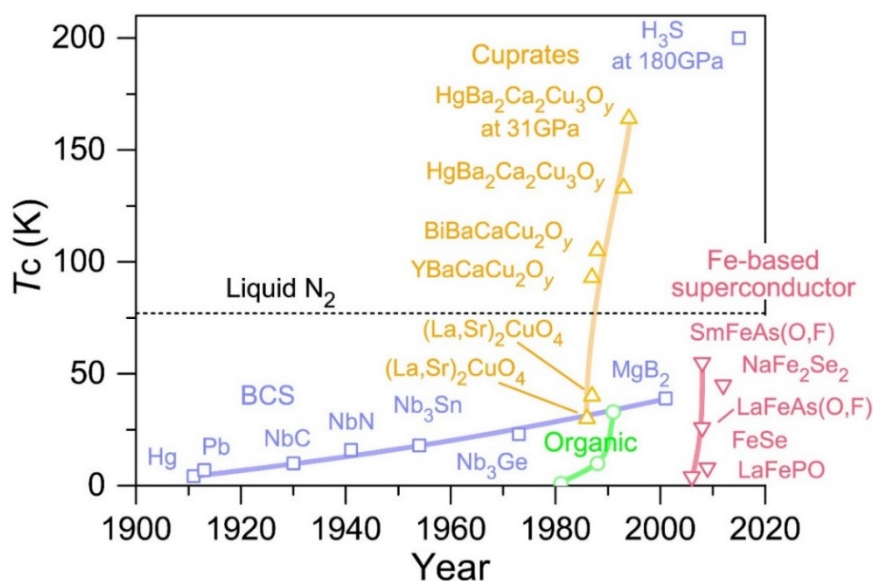


Figure 1-2. History of the discovery of superconductors. Blue squares, green circles, orange triangles, and red reversed-triangles represent T_c of BCS metals, organic, cuprates, and Fe-based superconductors, respectively.

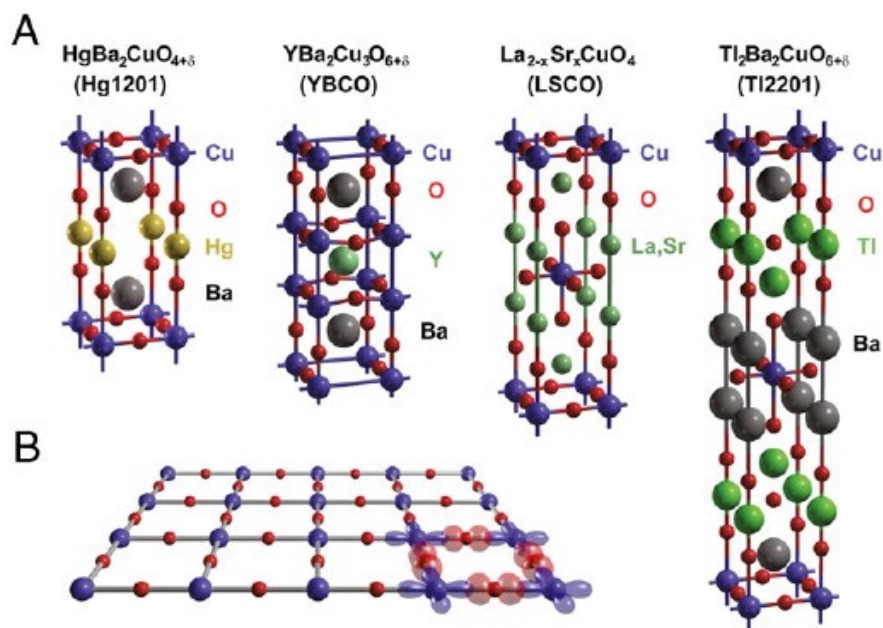


Figure 1-3. (a) Crystal structures of representative cuprate superconductors. (b) CuO₂ plane, where blue clovers and red dumbbells correspond to Cu 3*d*- and O 2*p*-orbitals [122].

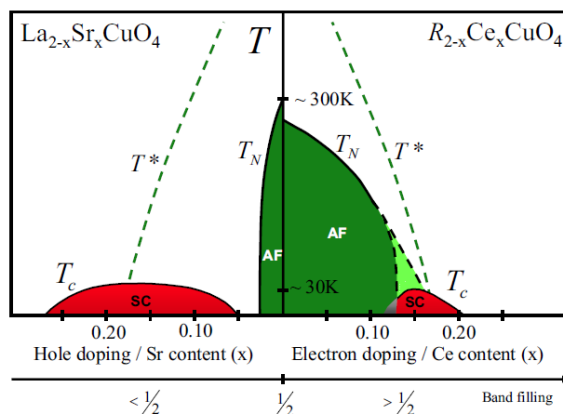


Figure 1-4. Electronic phase diagram of cuprates for electron- and hole-type dopings [8]. “AF” and “SC” filled in green and red denote antiferromagnetic and superconducting phases.

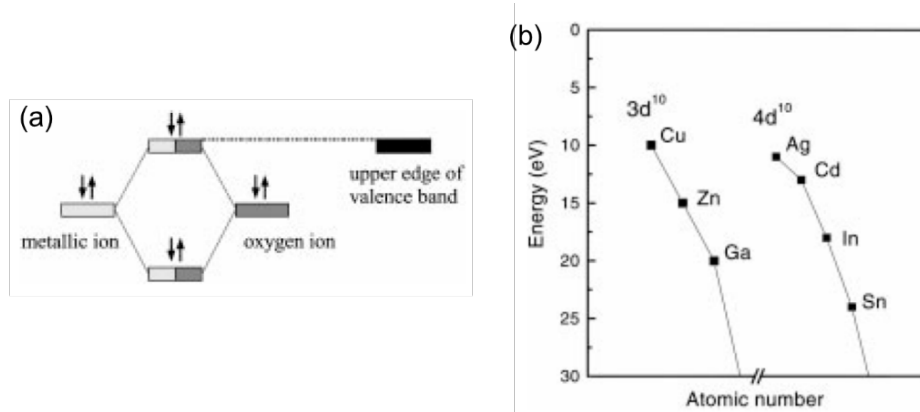


Figure 1-5. A chemical design concept to realize a wide gap p -type semiconductor using Cu $3d$ -orbitals [12]. (a) Chemical bonding between metal cation and oxygen. (b) Energy variation of $3d^{10}$ and $4d^{10}$ electrons of pTM .

Table 1-1. Summary of E_g , carrier polarity, and the mobilities of II-VI group semiconductors.

μ_n and μ_p denote mobilities of electron and hole.

| | E_g (eV) | Dopant | Mobility ($\text{cm}^2/\text{V}\cdot\text{s}$) |
|------|--------------------|---|--|
| ZnS | 3.6 (zinc blende) | n -type: Al^{3+} | |
| | 3.9 (wurtzite) | p -type: N^{3-} | |
| ZnSe | 2.8 (zinc blende) | n -type: Cl^{1-} , Al^{3+} , and Ga^{3+} | $\mu_e = \sim 700$ |
| | | p -type: N^{3-} | $\mu_h = \sim 15$ |
| ZnTe | 2.26 (zinc blende) | n -type: Cl^{1-} , Al^{3+} , and Ga^{3+} | $\mu_e = \sim 350$ |
| CdS | 2.42 (zinc blende) | n -type: In^{3+} | $\mu_e = \sim 120$ |
| | | p -type: Cu^{1+} | |
| CdSe | 1.74 (zinc blende) | n -type: Ga^{3+} | $\mu_e = \sim 580$ |
| | | p -type: N^{3-} | $\mu_h = \sim 50$ |
| CdTe | 1.5 (zinc blende) | n -type: Cl^{1-} | $\mu_e = \sim 57000$ |
| | | p -type: N^{3-} | $\mu_h = \sim 80$ |

Table 1-2. Summary of the E_g , hole mobility (μ_h) and carrier density (n) in $LnCuOCh$.

| | E_g (eV) | μ_h ($\text{cm}^2/\text{V}\cdot\text{s}$) | n (cm^{-3}) |
|---------|------------|---|--------------------------|
| YCuOSe | 2.58 | | |
| LaCuOS | 3.2 | 0.5 | 1×10^{19} |
| LaCuOSe | 2.8 | 8.0 | 2×10^{19} |
| LaCuOTe | | | |
| CeCuOS | | 0.8 | 3×10^{20} |
| PrCuOS | 3.03 | 0.5 | 1×10^{19} |
| NdCuOS | 2.98 | 0.3 | 1×10^{19} |

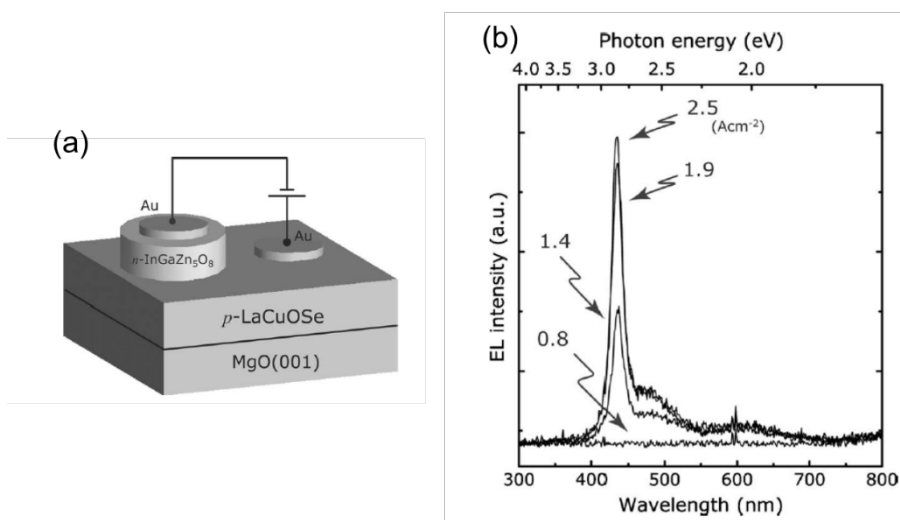


Figure 1-6. LED based on p -type LaCuOSe epitaxial layer [47]. (a) Device configuration of the LED, where InGaZn₅O₈ was employed as a n -type conductor. (b) Electroluminescence spectra of the LED at room temperature in each current density.

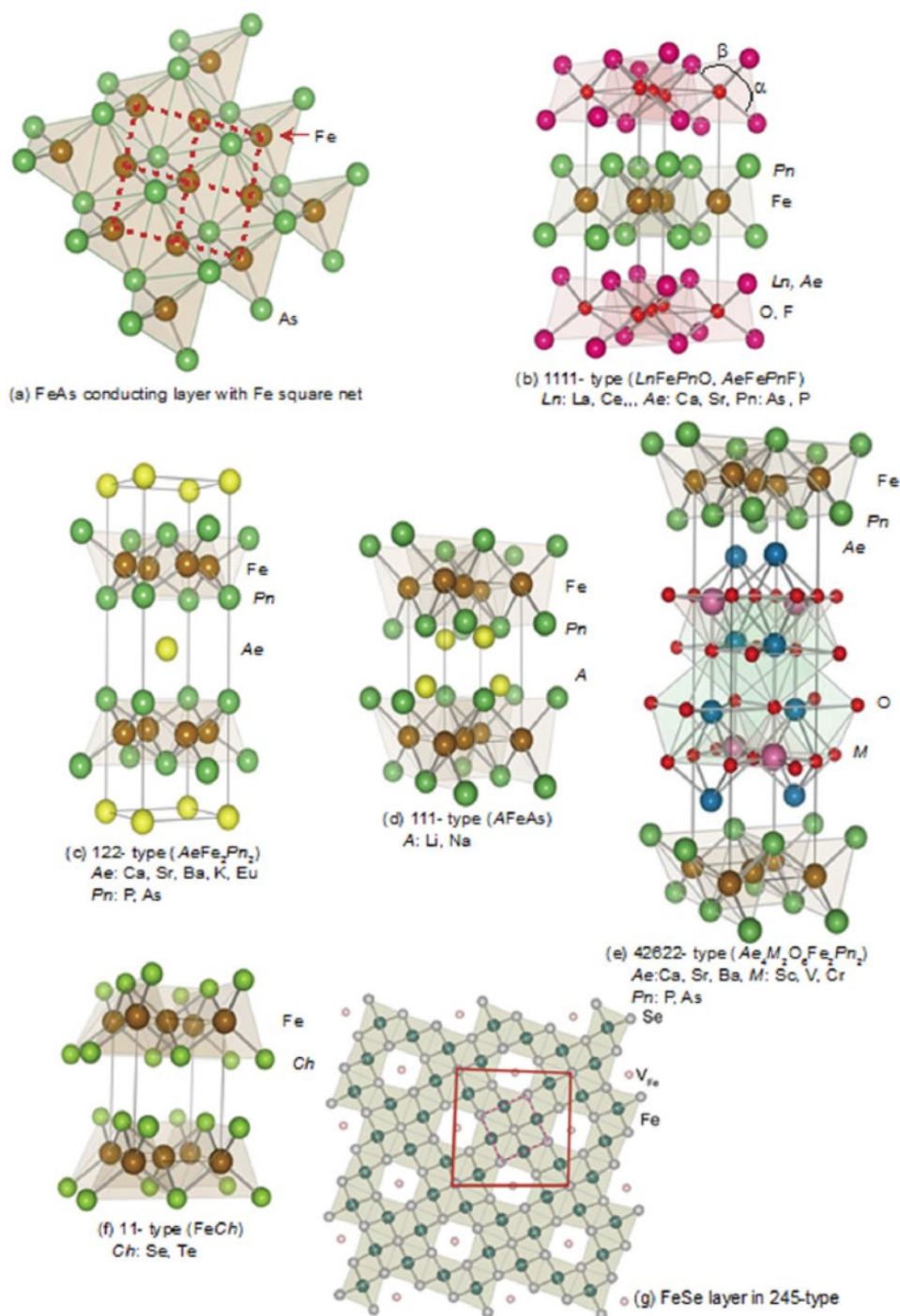


Figure 1-7. Crystal structures of some Fe-based superconductor families. (a) Common FePn/Ch conduction layer. Crystal structures of (b) 1111-, (c) 122-, (d) 111-, and (e) 42622-type FeAs -based superconductors. Unit cell of (d) 11-type FeCh and (e) the superstructure of 245-type FeCh -based compounds stimulated by Fe vacancy [123].

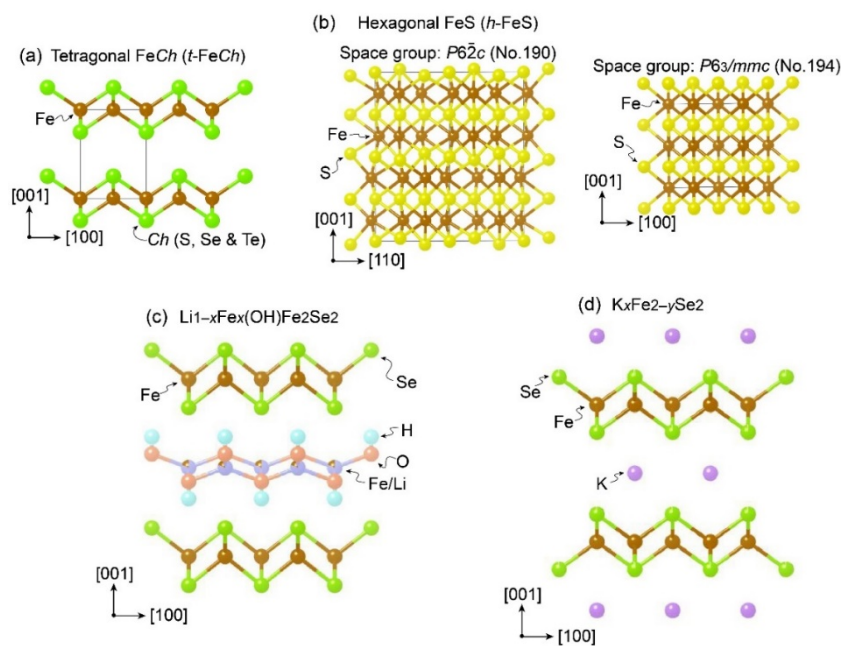


Figure 1-8. Crystal structure of (a) tetragonal FeCh, (b) competing two hexagonal phases, and intercalated FeCh; for instance, (c) $\text{Li}_{1-x}\text{Fe}_x(\text{OH})\text{Fe}_2\text{Se}_2$ and (d) $\text{K}_x\text{Fe}_{2-y}\text{Se}_2$.

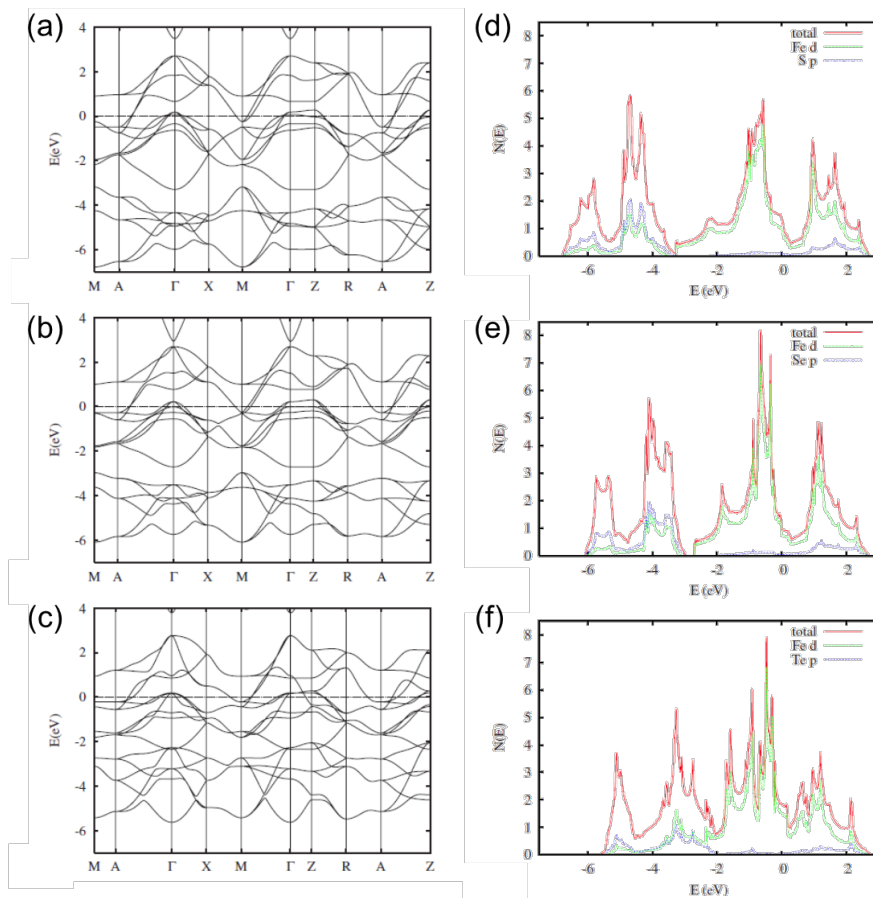


Figure 1-9. Calculated electronic structure of 11-type FeChs [64]. Band structures of (a) FeS, (b) FeSe, and (c) FeTe. Total (red) and partial (green for Fe 3*d*- and blue for Ch *p*-orbitals) density of states of (d) FeS, (e) FeSe, and (f) FeTe.

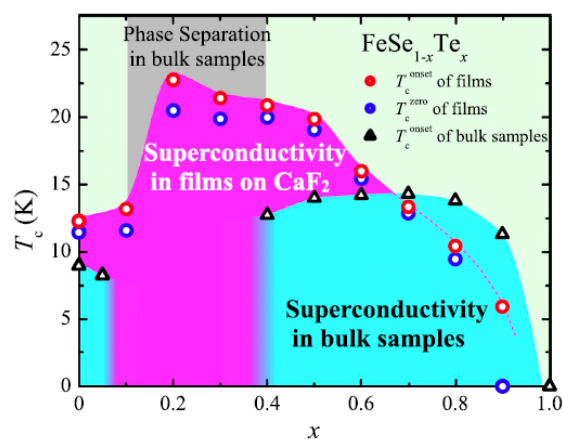


Figure 1-10. Phase diagram of Te-doped FeSe epitaxial thin films deposited on CaF₂ single crystal substrate [70].

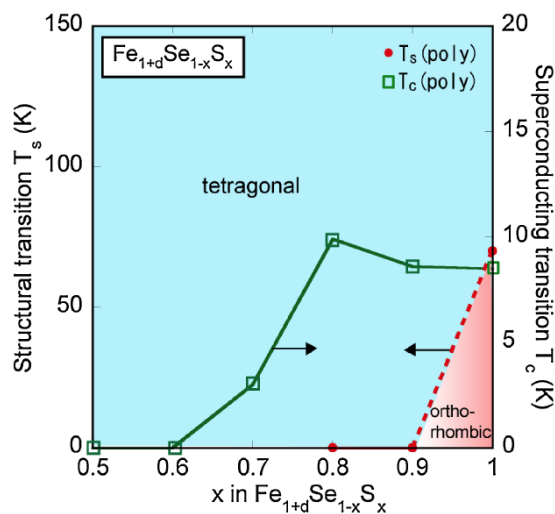


Figure 1-11. Phase diagram of S-doped FeSe [56].

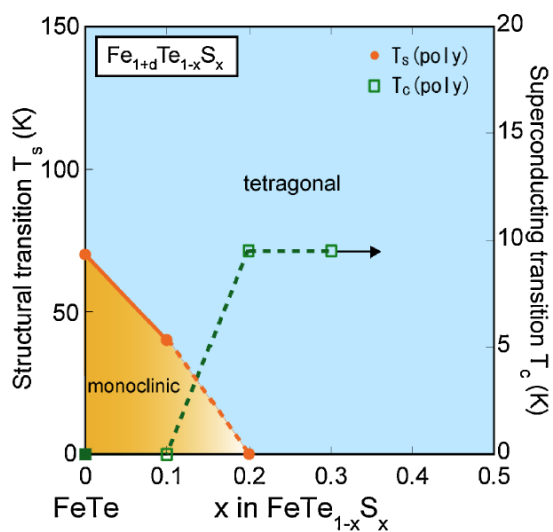


Figure 1-12. Phase diagram of S-doped FeTe [56].

Table 1-3. T_c of some FeCh-related compounds.

| Compounds | T_c (K) | Compounds | T_c (K) |
|---|-----------|---|-----------|
| FeS | 4 | $\text{Sr}_x\text{Fe}_{1-y}\text{Se}_2$ | 35 |
| FeSe | 8 | $\text{Ba}_x\text{Fe}_{1-y}\text{Se}_2$ | 39 |
| $\text{K}_x\text{Fe}_{1-y}\text{Se}_2$ | 32 | $\text{Eu}_x\text{Fe}_{1-y}\text{Se}_2$ | 40 |
| $\text{Rb}_x\text{Fe}_{1-y}\text{Se}_2$ | 32 | $\text{Yb}_x\text{Fe}_{1-y}\text{Se}_2$ | 42 |
| $\text{Cs}_x\text{Fe}_{1-y}\text{Se}_2$ | 29 | $\text{Li}_{0.6}(\text{NH}_2)_{0.2}(\text{NH}_3)_{0.8}\text{Fe}_2\text{Se}_2$ | 43 |
| $\text{Li}_x\text{Fe}_{1-y}\text{Se}_2$ | 44 | $\text{Na}_x(\text{NH}_3)_y\text{FeSe}$ | 32 |
| $\text{Na}_x\text{Fe}_{1-y}\text{Se}_2$ | 45 | $\text{Cs}_{0.4}(\text{NH}_3)_y\text{FeSe}$ | 31 |
| $\text{Ca}_x\text{Fe}_{1-y}\text{Se}_2$ | 40 | $\text{Li}_{1-x}\text{Fe}_x(\text{OH})\text{FeSe}$ | 43 |

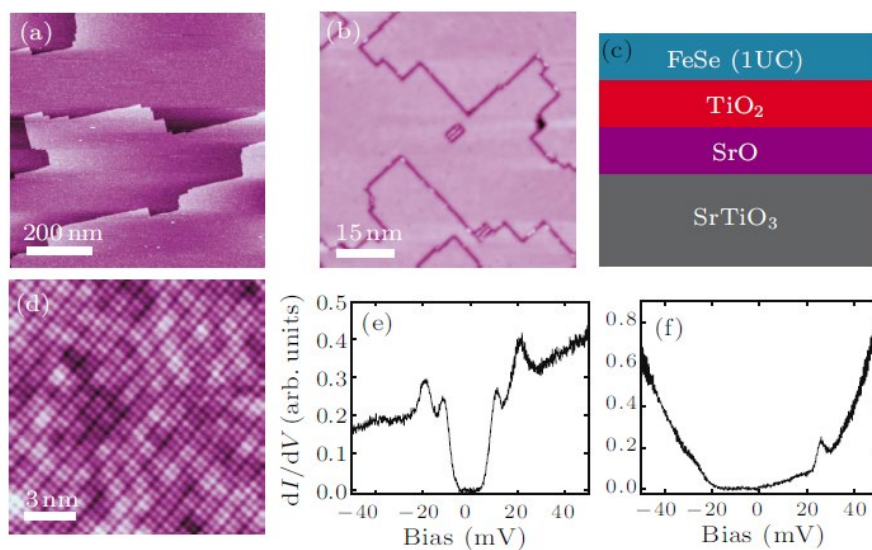


Figure 1-13. Monolayer FeSe fabricated on SrTiO₃ single crystal [83]. Scanning tunneling microscopy images of (a) SrTiO₃ and (b) monolayer FeSe surface. (c) Schematic configuration of monolayer FeSe. (d) High-resolution scanning tunneling microscopy image of the monolayer FeSe. Scanning tunneling spectra of (e) monolayer and (f) two-layer FeSe.

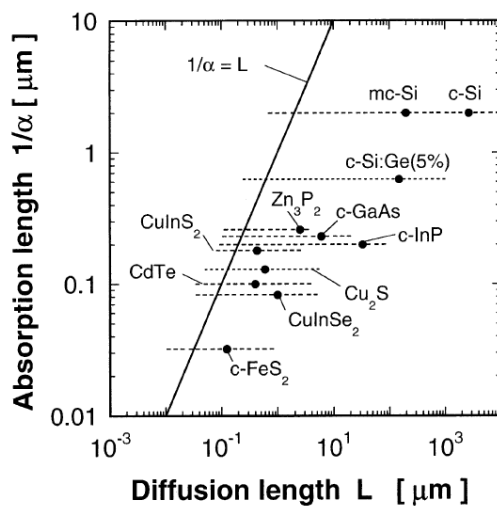


Figure 1-14. Absorption coefficient of some semiconductors [87].

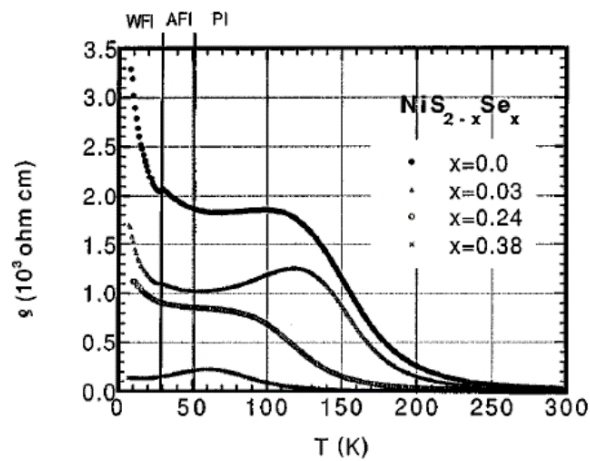


Figure 1-15. Temperature dependence of electric resistivity in Se-doped NiS_2 , as a function of Se-doping concentration [92].

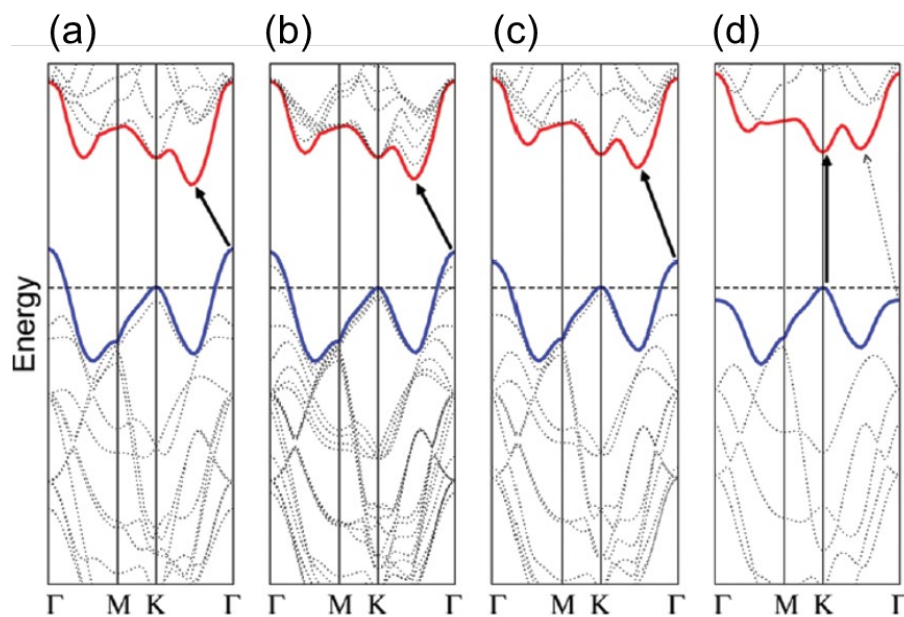


Figure 1-16. Thickness dependence of calculated band structure in MoS_2 [97]. The thickness decreases from (a) infinite (bulk), to (b) three layer, to (c), two layer, down to (d) monolayer. Red and blue lines trace the lowest energy bands of CBM and the highest energy bands of VBM at each k point.

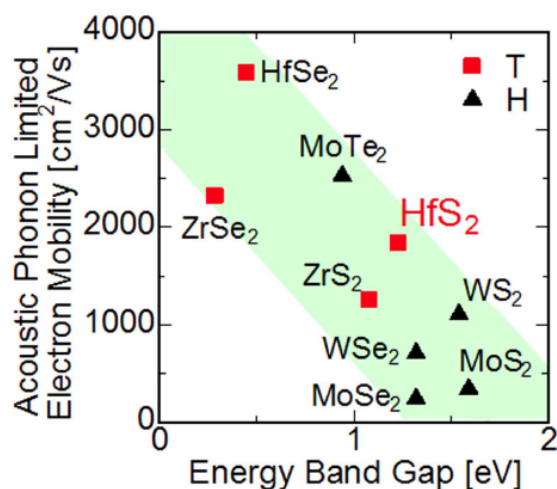


Figure 1-17. Relationship between electron mobility and band gap in some $TMCh_2$ [98]. Red squares and black triangles correspond to octahedral and triangle prism coordinate structures.

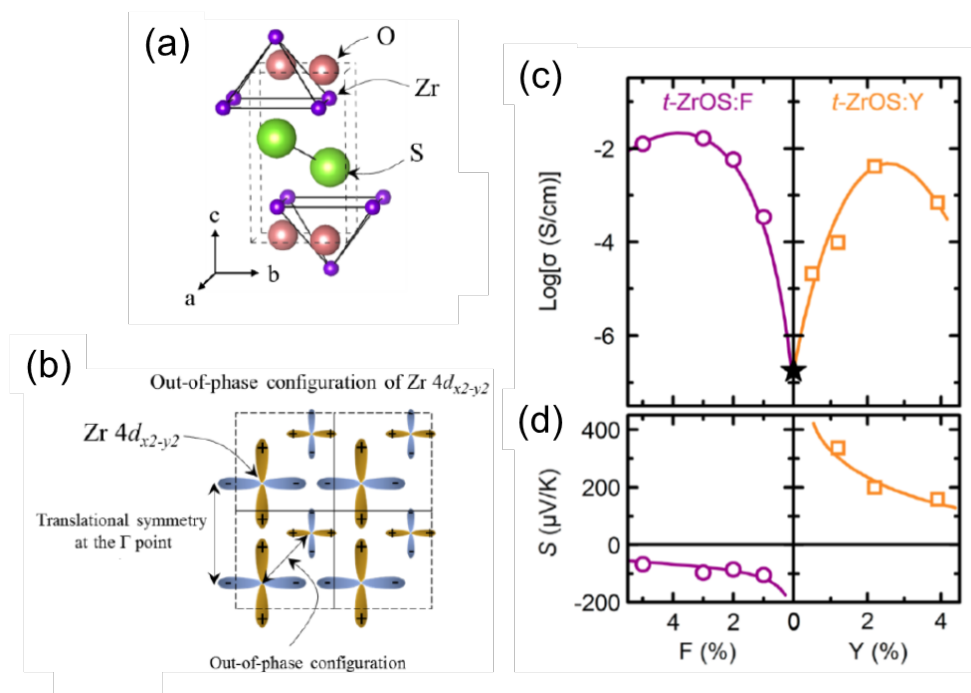


Figure 1-18. (a) Crystal structure of tetragonal ZrOS (t -ZrOS) [109]. (b) Orbital configuration of Zr $4d_{x^2-y^2}$ at Γ point, which constitutes CBM. (c) Electric conductivity and (d) Seebeck coefficient of t -ZrOS, as a function of F- and Y-substitution concentrations for electron- and acceptor-dopings, respectively.

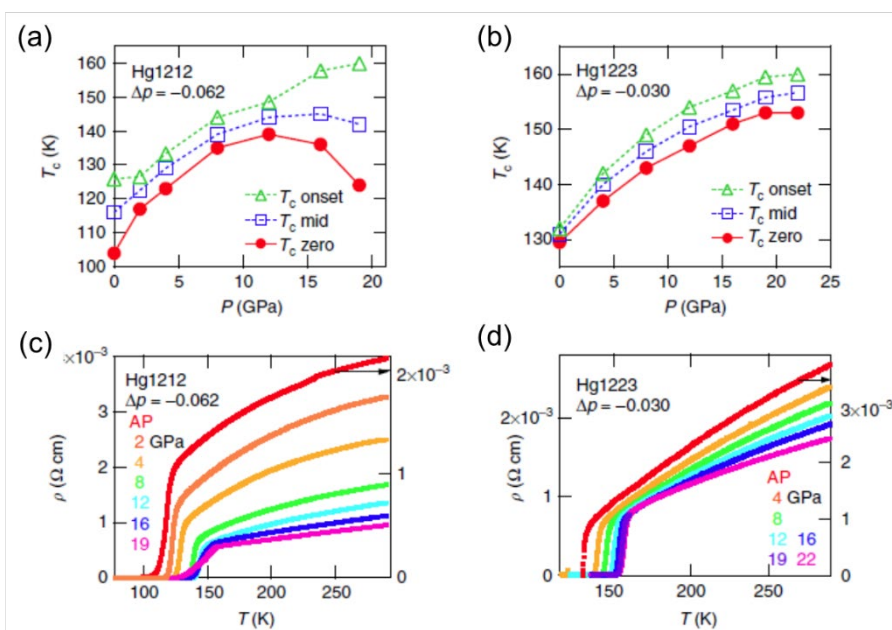


Figure 1-19. High pressure effects on superconductivity in cuprates [124]. Relationship between T_c and applied pressure in (a) Hg1212 ($\text{HgBa}_2\text{CaCu}_2\text{O}_{6+\delta}$) and (b) Hg1223 ($\text{HgBa}_2\text{Ca}_2\text{Cu}_3\text{O}_{8+\delta}$). Green triangles, blue squares, red circles denote onset, mid, and zero T_c , respectively. Temperature dependence of electric resistivity in (c) Hg1212 and (d) Hg1223 as a function of applied external pressure.

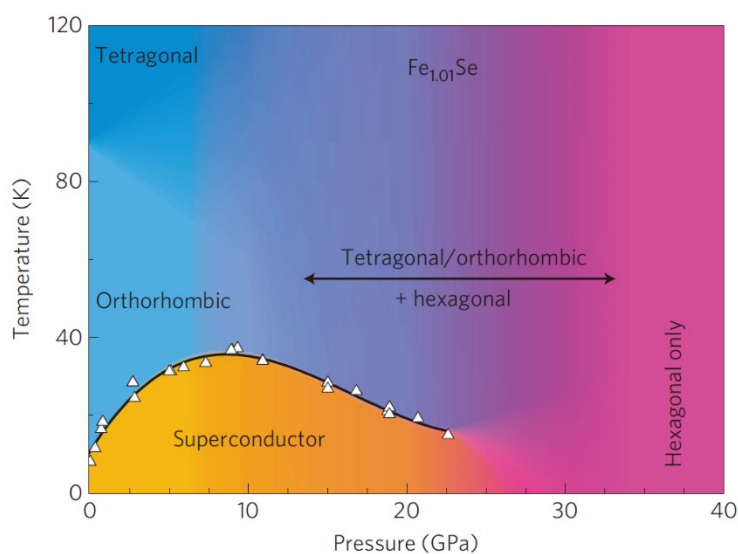


Figure 1-20. Phase diagram of FeSe under high pressure [112]. Open triangles indicate T_c at each pressure.

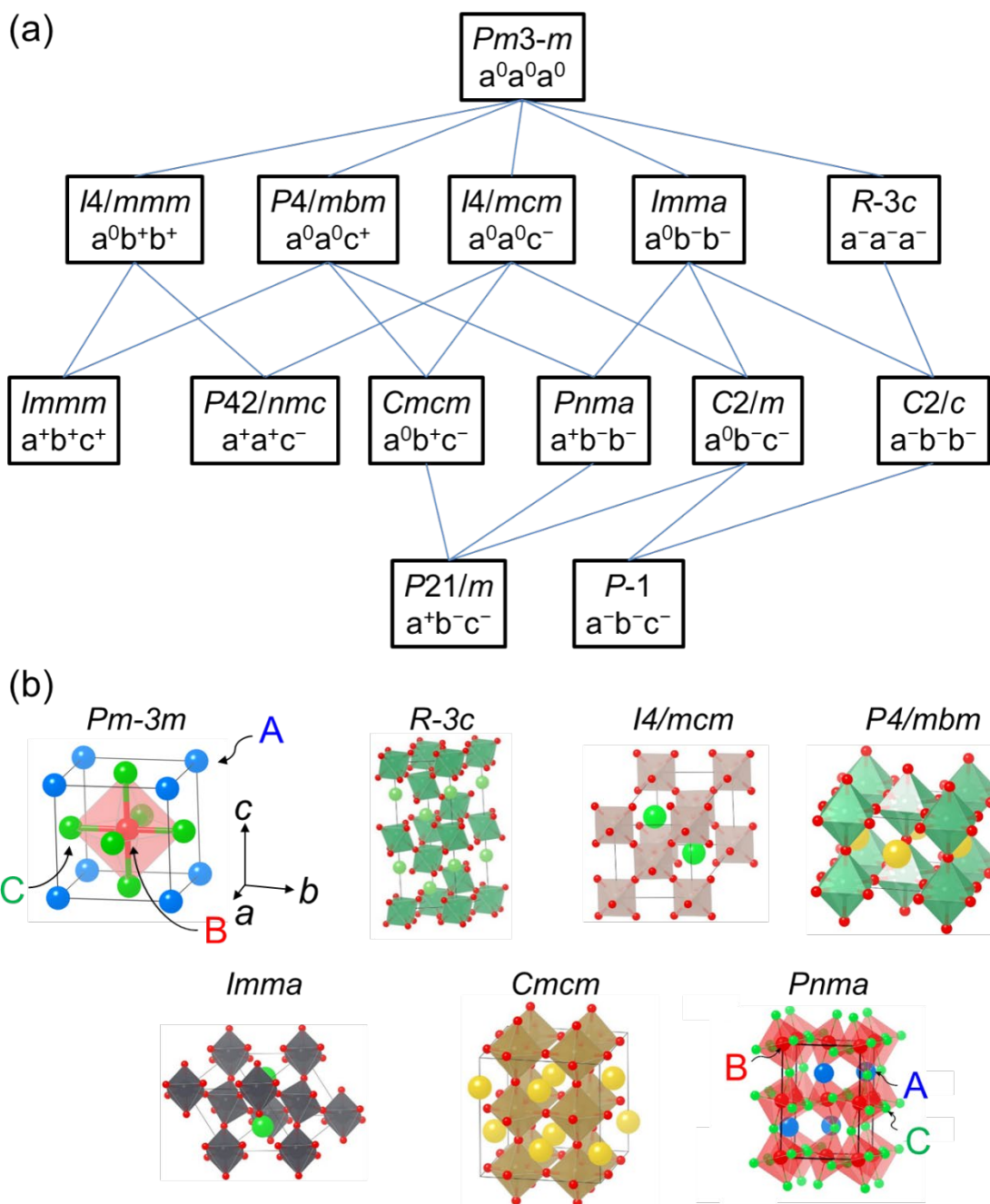


Figure 1-21. (a) Relationship between space groups associated with superstructure in perovskite-type structure [125]. (b) Primitive cells of some perovskite derivatives.

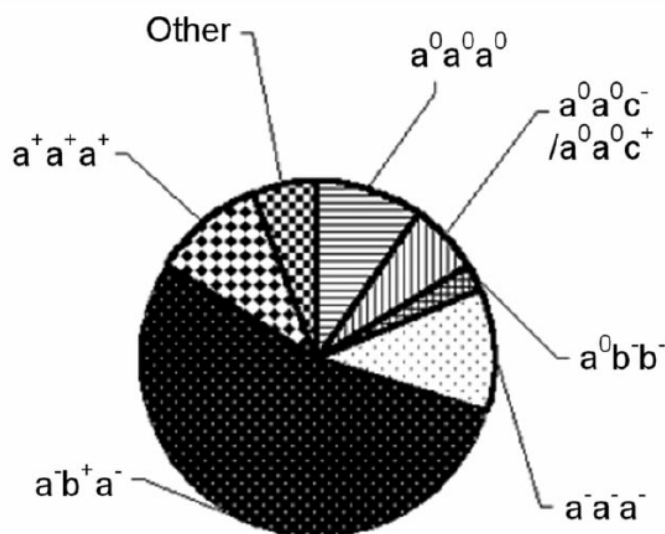


Figure 1-22. Distribution of crystal structure in simple perovskite-oxides in terms of tilting system [126].

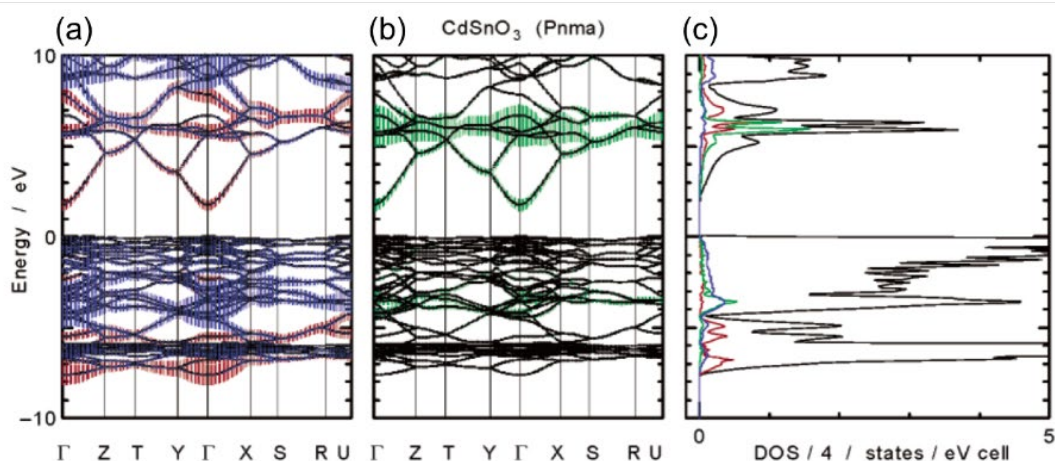


Figure 1-23. Electronic structure of CdSnO_3 with distorted perovskite-type crystal structure. The band structures with respect to (a) Sn 5s (red) and Sn 5p (blue), and (b) Cd 5s orbitals (green). (c) The density of states, where the black line corresponds to the total amount of partial density of states of O, Sn 5s- (red), Sn 5p- (blue), and Cd 5s-orbital (green) contribution.

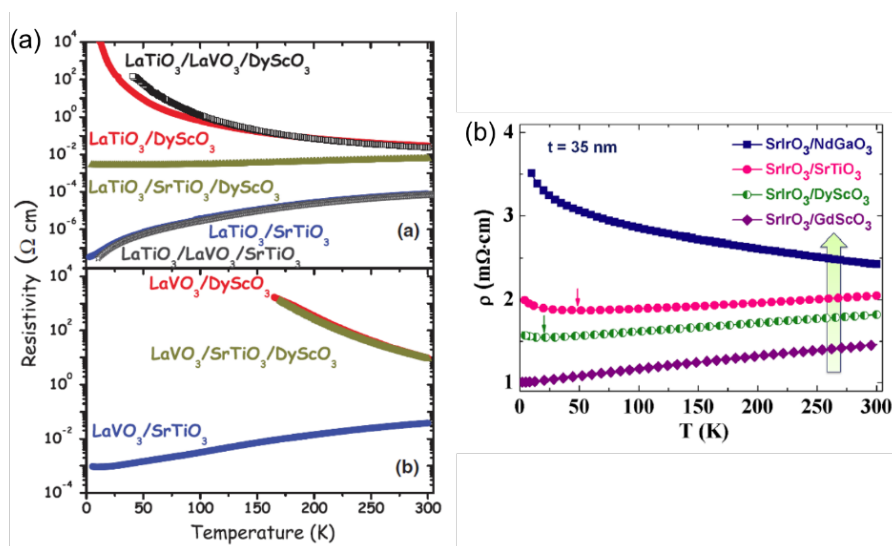


Figure 1-24. Temperature dependence of resistivity in some oxide Mott insulators, (a) $\text{La}(\text{Ti}/\text{V})\text{O}_3$ and (b) SrIrO_3 , epitaxial thin films as a function of single crystal substrates [116, 117].

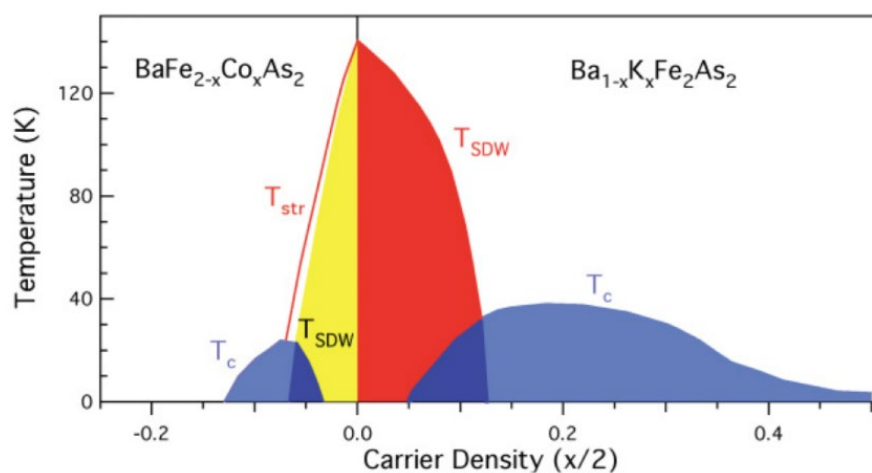


Figure 1-25. Electronic phase diagram of BaFe_2As_2 , as a function of electron- and hole-doping density [127].

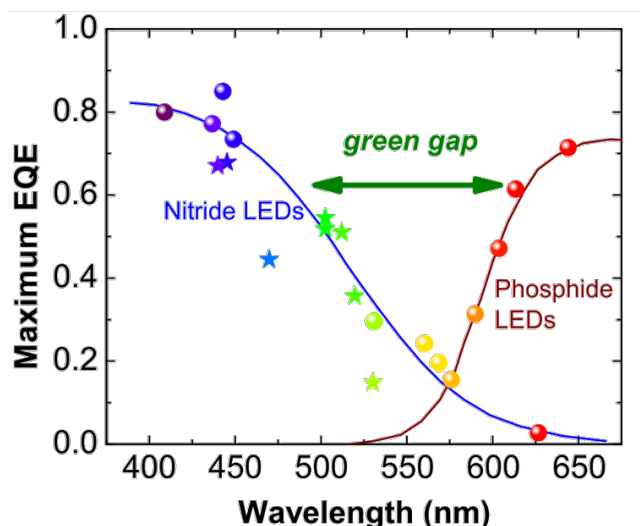


Figure 1-26. External quantum efficiency of III-nitride and III-phosphide based LEDs, as a function of the emission wavelength [121].

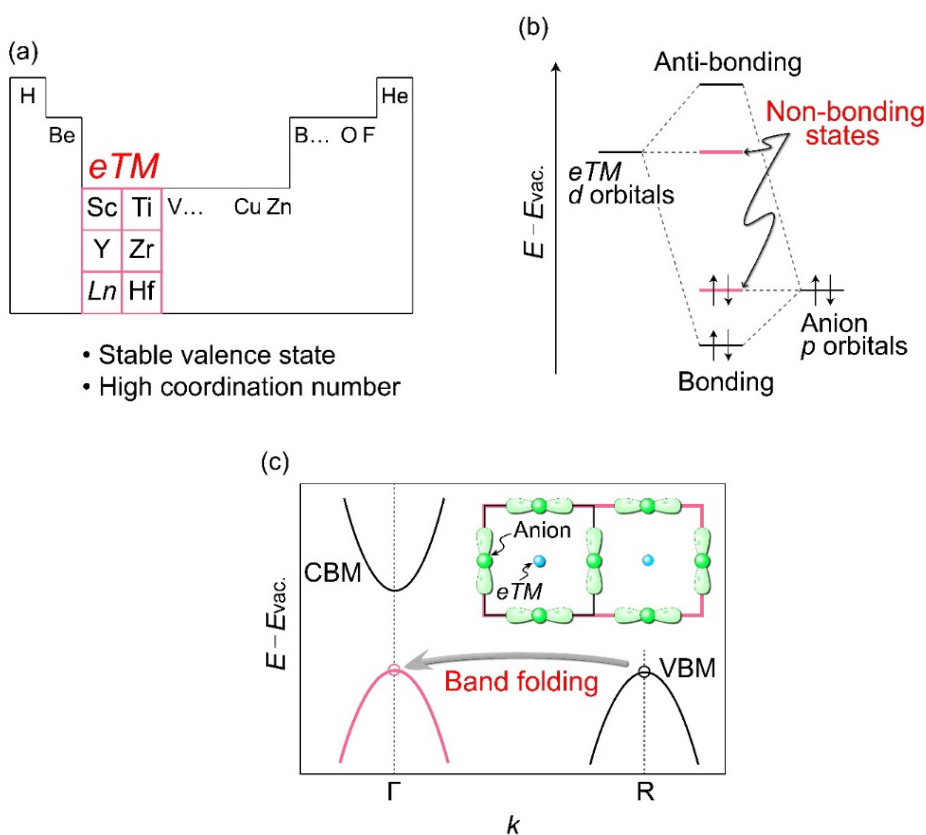


Figure 1-27. Schematic images of materials design concept to realize light-emitting *n*- and *p*-types semiconductors with high defect tolerance. (a) Schematic periodic table in terms of *eTM*. (b) Chemical bonding between metal cation and anion in ionic compound. (c) Band folding for realization of direct-type transition.

Chapter 2. Fabrication of Insulator-Like FeSe Thin Films and Determination of the Origin

2.1. Strategy on Enhancement of T_c in Fe-Based Superconductors

The iron (Fe)-based superconductor $\text{LaFeAsO}_{1-x}\text{F}_x$ was discovered in early 2008 [1] and has invoked intensive effort to explore new related superconductors as well as investigate their physical properties and the origin/mechanism of their superconductivity [2–4]. However the maximum critical temperature (T_c) of Fe-based superconductors have not exceeded that of cuprates, which have the highest T_c at ambient pressure; the maximum T_c of Fe-based superconductors is 55 K (F^{1-} - or H^{1-} -doped SmFeAsO) [5, 6], while that of cuprates is 134 K ($\text{HgBa}_2\text{Ca}_2\text{Cu}_3\text{O}_x$) [7]. Here it should be noted that prediction of new high- T_c superconductors is one of the most difficult issues in condensed matter physics, although theories and calculation methods have recently been very rapidly advancing [2]. Thus it is worthwhile exploring ways to enhance T_c of existing Fe-based superconductors.

It was considered that comparison of similarity and difference between Fe-based superconductors and cuprates should propose a strategy to enhance T_c in Fe-based superconductors. Their major similarities are i) the electronic phase diagram and ii) possession of a particular conduction layer. Each electronic phase diagram is seen in ref. 8 for cuprates and 9 for an Fe-based superconductors. Both of the parent phases (i.e., undoped states) generally do not exhibit superconductivity, but usually have long-range antiferromagnetic ordering. Through electron- or hole-type carrier doping of the parent phases, the magnetic ordering suppresses with increase in doping concentration and then vanishes. Corresponding to the vanishment, superconductivity appears. In the doping

process, the dopants supply carrier into conduction layers of FePn_4 or FeCh_4 octahedra layers in case of Fe-based superconductors, and CuO_2 layers in cuprates.

In contrast, the differences are i) maximum T_c in the systems, ii) parent electronic properties, and iii) superconducting pairing symmetry that is s -wave superconductivity in Fe-based superconductors; while d -wave one in cuprates. Difference of the T_c would be related to their parent electronic phases; that is, strength of electron-electron correlation. Parent phases of cuprates are Mott insulators with much higher Néel temperature (T_N) than room temperature due to the strong electron localization feature attributing to Cu and O; while those of Fe-based superconductors are metals with lower T_N than room temperature [10] due to weaker electron localization derived from Fe and Pn or Ch . These similarities and differences indicate that if there are Fe-based compounds with high T_N (i.e., strong electron correlation), it would be possible to actualize high T_c through doping.

One of the Fe-based superconductors, FeSe ($T_c = 8$ K at polycrystalline bulk state [11]), is an interesting material, because the electronic transport properties are easily tuned through the epitaxial thin film growth. T_c of an FeSe epitaxial film deposited on a CaF_2 substrate was raised up to 11.4 K [12] because of the introduced compressive in-plane lattice strain like application of external pressure [13, 14]. Conversely, when FeSe films were deposited on SrTiO_3 (STO) and MgO substrates, the electron transport properties of the films exhibited interesting thickness dependences. For thick films (≥ 200 nm), T_c was almost the same as that of the bulk; in contrast, for thin films (≤ 50 nm), superconductivity disappeared [15] and insulator-like behavior (i.e., increasing resistivity with decreasing temperature) was observed [16, 17]. Although the insulator-like behavior has been proposed to originate from the lattice strain in the film [15] and/or highly textured FeSe surface (i.e., the coexistence of non-superconducting and granular superconducting phases) [18, 19], the physical origin and

mechanism of the insulator-like behavior of the thin FeSe film have been still under debate. If the origin of the insulator-like behavior is related to change in the electron correlation, insulator-like FeSe is a promising candidate of high- T_c superconductor and may exhibit high T_c by electron doping.

Hence in this **Chapter**, relationship between the insulator-like behavior and epitaxial strain introduced through the thin film growth is examined by preparing ~10 nm thick FeSe epitaxial films with various chemical compositions.

2.2. Experimental Procedure

2.2.1. MBE Growth of FeSe thin films

Epitaxial FeSe thin films were grown by molecular beam epitaxy (MBE) using an EV-100/PLD-S growth chamber (Eiko, Japan) under a base pressure of $<1 \times 10^{-7}$ Pa. An (00 l)-oriented STO single crystal was used as a substrate, which was thermally annealed at 1050 °C in air after etching in buffered HF to obtain an atomically flat surface prior to film deposition [20]. The STO substrate was heated in the MBE growth chamber using an infrared semiconductor laser (LU0915C300-6, Lumics GmbH, Germany, $\lambda = 915$ nm) through a thin back-plate made of stainless steel to absorb the infrared laser irradiation and raise the substrate temperature (T_s) from 350 to 700 °C, which was calibrated using a thermocouple directly connected to a sapphire single-crystal plate. Fe (99.99%) and Se (99.999%) were evaporated from separate Knudsen cells and the flux of each element was controlled by the cell temperature with a beam flux monitor positioned just beneath the substrate.

2.2.2. Structural and compositional analyses

Crystalline phase and structure were characterized along the out-of-plane (i.e., vertical diffraction to the substrate surface) and in-plane (i.e., parallel to) directions by X-ray

diffraction (XRD) using a SmartLab diffractometer (Rigaku, Japan) with Cu $K\alpha_1$ radiation that was monochromated with a two-bounce Ge (220) crystal. The geometry of these axes of the XRD apparatus can be found in ref. 21. In situ reflection high energy electron diffraction (RHEED) observation at an acceleration voltage of 20 kV was also performed in the MBE growth chamber to confirm the heteroepitaxial growth of FeSe. Film crystallinity was evaluated using the rocking-curve full width at half maximum (FWHM) values of the out-of-plane 001 ($\Delta\omega$) and in-plane 200 ($\Delta\phi$) diffractions. In the out-of-plane rocking-curve measurements, an additional two-bounce Ge (220) crystal was mounted in front of the scintillation detector to achieve the higher angle-dispersion resolution of $\Delta\omega < 0.001^\circ$ instead of the usual optics with $\Delta\omega < 0.01^\circ$. The surface roughness was characterized by the root mean square roughness (R_{rms}) estimated from surface morphology in topography images captured by atomic force microscopy (AFM) on a MultiMode8 scanning probe microscope (Bruker Nano Inc., USA) using a tapping mode and optical cantilever. Film thickness was controlled in the ranges of 15–20 nm (to optimize T_s) and ~10 nm (to optimize chemical composition) to grow films that exhibited insulator-like behavior. Film thickness was precisely determined by X-ray reflectivity (XRR) or analysis of interference fringes around the FeSe 001 out-of-plane diffraction peak. For films with rough surfaces (i.e., thickness were not able to be determined by XRR and XRD), a stylus profiler (Alpha-Step D-120, KLA-Tencor, USA) was used to roughly estimate their thicknesses. Chemical compositions of the films (i.e., the atomic ratio of Fe to Se, [Fe]/[Se]) were determined by wavelength-dispersive X-ray fluorescence (XRF) using an S8 Tiger spectrometer (Bruker AXS, Germany). The XRF signals for Fe and Se were initially calibrated using quantitative analysis results of electron probe microanalysis obtained with a JXA-8530F analyzer (JEOL, Japan) because the quantitative reliability of this technique was confirmed in ref. 22. To determine the chemical compositions of large lateral-size segregated grains, field-emission

scanning electron microscopy (FE-SEM) using a JSM-7600F electron microscope (JEOL) with an energy-dispersive X-ray (EDX) detector in point-analysis mode were employed. The spatial resolution was comparable to the incident beam size (< 20 nm) because the films were so thin that extra fluorescence originating from secondary electrons scattered in the film did not occur.

2.2.3. Electronic transport and Hall effect measurements

Electronic transport properties of the obtained films were characterized by the temperature (T) dependence of their longitudinal resistivity ($\rho_{xx}=\rho$) and Hall effect measurements (i.e., transverse resistivity, ρ_{xy}) with a physical property measurement system (Quantum Design Inc., USA) at 4.2–300 K. In the ρ - T measurements, a four-probe geometry was used with Au electrodes deposited by direct-current sputtering using an SPF-332HS sputtering system (Canon Anelva, Japan). Hall effect measurements were conducted using a six-terminal Hall bar structure (500 μm long and 200 μm wide). A shadow mask was used in the patterning and lift-off process to form electrodes. An external magnetic field of up to $\mu_0 H = \pm 3$ T with an interval of 0.5 T was applied. To cancel out the offset effects, the net ρ_{xy} was calculated using the relation $\rho_{xy} = (\rho_{xy}^+ - \rho_{xy}^-) / 2$, where ρ_{xy}^+ and ρ_{xy}^- were measured under magnetic fields with opposite polarities.

2.2.4. Observation of electronic structure using ARPES

Electronic structures were observed directly by angle-resolved photoemission spectroscopy (ARPES) excited by monochromatic He I α light with a photon energy of 21.2180 eV from an MBS L-1 discharge lamp (MB Scientific AB, Sweden). Before the ARPES measurements, an all-in-situ sample transfer system was constructed [23] (i.e., to prevent sample exposure to any gasses such as air, pure N₂, or Ar), in which the growth

chamber, ARPES measurement chamber and sample carrier transfer chambers were connected in an ultrahigh vacuum of $<1 \times 10^{-7}$ Pa, because of the serious sensitivity of FeSe surfaces to air [24]. The ARPES measurements were carried out under an ultrahigh vacuum of $<4 \times 10^{-8}$ Pa and at a low temperature of ~ 10 K. Scanning direction is along the Γ -M line using a Scienta DA30 photoelectron analyzer (Scienta Omicron Inc., Germany). The detector resolutions were set to 10 meV for energy and 1° for angle. To precisely evaluate binding energies from the obtained results, the Fermi level (E_F) was calibrated by measuring the Fermi edge of a polycrystalline Au.

2.3. Results and Discussion

2.3.1. Phase diagram of FeSe grown on STO (001)

To easily understand the entire discussion, the relationships between the obtained crystalline phases, crystallite orientations, [Fe]/[Se], and T_s is first illustrated in **Fig. 2-1a**. Supporting data are presented and discussed point by point in the following sections. As will be explained, it was concluded that [Fe]/[Se] = 1.1 and $T_s = 500$ °C are the optimum conditions with respect to both the crystallinity and surface flatness of the FeSe thin films. Epitaxial growth of FeSe on STO single crystals was observed over a wide T_s range from 400–600 °C and a wide [Fe]/[Se] region from 0.7–1.25 around the optimum conditions (area with purple filled squares). In the Fe-poor and high- T_s region, the impurity phase Fe₇Se₈, which has a quite different crystal structure to that of tetragonal FeSe, segregated (open triangles), which was also reported in ref. 25. Note that Fe₇Se₈ and other impurity phases were not detected in the films grown at the optimum T_s . In the Fe-rich region, only Fe metal was detected as an impurity phase (orange filled triangles). Previous reports on bulk FeSe synthesized at 680 °C indicated that the Fe and FeSe phases clearly separated at high [Fe]/[Se] because the solubility limit of Fe in FeSe is as low as $\sim 5\%$ [26]. Conversely, phase separation was not

detected in obtained films up to an excess Fe concentration of ~25%, indicating that the non-equilibrium MBE growth process tolerates much higher Fe solubility without segregation.

Figure 2-1b illustrates the influence of introduced strain on the FeSe thin films. The FeSe film with $[\text{Fe}]/[\text{Se}] = 1.1$ (i.e., close to stoichiometric FeSe) is under tensile and compressive strain along the in-plane and out-of-plane directions, respectively, because the in-plane lattice parameter of the STO substrate is larger than that of FeSe. Conversely, in FeSe with $[\text{Fe}]/[\text{Se}] > 1.1$ (i.e., Fe-rich chemical composition), strain is introduced only in the in-plane direction; the out-of-plane lattice parameter is almost relaxed. Resulting from these different strain structures, the FeSe films with $[\text{Fe}]/[\text{Se}] \leq 1.1$ exhibit lower activation energies for electrical conductivity than those of films with $[\text{Fe}]/[\text{Se}] > 1.1$, even though insulator-like behavior is observed for all the obtained films. This behavior will be discussed in detail in Section 2.3.4–2.3.5.

2.3.2. Fabrication of FeSe epitaxial films with different chemical compositions

Here, I examine in detail the relationships between deposition conditions, crystalline phases, orientations, and crystallinity according to analysis of raw experimental data. After preliminary experiments, the ratio of Fe flux rate to Se flux rate was fixed at ~1:10, for which the temperatures of the Fe and Se cells were 1110 and 135 °C, respectively. Because of the much higher evaporation rate of Se than Fe during film growth, an Se flux rate that was ten times higher than that of Fe was used. **Figure 2-2a** shows out-of-plane XRD patterns of the FeSe films grown at T_s of 350–700 °C. The thicknesses of the films grown at T_s of ~350 °C (corresponding growth rate of ~2 Å/min) and ≥ 470 °C (~3 Å/min) were ~15 and ~20 nm, respectively. At $T_s > 600$ °C, Fe impurities and misoriented FeSe crystallite diffraction peaks

such as FeSe 101 were detected, which is consistent with ref. 17. An unidentified impurity phase (indicated by the solid circle in **Fig. 2-2a**) segregated at the lowest T_s examined (350 °C). Although this impurity phase should be most plausibly Fe₃Se₄, this could be not confirmed because other diffractions, such as FeSe 110, possibly appear at almost the same 2θ angles. Single-phase *c*-axis oriented FeSe films were obtained only at $T_s = 470$ and 530 °C (i.e., at ~500 °C). At these T_s , the obtained [Fe]/[Se] was ~1.0 (i.e., stoichiometric) because of the extremely high Se flux rate. **Figures 2-2b, 2-2c, and 2-2d** show the surface morphology of the films grown at $T_s = 700, 530,$ and 350 °C, respectively. The large grains with lateral sizes of 80–300 nm and heights of 30–60 nm from the FeSe surface in **Fig. 2-2b** were attributed to impurity Fe, which was detected at $2\theta = 44.6^\circ$ (Fe 110 diffraction) in the XRD pattern in **Fig. 2-2a** and confirmed with an FE-SEM/EDX point analysis. Small particles with lateral sizes of ~40 nm and heights of ~10 nm in **Fig. 2-2c** originated from surface degradation of the samples induced by air exposure during AFM observation [24]. For all the films, the crystallinity and surface roughness were evaluated along the *c*-axis from $\Delta\omega$ of the FeSe 001 diffraction and from R_{rms} , respectively. **Figure 2-2e** plots these values as a function of T_s . The minimum $\Delta\omega$ (0.05° at $T_s = 530$ °C) and R_{rms} (1.0 nm at $T_s = 470$ °C) are both located T_s of ~500 °C, indicating that 500 °C is the optimum T_s for FeSe film growth. Except at the optimum T_s , the segregation of the misorientated FeSe and impurity crystallites prevent lateral growth of *c*-axis-oriented FeSe domains, and consequently $\Delta\omega$ gradually increases ($\Delta\omega = 0.26^\circ$ for $T_s = 350$ °C and 0.19° for $T_s = 700$ °C). Additionally, formation of large Fe grains at higher T_s and the suppression of lateral migration at lower T_s both lead to inhomogeneous surfaces, as observed in **Figs. 2-2b and 2-2d**, and increasing R_{rms} with elevating T_s ($R_{\text{rms}} = 5.3$ nm for $T_s = 350$ °C and $R_{\text{rms}} = 20$ nm for $T_s = 700$ °C). Consequently, both $\Delta\omega$ and R_{rms} exhibit the inverted bell-shaped curves with respect to T_s , as seen in **Fig. 2-2e**.

Next, the chemical composition of the films was optimized by the varying the flux rates

of Fe and Se, which were controlled independently by the temperature of each Knudsen cell. The Fe and Se cells were heated at 1050–1100 and 127.5–140 °C, respectively. In these cell-temperature ranges, flux pressures were varied between 3×10^{-6} – 3×10^{-5} Pa for Fe and 2×10^{-5} – 2×10^{-4} Pa for Se. Here, the target film thickness was ~10 nm, which was exactly determined by XRR and interference detected in out-of-plane XRD measurements to avoid lattice relaxation and effectively introduce film strain. The other growth parameters were all fixed (e.g., the optimum $T_s = 500$ °C obtained in the previous section). **Figure 2-3a** shows out-of-plane XRD patterns of the films with [Fe]/[Se] of 0.7–1.9. All the films exhibited clear *c*-axis orientation in the out-of-plane direction. In the films with [Fe]/[Se]=1.3 and 1.9, small amounts of an Fe impurity were observed because the Fe flux rate was too high. **Figures 2-3b** and **2-3c** show RHEED patterns of the films with [Fe]/[Se] = 1.3 and 1.0, respectively. Clear streak patterns were observed in the RHEED patterns for both films, confirming their heteroepitaxial growth. As indicated by the red arrows in **Fig. 2-3c**, unidentified streak diffractions appeared, which are attributed to surface reconstruction within the shallow penetration depth of the incident electron beam (< 1 nm) [27]. In-plane growth along the STO in-plane lattice (i.e., [100] FeSe || [100] STO) and four-fold in-plane symmetry for the 200 diffraction originating from the tetragonal lattice of FeSe were detected for all the films (see **Fig. 2-4**), revealing that all the FeSe films grew heteroepitaxially on STO (001) substrates without any rotational domains at the optimum T_s of 500 °C irrespective of chemical composition.

The crystallinities along the *c*- and *a*-axes are plotted as a function of chemical composition in **Fig. 2-3d** (see **Fig. 2-5** for the raw diffraction patterns). These results suggest that chemical compositions close to stoichiometry can grow highly crystalline FeSe epitaxial films with small orientation twist and tilt angles along the in-plane direction ($\Delta\phi = 0.4^\circ$ for films with [Fe]/[Se] = 0.9 and 1.1) and out-of-plane direction ($\Delta\omega = 0.009^\circ$ for the film with

[Fe]/[Se] = 1.1). It should be noted that all the out-of-plane FWHMs (in the broadest case, $\Delta\omega = 0.054^\circ$ for the film with [Fe]/[Se] = 0.8) are narrower than those of previously reported films ($\Delta\omega = 0.2^\circ$ for a ~ 200 nm-thick FeSe film grown on an LaAlO_3 substrate via pulsed laser deposition [28]), which is probably because of the atomically flat surface of the pre-treated STO substrates and slow growth rate in MBE process. **Figures 2-3e – 2-3i** show the surface morphologies of FeSe films with [Fe]/[Se] = 0.7–1.9 (that with [Fe]/[Se] = 1.1 was reported in ref. 23). The films with [Fe]/[Se] = 1.0–1.3 have almost no surface pits; whereas many pits are observed in the films with [Fe]/[Se] = 0.7, 0.8, and 1.9. In the films with low [Fe]/[Se] (0.7 and 0.8), the origin of the pits would be evaporation of excess Se. This would be similar to the case of GaAs [29, 30], where oxide desorption from the GaAs surface generates surface pits. Similarly, excess Se prevents lateral growth of FeSe domains because the excess Se forms crystals on the substrate surface, which subsequently re-evaporate as the gas phase at $T_s = 500$ °C because T_s is higher than the Se evaporation temperature (< 150 °C). In the Fe-rich region, FeSe and Fe crystals coexist at the beginning of nucleation, which also suppresses lateral migration of FeSe deposition precursors. Corresponding to the generation of surface pits, the R_{rms} values of films with [Fe]/[Se] = 0.7, 0.8, and 1.9 in **Fig. 2-3j** were larger than those of films with [Fe]/[Se] = 0.9–1.3. The flattest surface was obtained for the FeSe film with [Fe]/[Se] = 1.1 ($R_{\text{rms}} = 0.6$ nm) [22] and the roughest surface with $R_{\text{rms}} = 5.0$ nm was observed for the film with [Fe]/[Se] = 0.7. From these results, it was concluded that [Fe]/[Se] = 1.1 is the optimum composition with respect to both crystallinity and surface flatness.

2.3.3. Effects of lattice strain on FeSe films

Figure 2-6a illustrates the variations of the a - and c -axis lattice parameters of the FeSe films with [Fe]/[Se] = 0.7–1.9 deposited at $T_s = 500$ °C, which were estimated from the FeSe

in-plane 200 diffraction and using the Nelson–Riley function [31] for out-of-plane $00l$ peaks, respectively (see **Figs. 2-3a** and **2-4a** for XRD data). There is a large in-plane lattice mismatch between tetragonal FeSe and the STO substrate; i.e., the in-plane lattice parameter of the STO substrate ($a_{\text{sub}} = 3.905 \text{ \AA}$) is larger than that of bulk $\text{Fe}_{1.09}\text{Se}$ ($a_{\text{bulk}} = 3.7734 \text{ \AA}$ when $[\text{Fe}]/[\text{Se}]$ is ~ 1.1 [32]), which gives a mismatch of $(a_{\text{sub}} - a_{\text{bulk}})/a_{\text{sub}} = 3.4 \%$. As a result, the a - and c -axis lattice parameters of the FeSe film with $[\text{Fe}]/[\text{Se}] = 1.1$ were expanded to 3.836 \AA by tensile strain along the a -axis, and compressed to 5.455 \AA by compressive strain along the c -axis, respectively. For the films at both ends of the chemical compositions, the lattice parameters were $a = 3.795 \text{ \AA}$ and $c = 5.530 \text{ \AA}$ for the film with $[\text{Fe}]/[\text{Se}] = 0.7$ and $a = 3.824 \text{ \AA}$ and $c = 5.533 \text{ \AA}$ for the film with $[\text{Fe}]/[\text{Se}] = 1.9$. The maximum a and minimum c values were observed for the film with $[\text{Fe}]/[\text{Se}] = 1.1$, which is close to stoichiometric value ($[\text{Fe}]/[\text{Se}] = 1.0$).

Note that the lattice parameters of bulk FeSe vary with $[\text{Fe}]/[\text{Se}]$. In the region where $[\text{Fe}]/[\text{Se}] < 1.0$ (Se-rich), it is known that Fe-vacancy sites appear in the FeSe structure. Although the vacancy sites are usually randomly distributed (i.e., disordered), it has been reported that ordered states are stabilized via hydrothermal or high pressure synthesis processes [33], where the primitive unit cell is extended to a $\sqrt{2} \times \sqrt{2} \times 1$ superlattice structure [33] and the phase with the Fe-vacancy superstructure exhibits insulator-like behavior. The Fe-vacancy ordering (i.e., emergence of superlattice diffractions in XRD) shrinks the a -axis lattice parameter ($a = 3.67(1) \text{ \AA}$ and $c = 5.70(3) \text{ \AA}$ for $\text{Fe}_{0.75}\text{Se}$ [33]) and expands the c -axis one. For films with chemical compositions ranging from $[\text{Fe}]/[\text{Se}] = 0.7$ – 1.0 , the trend of the lattice parameter variation for a - and c -axes is similar to that for bulk FeSe, as shown by the red filled circles and blue filled squares in **Fig. 2-6a**, respectively, although the absolute values between the present epitaxial films and bulk samples for each chemical composition are different because of the introduced strain in the former. Because no superlattice

diffraction peak was detected in the films with $[\text{Fe}]/[\text{Se}] \leq 1.0$, Fe vacancies would be disordered or the volume fraction of the ordered superstructure was too small to detect by XRD.

In the $[\text{Fe}]/[\text{Se}] \geq 1$ region, both the a - and c -axis lattice parameters scarcely changed despite the increase of excess Fe concentration ($a = 3.7692 \text{ \AA}$ and $c = 5.5137 \text{ \AA}$ in $\text{Fe}_{1.33}\text{Se}$ [26]) compared with those of stoichiometric FeSe ($a = 3.7720 \text{ \AA}$ and $c = 5.5161 \text{ \AA}$ [26]) because of the low solubility limit of Fe ($\sim 5\%$); i.e., almost all excess Fe was segregated as impurity Fe. However, in the films, lattice parameters varied dramatically with increasing $[\text{Fe}]/[\text{Se}]$, suggesting that the excess Fe exceeding the equilibrium solubility limit was incorporated into the FeSe lattice, which was probably facilitated by the non-equilibrium film growth process. Thus, there are two possibilities for the origin of the change in lattice parameters of the films with composition; i.e., mechanical strain introduced from the substrate and chemically induced strain caused by varying the chemical composition. Because these two factors could not be exactly distinguished from the variations of the c - to a -axis ratio (c/a) and the volume of the structure (see **Fig. 2-7**), the changes of the lattice parameters from stoichiometric bulk FeSe were defined as measures of the introduced strain $\Delta a = (a_{\text{film}} - a_{\text{bulk}})/a_{\text{bulk}}$ and $\Delta c = (c_{\text{film}} - c_{\text{bulk}})/c_{\text{bulk}}$, where $a_{\text{bulk}} = 3.7735 \text{ \AA}$ and $c_{\text{bulk}} = 5.5238 \text{ \AA}$ when $[\text{Fe}]/[\text{Se}] = 1.0$ [32]. These parameters are plotted in **Fig. 2-6b** as a function of $[\text{Fe}]/[\text{Se}]$. The change ratios for the optimum composition of $[\text{Fe}]/[\text{Se}] = 1.1$ are $\Delta a = +1.66 \%$ and $\Delta c = -1.24 \%$. In the region with $[\text{Fe}]/[\text{Se}] < 1.0$ (Se-rich), Δa decreases and Δc increases with decreasing $[\text{Fe}]/[\text{Se}]$ from stoichiometric ($\Delta a = +1.37 \%$ and $\Delta c = -0.99 \%$) to the lowest ratio ($\Delta a = +0.56 \%$ and $\Delta c = +0.11 \%$). In the $[\text{Fe}]/[\text{Se}] \geq 1$ region, Δa decreases and Δc increases with increasing $[\text{Fe}]/[\text{Se}]$. Because the chemically induced strain originates from Fe vacancies in films with $[\text{Fe}]/[\text{Se}] < 1.0$ and excess Fe in the crystal lattice in films

with $[\text{Fe}]/[\text{Se}] > 1$, Δa and Δc exhibit the bell-shaped curves.

In the FeSe film with $[\text{Fe}]/[\text{Se}] = 1.9$, the c -axis lattice parameter almost relaxed ($\Delta c = +0.16\%$) to that of the bulk and the a -axis lattice parameter remained under tensile strain ($\Delta a = +1.34\%$) like the optimally grown FeSe film with $[\text{Fe}]/[\text{Se}] = 1.1$ ($\Delta a = +1.66\%$), although slight relaxation occurred. The possible origin of this uniaxial relaxation is mainly the excess Fe incorporated in the FeSe lattice, although the site of the excess Fe could not be precisely determined. A possible site of the stabilized excess Fe inside the lattice is the $2c$ site (represented by multiplicity and Wyckoff letter) in the tetragonal $P4/nmm$ (No. 129) structure (**Fig. 2-8**), similar to the analogous iron chalcogenide tetragonal Fe_{1+y}Te [34, 35]. Excess Fe should expand the c -axis lattice parameter because it increases the repulsion between layers and/or neutralizes the charge of the top and bottom Se layers, which should be achieved by the non-equilibrium growth process in the Fe-rich flux atmosphere. These factors would provoke the anisotropic relaxation of the crystal lattice. Because the relaxation trends of the FeSe lattice are different in the regions with low and high $[\text{Fe}]/[\text{Se}]$, Δa vs. Δc relations are re-plotted in **Fig. 2-6c**, giving two straight lines for $[\text{Fe}]/[\text{Se}] = 0.7\text{--}1.1$ (slope of ~ 1.2) and for $1.1\text{--}1.9$ (slope of ~ 4.2). The different slopes imply that different strain effects are present in the two regions. The electronic structure should also be different between the regions with low and high $[\text{Fe}]/[\text{Se}]$ because the electronic structure of FeSe is quite sensitive to structural changes [12, 15, 36].

2.3.4. Chemical composition dependence of insulator-like electronic transport properties in strained FeSe

To investigate the effects of the two different strain effects seen in **Fig. 2-6c** on the electronic transport properties of the sample, ρ - T relationships were examined. **Figure 2-9a**

shows ρ - T curves of the films with $[\text{Fe}]/[\text{Se}] = 0.8$ – 1.9 grown at the optimum T_s of 500 °C. For the two Fe-rich films (i.e., $[\text{Fe}]/[\text{Se}] = 1.3$ and 1.9), insulator-like behavior (i.e., increasing ρ with decreasing T) was observed, and the increase of ρ was particularly enhanced at < 50 K. The films with $[\text{Fe}]/[\text{Se}]$ ratios of ≤ 1.1 also exhibited insulator-like behavior, especially at lower temperatures (< 30 K), as shown in **Fig. 2-9b**. To clarify differences in these insulator-like behaviors, Arrhenius plots were constructed with the proportional relation of the logarithm of electrical conductivity ($\sigma = 1/\rho$) to T^{-1} in **Figs. 2-9c** and **2-10a** (i.e., $\sigma = \sigma_0 \exp(-E_a/k_B T)$, where E_a , σ_0 , and k_B are the activation energy, a prefactor constant, and the Boltzmann constant, respectively) and to $T^{-1/4}$ for the films with $[\text{Fe}]/[\text{Se}] \leq 1.1$ in **Fig. 2-9d**, ≥ 1.3 in **Fig. 2-9e**, and the whole $[\text{Fe}]/[\text{Se}]$ range in **Fig. 2-10b** (corresponding to the Mott's variable range hopping model [37], $\sigma = \sigma_0 \exp(-(T_0/T)^{1/4})$, where σ_0 and T_0 are a constant and a hopping parameter, respectively). $T^{-1/4}$ was used because the fitting result obtained by $T^{-1/4}$ (i.e., three-dimensional) was the best among the fitting results with $T^{-1/n}$ where $n = 2$ – 4 (see **Fig. 2-11** and **Table 2-I**); i.e., the minimum standard deviation was obtained in the case of $T^{-1/4}$ fitting. Linear proportional relationships between σ and T^{-1} were clearly observed for all the films in the high- T region but not in the low- T region. In contrast, the σ - $T^{-1/4}$ plots also presented straight lines in the low- T region. From these relationships, E_a and T_0 were estimated for each film and are plotted in **Fig. 2-9f**. Both E_a and T_0 increased discontinuously for films with $[\text{Fe}]/[\text{Se}]$ above and below 1.1 , indicating that the electronic structures in films with $[\text{Fe}]/[\text{Se}] \geq 1.3$ ($E_a = 23$ meV and $T_0 = \sim 1 \times 10^6$ K for the film with $[\text{Fe}]/[\text{Se}] = 1.9$) were quite different from those in $[\text{Fe}]/[\text{Se}] \leq 1.1$ ($E_a = 1.2$ meV, $T_0 = \sim 100$ K for the film with $[\text{Fe}]/[\text{Se}] = 0.8$ and $E_a = 1.1$ meV and $T_0 = \sim 13$ K for the film with $[\text{Fe}]/[\text{Se}] = 1.1$). The transition composition corresponds well to that of the strain effect boundary in **Fig. 2-6c** (i.e., $[\text{Fe}]/[\text{Se}] = 1.1$), which is the best composition with respect to both crystallinity and surface flatness (see **Figs. 2-3d** and **2-3j**).

2.3.5. Electronic structure of insulator-like FeSe films

The electron transport properties in **Fig. 2-9** revealed that all the fabricated FeSe thin films exhibited up-turn ρ - T relationships, which are usually interpreted as typical of electrical insulators. Here it should be noted that such up-turn behavior of ρ - T is observed even for metals because of magnetic impurity scattering known as the Kondo effect. However, the relationship of linear ρ vs. $\ln T$ at low T , which is consistent with the Kondo effect, was not observed for the FeSe films (**Fig. 2-12**), indicating that the observed insulator-like behavior should not be related to the Kondo effect. Furthermore because all fabricated FeSe has flat surfaces seen in **Figs. 2-3e – 2-3i**, the insulator-like behavior does not originate from textured surface coexisting non-superconducting and granular superconducting phases. The possible origins of the up-turn behavior include (i) the change in the electronic structure from metallic to insulating (i.e., open band gaps) and/or (ii) decrease of carrier mobility attributing to electron correlation and/or scattering of conducting carriers (e.g., potential barrier).

Therefore, ARPES measurements were performed to directly examine whether the FeSe films had open bandgaps. Fabricated thin FeSe films were transferred in situ from the growth chamber to the ARPES measurement chamber under an ultrahigh vacuum of $< 1 \times 10^{-7}$ Pa to measure the electronic structure without any surface pre-treatment such as thermal annealing or sputtering. **Figures 2-13a** and **2-13b** show ARPES spectra measured at ~ 10 K for the optimally grown FeSe film with $[\text{Fe}]/[\text{Se}] = 1.1$ around the Γ - and M-points, respectively. To clearly visualize the band dispersion around E_F , second derivative spectra with respect to energy around the Γ - and M-points are presented in **Figs. 2-13c** and **2-13d**, respectively. At the Γ -point, a hole-like band derived from Fe $3d$ orbitals [38] intersected E_F and its top was located at a binding energy of $E_b - E_F = -15$ meV. At the M-point, an electron-like band

crossed E_F and its bottom was located at $E_b - E_F = +5$ meV. These results confirm that the electronic structure in the insulator-like FeSe is metallic (i.e., the band gap is not opened at E_F) even though separated hole- and electron-like bands exist around E_F (i.e., multi-band structure), like bulk FeSe [39]. Here, it should be noted that their energy overlap (i.e., the difference of E_b between the top of the hole-like band at Γ and the bottom of the electron-like band at M) is as small as ~ 20 meV, which is the same value as that determined by ARPES for FeSe with in-plane tensile lattice strain [40]. Because a small energy overlap results in enhancement of nematic instability [40], the lack of superconductivity in all FeSe films would also originate from nematic instability.

Here it should be noted that the introduced strain varies the structural anisotropy as well as length and angle of chemical bonding between Fe and *Ch*. This would result in change in the electron correlation, because charge transfer and Coulomb interaction are strongly related to overlap between the wave functions and polarizabilities of the ions. To investigate the change, renormalization factor (Z^{-1}) was estimated by using following equation; $Z^{-1} = m^{\text{ARPES}}/m^*$, where m^{ARPES} and m^* are effective masses obtained from fitting of the band observed in ARPES and first-principal calculation not including influence of electron correlation seen in **Fig. 2-14**, respectively. When electron correlation is enhanced, the band width of Fe 3*d*-orbitals becomes narrower than that without electron correlation; i.e., Z^{-1} increases. The estimated m^{ARPES} and m^* at Γ point (i.e., hole effective mass) were 5.60 and $1.28 m^0$, where m^0 is free electron mass. Although FeSe single crystal without any strain has higher Z^{-1} (3.2 [41]) than 1 due to the component Fe, strained insulator-like FeSe has much higher Z^{-1} of ~ 4.3 . Therefore it was concluded that the electron correlation of insulator-like FeSe was enhanced owing to introduction of the strain, even though it was not high enough to open the Mott gap.

2.3.6. Potential barrier for percolation conduction

Next, because superficially antagonistic results were obtained for the electric transport properties and ARPES measurements (i.e., a linear proportional relation between $\ln \sigma$ and $T^{-1/4}$ despite the metallic electronic structure), Hall effect measurements were performed for two representative films in the two regions; that is, $[\text{Fe}]/[\text{Se}] = 1.1$ (the most strained and almost stoichiometric film) and 1.9 (the most Fe-rich one). **Figures 2-15a** and **2-15b** show the magnetic field (H) dependences of transverse resistivity (ρ_{xy}) for the films with $[\text{Fe}]/[\text{Se}] = 1.1$ and 1.9, respectively. Because the slopes of the plots in **Figs. 2-15a** and **2-15b** are both positive, the dominant carrier type in the two films at room temperature is holes, which is similar behavior to that reported in ref. 42. The dominant carrier changed to electrons around 120 and 170 K for the films with $[\text{Fe}]/[\text{Se}] = 1.1$ and 1.9, respectively, where linear relations of ρ_{xy} against H were not observed, presumably because the number of hole carriers became comparable to that of electrons and Hall voltages were compensated. From 300 K to the lowest temperature where definite Hall voltages were observed, the Hall coefficients (R_H) were estimated. They are presented in **Fig. 2-15c**. Although the R_H - T behavior of both films was roughly similar; i.e., R_H increased and then decreased with decreasing temperature, R_H for the film with $[\text{Fe}]/[\text{Se}] = 1.9$ was ca. two orders of magnitude higher than that for the film with $[\text{Fe}]/[\text{Se}] = 1.1$ over the whole T range. Carrier concentration (n) was estimated based on the single carrier model relation of $1/q|R_H|$, where q is elementary charge, irrespective of the multi-band electronic structure observed in the ARPES measurements (**Fig. 2-12**). It was found that n in the film with $[\text{Fe}]/[\text{Se}] = 1.1$ was $\sim 2 \times 10^{21} \text{ cm}^{-3}$ at 300 K, which is approximately one order of magnitude higher than that of bulk FeSe ($\sim 3 \times 10^{20} \text{ cm}^{-3}$) [43] but lower than that of superconducting thin films with $T_c = 11.4 \text{ K}$, where $R_H = \sim 0.5 \text{ cm}^{-3}/\text{C}$ at 300 K ($n = \sim 10^{22} \text{ cm}^{-3}$) [44]. Meanwhile, n in the film with $[\text{Fe}]/[\text{Se}] = 1.9$ was

two orders of magnitude lower ($\sim 1 \times 10^{20} \text{ cm}^{-3}$ at 300 K) than that in the $[\text{Fe}]/[\text{Se}] = 1.1$ sample. This difference should arise from ionic Fe^{2+} inside the lattice, which acts as electron donor via isovalent doping [45], in the film with $[\text{Fe}]/[\text{Se}] = 1.9$.

The mobility (μ) of the two films was estimated from the inverse of ρ in **Fig. 2-9a** and estimated n . μ at 300 K were $\sim 3 \times 10^0$ and $\sim 4 \times 10^{-3} \text{ cm}^2/(\text{V}\cdot\text{s})$ in the films with $[\text{Fe}]/[\text{Se}] = 1.1$ and 1.9, respectively; these values are respectively one and four orders of magnitude smaller than that of bulk FeSe ($\sim 25 \text{ cm}^2/(\text{V}\cdot\text{s})$ at 300 K [43]). Considering the relationship between σ and n , the difference in μ should be strongly related to the different E_a in the insulator-like behavior of the two thin films. μ in the films with $[\text{Fe}]/[\text{Se}] = 1.1$ and 1.9 decreased to 8×10^{-1} and $1 \times 10^{-3} \text{ cm}^2/(\text{V}\cdot\text{s})$, respectively, at the lowest temperatures (150 and 200 K, respectively). This indicates that there is a potential barrier derived from conduction carrier scattering. To unveil the potential barrier, $\ln(\mu)$ versus T^{-1} is plotted in **Fig. 2-15d**. This plot corresponds to the percolation conduction model with distributed potential barriers, $\mu(T) = \mu_0 \exp(-e(\Phi_0 - (e\sigma_\phi^2/2k_B T))/k_B T)$ [46, 47], where μ_0 , Φ_0 , and σ_ϕ denote a virtually T -independent constant, average potential barrier, and the distribution width of the potential barrier, respectively. The solid curves in **Fig. 2-15d** represent the fitting results obtained using the above equation, which reproduce the experimental results well. The calculated Φ_0 and σ_ϕ values were ~ 77 and $\sim 43 \text{ meV}$ for the film with $[\text{Fe}]/[\text{Se}] = 1.1$ and ~ 150 and $\sim 74 \text{ meV}$ for that with $[\text{Fe}]/[\text{Se}] = 1.9$, respectively. Even the film with $[\text{Fe}]/[\text{Se}] = 1.1$ has high and wide potential barriers, like disordered oxide semiconductors [46, 47].

The origin of the potential barrier was considered in a point of view of structural variation caused by excess Fe and introduced strain. Even though the FeSe film with higher μ ($[\text{Fe}]/[\text{Se}] = 1.1$) shrinks along the c -axis, that with lower μ ($[\text{Fe}]/[\text{Se}] = 1.9$) relaxes to resemble a bulk state (see **Fig. 2-6a**), indicating that two-dimensionality is enhanced along

the in-plane direction in the film with $[\text{Fe}]/[\text{Se}] = 1.9$. Thus, the structural change in $[\text{Fe}]/[\text{Se}] = 1.9$ not only suppresses conduction along the in-plane direction but also decreases the dimensionality in the out-of-plane direction, causing μ to lower dramatically (i.e., the potential barrier becomes higher) compared with that in the film with $[\text{Fe}]/[\text{Se}] = 1.1$. Overall, it was succeeded to tune the electronic transport properties of insulator-like FeSe through structural variation stimulated by introducing excess Fe and lattice strain via a non-equilibrium MBE film growth process.

2.3.7. Origin of the insulator-like behavior

According to above results of ARPES and Hall effect measurements, it was concluded that origin of the insulator-like behavior was decrease of μ from a point of view of the closed-bandgap metallic electronic structure. The enhancement of electron correlation makes the effective mass heavier, resulting in suppression of the carrier conduction. However the effect cannot explain the one order of magnitude lower μ of insulator-like FeSe than that of single crystal, completely. Hence the decrease of μ is attributed to not only enhancement of the electron correlation but also generation of the potential barrier, which are induced by the introduced strain.

2.4. Conclusion

~ 10 nm-thick insulator-like FeSe films with $[\text{Fe}]/[\text{Se}] = 0.8\text{--}1.9$ were fabricated at the optimized growth temperature of $500\text{ }^\circ\text{C}$ by MBE and investigated their electronic transport properties and electronic structure. It was found that the lattice strain introduced in the films exhibited unusual behavior; the almost stoichiometric film with $[\text{Fe}]/[\text{Se}] = 1.1$ had the largest in-plane tensile strain, whereas the lattice parameters approached the unstrained

values for the films with $[\text{Fe}]/[\text{Se}]$ values that were non-stoichiometric. In the films with $[\text{Fe}]/[\text{Se}] < 1.1$ (Se-rich region), the FeSe lattice contracted in plane and expanded perpendicular to the substrate, probably because of the introduction of disordered Fe vacancies. In the Fe-rich region, both the a - and c -axes were expanded from the unstrained values, which originated from the excess interstitial Fe stabilized by the non-equilibrium MBE film growth process. ρ - T measurements and electronic structure observations provide apparently contradicting results. It was found that all films exhibited insulator-like behavior, whereas ARPES measurements indicated that the films had metallic electronic structures although the electron correlation was enhanced. The insulator-like behavior was classified into two regions according to E_a with the boundary composition of $[\text{Fe}]/[\text{Se}] = 1.1$; E_a of the Fe-rich films were one order of magnitude higher than those of the Se-rich films. μ of the $[\text{Fe}]/[\text{Se}] = 1.1$ film with small E_a was three orders of magnitude higher than that of the Fe-rich film with large E_a , which originated from the potential barrier distributed in the conduction band. Such a high potential barrier is tentatively attributed to the presence of large amounts of excess Fe. These findings explain the above contradicting results of the coexistence of metallic electronic structure and insulating electrical properties. It was unveiled that origin of the insulator-like behavior was introduced epitaxial strain, resulting in enhancement of the electron correlation and generation of the potential barrier. Thus strained insulator-like FeSe is a promising candidate for high- T_c superconductor owing to the enhanced electron correlation.

References

1. Y. Kamihara, T. Watanabe, M. Hirano, and H. Hosono, *J. Amer. Chem. Soc.*, **130**, 3296–3297 (2008).
2. H. Hosono, and K. Kuroki, *Physica C*, **514**, 399–422 (2015).

3. H. Hosono, A. Yamamoto, H. Hiramatsu, and Y. Ma, *Materials Today*, **21**, 278–302 (2018).
4. G. R. Stewart, *Rev. Mod. Phys.*, **83**, 1589 (2011).
5. Z-A, Ren, W. Lu, J. Yang, W. Yi, X-L. Shen, C. Zheng, G-C. Che, X-L. Dong, L-L. Sun, and F. Zhou, *Chin. Phys. Lett.*, **25**, 2215–2216 (2008).
6. T.Hanna, Y. Muraba, S. Matsuishi, N. Igawa, K. Kodama, S. Shamoto, and H. Hosono, *Phys. Rev. B*, **84**, 024521 (2011).
7. A. Schilling, M. Cantoni, J. D. Guo, and H. R. Ott, *Nature*, **363**, 56 (1993).
8. N. P. Armitage, P. Fournier, and R. L. Greene, *Rev. Mod. Phys.*, **82**, 2421 (2010).
9. S. Avci, O. Chmaissem, D. Y. Chung, S. Rosenkranz, E. A. Goremychkin, J. P. Castellán, I. S. Todorov, J. A. Schlueter, H. Claus, A. Daoud-Aladine, D. D. Khalyavin, M. G. Kanatzidis, and R. Osborn, *Phys. Rev. B*, **85**, 184507 (2012).
10. Y. Kamihara, T. Watanabe, M. Hirano, and H. Hosono, *J. Am. Chem. Soc.*, **130**, 3296 (2008).
11. F.-C. Hsu, J.-Y. Luo, K.-W. Yeh, T.-K. Chen, T.-W. Huang, P. M. Wu, Y.-C. Lee, Y.-L. Huang, Y.-Y. Chu, D.-C. Yan, and M.-K. Wu, *Proc. Nat. Acad. Sci. USA.*, **105**, 14262–14264 (2008).
12. F. Nabeshima, Y. Imai, M. Hanawa, I. Tsukada, and A. Maeda, *Appl. Phys. Lett.*, **103**, 172602 (2013).
13. S. Medvedev, T. M. McQueen, I. A. Troyan, T. Palasyuk, M. I. Eremets, R. J. Cava, S. Naghavi, F. Casper, V. Ksenofontov, G. Wortmann, and C. Felser, *Nat. Mater.*, **8**, 630–633 (2009).
14. Y. Mizuguchi, F. Tomioka, S. Tsuda, T. Yamaguchi, and Y. Takano, *Appl. Phys. Lett.*, **93**, 15, 152505 (2008).

15. Y. F. Nie, E. Brahim, J. I. Budnick, W. A. Hines, M. Jain, and B. O. Wells, *Appl. Phys. Lett.*, **94**, 242505 (2009).
16. A. Tsukada, K. E. Luna, R. H. Hammond, M. R. Beasley, J. F. Zhao, and S. H. Risbud, *Appl. Phys. A*, **104**, 311-318 (2011).
17. M. J. Wang, J. Y. Luo, T. W. Huang, H. H. Chang, T. K. Chen, F. C. Hsu, C. T. Wu, P. M. Wu, A. M. Chang, and M. K. Wu, *Phys. Rev. Lett.*, **103**, 117002 (2009).
18. R. Schneider, A. G. Zaitsev, D. Fuchs, and H. v. Löhneysen, *J. Low. Temp. Phys.*, **178**, 118–127 (2014).
19. R. Schneider, A. G. Zaitsev, D. Fuchs, and H. v. Löhneysen, *Eur. Phys. J. B*, **88**, 14 (2015).
20. M. Kawasaki, K. Takahashi, T. Maeda, R. Tsuchiya, M. Shinohara, O. Ishiyama, T. Yonezawa, M. Yoshimoto, and H. Koinuma, *Science*, **266**, 1540–1542 (1994).
21. H. Hiramatsu, T. Kamiya, M. Hirano, and H. Hosono, *Physica C*, **469**, 657–666 (2009).
22. K. Hanzawa, H. Sato, H. Hiramatsu, T. Kamiya, and H. Hosono, *Proc. Nat. Acad. Sci. USA.*, **113**, 3986–3990 (2016).
23. T. Hanna, H. Hiramatsu, I. Sakaguchi, and H. Hosono, *Rev. Sci. Instrum.*, **88**, 053103 (2017).
24. H. Hiramatsu, K. Hanzawa, T. Kamiya, and H. Hosono, *Journal of Superconductivity and Novel Magnetism*, published online (2019). DOI: 10.1007/s10948-019-5020-9.
25. S. Agatsuma, T. Yamagishi, S. Takeda, and M. Naito, *Physica C* **470**, 1468–1472 (2010).
26. Z. Li, J. Ju, J. Tang, K. Sato, M. Watahiki, and K. Tanigaki, *J. Phys. Chem. Solids*, **71**, 495–498 (2009).

27. F. Kurth, E. Reich, J. Hänisch, A. Ichinose, I. Tsukada, R. Hühne, S. Trommler, J. Engelmann, L. Schultz, B. Holzapfel, and K. Iida, *Appl. Phys. Lett.*, **102**, 142601 (2013).
28. Y. Han, W. Y. Li, L. X. Cao, S. Zhang, B. Xu, and B. R. Zhao, *J. Phys.: Condens. Matter.*, **21**, 235702 (2009).
29. A Guillen-Cervantes, Z. Rivera-Alvarez, M. López-López, E. López-Luna, and I. Hernández-Calderón, *Thin. Solid. Films.*, **373**, 159–163 (2000).
30. D. Yan, W. Wu, H. Zhang, X. Wang, H. Zhang, W. Zhang, Z. Xiong, Y. Wang, L. Peng, S. Han, and M. Zhou, *Appl. Surf. Sci.*, **258**, 1417–1421 (2011).
31. B. E. Warren, “X-ray Diffraction”, Dover publications, New York (2012).
32. E. Pomjakushina, K. Conder, V. Pomjakushin, M. Bendele, and R. Khasanov, *Phys. Rev. B*, **80**, 024517 (2009).
33. T-K. Chen, C-C. Chang, H-H. Chang, A-H. Fang, C-H. Wang, W-H. Chao, C-M. Tseng, Y-C. Lee, Y-R. Wu, M-H. Wen, H-Y. Tang, F-R. Chen, M-J. Wang, M-K. Wu, and D. V. Dyck, *Proc. Nat. Acad. Sci. USA.*, **111**, 63–68 (2014).
34. W. Bao, Y. Qiu, Q. Huang, M. A. Green, P. Zajdel, M. R. Fitzsimmons, M. Zhernenkov, S. Chang, Minghu Fang, B. Qian, E. K. Vehstedt, Jinhu Yang, H. M. Pham, L. Spinu, and Z. Q. Mao, *Phys. Rev. Lett.*, **102**, 247001 (2009).
35. C. Koz, S. Rößler, A. A. Tsirlin, S. Wirth, and U. Schwarz, *Phys. Rev. B*, **88**, 094509 (2013).
36. S. Medvedev, T. M. McQueen, I. A. Troyan, T. Palasyuk, M. I. Erements, R. J. Cava, S. Naghavi, F. Casper, V. Ksenofontov, G. Wortmann, and C. Felser, *Nature Mater.*, **8**, 630–633 (2009).
37. B. Lei, J. H. Cui, Z. J. Xiang, C. Shang, N. Z. Wang, G. J. Ye, X. G. Luo, T. Wu, Z. Sun, and X. H. Chen, *Phys. Rev. Lett.*, **116**, 077002 (2016).

38. W. K. Wang, Y. Liu, J. Y. Yang, H. F. Du, W. Ning, L. S. Ling, W. Tong, Z. Qu, Z. R. Yang, M. L. Tian, and Y. H. Zhang, *Chin. Phys. Lett.*, **33**, (2016).
39. J. Shiogai, T. Miyakawa, Y. Ito, T. Nojima, and A. Tsukazaki, *Phys. Rev. B* **95**, 115101 (2017).
40. T. Katase, H. Hiramatsu, T. Kamiya, and H. Hosono, *Proc. Natl. Acad. Sci. USA.*, **111**, 3979–3983 (2014).
41. M. D. Watson, T. K. Kim, A. A. Haghighirad, N. R. Davies, A. McCollam, A. Narayanan, S. F. Blake, Y. L. Chen, S. Ghannadzadeh, A. J. Scofield, M. Hoesch, C. Meingast, T. Wolf, and A. I. Coldea, *Phys. Rev. B*, **91**, 155106 (2015).
42. X. J. Wu, D. Z. Shen, Z. Z. Zhang, J. Y. Zhang, K. W. Liu, B. H. Li, Y. M. Lu, B. Yao, D. X. Zhao, B. S. Li, C. X. Shan, X. W. Fan, H. J. Liu, and C. L. Yang, *Appl. Phys. Lett.*, **90**, 112105 (2007).
43. M. D. Watson, T. Yamashita, S. Kasahara, W. Knafo, M. Nardone, J. Béard, F. Hardy, A. McCollam, A. Narayanan, S. F. Blake, T. Wolf, A. A. Haghighirad, C. Meingast, A. J. Schofield, H. v. Löhneysen, Y. Matsuda, A. I. Coldea, and T. Shibauchi, *Phys. Rev. Lett.*, **115**, 027006 (2015).
44. A. Maeda, F. Nabeshima, H. Takahashi, T. Okada, Y. Imai, I. Tsukada, M. Hanawa, S. Komiya and A. Ichinose, “Synthesis, characterization, *Appl. Surf. Sci.*, **312** 43–49 (2014).
45. F-Y. Ran, Z. Xiao, Y. Toda, H. Hiramatsu, H. Hosono, and T. Kamiya, *Sci. Rep.* **5**, 10428 2015.
46. T. Kamiya, K. Nomura, and H. Hosono, *J. Display Technol.*, **5**, 462–467 (2009).
47. T. Kamiya, K. Nomura, and H. Hosono, *Appl. Phys. Lett.*, **96**, 122103 (2010).

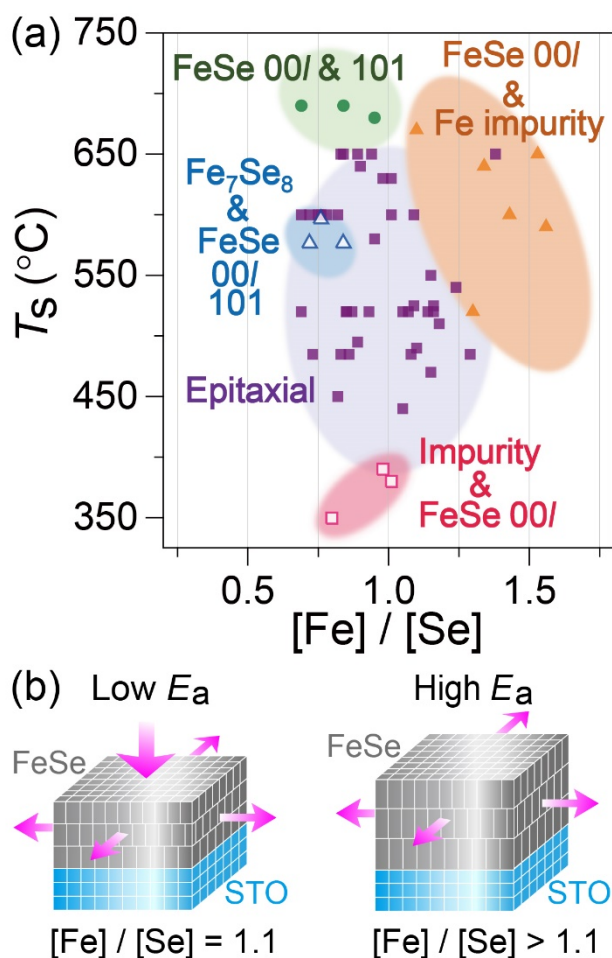


Figure 2-1. Overview of FeSe thin films grown by MBE. (a) Relationship between T_s and chemical composition ($[Fe]/[Se]$) of the fabricated films. Different symbols represent the obtained crystalline phases and orientations. Filled squares denote the epitaxial growth region, open squares the 00l-oriented FeSe and an unidentified impurity, closed triangles the 00l-oriented FeSe and impurity Fe, open triangles the 00l-preferentially oriented FeSe with other orientations and Fe₇Se₈, and closed circles the 00l-preferentially oriented FeSe with other orientations. (b) Schematics of the strain in FeSe thin films with $[Fe]/[Se] = 1.1$ (left) and > 1.1 (right) introduced via thin film growth. The arrows indicate the directions of the introduced strain. E_a is the activation energy obtained from the electronic transport properties for each strained film.

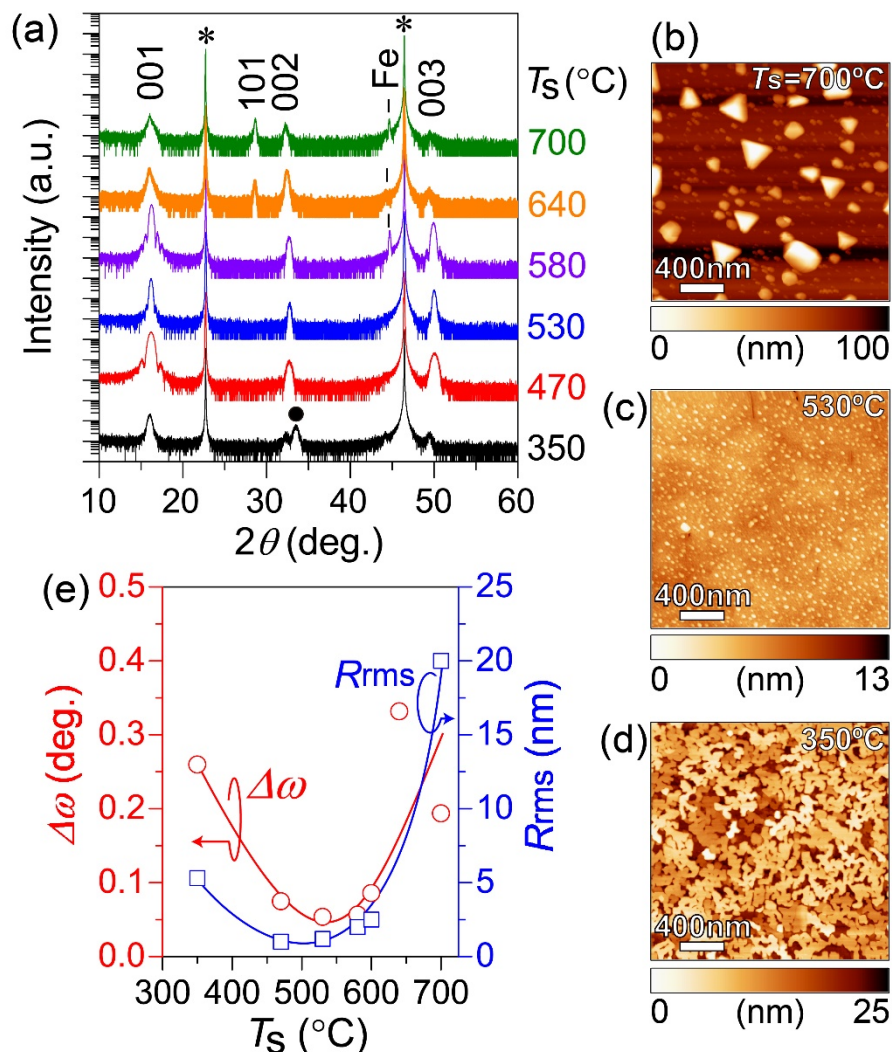


Figure 2-2. Structure and surface morphology of FeSe films grown at a constant ratio of Fe flux rate to Se flux rate of $\sim 1:10$ and $T_s = 350\text{--}700^\circ\text{C}$. (a) Out-of-plane XRD patterns. The asterisks indicate the substrate diffraction peaks, the solid circle at $2\theta = 33.5^\circ$ an unidentified phase, and ‘Fe’ at $2\theta = 44.6^\circ$ iron metal. AFM images of films grown at T_s of (b) 700, (c) 530, and (d) 350 °C. Horizontal bars represent height scales. (e) Out-of-plane rocking-curve FWHM for the FeSe 001 diffraction ($\Delta\omega$, red circles) and root mean square roughness (R_{rms} , blue squares) of the film surface as a function of T_s .

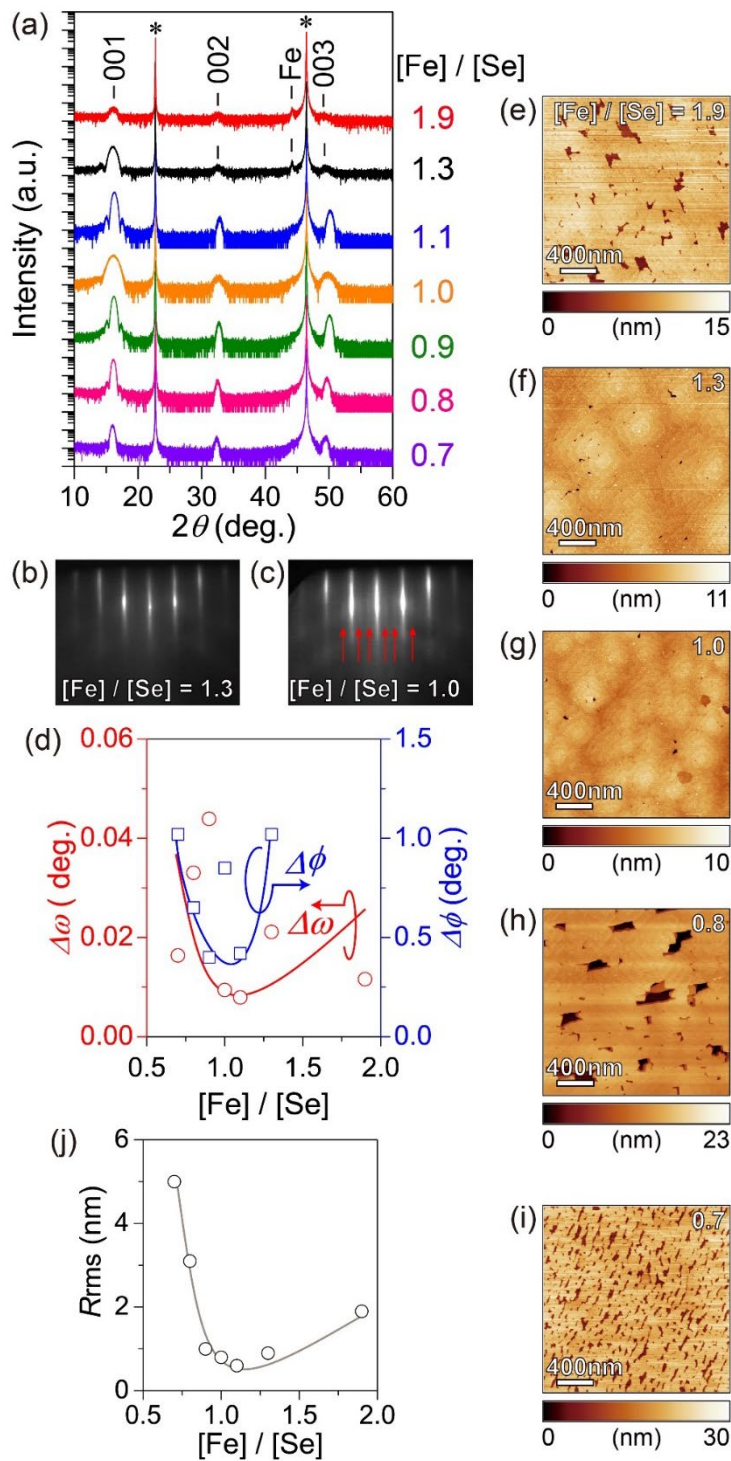


Figure 2-3. Quality of FeSe thin films with different chemical compositions ($[\text{Fe}]/[\text{Se}] = 0.7\text{--}1.9$) grown at the optimum T_s of 500 °C. (a) Out-of-plane XRD patterns of the films with different $[\text{Fe}]/[\text{Se}]$. The black vertical bars and asterisks denote FeSe 00 l diffractions and STO (001) substrate peaks, respectively. ‘Fe’ indicates the 110 diffraction peak ($2\theta =$

44.6°) of impurity Fe, which segregates at $[\text{Fe}]/[\text{Se}] \geq 1.3$. RHEED patterns of FeSe films with $[\text{Fe}]/[\text{Se}] =$ (b) 1.3 and (c) 1.0. The red vertical arrows in (c) are unidentified diffractions. (d) Rocking-curve FWHMs along the out-of-plane ($\Delta\omega$, red circles) and in-plane ($\Delta\phi$, blue squares) directions taken from the FeSe 001 and 200 diffractions, respectively. (e)–(i) AFM images of FeSe films with $[\text{Fe}]/[\text{Se}] = 0.7$ –1.9 (indicated in each AFM image). An AFM image of FeSe with $[\text{Fe}]/[\text{Se}] = 1.1$ was reported in ref. 22. Horizontal bars represent height scales. (j) Surface roughness (R_{rms}) estimated from (e)–(i) as a function of $[\text{Fe}]/[\text{Se}]$.

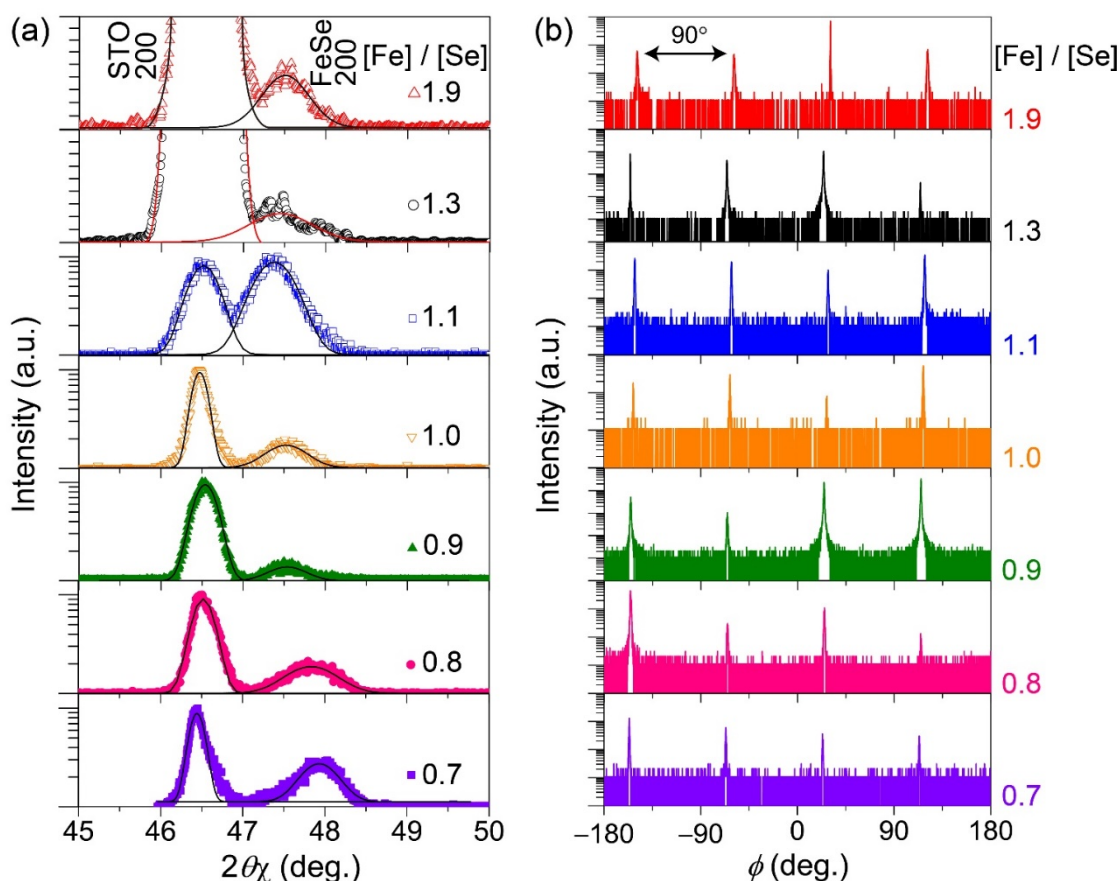


Figure 2-4. In-plane structure analyses of FeSe thin films grown at 500 °C with $[\text{Fe}]/[\text{Se}] = 0.7$ –1.9. (a) In-plane XRD patterns around the STO 200 diffraction. Solid lines are the fitting results for STO and FeSe 200 diffractions. (b) ϕ -scans of FeSe 200 diffractions.

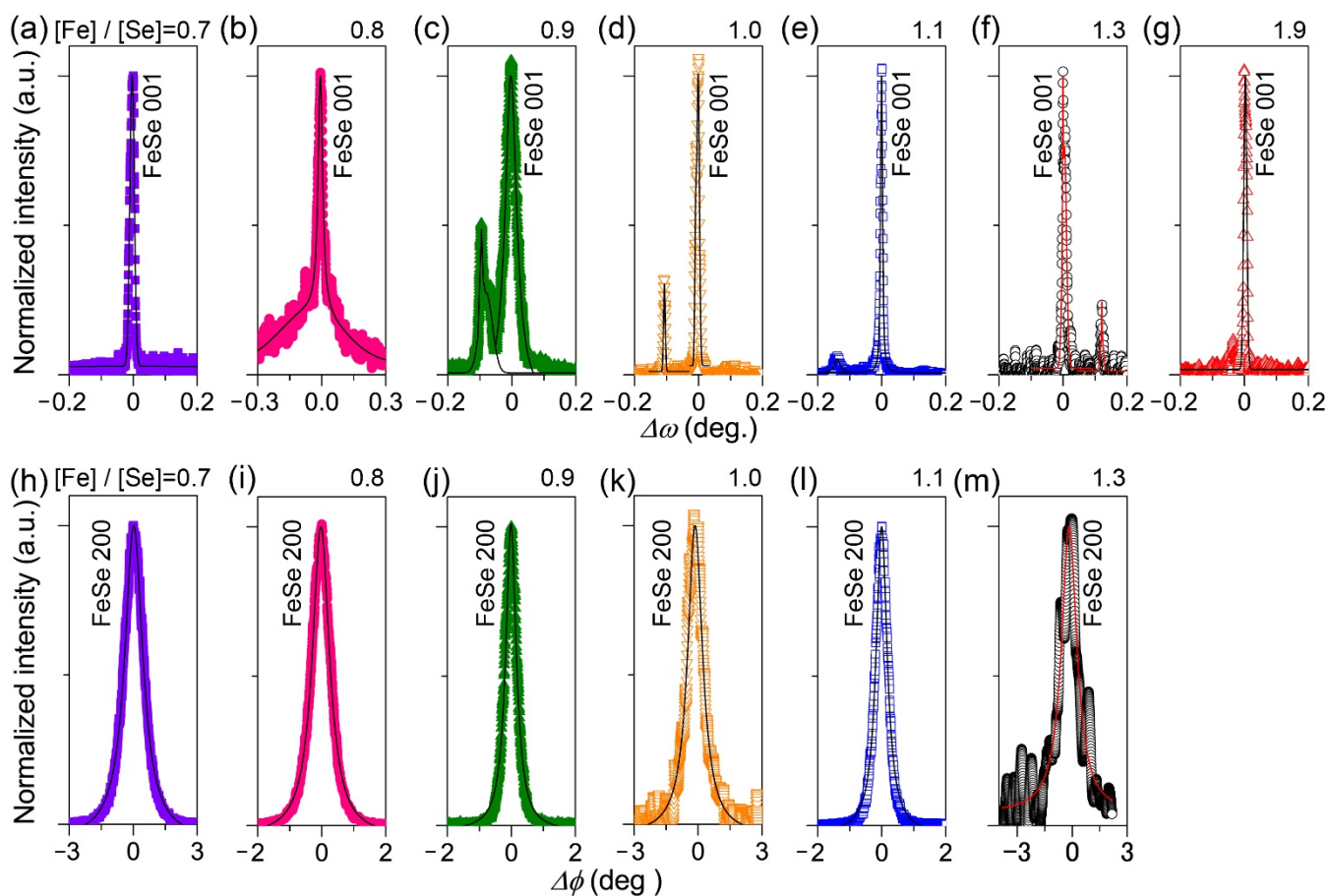


Figure 2-5. Results of X-ray rocking curve measurements for out-of-plane and in-plane directions. (a)–(g) Rocking curve patterns for the out-of-plane FeSe 001 diffraction of films grown at 500 °C with [Fe]/[Se] = 0.7–1.9. (h)–(m) Rocking curve patterns for the in-plane FeSe 200 diffraction of the films with [Fe]/[Se] = 0.7–1.3.

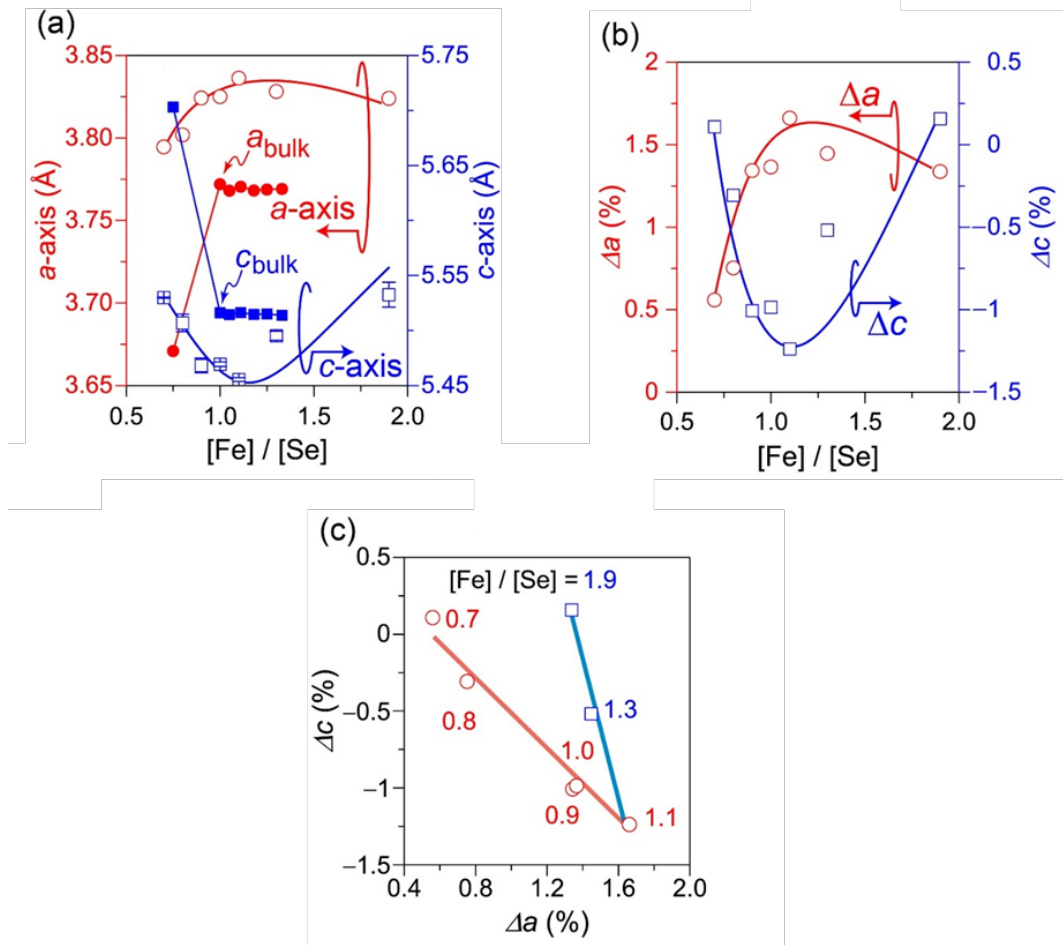


Figure 2-6. Relationship between the lattice strain and chemical composition of FeSe films grown at the optimum T_s of 500 °C with [Fe]/[Se] = 0.7–1.9. (a) *a*-axis (open red circles) and *c*-axis (open blue squares) lattice parameters. The red closed circles and blue closed squares denote the *a*-axis (a_{bulk}) and *c*-axis (c_{bulk}) lattice parameters of bulk FeSe [26, 32, 33]. (b) Introduced strain for the *a*-axis (red circles) and *c*-axis (blue squares) calculated by $\Delta a = (a_{\text{film}} - a_{\text{bulk}}) / a_{\text{bulk}}$ and $\Delta c = (c_{\text{film}} - c_{\text{bulk}}) / c_{\text{bulk}}$ ($a_{\text{bulk}} = 3.7735$ and $c_{\text{bulk}} = 5.5238$ Å at [Fe]/[Se]=1.0 [29]). (c) Lattice strain along the out-of-plane direction (Δc) versus that along the in-plane direction (Δa). The values in the figure indicate the [Fe]/[Se] values.

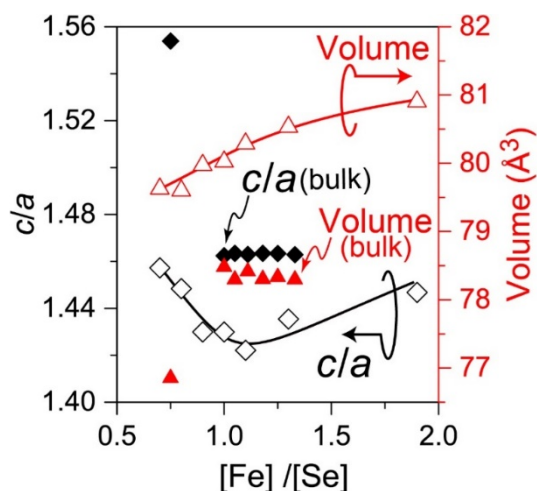


Figure 2-7. c -axis to a -axis lattice parameter ratio (c/a , open black triangles) and cell volume (open red triangles), which were calculated from the values in **Fig. 2-6a**, as a function of $[\text{Fe}]/[\text{Se}]$. Filled triangles and diamonds indicate the c/a ratio and volume for some bulk FeSe samples, respectively [26, 32, 33].

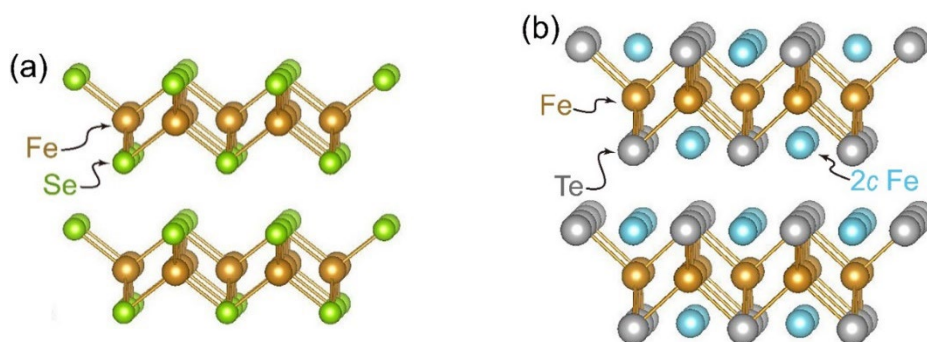


Figure 2-8. Crystal structure of (a) β -FeSe and (b) β -Fe $_{1+x}$ Te with a space group of $P4/nmm$ (space group: 129), where brown, green, and gray spheres represent Fe, Se, and Te sites, respectively. In Fe $_{1+x}$ Te, excess Fe statistically occupies the interlayer $2c$ sites (blue spheres).

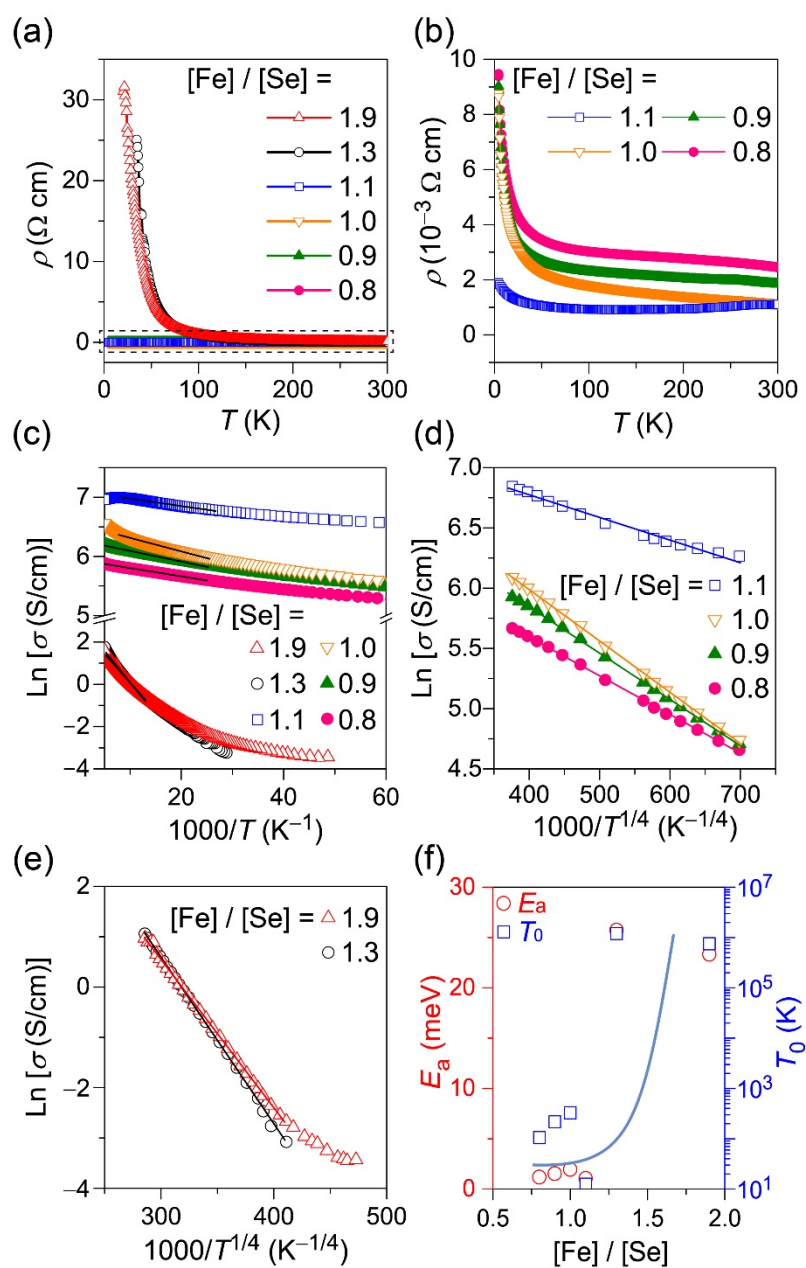


Figure 2-9. Electronic transport properties of FeSe films with [Fe]/[Se] = 0.8–1.9 grown at the optimum T_s of 500 °C. (a) Temperature (T) dependence of resistivity (ρ). (b) Enlarged ρ - T curves inside the dashed square in (a). (c) Arrhenius plots of electrical conductivity (σ) against T^{-1} . (d, e) $\ln\sigma$ vs. $T^{-1/4}$ plots for the films with [Fe]/[Se] of (d) 0.8–1.1 and (e) 1.3 and 1.9. The straight lines in (c) and (d) are the results of the linear least-squares fitting. (f) Activation energy (E_a , circles) estimated from the straight lines in (c) and hopping parameter

of the variable range hopping model (T_0 , squares) estimated from (d) and (e) as a function of $[\text{Fe}]/[\text{Se}]$.

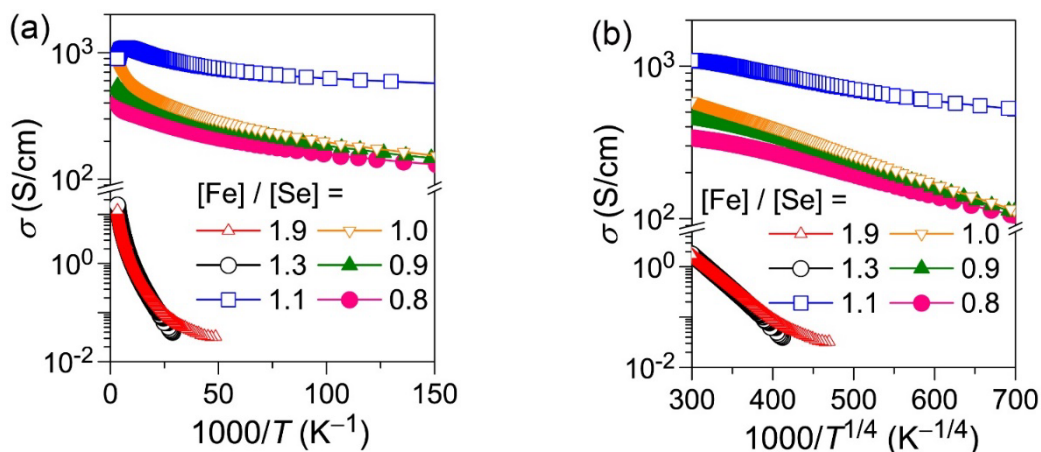


Figure 2-10. Relationships between σ and (a) T^{-1} and (b) $T^{-1/4}$.

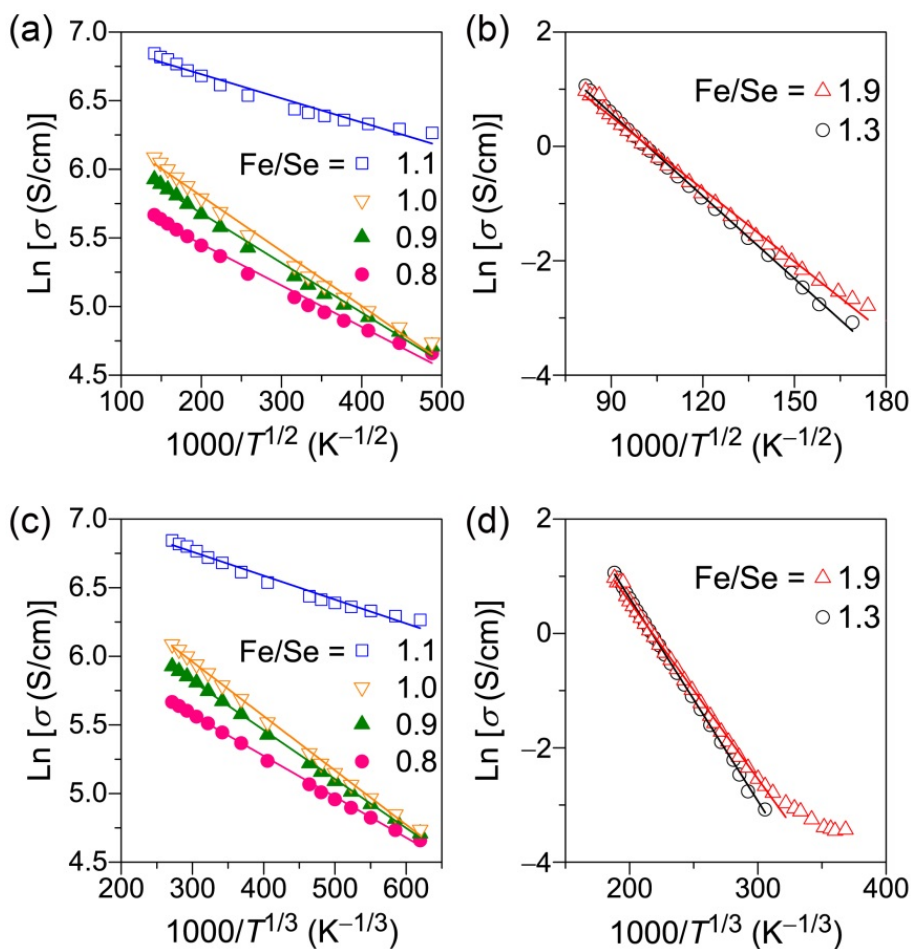


Figure 2-11. Plots of (a) and (b) $\text{Ln}\sigma$ vs. $T^{-1/2}$ and (c) and (d) $\text{Ln}\sigma$ vs. $T^{-1/3}$ for FeSe thin films with different compositions.

Table 2-I. Summary of results obtained from fitting by $T^{-1/n}$ ($n = 2 - 4$). SD is the standard deviation for each fitting.

| [Fe]/[Se] | $\sigma = \sigma_0 \exp(-(T_0/T)^{1/2})$ | | | $\sigma = \sigma_0 \exp(-(T_0/T)^{1/3})$ | | | $\sigma = \sigma_0 \exp(-(T_0/T)^{1/4})$ | | |
|-----------|--|------------------------------------|-------|--|------------------------------------|---------------------|--|------------------------------------|---------------------|
| | $-T_0^{1/2}$ | SD | T_0 | $-T_0^{1/3}$ | SD | T_0 | $-T_0^{1/4}$ | SD | T_0 |
| | /K ^{1/2} | /10 ⁻⁵ K ^{1/2} | /K | /K ^{1/3} | /10 ⁻⁵ K ^{1/3} | /K | /K ^{1/4} | /10 ⁻⁵ K ^{1/4} | /K |
| 0.8 | 3.02 | 7.95 | 9.1 | 2.98 | 3.81 | 26.5 | 3.21 | 2.31 | 106.2 |
| 0.9 | 3.62 | 7.89 | 13.1 | 3.57 | 3.04 | 45.5 | 3.84 | 1.87 | 217.4 |
| 1.0 | 4.01 | 9.86 | 16.1 | 4.01 | 4.31 | 64.4 | 4.26 | 2.26 | 329.3 |
| 1.1 | 1.75 | 9.64 | 3.1 | 1.74 | 7.07 | 5.3 | 1.88 | 6.30 | 12.5 |
| 1.3 | 35.50 | 17.86 | 1260 | 48.12 | 42.10 | 1.1×10 ⁵ | 33.12 | 19.08 | 1.2×10 ⁶ |
| 1.9 | 30.95 | 34.69 | 958 | 42.19 | 61.46 | 7.5×10 ⁴ | 29.47 | 20.34 | 7.5×10 ⁵ |

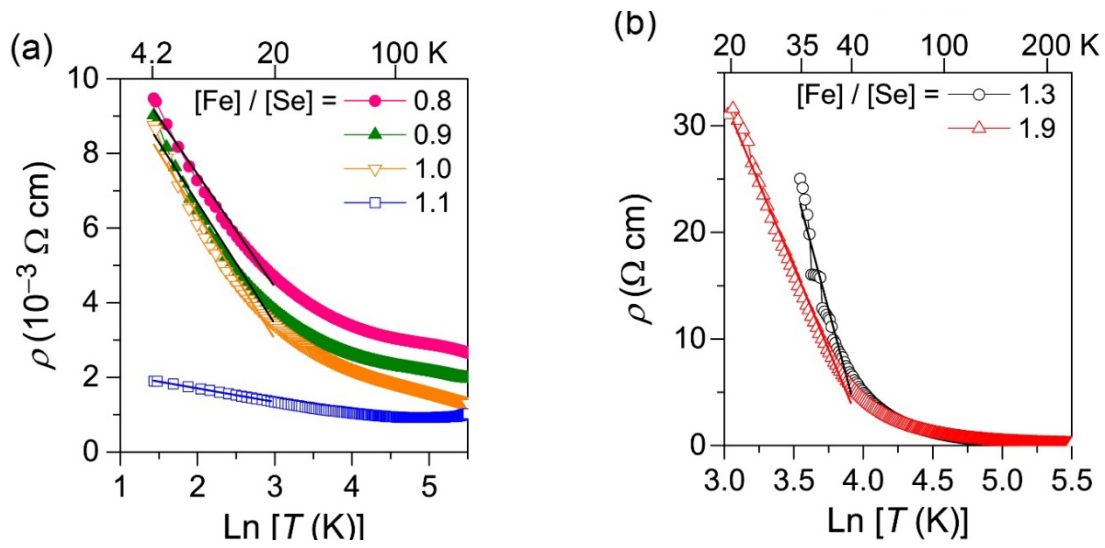


Figure 2-12. ρ versus $\ln(T)$ for FeSe films with $[\text{Fe}]/[\text{Se}]$ of (a) 0.8–1.1 and (b) 1.3 and 1.9.

Solid lines in each figure are linear least-squares fitting results.

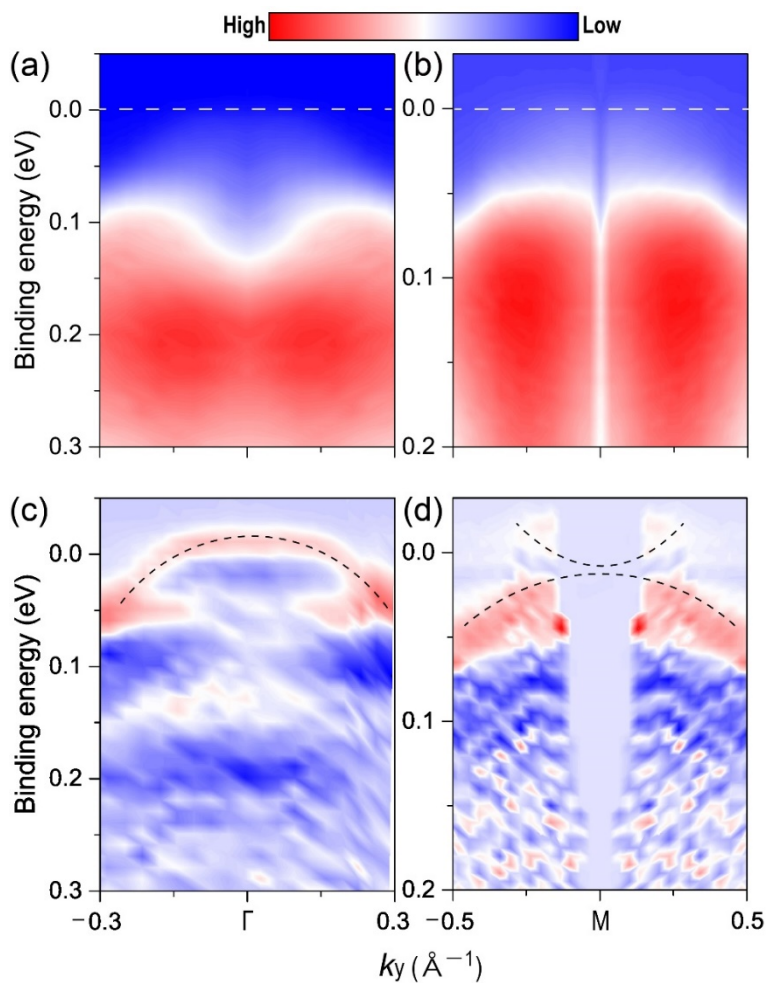


Figure 2-13. Fermi surface of the FeSe film grown at the optimum T_s of 500 °C with $[\text{Fe}]/[\text{Se}] = 1.1$ directly observed by ARPES at ~ 10 K. The horizontal bar indicates photoelectron intensity. ARPES responses around the (a) Γ - and (b) M-points. White dashed lines in (a) and (b) represent the Fermi level calibrated using Au as a reference. Second-derivative spectra with respect to energy, where (c) and (d) correspond to (a) and (b), respectively. Black dashed curves in (c) and (d) are a visual guide to help trace the dispersions.

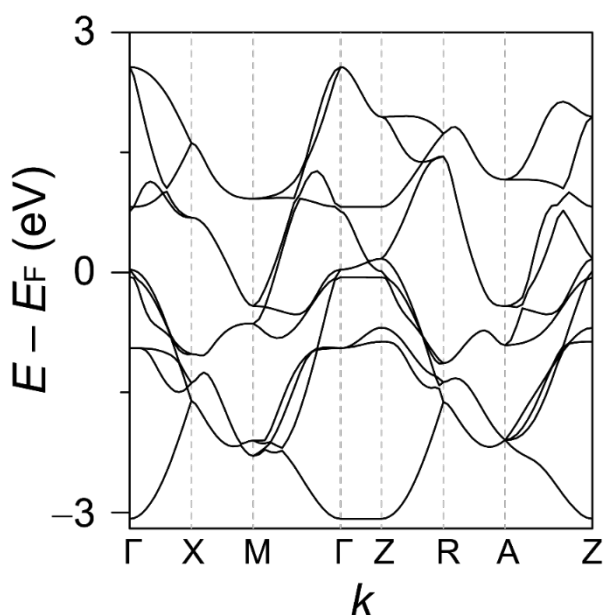


Figure 2-14. Calculated Electronic structure of FeSe. The calculation was performed by using vasp code with PBE potential.

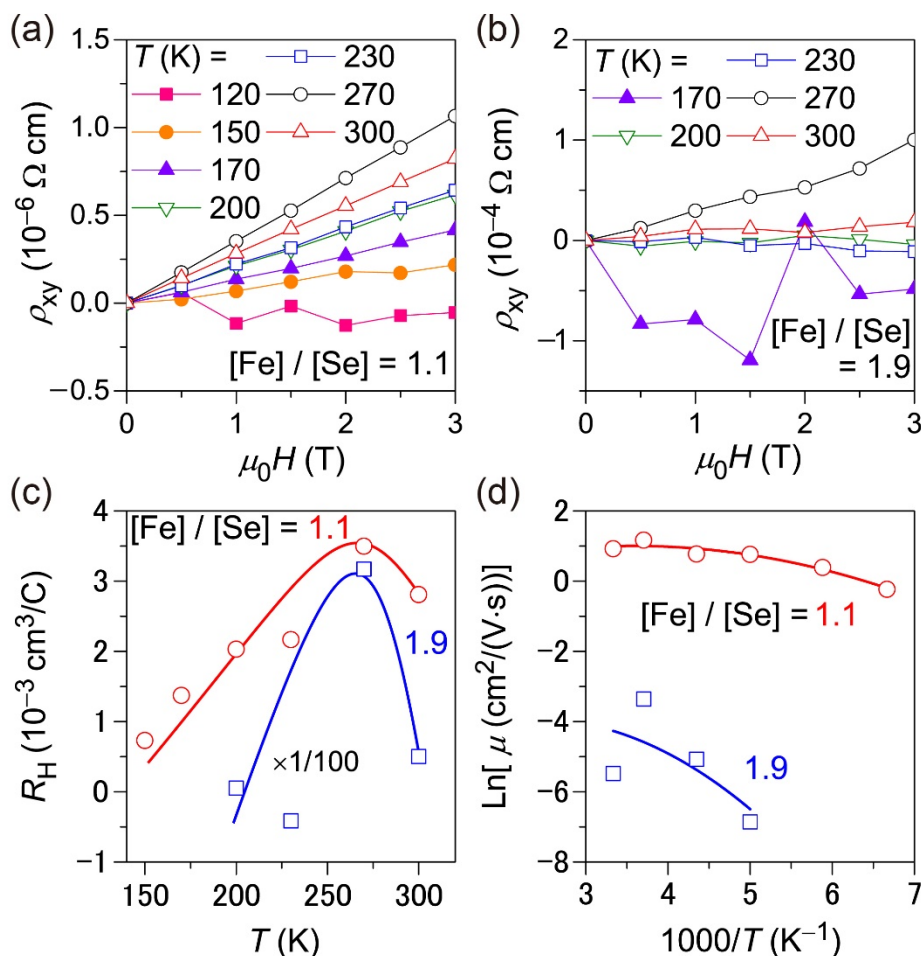


Figure 2-15. Results of Hall effect measurements for FeSe films grown at the optimum T_s of 500 °C with $[\text{Fe}]/[\text{Se}] = 1.1$ and 1.9. (a, b) Transverse resistivity (ρ_{xy}) as a function of external magnetic field (H) at (a) $T = 120\text{--}300$ K for the film with $[\text{Fe}]/[\text{Se}] = 1.1$ and (b) $T = 170\text{--}300$ K for the film with $[\text{Fe}]/[\text{Se}] = 1.9$. (c) Dependence of the Hall coefficient (R_H) of the films with $[\text{Fe}]/[\text{Se}] = 1.1$ and 1.9 on T estimated from (a) and (b), respectively. For the film with $[\text{Fe}]/[\text{Se}] = 1.9$, the R_H values are magnified by hundred times. (d) Dependence of the mobilities (μ) on T estimated from the results in (c) and ρ in **Figure 2-9a**. Red circles and blue squares in (c) and (d) correspond to the films with $[\text{Fe}]/[\text{Se}] = 1.1$ and 1.9, respectively. Red and blue solid curves in (d) denote quadratic-polynomial fitting results for the films with $[\text{Fe}]/[\text{Se}] = 1.1$ and 1.9.

Chapter 3. Stability of FeSe Epitaxial Films against Air Exposure

3.1. Importance of Surface Stability for Electric Field-Induced Carrier Doping

In a previous **Chapter 2**, FeSe epitaxial thin films were fabricated on SrTiO₃ single crystal by molecular beam epitaxy with various growth conditions, where the highest quality epitaxial film was obtained at growth temperature of 500 °C and [Fe]/[Se] atomic ratio of 1.1 [1]. The fabricated FeSe thin films received strains both for in-plane and out-of-plane, and exhibited insulator-like electric transport properties as previously reported [2, 3]. As results of direct observation of the electronic structure using ARPES and Hall effect measurements, it was clarified that the insulator-like behavior is attributed to enhancement of the electron-electron correlation as well as generation of potential barrier to scatter carrier for percolation conduction [4, 5]. Therefore insulator-like FeSe is regarded as a promising candidate for high- T_c superconductor based on a strategy; doping of Fe-based compound with strong electron correlation leads to appearance of high- T_c superconductivity.

So far in FeChs, carrier polarity of doping is limited to electron-type. The general ways of electron injection are isovalent substitution [7] and intercalation of charged atom or molecular into a space between FeCh₄ layers [8-11]. In isovalent doping, chemical pressure is introduced by replacement of a Ch-site with other Ch having different ionic radius and then leads to resultant supply of electron; e.g., in Te-doped FeSe and S-doped FeSe, the T_c is enhanced from 8 K (pristine FeSe [6]) up to 15.3 K [7] and 15.5 K [7], respectively. On the other hand, intercalation provokes charge transfer from the inserted ion to FeCh₄

conduction layers and contributes to much higher T_c than that achieved by isovalent doping; e.g., in $\text{KFe}_{2-y}\text{Se}_2$ and $\text{Li}_x(\text{NH}_2)_y(\text{NH}_3)_{1-y}\text{Fe}_2\text{Se}_2$, the T_c is 30 K [8] and 43 K [10].

Here it should be noted that these chemical doping methods are not preferred for the insulator-like FeSe, because the insulator-like behavior is stimulated by the epitaxial strain. Hence I focus on electric field-induced electrostatic carrier injection, which is performed by constructing a transistor structure. It should be the most suitable doping process for this system, because carrier can be accumulated without any chemical substitution for the strained epitaxial thin film. In such electric field-induced carrier doping, the interface between a channel layer and gate insulator is one of the most considerable factors. Thus in this **Chapter**, the influence of air exposure on the surface degradation of the FeSe epitaxial films were examined.

3.2. Experimental Procedure

3.2.1. Fabrication of FeSe epitaxial films and the EDLTs

In this work, ~10-nm-thick FeSe films were grown heteroepitaxially on (001)-oriented SrTiO_3 (STO) single crystals (size: $10 \times 10 \text{ mm}^2$, 0.5-mm thick) using molecular beam epitaxy (MBE, EV-100/PLD-S made by Eiko Co.). Details of the film growth conditions and electric-double layer transistor (EDLT) structure are provided in **Chapters 2** [1] and **4** [2]. The FeSe films were stored in an Ar-filled glove box (MDB-1BKHTMK type 2, Miwa Manufacturing Co., Ltd.), which was directly connected with the load lock/preparation chamber of the MBE system. The oxygen concentration and dew point of the glove box were $\ll 1 \text{ ppm}$ and approximately $-100 \text{ }^\circ\text{C}$, respectively.

An EDLT device was fabricated using a film patterned with a shadow mask and exposed to air for a few tens of minutes, and then, the temperature dependence of the sheet resistance (R_s) of the EDLT channel under a gate bias (V_G) was measured to determine the effect of the

air exposure. Structural and chemical analyses (i.e., except the EDLT) were performed using $10 \times 10 \text{ mm}^2$ samples. The temperature dependences of the electrical resistivity (ρ) of the as-grown and air-exposed films were measured using the four-probe method using a physical property measurement system.

3.2.2. Structure and surface analyses of FeSe films

θ -coupled 2θ scan X-ray diffraction (XRD, SmartLab, Rigaku Co.) using $\text{CuK}\alpha$ radiation with a rotation Cu anode and power of $45 \text{ kV} \times 200 \text{ mA}$ was performed using Bragg–Brentano geometry to determine the crystalline phases of the films. Note that the Bragg–Brentano geometry is unsuitable for evaluating epitaxial films because the X-ray scattering angle and line-width are large for the crystallite orientation distribution and diffraction peak widths of high-quality epitaxial films; therefore, the monochromatic parallel beam configuration is usually used. However, the use of the Bragg–Brentano geometry is an effective method to detect small amounts of impurity phases because a blighter incident X-ray beam can be used than that of the monochromatic parallel one. XRD patterns of the as-grown films were obtained without air exposure using an O-ring sealed Ar-filled measurement holder to avoid surface degradation during the measurements. However, atomic force microscopy measurements (AFM, MultiMode 8 made by Bruker Nano Inc.), which were performed to observe the surface morphology, could not be conducted without air exposure. To transfer the films from the load lock/preparation chamber of the MBE apparatus to the AFM stage required $\sim 200 \text{ s}$ after air exposure of the films. However, only $\sim 30 \text{ s}$ was needed to transfer the film from the glove box to the AFM stage because the sample was removed from the substrate holder in the glove box (i.e., not in air) in this case. The surfaces of the films were exposed to air during AFM observation for 260 s per single scan.

3.2.3. Chemical composition analysis of FeSe surface

The chemical composition of the surface was analyzed using field-emission scanning auger electron spectroscopy (FEAES, PHI 700, ULVAC PHI Inc.), in which four elements (C, O, Fe, and Se) were focused on under electron acceleration conditions of 10 kV and 10 nA to minimize damage by the electron beam. The observation points were selected using the scanning electron microscopy (SEM) mode of the PHI 700 instrument. The specification spatial resolution of the PHI 700 is 6 nm in SEM mode and 8 nm in AES mode. For the actual observation conditions, the lateral beam size and analysis depth (inelastic mean free path (IMFP) of emitted electrons) were estimated to be 20–30 and 3 nm.

3.3. Results and Discussion

3.3.1. Generation of nano-sized particular structures at film surface by air exposure

Figures 3-1a – 3-1c present AFM images of the FeSe film, which was transferred from the load lock/preparation chamber to the AFM stage directly after film growth. The AFM scans were repeated three times in the same observation area. As observed in the cross section (Fig. 3-1d, the line indicated by the black and red arrows in Fig. 3-1a), two particular structures were observed in the first scan. One structure had a lateral size of ~20 nm and a height of ~3 nm at the position = 235 nm (indicated by the red vertical arrow); the other structure had a lateral size of ~20 nm and height of ~1 nm at the position = 87 nm (indicated by the black vertical arrow). Then, in the second scan image, the particular structure at position = 78 nm grew to a vertical size of ~4 nm (the black arrow), whereas the size of the particular structure at the position = 235 nm in the first scan image did not change. In the third scan, the sizes of both particular structures were almost the same; however, the observed position of one of them (that indicated by the black arrow) slightly changed for

each scan. This result indicates that the small-sized particular structures grew to ~ 4 nm height within 260 s (= 1 scan time) and that adsorption of the particular structures to the surface would be very weak (i.e., the AFM probe would scratch and slightly manipulate them.). It should be noted that such fast air-degradation was not observed in another FeSe-related material, $\text{TlFe}_{1.6}\text{Se}_2$ [12]. Therefore, this phenomenon is unique to FeSe. Other locations (the lines indicated by the green, blue, and pink arrows) were also examined during the second and third scans, as shown in **Fig. 3-1e**. At this point, no significant change in the size or structure was observed. These results imply that the generation and growth of particular structures at the FeSe film surface are fast processes occurring within 260 s and that their growth almost appears to be saturated at a height of ~ 4 nm at this time scale (within 980 s).

Next, I examined the effect of exposure to air for longer times of up to 1 h. The sample was stored in an Ar-filled glove box for 5 days, transferred to the AFM stage in air, and the AFM observation was started immediately. In the first scan image (**Fig. 3-2a**), almost the same size of the particular structures as that observed in **Fig. 3-1a** was observed. However, the density of the structures in **Fig. 3-2a** looks higher than that in **Fig. 3-1a**, suggesting that the degradation rate was suppressed but that moderate degradation proceeded even in the Ar-filled glove box. After exposure to air for 30 min (**Fig. 3-2b**) and 60 min (**Fig. 3-2c**), the size of the particular structures became larger in both the lateral and height directions. The lateral sizes of the structures were ~ 20 nm for the 30-min sample and 30 nm for the 60-min sample. However, the lateral coverage of the particular structures almost remained the same. Compared with the result in **Figs. 3-1c** and **3-1e** (after ~ 16 min), the size almost doubled after air exposure for 1 h. This result implies that the growth rate of the particular structures was low, whereas they gradually grew at the initial growth points with air exposure.

3.3.2. Investigation of origin of nano-sized particular structures

To determine the origin of the particular structures at the FeSe film surface, XRD measurements of the air-exposed films (**Fig. 3-3**) were firstly performed. However, no additional impurity phase was observed. It was also confirmed that the *c*-axis lattice parameter did not change by comparing the peak positions of the FeSe 004 diffraction peak at $2\theta \approx 68.8^\circ$ of the as-grown and air-exposed films (see the vertical dotted line in **Fig. 3-3**). However, the full widths at half maximum (1.03°) of the FeSe 004 diffraction peak of the air-exposed film was wider than that (0.96°) of the as-grown film, suggesting that slight disorder of the layered structure and/or a slight decrease in the crystallite size occurred with air exposure. However, I did not detect any indication of this disorder or decrease in the crystallite size from the crystal structure or crystalline phase from the XRD measurements.

Then chemical composition point analysis of the FeSe film exposed to air for 150 min was performed using FEAES. Many particular structures were observed on the FeSe film surface in the SEM image (**Fig. 3-4a**), and then the two observation points were selected as indicated by the circles. One point was the position of a particular structure, and the other point was in the flat surface region without any particular structure. The lateral size of the particular structure was ~ 100 nm, which is larger than that of the sample exposed for 60 min (**Fig. 3-2c**), mainly because of the longer exposure time. The diameter of the incident electron beam and the IMFP of the emitted electrons under the observation condition were estimated to be 20–30 and 3 nm, respectively. These conditions guarantee that the electron beam is irradiated only within the particular structure and that the AES signal comes only from the particle structure. **Figs. 3-4b** and **3-4c** present the FEAES spectra of both regions. Although clear signals were observed for the main constituent elements (Fe and Se), significant contamination of carbon and oxygen was also detected. This result indicates that the entire top surface of the FeSe film exhibits similar air-sensitivity, regardless of the

presence of the particular structures. Although the spectra were similar, subtraction was performed between **3-4b** and **3-4c**. As indicated by the two vertical arrows, small difference peaks were observed for the C and O signals, whereas no difference was detected for Fe and Se. It was also confirmed using SEM that the particular structures disappeared in the FEAES measurement chamber for longer observation times or higher acceleration voltages. I cannot propose the exact origin of the particular structures from the FEAES results; however, these results suggest that the generated structures were composed of and reacted with light elements in air such as O, C, H, and N.

The above speculation for the origin (i.e., light elements in air) is also supported by findings regarding specimen preparation for transmission electron microscopy (TEM) observation. It was attempted to fabricate TEM specimens using a film exposed to air for 3 h that was covered with a gold film as a protection layer using a standard thinning technique combined with cutting, bonding, ion milling, and dimpling. However, the particular structures could not be found in the TEM specimens (the usual lateral size in the thinned region of TEM specimens is a few μm^2), implying that the particular structures easily disappeared with mechanical contact (during the cutting and bonding processes) and/or ion damage (during milling and dimpling) and not only with irradiation of the electron beam.

3.3.3. EDLT using air-exposed FeSe channel layer

Next, the influence of the surface degradation was investigated on the electric-double layer transistor (EDLT) properties, where electrostatic carrier is doped by application of gate bias (V_G). The detailed explanation of EDLT is seen in **Chapter 4**. The temperature dependence of the sheet resistance (R_s) was measured for an EDLT channel using an FeSe film air-exposed for a few tens of minutes (**Fig. 3-5**). This initial insulator-like R_s behavior is similar to that of the EDLT without exposure to air reported in Refs. [2, 3], although the

R_S behavior in the low-temperature region was different. However, even though a high V_G of +4.0 V was applied, no phase transition was detected and R_S monotonously increased over the entire temperature range; clear modulation of the drain current and phase transition were not observed. These findings suggest that the particular structures generated at the surface act as an obstacle to field-induced phase transition and superconductivity in the FeSe EDLTs. For this reason, electrochemical etching [13, 14, 15], which should be able to remove the particular structures, is effective for achieving high- T_c EDLTs if the FeSe channels must be exposed to air during the device fabrication process.

3.3.4. Long-time stability of epitaxial FeSe film preserved in Ar

Finally, the long-time stability of FeSe films is discussed. **Figure 3-6** summarizes the results for the film stored in a glove box for ~ 2 years. **Figures 3-6a** and **3-6b** present XRD patterns of the film. In this case, no additional impurity phase was detected, as shown in **Fig. 3-6a**. However, compared with the as-grown film, the c -axis of the long-time-stored film expanded and approached the bulk value, as indicated by the vertical dotted line in **3-6b**. This result indicates that the film stored for a long time was almost fully relaxed similar to the bulk FeSe sample. **Figures 3-6c – 3-6e** show the surface morphology of the film stored for a long time. Although the film was stored in a glove box, much larger particular structures were observed than those in **Figs. 3-1** and **3-2**. This result suggests that a very small amount of oxygen or related air-constituting element can enhance the growth of the structures, although the glove box maintains a very-high-purity inert and dry atmosphere with an oxygen concentration $\ll 1$ ppm and a dew point of approximately -100 °C. **Figure 3-6f** shows the temperature dependence of the resistivity ($\rho - T$) curves. Air exposure for 60 min slightly increased ρ . However, a remarkable increase in ρ was observed for the sample stored for a long time, especially in the low-temperature region (a hump structure is observed at ~ 30 K in the $\rho - T$ curve of the sample stored for 2 years; however, the origin is currently

unclear). Before this experiment, we expected that superconductivity may be observed because the lattice parameter is fully relaxed, as observed in **Fig. 3-6a** and **3-6b**. However, superconductivity was not observed. Therefore, surface contamination (i.e., the particular structures) dominated the ρ - T behavior of the sample stored for 2 years.

4.4. Conclusion

The generation of particular structures was observed at the surface of FeSe epitaxial films directly after exposure to air. The origin of their generation remains unclear because no clear difference was detected in the chemical compositions of the particular structures and the flat bulk region. The origin should be related to light elements in air such as O, C, H, and N based on the Auger electron spectroscopy results. An electric-field-induced modulation was not observed for the EDLT using the air-exposed FeSe under the application of a positive gate bias (i.e., electron doping). These results indicate that an *in-situ* device fabrication process without exposure to air [16] is necessary for electric field-induced superconductivity in FeSe EDLTs if an electrochemically etching process [13, 14, 15] is not employed.

References

1. K. Hanzawa, Y. Yamaguchi, Y. Obata, S. Matsuishi, H. Hiramatsu, T. Kamiya, and H. Hosono, *Phys. Rev. B*, **99**, 035148-1 – 035148-11 (2019).
2. K. Hanzawa, H. Sato, H. Hiramatsu, T. Kamiya, H. Hosono, *Proc. Natl. Acad. Sci. USA.*, **113**, 3986 – 3990 (2016).
3. K. Hanzawa, H. Sato, H. Hiramatsu, T. Kamiya, H. Hosono, *IEEE Trans. Appl. Supercond.*, **27**, 7500405 (2017).
4. T. Kamiya, K. Nomura, and H. Hosono, *J. Display Technol.*, **5**, 462–467 (2009).

5. T. Kamiya, K. Nomura, and H. Hosono, *Appl. Phys. Lett.*, **96**, 122103 (2010).
6. F.-C. Hsu, J.-Y. Luo, K.-W. Yeh, T.-K. Chen, T.-W. Huang, P.M. Wu, Y.-C. Lee, Y.-L. Huang, Y.-Y. Chu, D.-C. Yan, and M.-K. Wu, *Proc. Natl. Acad. Sci. USA.*, **105**, 14262 – 14264 (2008).
7. Y. Mizuguchi, F. Tomioka, S. Tsuda, T. Yamaguzhi, and Y. Takano, *J. Phys. Soc. Jpn.*, **78**, 074712 (2009).
8. J. Guo, S. Jin, G. Wang, S. Wang, K. Zhu, T. Zhou, M. He, and X. Chen, *Phys. Rev. B*, **82**, 180520(R) (2010).
9. T. P. Ying, X. L. Chen, G. Wang, S. F. Jin, T. T. Zhou, X. F. Lai, H. Zhang, W. Y. Wang, *Sci. Rep.*, **2**, 426 (2012).
10. M. Burrard-Lucas, D. G. Free, S. J. Sedlmaier, J. D. Wright, S. J. Cassidy, Y. Hara, A. J. Corkett, T. Lancaster, P. J. Baker, S. J. Blundell, and S. J. Clarke, *Nat. Mater.*, **12**, 15 – 19 (2013).
11. J. Guo, H. Lei, F. Hayashi, and H. Hosono, *Nat. Commun.*, **5**, 4756 (2014).
12. T. Katase, H. Hiramatsu, T. Kamiya, and H. Hosono, *Proc. Natl. Acad. Sci. USA.*, **111**, 3979 – 3983 (2014).
13. J. Shiogai, Y. Ito, T. Mitsuhashi, T. Nojima, and A. Tsukazaki, *Nat. Phys.*, **12**, 42 – 46 (2016).
14. J. Shiogai, T. Miyakawa, Y. Ito, T. Nojima, and A. Tsukazaki, *Phys. Rev. B*, **95**, 115101 (2017).
15. S. Kouno, Y. Sato, Y. Katayama, A. Ichinose, D. Asami, F. Nabeshima, Y. Imai, A. Maeda, and K. Ueno, *Sci. Rep.*, **8**, 14731 (2018).
16. H. Hiramatsu, H. Hosono, *TEION KOGAKU* (J. Cryo. Soc. Jpn) **52**, 433 – 442 (2017).
(in Japanese)

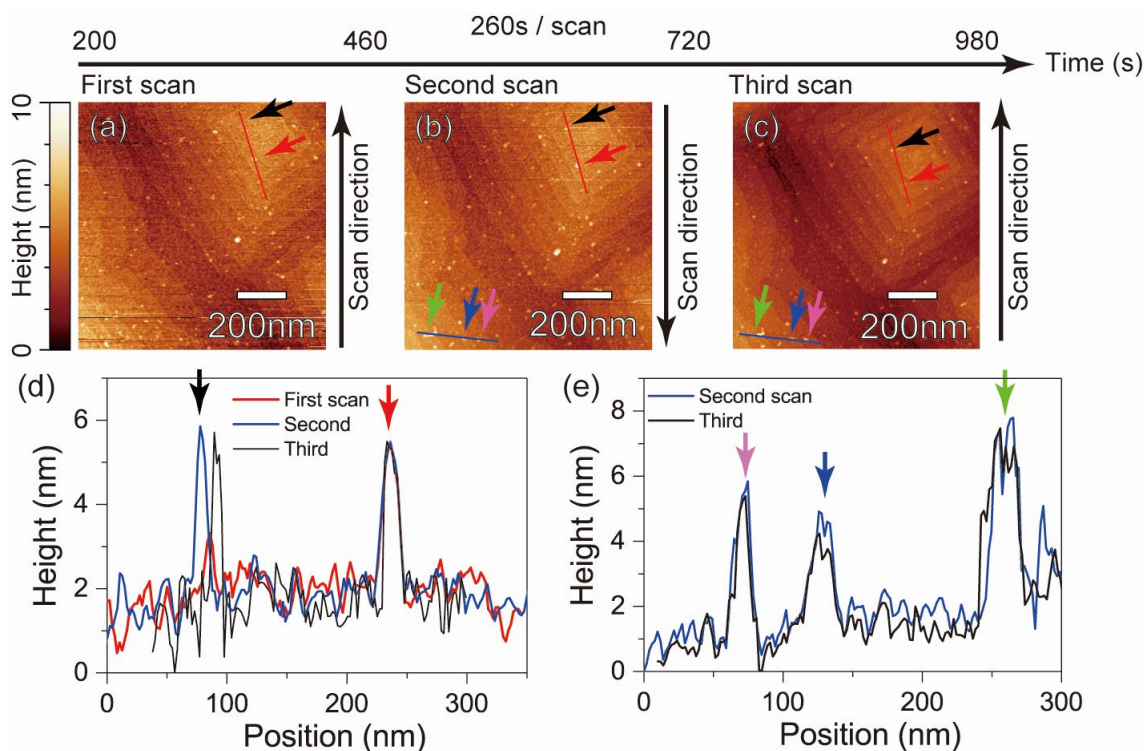


Figure 3-1. Surface morphology of FeSe film measured in air. (a)–(c) AFM images. The color bar indicates the height scale in the images. (a), (b), and (c) are results of a continuous repeating observation of the first, second, and third scans, respectively. The top horizontal arrow indicates the time after air exposure of the film, and the vertical arrows on the right of (a)–(c) are the scan direction of the AFM observation. The observation start time corresponds to 200 s because transferring the film from the load lock/preparation chamber of the MBE apparatus to the AFM stage required 200 s. (d) and (e) Cross-section profiles at the lines indicated by (d) vertical lines in (a)–(c) and (e) horizontal lines in (b)–(c).

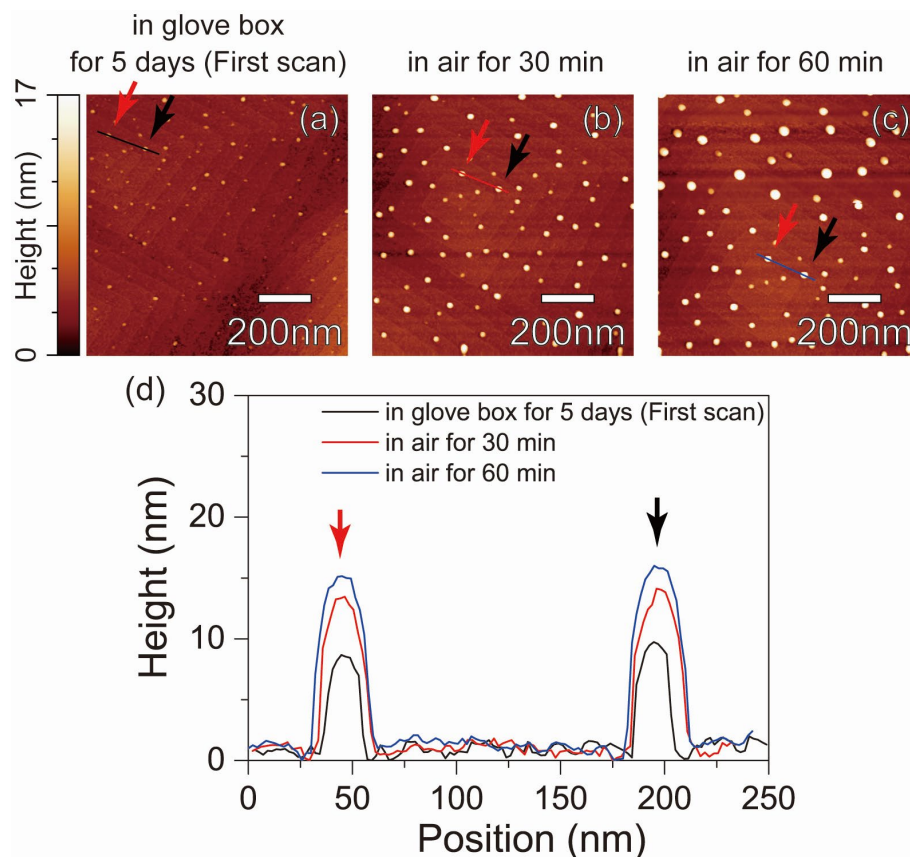


Figure 3-2. Change in surface morphology of air-exposed FeSe film for long times up to 1 h. (a)–(c) AFM images. The color bar indicates the height scale in the images. (a) First scan measured after storage for 5 days in Ar-filled glove box. (b) and (c) Images of sample (a) exposed to air for (b) 30 and (c) 60 min. (d) Cross-section profiles at lines in (a)–(c).

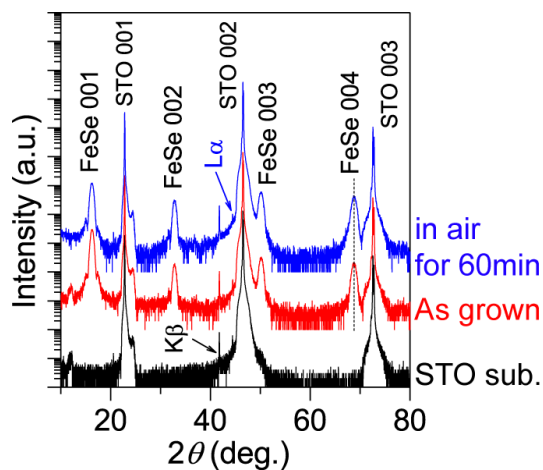


Figure 3-3. Out-of-plane XRD patterns of FeSe films. (Middle) As-grown film. These data were taken without air exposure using an Ar-filled measurement holder to avoid surface degradation during the measurements. (Top) Film with air exposure for 60 min. (Bottom) Pattern of bare STO single-crystal substrate for comparison. Weak diffraction peaks originating from Cu K β , W L α , and some multiple reflections are observed from the single-crystal STO substrate.

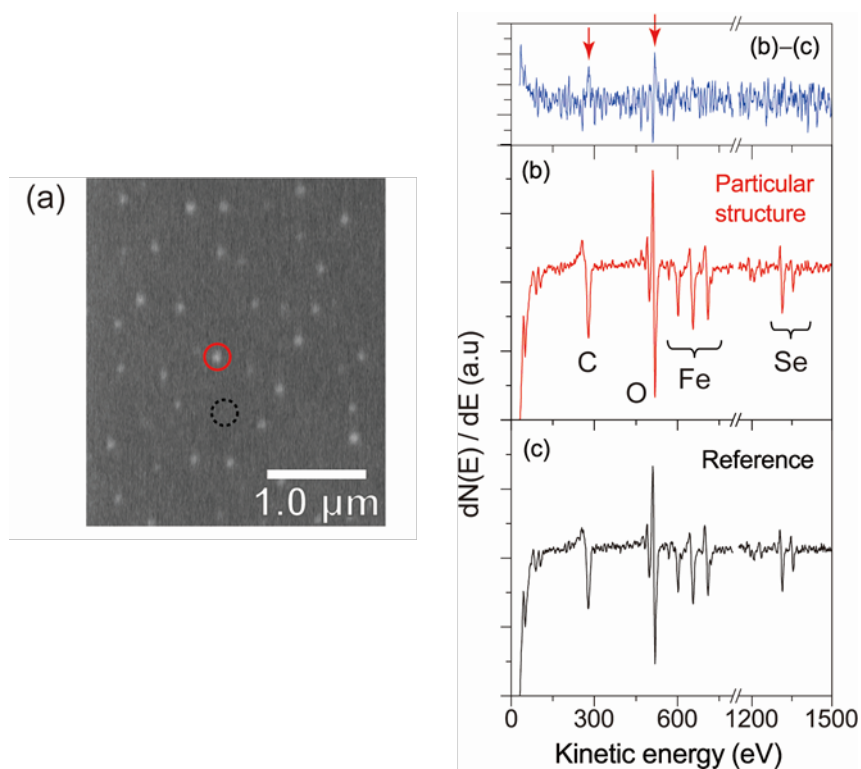


Figure 3-4. Chemical composition point analysis of FeSe film surface exposed to air for

150 min using FEAES. (a) SEM image of FeSe film to determine observation points. The red and the dotted black circles are the observation points corresponding to [(b): a particular structure position] and [(c): a flat surface position for reference]. The top figure over (b) is the subtraction spectrum between (b) and (c).

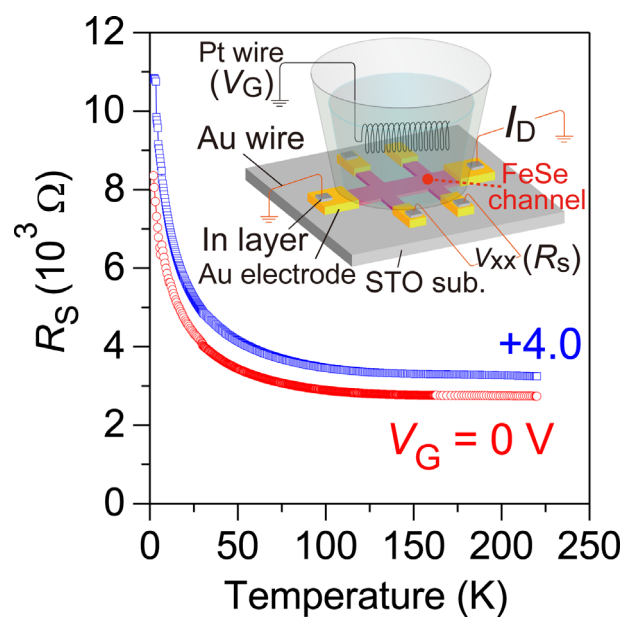


Figure 3-5. Temperature dependence of sheet resistance (R_s) of an EDLT device using an FeSe channel layer exposed to air for a few tens of minutes under gate bias voltages (V_G) of 0 and +4 V. The inset presents a schematic illustration of the EDLT.

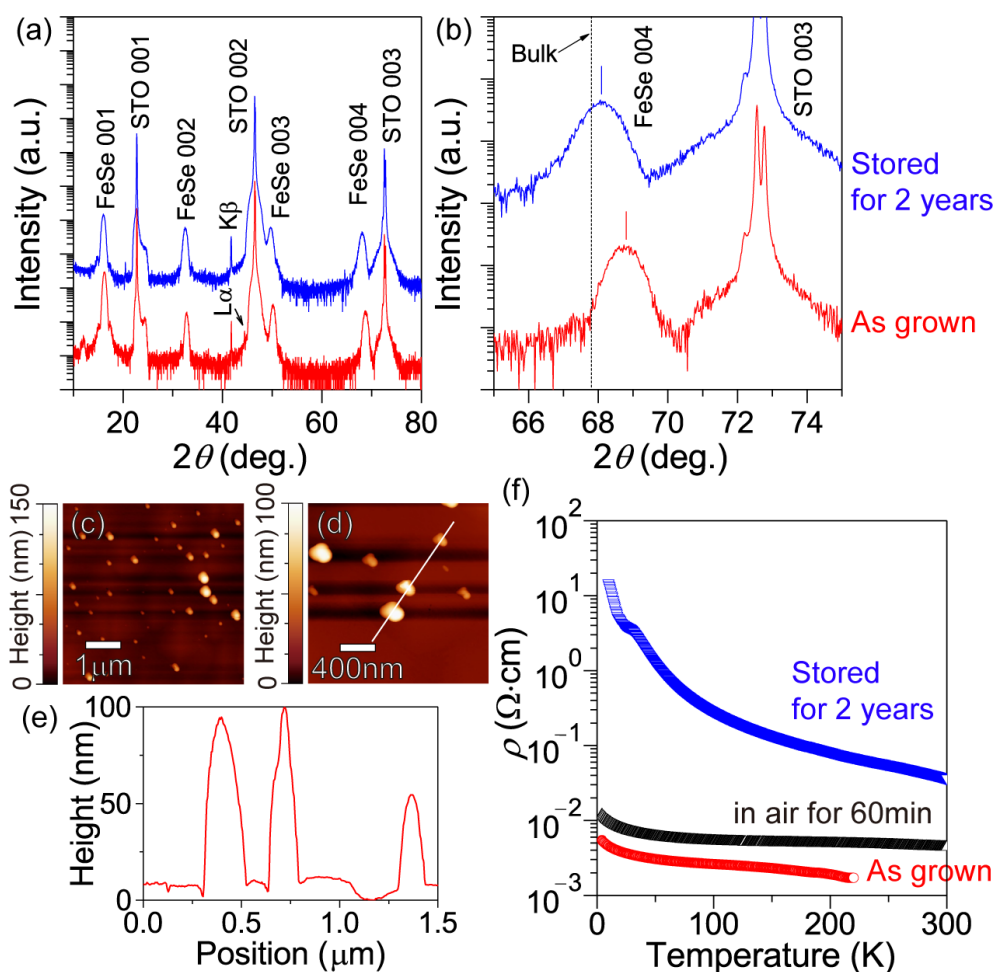


Figure 3-6. Structural and electrical properties of FeSe films stored in a glove box for 2 years. (a, b) Out-of-plane XRD pattern. (b) Enlarged pattern in the high 2θ region. (c)–(e) Surface morphology. (c, d) AFM images of the film surface. The color bars show the height scale for each image. (d) Enlarged image of (c). (e) Cross-section profile of the line in (d). (f) Temperature dependence of resistivity (ρ) of the film. Data for the as-grown film and film exposed to air for 60 min are shown for comparison.

Chapter 4. Electric Field-Induced Superconducting Transition of Insulator-like FeSe Thin Film at 35 K

4.1. EDLT for Electrostatic Carrier Doping

In **Chapter 2**, it was unveiled that insulator-like FeSe [1, 2] has strain-induced stronger electron-electron correlation than that of the single crystal. This represents that doping of the insulator-like FeSe would lead to high- T_c superconductivity, according to the strategy for enhancement of T_c discussed in **Chapter 2**. To stimulate superconducting phase in the insulator-like FeSe epitaxial layer, electric field-induced electrostatic carrier doping should be the most preferred method, because the insulator-like behavior originates from the epitaxial strain. As a result of preliminary investigation of surface stability of the FeSe epitaxial thin film, it was clarified that the surface of the FeSe film is easily deteriorated through air exposure [3], suggesting necessity to fabricate device for electric field-induced electron doping in an *in-situ* process.

An electric double-layer transistor (EDLT) structure with an ion-liquid gate is employed in this study. Research on carrier accumulation using the EDLT has been provoked since observation of insulator-superconductor transition at 0.4 K in SrTiO₃ [4]. Subsequently, EDLT structures were constructed and the electronic properties under electric field were examined not only for band insulators such as CdSe [5], MoS₂ [6, 7], and ZrNCI [8], but also for Mott insulators such as NiO [9], NdNiO₃ [10], and cuprates [11–14]. For Fe-based compounds, research using the EDLT structure was firstly developed in 2014 for a Mott insulator TlFe_{1.6}Se₂ [15], where insulator-metal transition was successfully observed. This result denotes that carrier doping utilizing the EDLT structure is effective for FeCh-based compounds, although superconductivity was not induced so far.

The most remarkable advantage of use of the EDLT is accumulated carrier concentration. Due to the very thin Helmholtz layer (~ 1 nm) and the resultant large capacitance of the ion-liquid, extremely high-density carrier can be accumulated ($\sim 8 \times 10^{14}$ cm $^{-2}$ [16–19]), which is approximately one order of magnitude higher than that induced by using a thin film transistor structure with a conventional solid state gate ($\sim 2 \times 10^{13}$ cm $^{-2}$ for SiO $_2$ [16]). Furthermore accumulated carrier density is controllable, because the EDLT does not require any chemical substitution for doping.

Hence in this **Chapter**, research objective is to demonstrate insulator-superconductor phase transition at high T_c in strained insulator-like FeSe via high-density carrier doping using EDLT structure, which is constructed in developed *in-situ* process, and to discuss on origin of the high- T_c superconductivity.

4.2. Experimental Procedure

4.2.1. Epitaxial thin film growth of ~ 10 nm thick FeSe

Heteroepitaxial FeSe thin films were grown on (001)-oriented SrTiO $_3$ (STO) single crystals by the molecular beam epitaxy (MBE) technique. To obtain an atomically flat substrate surface, I performed wet etching of as-received STO using a buffered HF solution, and then thermally annealed at 1050 °C just prior to film growth [20]. The base pressure of the MBE growth chamber was $< 1 \times 10^{-7}$ Pa. Two types of Knudsen cells (K-cells) were used to extract pure Fe and Se molecular beams: a high-temperature K-cell with a carbon heater for Fe (purity: 99.99%) and a normal K-cell with a tantalum heater for Se (purity: 99.999%). The temperatures of both K-cells were optimized to 1100 °C for Fe and 140 °C for Se using a beam flux monitor near the substrate. The optimized substrate temperature was 500 °C. The film thicknesses were ~ 10 and 110 nm, which were determined by least-squares fitting to a fringe pattern obtained by x-ray reflectivity spectroscopy using Cu K α_1 monochromated

by a Ge (220) crystal. The surfaces of the STO substrates and the FeSe films were observed by *in situ* reflective high-energy electron diffraction (RHEED) and atomic force microscopy (AFM) in ambient atmosphere.

4.2.2. Structure analysis of FeSe thin film

The structures of the films, such as the crystal orientation, were precisely examined by x-ray diffraction (XRD, source: monochromatic Cu $K\alpha_1$) with an analyser crystal located in front of the detector. The ω -coupled 2θ scans in the out-of-plane XRD measurements provided the crystallographic orientation of the film normal to the substrate surface. The tilting angle of the crystallites was obtained by 2θ -fixed ω scans (out-of-plane x-ray rocking curve (XRC)). The in-plane crystallographic orientation (i.e., orientation parallel to the substrate surface) was determined by ϕ -coupled $2\theta_\chi$ scans. A $2\theta_\chi$ -fixed ϕ scan also provided the rotational symmetry of the lattice/crystallites in the film plane. All of the axis relations of HRXRD can be found in [21]. The chemical compositions of the films (i.e., atomic ratio of Fe and Se) were determined with an electron probe microanalyser (EPMA) using wavelength dispersive spectroscopy mode.

4.2.3. In-situ fabrication of EDLT using FeSe as a channel

Approximately 10-nm-thick FeSe epitaxial films on the STO (001) substrates were used as the transport channel of the EDLT. The FeSe channel layer with a six-terminal Hall bar geometry (channel size: 500 μm long and 200 μm wide) and the Au pad electrodes were deposited using shadow masks. After bonding metal wires to the Au pads with In metal, the channel region was covered with a silica-glass cup (fixed with an epoxy adhesive) to add the ionic liquid. The ionic liquid DEME-TFSI was used as the medium for the gate insulator. The ionic liquid was poured into the silica-glass cup, and then a Pt coil was inserted into the ionic liquid to serve as the gate electrode. All of these device setup processes were performed without exposure to air. The device structure is shown in **Fig. 4-1**.

4.2.4. Electronic transport measurements of FeSe-EDLT

Transfer curves (i.e., the V_G dependence of the drain current I_D) were measured with a semiconductor parameter analyzer at 220 K. The temperature dependences of the resistivity and sheet resistance ($\rho-T$ and R_s-T), and transverse resistance (R_{xy} , i.e., Hall effect) at 40 K of the films and EDLTs were measured by the four-probe method under external magnetic fields of up to 9 T under an applied gate bias (V_G) from 0 to +5.5 V. V_G was applied at 220 K because chemical reaction between FeSe layers and DEME-TFSI occurs at higher temperatures [22] and this temperature is well above the rubber phase transition temperature of DEME-TFSI 190 K [23].

4.3. Results and Discussion

4.3.1. FeSe epitaxial thin film exhibiting insulator-like electric behavior

Figure 4-2 summarizes the structure and the relationship between the temperature (T) and the resistivity (ρ) of ~10-nm-thick FeSe epitaxial films on SrTiO₃ (STO) (001) grown by molecular beam epitaxy (MBE). **Figures 4-2a** and **4-2b** show an out-of-plane x-ray diffraction (XRD) pattern and an out-of-plane x-ray rocking curve (XRC) of FeSe 001 diffraction, respectively, indicating strong c -axis preferential orientation of the films (a wide-range pattern for $2\theta = 10-80^\circ$ is shown in **Fig. 4-3a**, confirming that there is no impurity phase). Because of the atomically flat surface of STO substrate, clear Kikuchi patterns in the reflective high-energy electron diffraction (RHEED) pattern, a step-and-terrace structure with a terrace width of ~120 nm, and no step-bunching are observed in **Figs. 4-2c** and **4-2e** (see the cross-section of the STO substrate surface in **Fig. 4-5b**). Heteroepitaxial growth of the FeSe film on STO is confirmed by the RHEED pattern in **Fig. 4-2d** ($2\theta_\chi$ -fixed ϕ scan of FeSe 200 in-plane diffraction is also shown in **Fig. 4-3b**), and the film has an atomically flat surface with root-mean-square roughness of 0.6 nm (**Fig. 4-2f**). It was confirmed that the chemical composition is 1.1:1 in the [Fe]:[Se] atomic ratio (measured with an electron probe

microanalyzer).

Figure 4-4a shows ρ - T curves of the 11-nm-thick FeSe film compared with a 110-nm-thick film. The thick film (110 nm) did not show zero resistance when T was decreased to 4 K, while superconductivity with an onset $T_c \approx 9$ K was confirmed by its external magnetic field dependence (**Fig. 4-4b**), i.e., a negative shift of T_c with increasing external magnetic field. However, in the case of the thin films (11 nm thick, see **Fig. 4-6** for determination of the thickness by x-ray reflectivity measurement), the ρ - T curve shows insulator-like behavior, i.e., ρ increased with decreasing T . The lattice parameters of the 11-nm-thick films are $a_{\text{film}} = 0.3838$ nm for the a axis (see **Fig. 4-7** for in-plane XRD patterns) and $c_{\text{film}} = 0.5448$ nm for the c axis (calculated from the peak position of out-of-plane FeSe 004 diffraction, See **Fig. 4-3a**). Because the values of a bulk sample are reported to be $a_{\text{bulk}} = 0.37704$ nm and $c_{\text{bulk}} = 0.55161$ nm [24], there is in-plane tensile strain [$(a_{\text{film}} - a_{\text{bulk}})/a_{\text{bulk}} = \Delta a/a_{\text{bulk}} = +1.8\%$] but out-of-plane compressive strain ($\Delta c/c_{\text{bulk}} = -1.2\%$). Because the insulator-like state is the main focus of this study, the thin (~ 10 nm) FeSe epitaxial layer was selected as an active channel layer for the EDLT.

4.3.2. Device properties of EDLT using an insulator-like FeSe channel

I fabricated EDLTs using a thin insulator-like FeSe layer, as shown in **Fig. 4-1**. The ionic liquid N,N -diethyl- N -methyl- N -(2-methoxyethyl)-ammonium bis-(trifluoromethylsulfonyl)imide (DEME-TFSI) was used as the gate insulator. **Figure 4-8** shows the cyclic transfer characteristics [drain current (I_D) versus gate bias (V_G)] of the FeSe EDLT under a drain voltage $V_D = +0.5$ V measured at $T = 220$ K. A positive V_G up to +4 V was applied to the gate electrode, which accumulates carrier electrons in the FeSe surface. When $V_G = +3.1$ V was applied, I_D began increasing. The maximum I_D in the transfer curve reached 45 μA at $V_G = +4$ V, along with an on-off ratio of ~ 2 . The gate leakage current (I_G , shown in the bottom panel of **Fig. 4-8**) also increased with increasing V_G up to +4 V, but it

was three orders of magnitude lower than I_D in the whole V_G region. After applying $V_G = +4$ V, I_D returned to the initial value when V_G was decreased to 0 V. A large hysteresis loop is observed because of the slow response of ion displacement in the ionic liquid. Notwithstanding there is a slight parallel shift in the second I_D - V_G loop and I_D becomes almost double, 84 μ A at $V_G = +4$ V, its origin is considered to be the slow response of ion displacement, which is the same as the hysteresis loop. This is because the shape and hysteresis width in the second loop are very similar to those in the first loop. In addition, it was confirmed that there was no change in the I - V characteristics in the channel layer at $V_G = 0$ before and after the cyclic measurements (see **Fig. 4-9** for the I - V characteristics). Here, I would like to point out that it has been reported EDLT using a STO channel exhibits similar characteristics, i.e., it also turns on at about $V_G = +3$ V [4]. In addition, it has recently been reported that oxygen vacancies are induced in an oxide-based EDLT and the metal state is stabilized even after removing the gate bias and ionic liquid [18]. However, the above results in **Figs. 4-8** and **4-9** guarantee that the observed results are reversible and reproducible. These results demonstrate that the origin of superconductivity by applying gate bias, which will be shown in **Fig. 4-10** later, is not due to the modification of the surface chemical/mechanical structures but the electrostatically accumulated carriers.

4.3.3. Electric field-induced superconductivity at 35 K

Figure 4-10 summarizes carrier transport properties of the FeSe EDLT, where V_G was applied at 220 K and kept constant during the measurements with decreasing T . As shown in **Fig. 4-10a**, the sheet resistance (R_s)- T curves at $V_G = 0 - +3.5$ V almost overlap in the whole T range. In contrast, when V_G is increased to +3.75 V, R_s in the normal-state region slightly decreases, indicating that the induced carrier density is increased by applying $V_G = +3.75$ V. When $V_G = +4$ V is applied, a broad R_s drop is observed at 8.6 K (see **Fig. 4-10b**). With further increase in V_G , this R_s drop shifts to higher T . It should be noted that zero

resistance is clearly observed at 4 K along with the onset $T = 24$ K when $V_G = +5$ V is applied. From $V_G = +5$ V to $+5.5$ V, there is a clear enhancement of the onset T of the R_s drop (from 24 to 35 K) along with reduction of the normal-state resistivity. **Figure 4-10c** shows the magnetic field dependence at $V_G = +5.5$ V, confirming its superconducting transition, i.e., the onset T_c shifts to lower T with increasing magnetic field. The superconducting state remains even when the external magnetic field is increased to 9 T, indicating that the upper critical magnetic field is considerably higher than 9 T. The upper critical field estimated from **Fig. 4-10c** using Werthamer–Helfand–Hohenberg theory [25] is ~ 70 T (See **Fig. 4-11**), which is much higher than that (30 T) of bulk FeSe [26].

4.3.4. Accumulated carrier density in superconducting FeSe-EDLT

To confirm high-density carrier accumulation in the EDLT, Hall effect measurements were performed under applying V_G up to $+5.5$ V. **Figure 4-10d** shows Hall coefficients R_H at 40 K. Positive R_H are obtained at each V_G applied, indicating that major carrier in the insulator-like FeSe epitaxial films is hole and consistent with the result in a FeSe single crystal [27] although negative R_H in low magnetic fields are also reported in this temperature range [28]. At $V_G = 0$ V, the R_H is $+1.1 \times 10^{-2}$ cm³/C, which is slightly higher than $(+2 \times 10^{-3}$ cm³/C) as reported in [27]. With increase in V_G to $+3.5$ V, R_H remains almost constant, which is consistent with R_s – T curves in **Fig. 4-10a**; i.e., they almost overlap in the whole T range. With further increase in V_G up to $+5.5$ V, R_H decreases linearly to $+2.7 \times 10^{-3}$ cm³/C. It is reported that FeSe bulk is a multi-band metal, indicating that high-density electrons and holes (both are orders of 10^{20} cm⁻³.) [28] intrinsically coexist and make its carrier transport properties very complicated. However, to roughly estimate the electron density accumulated in the channel surface by positive V_G , I subtracted the $1 / eR_H$ value (corresponds to the carrier density for a single band model) at $V_G = 0$ V from all the $1 / eR_H$ values on an assumption that the linear decrease in R_H with increasing V_G in the V_G range from 3.75 to 5.5

V corresponds to the increase in the sheet density of the accumulated electrons [$\Delta N_e = (1 / eR_H(V_G = x) - 1 / eR_H(V_G = 0)) \times t$, where t is thickness of the FeSe channel (8.3 nm)]. Then a phase diagram was built (see **Fig. 4-12**). T_c vs. (V_G or R_H at 40 K) are also shown in **Fig. 4-13** for comparison. At $8.1 \times 10^{13} \text{ cm}^{-2}$ ($V_G = +4 \text{ V}$), onset T_c of 8.6 K, which is close to that of bulk [29], was observed as seen in **Fig. 4-10b**. Supposing that the whole channel layer is accumulated by electrons, the average electron density is estimated to be $9.8 \times 10^{19} \text{ cm}^{-3}$. This value is consistent with the native carrier concentration in bulk FeSe, the order of 10^{20} cm^{-3} [28]. With linear increase in ΔN_e up to $1.4 \times 10^{15} \text{ cm}^{-2}$ (the average carrier density of $1.7 \times 10^{21} \text{ cm}^{-3}$), the maximum onset T_c of 35 K was observed. This result suggests that high T_c of the FeSe is owing to high-density carrier doping like reports, where external high pressures lead to this high- T_c range superconductivity (27–37 K) [30, 31] without impurity doping.

4.3.5. Discussion: origin of the high- T_c superconductivity

The above observation suggests that applying a gate bias changes the structure and/or the electronic state of the FeSe epitaxial films. Thus, I would like to discuss the origin of this high- T_c superconductivity. First discuss is the possibility of a chemical reaction between the FeSe channel and the DEME-TFSI ionic liquid. **Figure 4-14a** shows XRD patterns of the FeSe film dipped in DEME-TFSI without an applied gate bias. No impurity phase was detected, which is confirmed by the wide-range pattern from $2\theta = 10\text{--}80^\circ$ in **Fig. 4-15a**, indicating that neither a chemical reaction between the FeSe film and DEME-TFSI nor a lattice parameter change occurs. Next, the effect of applying $V_G = +5 \text{ V}$ for 30 min (**Fig. 4-14b**) was examined. In this case, it was also not observed to change the XRD patterns (no impurity phase was detected, as confirmed by the wide-range pattern from $2\theta = 10\text{--}80^\circ$ in **Fig. 4-15b**). These results indicate that the FeSe layer is stable against DEME-TFSI solution, and the ions in DEME-TFSI do not intercalate into the FeSe lattice (the interaction of

molecules with the FeSe lattice induces a distinct expansion of the c -axis length [32]). Thus, it is plausible that the origin of this superconductivity is field-accumulated carrier doping. Moreover I speculate that high T_c of the field-induced superconductivity is attributed to the electron correlation enhanced by introduction of the epitaxial strain, because in unconventional high- T_c superconductors such as cuprates, whose parent phases are Mott insulators, the T_c is strongly related their electron correlations; i.e., Coulomb interaction.

4.4. Conclusion

I grew high-quality ~ 10 -nm-thick FeSe epitaxial films on STO (001) substrates by MBE and confirmed its insulator-like electrical property. Using the high-quality thin film as a channel layer, an EDLT was fabricated to induce high- T_c superconductivity. Upon applying $V_G = +5.0$ V, an insulator–superconductor transition was induced with an onset $T_c = 24$ K. The highest T_c of 35 K was obtained by applying $V_G = +5.5$ V. This T_c value is significantly enhanced compared with the value of bulk FeSe ($T_c \approx 8$ K). Note that the origin of the superconductivity is not in the STO substrate because the T_c of STO is as low as 0.2 – 0.4 K even if an EDLT structure is employed [4, 33]. Hall effect and ARPES (shown in **Chapter 2**) measurements suggest that the high- T_c superconductivity comes from the highly accumulated electron carries in the FeSe channel surface and would be related to the electron correlation enhanced by the epitaxial strain. The relationship between T_c and accumulated carrier density indicates that T_c in FeSe channel increases monotonically to a breakdown voltage ($V_G > +5.5$ V). The present study provides a way to investigate superconducting transitions even with an insulating parent phase without alteration/deterioration by impurity doping and would support effectiveness of the strategy, where Fe-based parent phases with strong electron correlation is a key to achieve high T_c .

References

1. M. J. Wang, J. Y. Luo, T. W. Huang, H. H. Chang, T. K. Chen, F. C. Hsu, C. T. Wu, P. M. Wu, A. M. Chang, and M. K. Wu, *Phys. Rev. Lett.*, **103**, 117002 (2009).
2. Y. F. Nie, E. Brahim, J. I. Budnick, W. A. Hines, M. Jain, and B. O. Wells, *Appl. Phys. Lett.*, **94**, 242505 (2009).
3. H. Hiramatsu, K. Hanzawa, T. Kamiya, and H. Hosono, *Journal of Superconductivity and Novel Magnetism*, published online (2019). DOI: 10.1007/s10948-019-5020-9
4. K. Ueno, S. Nakamura, H. Shimotani, A. Ohtomo, N. Kimura, T. Nojima, H. Aoki, Y. Iwasa, and M. Kawasaki, *Nat. Mater.*, **7**, 855–858 (2008).
5. M. S. Kang, A. Sahu, D. J. Norris, and S. D. Frisbie, *Nano Lett.*, **10**, 3727 (2010).
6. Y. Zhang, J. Ye, Y. Matsushashi, and Y. Iwasa, *Nano Lett.*, **12**, 1136 (2012).
7. K. Taniguchi, A. Matsumoto, H. Shimotani, and H. Takagi, *Appl. Phys. Lett.*, **101**, 042603 (2012).
8. J. T. Ye, S. Inoue, K. Kobayashi, Y. Kasahara, H. T. Yuan, H. Shimotani, and Y. Iwasa, *Nat. Mater.*, **9**, 125 (2010).
9. H. Shimotani, H. Suzuki, K. Ueno, M. Kawasaki, and Y. Iwasa, *Appl. Phys. Lett.*, **92**, 242107 (2008).
10. S. Asanuma, P. H. Xiang, H. Yamada, H. Sato, I. H. Inoue, H. Akoh, A. Sawa, K. Ueno, H. Shimotani, H. Yuan, M. Kawasaki, and Y. Iwasa, *Appl. Phys. Lett.*, **97**, 142110 (2010).
11. A. S. Dhoot, S. C. Wimbush, T. Benseman, J. L. MacManus-Driscoll, J. R. Cooper, and R. H. Friend, *Adv. Mater.*, **22**, 2529 (2010).
12. A. T. Bollinger, G. Dubuis, J. Yoon, D. Pavuna, J. Misewich, and I. Bozovic, *Nature*, **458**, 472 (2011).
13. X. Leng, J. G. Garcia-Barriocanal, S. Bose, Y. Lee, and A. M. Goldman, *Phys. Rev. Lett.*, **107**, 027001 (2011).
14. T. Nojima, H. Tada, S. Nakamura, N. Kobayashi, H. Shimotani, and Y. Iwasa, *Phys. Rev.*

- B*, **84**, 020502 (2011).
15. T. Katase, H. Hiramatsu, T. Kamiya, and H. Hosono, *Proc Natl Acad Sci USA.*, **111**, 3979–3983 (2014).
 16. K. Ueno, H. Shimotani, H. Yuan, J. Ye, M. Kawasaki, and Y. Iwasa, *J. Phys. Soc. Jpn.*, **83**, 032001 (2014).
 17. M. Nakano, K. Shibuya, D. Okuyama, T. Hatano, S. Ono, M. Kawasaki, Y. Iwasa, and Y. Tokura, *Nature*, **487**, 459–462 (2012).
 18. J. Jeong, N. Aetukuri, T. Graf, T. D. Schladt, M. G. Samant, S. S. Parkin, *Science*, **339**, 1402–1405 (2013).
 19. For a review, T. Fujimoto and K. Awaga, *Phys. Chem. Chem. Phys.*, **15**, 8983–9006 (2013).
 20. M. Kawasaki, K. Takahashi, T. Maeda, R. Tsuchiya, M. Shinohara, O. Ishiyama, T. Yonezawa, M. Yoshimoto, and H. Koinuma, *Science*, **266**, 1540–1542 (1994).
 21. H. Hiramatsu, T. Kamiya, M. Hirano, and H. Hosono, *Physica C*, **469**, 657–666 (2009).
 22. H. Yuan, H. Shimotani, J. Ye, S. Yoon, H. Aliah, A. Tsukazaki, M. Kawasaki, and Y. Iwasa, *J. Am. Chem. Soc.*, **132**, 18402–18407 (2010).
 23. H. Yuan, H. Shimotani, A. Tsukazaki, A. Ohtomo, M. Kawasaki, and Y. Iwasa, *Adv. Funct. Mater.*, **19**, 1046–1053 (2009).
 24. Z. Li, J. Ju, J. Tang, K. Sato, M. Watahiki, and K. Tanigaki, *J. Phys. Chem. Solids*, **71**, 495–498 (2010).
 25. N. R. Werthamer, E. Helfand, and P. C. Hohenberg, *Phys. Rev.*, **147**, 295–302 (1966).
 26. S. I. Vedenev, B. A. Piot, D. K. Maude, and A. V. Sadakov, *Phys. Rev. B*, **87**, 134512 (2013).
 27. H. Lei, D. Graf, R. Hu, H. Ryu, E. S. Choi, S. W. Tozer, and C. Petrovic, *Phys. Rev. B*, **85**, 094515 (2012).
 28. M. D. Watson, T. Yamashita, S. Kasahara, W. Knafo, M. Nardone, J. Béard, F. Hardy, A. McCollam, A. Narayanan, S. F. Blake, T. Wolf, A. A. Haghighirad, C. Meingast, A. J. Schofield, H. v. Löhneysen, Y. Matsuda, A. I. Coldea, and T. Shibauchi, *Phys. Rev. Lett.*, **115**, 027006 (2015).
 29. F. C. Hsu, J. Y. Luo, K. W. Yeh, T. K. Chen, T. W. Huang, P. M. Wu, Y. C. Lee, Y. L. Huang, Y. Y. Chu, D. C. Yan, and M. K. Wu, *Proc. Natl. Acad. Sci. USA.*, **105**, 14262–

- 14264 (2008).
30. Y. Mizuguchi, F. Tomioka, S. Tsuda, T. Yamaguchi, and Y. Takano, *Appl. Phys. Lett.*, **93**, 152505 (2008).
31. S. Medvedev, T. M. McQueen, I. A. Troyan, T. Palasyuk, M. I. Eremets, R. J. Cava, S. Naghavi, F. Casper, V. Ksenofontov, G. Wortmann, and C. Felser, *Nat. Mater.*, **8**, 630–633 (2009).
32. M. Burrard-Lucas, D. G. Free, S. J. Sedlmaier, J. D. Wright, S. J. Cassidy, Y. Hara, A. J. Corkett, T. Lancaster, P. J. Baker, S. J. Blundell, and S. J. Clarke, *Nat. Mater.*, **12**, 15–19 (2013).
33. J. F. Schooley, W. R. Hosler, E. Ambler, J. H. Becker, M. L. Cohen, and C. S. Koonce, *Phys. Rev. Lett.*, **14**, 305–307 (1965).

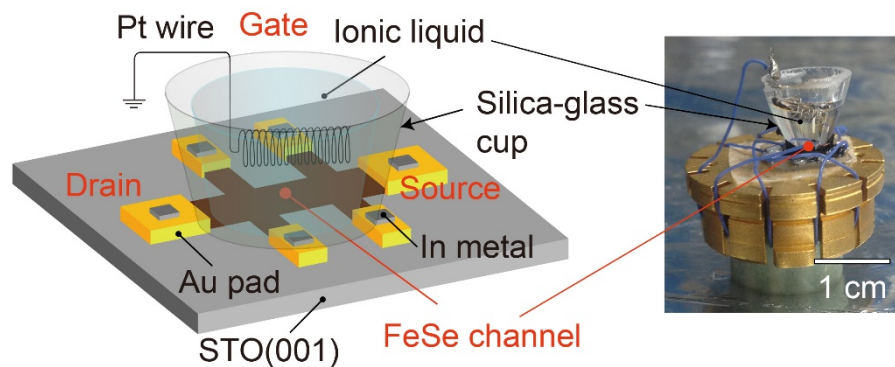


Figure 4-1. Device structure and photograph of the EDLT using the thin insulator-like FeSe layer as a channel.

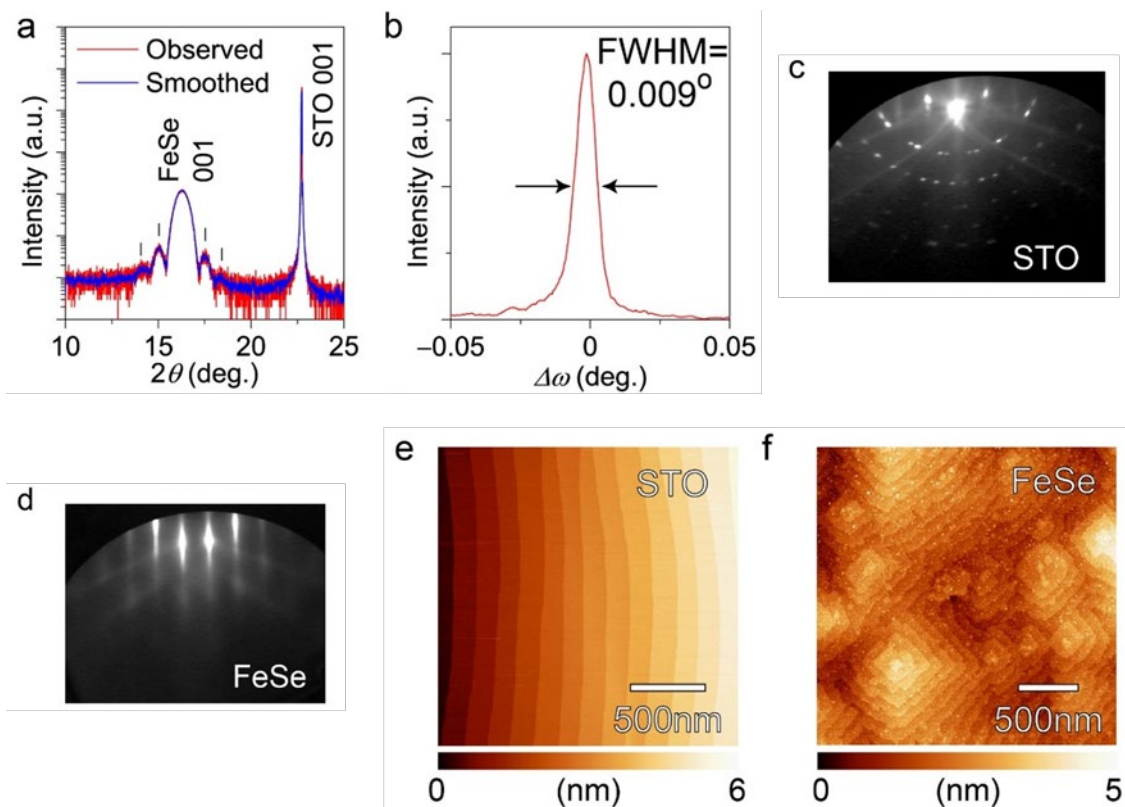


Figure 4-2. ~10-nm-thick FeSe films grown on STO (001) single-crystal substrates by MBE. (a) Out-of-plane XRD pattern. Vertical bars indicate Pendellösung interference fringes around FeSe 001 diffraction, originating from its flat surface. (b) Out-of-plane XRC of FeSe 001 diffraction. The full width at half maximum is 0.009° . RHEED patterns of the (c) STO substrate and (d) as-grown FeSe film surfaces. AFM images of the (e) STO substrate and (f) FeSe film surfaces. Horizontal bars indicate the height scales for each image.

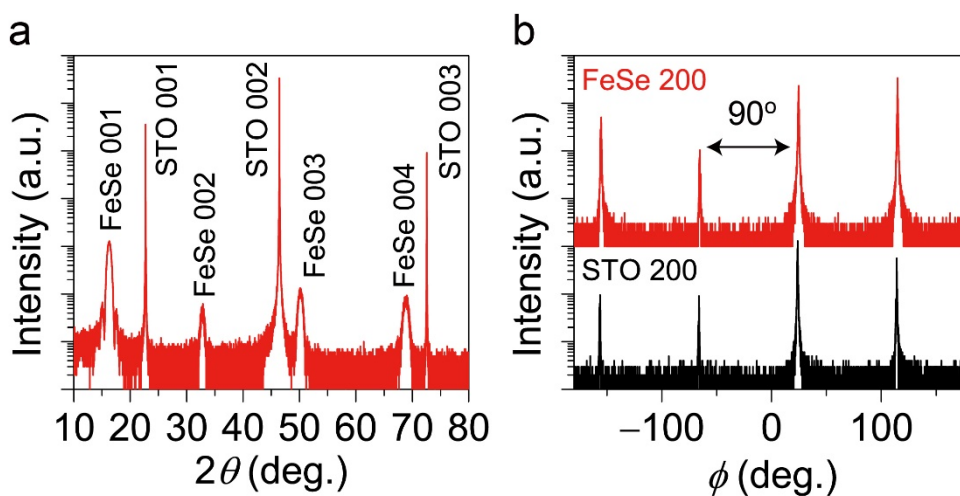


Figure 4-3. XRD patterns of the epitaxial FeSe film grown on the STO (001) substrate. (a) Out-of-plane XRD pattern. (b) In-plane ϕ scans of STO 200 (bottom) and FeSe 200 (top) diffractions. These results indicate that the FeSe film grows heteroepitaxially on STO with the epitaxial relationship of $[001]$ FeSe \parallel $[001]$ STO for out-of-plane and $[100]$ FeSe \parallel $[100]$ STO for in-plane.

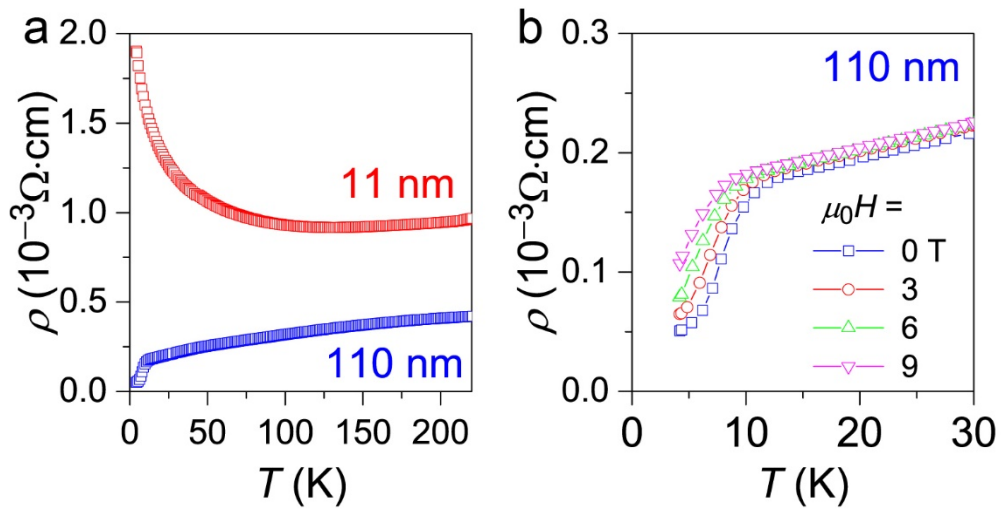


Figure 4-4. (a) ρ - T curves of the 11-nm-thick film compared with a 110-nm-thick film. (b) External magnetic field dependence of the ρ - T curves of the 110-nm-thick sample, confirming that the film is a superconductor.

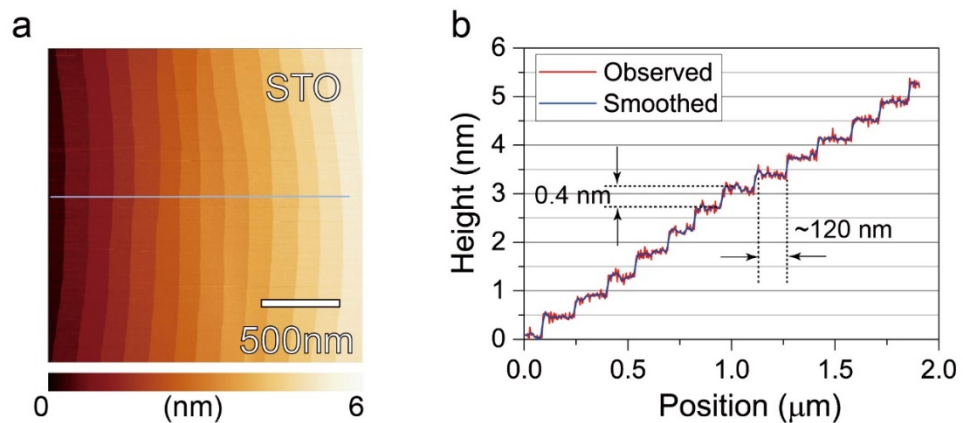


Figure 4-5. (a) AFM image of the STO (001) substrate. This data is the same as that in Fig.

1E. (b) Cross-section along the horizontal line in (a), indicating that the step height and terrace width are 0.4 and 120 nm, respectively. The step height is the same as the unit cell size of STO.

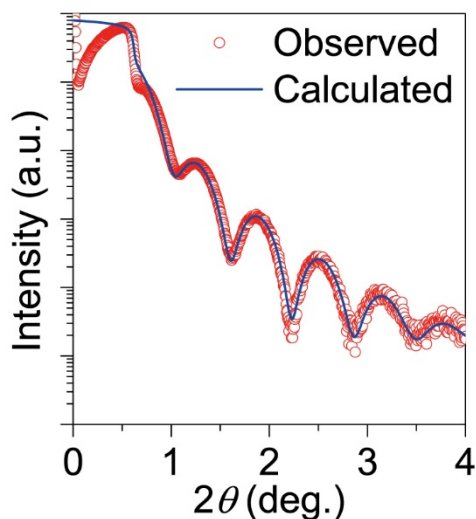


Figure 4-6. X-ray reflectivity spectrum of the ~10-nm-thick FeSe epitaxial film. The thickness of this film is determined to be 12.4 nm from the fitting result.

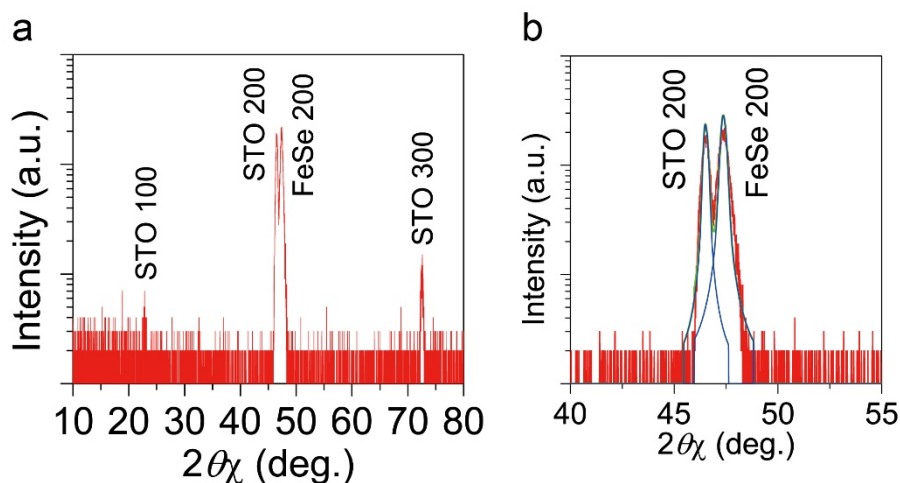


Figure 4-7. In-plane XRD patterns of the 11-nm-thick FeSe film. (a) ϕ -coupled $2\theta_\chi$ scan, and (b) enlarged pattern and deconvolution result to determine the in-plane lattice parameter.

The calculated a -axis length is 0.3838 nm. ϕ

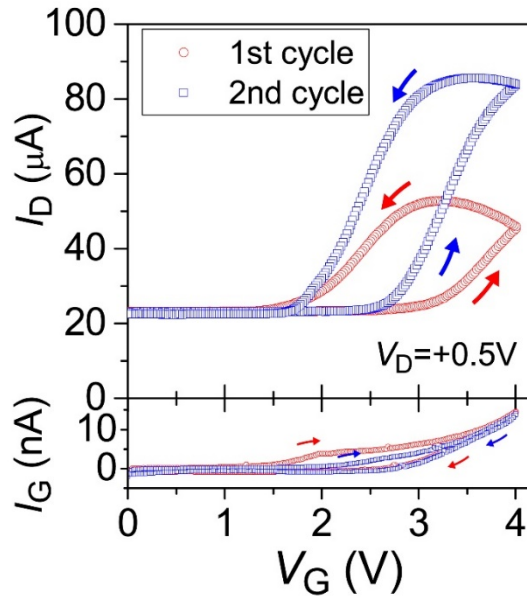


Figure 4-8. Transfer characteristics (drain current I_D versus gate bias V_G) of the FeSe EDLT under $V_D = +0.5$ V at $T = 220$ K cyclically measured for two loops. The arrows indicate the V_G -sweep directions starting from $V_G = 0$ V. The leakage current (I_G) versus V_G is also shown at the bottom of the figure.

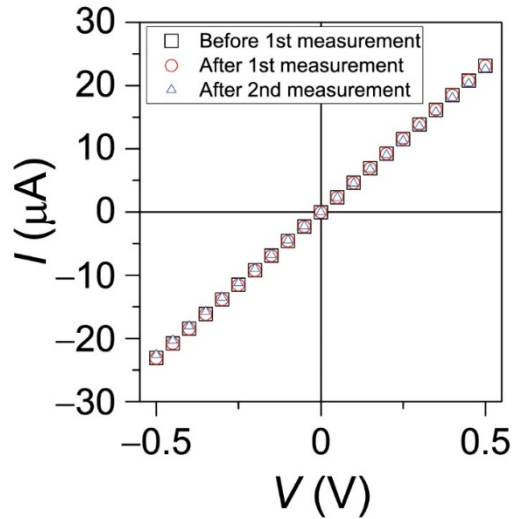


Figure 4-9. I - V characteristics of the FeSe EDLT at $V_G = 0$ measured at 220 K. Before (squares) and after (circles) the 1st cyclic measurement of the I_D - V_G curve in Fig. 8. The latter characteristic was unchanged before the 2nd cyclic measurement. After the 2nd cyclic

measurement of the I_D-V_G curve in Fig. 4-8 (triangles). These results confirm that there is no change in the channel layer.

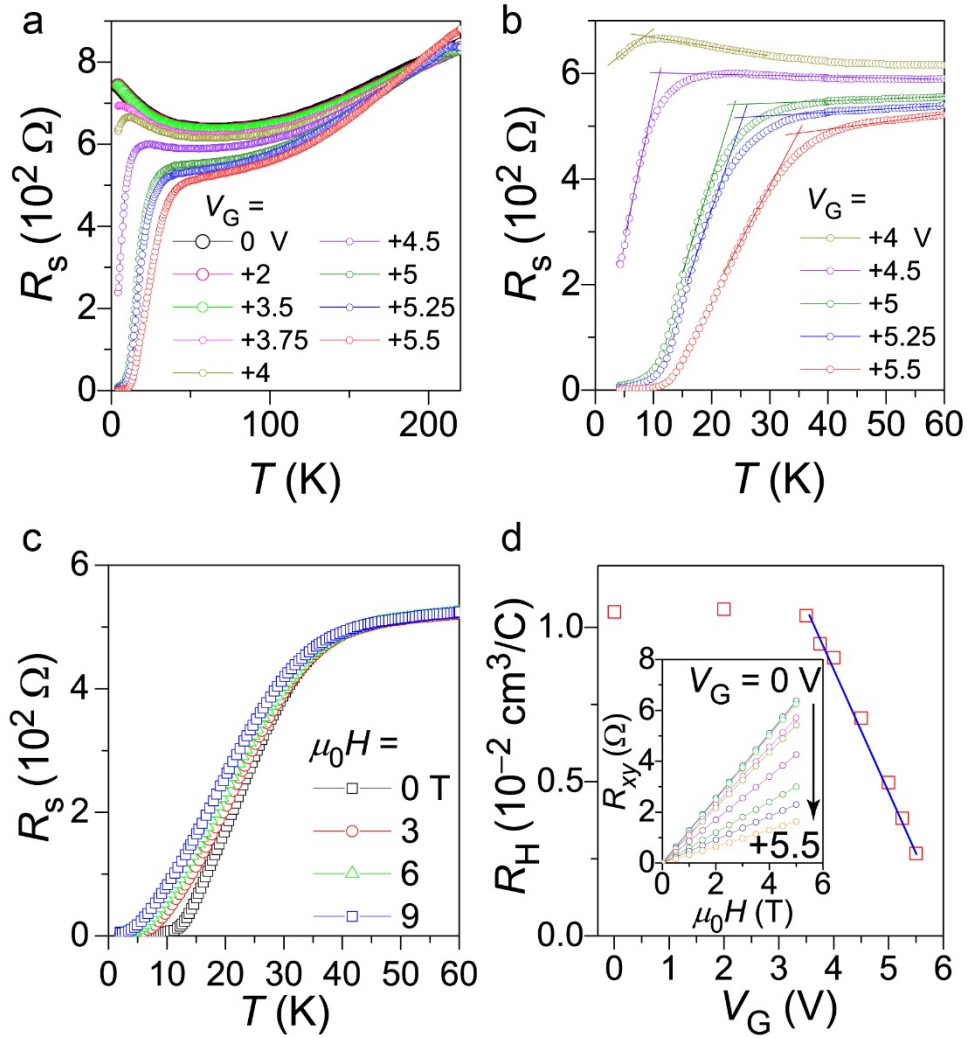


Figure 4-10. Carrier transport properties of the FeSe EDLT under applied biases $V_G = 0 - +5.5$ V. (a) R_s-T curves. (b) Enlarged image of (a) in the T range 0 – 60 K at $V_G = +4 - +5.5$ V. Solid lines are used to determine the onset T_c . (c) External magnetic field dependence of R_s-T curves at $V_G = +5.5$ V. (d) Hall coefficients (R_H) at 40 K as a function of V_G . The inset shows transverse Hall resistance (R_{xy}) at 40 K under external magnetic fields up to 5 T in order to obtain R_H .

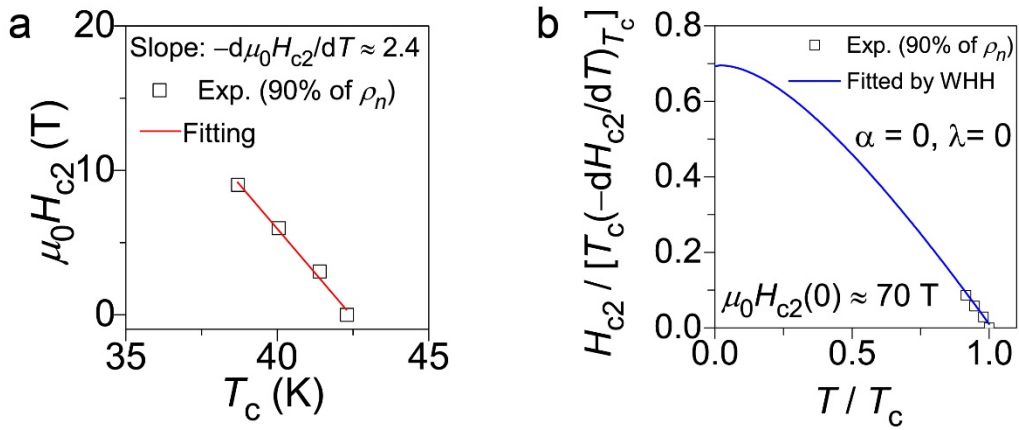


Figure 4-11. Upper critical field ($\mu_0 H_{c2}$) as a function of temperature of FeSe EDLT under applying $V_G = +4.0$ V (See **Fig. 4-10**). (a) Least square fitting result. (b) The estimated $\mu_0 H_{c2}$ at 0 K using Werthamer–Helfand–Hohenberg (WHH) theory (Ref. 25 in the main text) is 70 T. α and λ denote Pauli spin paramagnetism and spin-orbit interaction parameters, respectively. Here, we select $\alpha = 0$ and $\lambda = 0$.

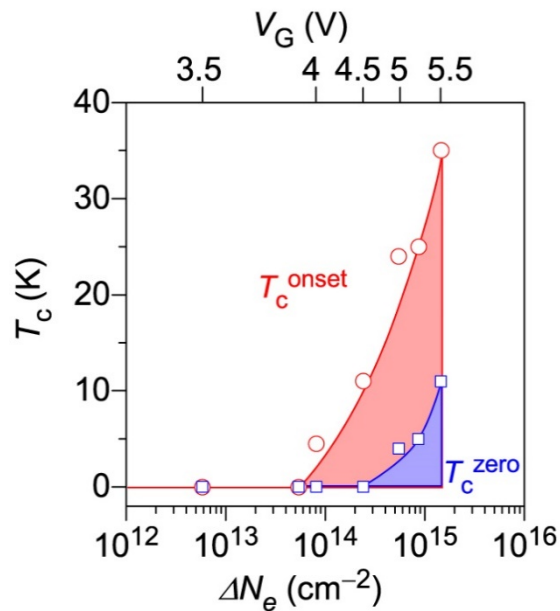


Figure 4-12. Electronic phase diagram of the FeSe EDLT. ΔN_e indicates the accumulated electron sheet carrier density (estimated) under V_G . The corresponding V_G are shown in the upper horizontal axis.

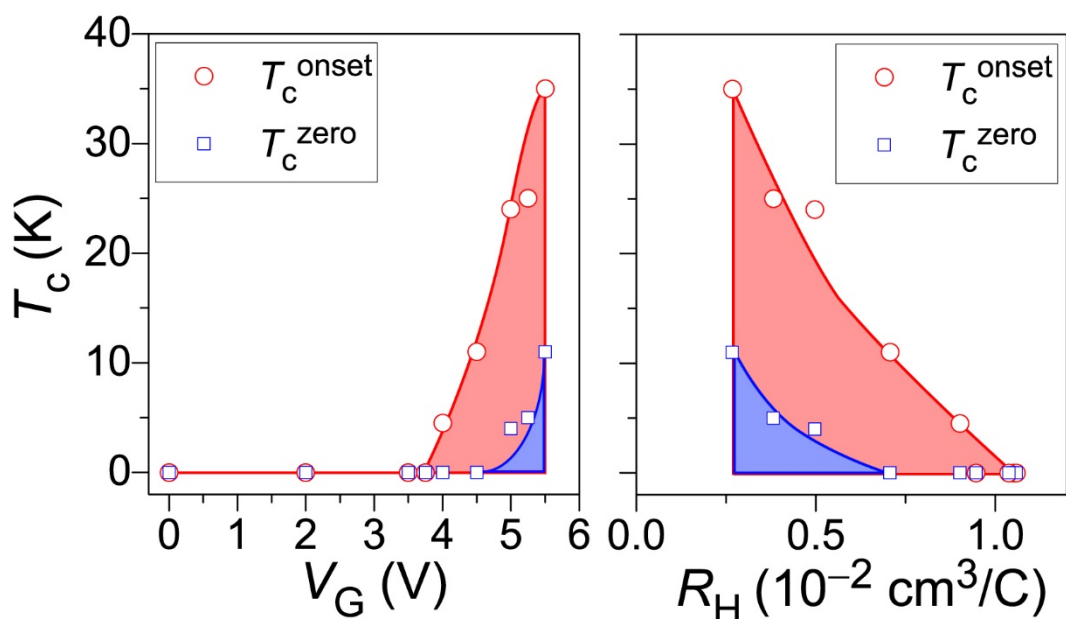


Figure 4-13. Electronic phase diagrams of the FeSe EDLT. (Left) T_c vs. V_G and (Right) T_c vs. R_H at 40 K. Circles and squares show onset T_c (T_c^{onset}) and zero resistivity temperature (T_c^{zero}), respectively.

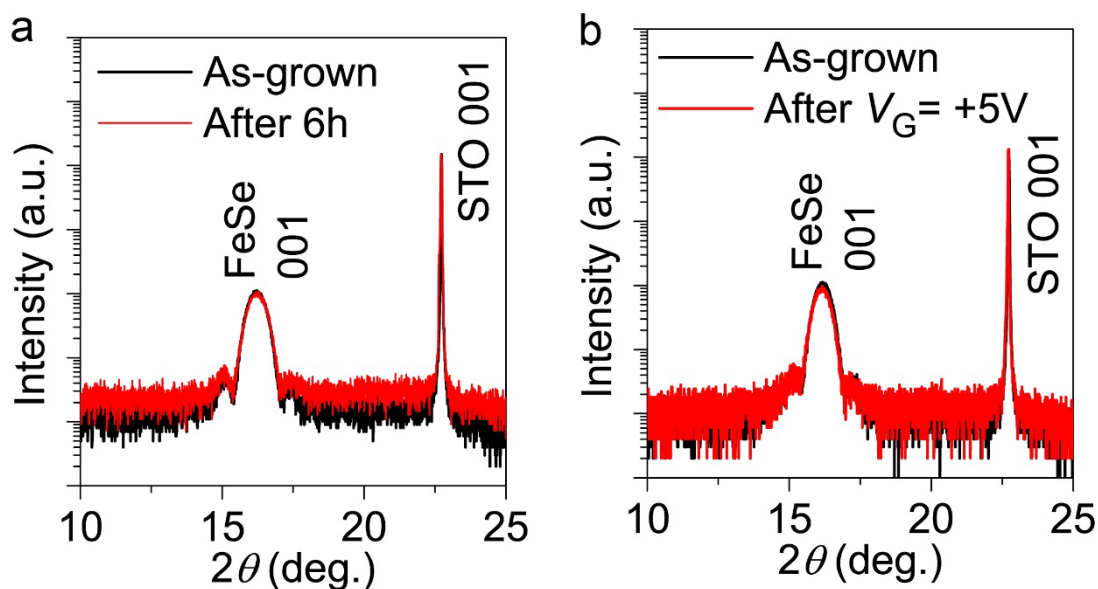


Figure 4-14. XRD patterns of FeSe films dipped in DEME-TFSI. The intensity is normalized by that of STO 001 diffraction of the as-grown sample. (a) Dipped in DEME-

TFSI for 6 h under a vacuum without applying a bias voltage. (b) Dipped in DEME-TFSI for 2 hours under a vacuum with $V_G = +5$ V.

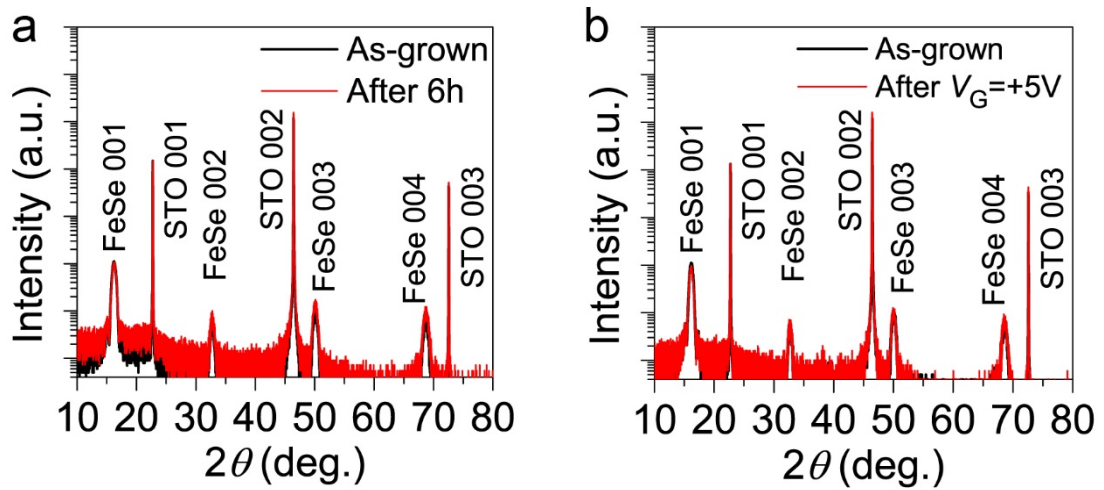


Figure 4-15. XRD patterns of FeSe films dipped in DEME-TFSI. The intensity is normalized by that of STO 001 diffraction of the as-grown sample. (a) Dipped for 6 h under vacuum without an applied bias. (b) Dipped under vacuum with $V_G = +5$ V.

Chapter 5. Carrier Density Dependence of T_c in FeSe-EDLT under Electric Field

5.1. FeSe-Related EDLTs

In **Chapter 4**, an EDLT was fabricated using a very thin (≈ 10 nm thick) insulator-like FeSe channel on SrTiO₃ (STO) with expectation; an important key strategy to obtaining high T_c is to dope carriers into an Fe-based parent phase with strong electron correlation. As a result of application of electric field, a superconductor transition was induced directly from the insulator-like phase with the maximum $T_c = 35$ K [1].

Some EDLT researches using FeSe-related compounds as channel layers were reported; for instance, doping in vacancy sites [2] and electrochemical etching [3] of FeSe-related EDLTs. Those mechanisms include complicated chemical reactions, so that it is difficult to make a definitive conclusion. Although a similar EDLT research was also reported on a superconducting FeSe single crystal [4], the detailed mechanism of the high T_c in FeSe-EDLTs still remains unclear. Thus determination of the key factors to inducing the high- T_c superconductivity is of importance to seek new superconductors and induce higher- T_c superconductivity in Fe-based compounds.

In this **Chapter**, I examine conditions to induce the high- T_c superconductivity through fabrication of EDLTs using insulator-like FeSe channels exhibiting different carrier transport properties.

5.2. Experimental Procedure

5.2.1. Preparation of three different FeSe epitaxial thin films

FeSe epitaxial films with ≈ 10 nm in thickness were grown at 500 °C on (001)-oriented STO single-crystal substrates by molecular beam epitaxy. Prior to the film growth, the STO

surface was chemically etched in a buffered-HF solution and annealed thermally in air at 1050 °C for 1 hour to obtain an atomically flat surface [5]. Compared with the study in **Chapter 4**, only the film-growth rate was changed by tuning Fe-flux rates at 2, 4, and 6×10^{-6} Pa for samples #1, #2, and #3, respectively with a constant Se flux ($\approx 2 \times 10^{-5}$ Pa; i.e., the Fe flux increased in the order of #1, #2, and #3). The corresponding growth rates were 1.1, 1.3, and 1.4 Å/min. Film thicknesses and growth rates were estimated by X-ray reflectivity analysis. Other conditions are found in previous **Chapter 4**.

5.2.2. Analyses of structure parameters and chemical compositions

The structure parameters of the films were determined by out-of-plane and in-plane X-ray diffraction (XRD). Full widths at half maximum (FWHMs) of rocking curves of out-of-plane 001 ($\Delta\omega$) and in-plane 200 ($\Delta\phi$) were employed as the measure of crystallinity of the films. Surface morphology was observed by atomic force microscopy (AFM). The chemical compositions were determined by X-ray fluorescence (XRF) spectroscopy, in which the XRF intensities were calibrated by the quantitative results taken from an electron-probe microanalyzer.

5.2.3. Evaluation of electronic transport properties of three different FeSe-EDLTs

EDLTs using the insulator-like FeSe channels with a Hall bar structure were fabricated through an *in-situ* process to avoid surface degradation in air (i.e., the EDLTs were processed only in Ar or vacuum atmosphere without exposure to air). Shadow masks with the Hall bar structure were used for depositing the FeSe channel layers and Au electrodes. N,N-diethyl-N-methyl-N-(2-methoxyethyl)-ammonium bis-(trifluoromethylsulfonyl) imide (DEME-TFSI) was employed as an ionic-liquid gate insulator. The detailed device fabrication process and the structure are described in **Chapter 4**.

Temperature dependence of carrier transport properties such as resistivity (ρ) of the films

and sheet resistance (R_s) of EDLT channels were measured at 4.2–220 K. Positive gate voltages (V_G) up to +5.5 V were applied and changed at 220 K because electrochemical etching/reaction is provoked at higher temperatures [3, 6] while it should be higher than the rubber–glass phase transition of DEME-TFSI (≈ 190 K) [7]. The applied V_G was kept during each temperature-sweep measurement. For Hall effect measurements, external magnetic fields (H) up to $\mu_0 H = 5$ T were applied at 40 K.

5.3. Results and Discussion

5.3.1. Three kinds of FeSe epitaxial thin films

The evaluated structure parameters and chemical compositions for samples #1–3 are summarized in **Table 5-I**. The chemical composition (i.e., the [Fe]/[Se] atomic ratio) of sample #1 is stoichiometric ([Fe]/[Se] ≈ 1.0), but those of #2 and #3 are of 10 % Fe rich ([Fe]/[Se] ≈ 1.1), which is consistent with the lower Fe-flux rate of #1 than those of #2 and #3.

Figure 5-1a shows the out-of-plane XRD patterns around FeSe 003 diffraction peaks. The c -axis lattice parameters of samples #2 (5.448 Å, the strain with respect to that of bulk = -1.4 %) and #3 (5.479 Å, -0.8 %) shrunk compared with that of ≈ 10 % Fe-rich bulk FeSe_{0.92} (5.52368(8) Å [8]), but only sample #1 (5.513 Å, -0.2 %) had almost the same lattice parameter as that of a stoichiometric bulk FeSe (5.52382(7) Å [8]), indicating that structure of #1 was fully relaxed along the c -axis. In contrast, the a -axis lattice parameters of all the samples expanded due mainly to in-plane lattice mismatch between FeSe and STO ($(a_{\text{STO}} - a_{\text{bulk}}) / a_{\text{STO}} \approx +3.37\%$, $a_{\text{bulk}} = 3.77335(4)$ Å for Fe-rich FeSe_{0.92}, $a_{\text{bulk}} = 3.77353(4)$ Å for stoichiometric FeSe [8]) (**Fig. 5-1b**). Although the a - and c -axis lattice parameters of the bulks decreased with increase in excess Fe [8], those lattice parameter changes are too large to understand solely by the 10 % excess Fe; i.e., other origins for the lattice distortions should be considered. The c/a ratio of #1 is closer to that of a bulk

(1.464 for FeSe_{0.92} and stoichiometric FeSe [8]) than those of #2 and #3. Comparing the Poisson's ratios defined as $(\Delta c/c) / (\Delta a/a)$, that of #1 is 18 %, which is much smaller than those of #2 (80 %) and #3 (73 %). This difference suggests that #1 has a more peculiar electronic structure and consequent structural properties than those of the other samples, which would be plausible because a bulk FeSe has a complex multiband electronic structure [9, 10] (i.e., the electronic structure easily changes with trace changes in composition and/or external pressures [11 – 13]). Based on the FWHMs in **Figs. 5-1a** and **5-1b**, crystallite sizes were estimated from the Sherrer's equation (crystallite size $D = K \cdot \lambda / (\Delta\theta \cdot \cos\theta)$, where K , λ , and $\Delta\theta$ denote Sherrer constant ($K = 0.94$), the wavelength of X-ray (Cu $K\alpha_1$, 1.54056 Å), and FWHM of FeSe 001 or 200 diffraction, respectively) and summarize them in **Table 5-I**, which will be discussed later on.

Figures 5-1c and **d** show rocking curves for out-of-plane 001 and in-plane 200 diffractions of FeSe, respectively. The $\Delta\omega$ of #1 is 0.013°, which is broader than those of #2 and #3 (0.009°), although all of them are much narrower than that ($\approx 0.2^\circ$) reported in [14, 15]. This broad $\Delta\omega$ of #1 would originate from its strained lattice parameters; i.e., its relaxed structure along the c -axis and expanded structure along the a -axis. For in-plane, $\Delta\phi$ of #2 (0.5°) is the narrowest among these three samples and those of #1 (0.8 °) and #3 (0.9°) are almost the same with each other. Thus, I can conclude that #2 has the best quality in terms of crystallinity.

The root-mean-square roughness (R_{rms}), estimated from the AFM images in **Figs. 5-2a – 5-2c**, indicates that all the films had atomically flat surfaces (i.e., $R_{\text{rms}} \leq 1$ nm). While, many pits with lateral sizes 10 – 40 nm were observed only in the sample #3. It is considered that lateral growth was relatively suppressed for #3 because of the higher growth rate, and consequently three dimensional growth was dominant. According to the surface roughness, #2 has the best quality. Here it should be noted that both the thickness and the average

grain size of the films for out-of-plane are approximately 10 nm with the small surface roughness of ~ 1 nm. These results suggest that they are not single domain in plane although the films are grown epitaxially on STO.

These differences in structures led to different electrical properties (ρ - T in **Fig. 5-3**). As reported in [16, 17], all the films exhibited insulator-like behaviors; i.e., ρ increases with decrease in temperature especially in low temperature regions. The absolute values of ρ decreased with increase in growth rate. The [Fe]/[Se] ratio of #1 was 10 % lower than those of the others, but the ρ distribution of the present samples in **Fig. 5-3** was much larger than those reported by excess Fe (e.g., the ρ change by 10 % excess Fe is no more than the order of $1 \times 10^{-4} \Omega \cdot \text{cm}$ at 300 K [18]). Thus, the difference in the carrier concentration due to the different Fe/Se ratios cannot explain this different ρ behavior satisfactorily. Considering that different ρ behaviors were observed also in #2 and #3 with the same [Fe]/[Se] ratios, these difference in ρ behaviors do not come from compositional differences, but should be ascribed mainly to the complicated differences in structural parameters.

5.3.2. Electronic transport properties of three FeSe-EDLTs

Then, carrier transport properties were examined for the EDLTs using #1, #2 and #3 as channels. The properties of device #2 are shown in **Chapter 4**, in which an insulator–superconductor transition was observed at $V_G = +4.0$ – $+5.5$ V with the maximum onset $T_c = 35$ K. I concluded from the results of Hall effect measurements that the origin of this high T_c is due to high-density electron doping. **Figure 5-4a** shows the temperature dependences of sheet resistance (R_s - T) under various V_G for device #1, which had the most relaxed c -axis lattice and the largest normal state ρ . Up to $V_G = +3$ V, the R_s - T behavior did not change at all and kept the insulator-like state. On the other hand, a superconductivity appeared at $V_G = +4$ V with onset T_c of 12 K (see **Fig. 5-4b**). The onset T_c increased up to 20 K with increase in V_G . **Figure 5-4c** shows R_s - T curves for device #3. Also in this case, an

insulator–superconductor transition was observed at $V_G = +3.75$ V with onset T_c of 8 K (see **Fig. 5-4d**). Then the maximum onset T_c reached 22 K. Note that a saturation of T_c was observed in #3 at $V_G \geq +4$ V. Although clear zero resistance was detected at $V_G \geq +5$ V in #2 [1], neither #1 nor #3 exhibited zero resistance even at $V_G = +5.5$ V (see **Figs. 5-4b** and **5-4d**) probably because their superconducting transition widths were broad similar to a previous result in **Chapter 4**, and these onset T_c were lower than that of #2. From these results, the relationship between onset T_c and applied V_G is built in **Fig. 5-5**. The insulator–superconductor transition was induced in all of the three samples at $V_G \approx +4$ V, but only #2, which had the highest crystallinity, exhibited the highest T_c .

5.3.3. Discussion: origin of difference of T_c among three FeSe-EDLTs

To discuss the origin of this different R_s - T behaviors, Hall effect measurements were performed for each EDLT under V_G . **Figure 5-6** shows external magnetic-field (H) dependence of Hall resistance (R_{xy}) for devices (a) #1 and (b) #3 at $V_G = 0$ – $+5.5$ V. That of #2 is given in **Chapter 4**. For device #1, the slope of R_{xy} changed from positive to negative; i.e., the majority carrier type changed from holes to electrons. Additionally, the negative slopes increased with increase in V_G from +4 to +5.5 V, suggesting that electron density decreased. A similar behavior is also found in ref. 4. As it is difficult to estimate a volume carrier density because the accumulation layer thickness is unknown, two-dimensional sheet carrier densities (n_{2D}) without and with V_G were estimated and their difference (Δn_{2D}) was employed for the following discussion [1]. Δn_{2D} of #1 were 4.8 and $4.2 \times 10^{15} \text{ cm}^{-2}$ for $V_G = +4$ and +5.5 V, respectively. These values are ca. 3–4 times higher than that of #2 (the maximum $\Delta n_{2D} = 1.4 \times 10^{15} \text{ cm}^{-2}$ [1]), implying that over-electron doping than #2 occurs in #1. I speculate that such over doping would be related to its peculiar stress structure for #1, in which the cell volume is the largest with tensile strain along the a -axis and the relaxed c -axis. Only the Poisson's ratio of #1 was very small. Considering the complicated multiband

structure, the electronic structure and the chemical bonding at the Fermi level (E_F) in the doped states should be very different. Although there would be no state at E_F at $V_G = 0$ due to its insulator-like state, the density of states at E_F under electron doping by positive V_G should increase and lead to the insulator–superconductor transition.

For device #3 (**Fig. 5-6b**), the slope of R_{xy} decreased with increase in V_G up to +4 V. This result indicates that electron carrier density increased, which was similar to the result of device #2 [1]. But with further increase in V_G from +4 to +5.5 V, the slope did not change, suggesting that carrier density in #3 kept constant in this V_G range. The maximum Δn_{2D} of #3 was $1.6 \times 10^{14} \text{ cm}^{-2}$, which is one order of magnitude lower than that of #2. This difference indicates that the induced carrier density was too small to exhibit the high T_c in #3 (i.e., the doping concentration of #3 should be in an under-doped region). The crystallite sizes along the a -axis (D_a) and c -axis (D_c) of #3 were smaller than those of #2 (see **Table 5-I**). There is a possibility that such smaller size crystallites generate more one-dimensional defects, and the accumulated carriers are trapped in these defects. Although this story seems to be consistent with the lower in-plane crystallinity ($\Delta\phi$ of #3 = 0.9°), the present results suggest that such defects should not work in this system because it was found that over doping occurred in #1 with similar small size crystallites (D_a of #1 $\approx 159 \text{ \AA}$, $D_c \approx 85 \text{ \AA}$) and in-plane crystallinity ($\Delta\phi$ of #1 = 0.8°). Therefore the possible origin would be an influence of pits at the channel surface. Since only the surface of #3 had many pits (see **Fig. 5-2c**), these pits trap the induced carriers [19 – 21], leading to its under-doped state and low T_c . These results suggest that the optimum doping in the channel is the most important to induce the high- T_c superconductivity in the insulator-like FeSe thin films, and the doping levels depend not only on chemical composition but also on the structures of the channels such as strain, crystallinity, and/or surface defects (pits).

5.4. Conclusion

Three kinds of EDLTs were fabricated with ≈ 10 nm-thick FeSe channel layers grown at different growth rates. XRD analysis revealed that #2 grown at the intermediate (optimum) growth rate had the highest crystallinity. The unit cell volume of #1 grown at the lowest growth rate was the largest due to its in-plane tensile strain and the relaxed c -axis lattice, leading to the smallest Poisson's ratio. Combined with the multiband nature of FeSe, these results suggest that the electronic structure of #1 seems to be totally different from the others. #3 grown at the highest growth rate had many pits at the surface. An insulator–superconductor transition was observed at V_G above the common value $\approx +4$ V in all the EDLTs. However, only device #2 exhibited the maximum T_c of 35 K and zero resistance. The estimation of the induced carrier density revealed that #1 was over electron doped compared to #2 and #3. Its lower T_c would originate from such over doping due probably to its unique structural stress, which generates a unique electronic structure. The induced carrier density of #3 was the lowest probably because of the many pits and/or the small crystallite sizes and consequent electron trapping.

To discuss more detailed mechanism, further examination is required, but this study clarified that rather high-density electron doping is inevitable to induce the high- T_c superconductivity while the optimum-concentration doping is achieved only in FeSe thin films with high crystallinity and atomically flat surfaces. This knowledge will contribute to establishing higher T_c field-induced superconductivity.

References

- 1 K. Hanzawa, H. Sato, H. Hiramatsu, T. Kamiya, and H. Hosono, *Proc. Natl. Acad. Sci. USA.*, **113**, 3986–3990 (2016).

- 2 B. Lei, Z. J. Xiang, X. F. Lu, N. Z. Wang, J. R. Chang, C. Shang, A. M. Zhang, Q. M. Zhang, X. G. Luo, T. Wu, Z. Sun, and X. H. Chen, *Phys. Rev. B*, **93**, 060501(R) (2016).
- 3 J. Shiogai, Y. Ito, T. Mitsuhashi, T. Nojima, and A. Tsukazaki, *Nat. Phys.*, **12**, 42–46 (2016).
- 4 B. Lei, J. H. Cui, Z. J. Xiang, C. Shang, N. Z. Wang, G. J. Ye, X. G. Luo, T. Wu, Z. Sun, and X. H. Chen, *Phys. Rev. Lett.*, **116**, 077002 (2016).
- 5 M. Kawasaki, K. Takahashi, T. Maeda, R. Tsuchiya, M. Shinohara, O. Ishiyama, T. Yonezawa, M. Yoshimoto, and H. Koinuma, *Science*, **266**, 1540–1542, (1994).
- 6 H. Yuan, H. Shimotani, J. Ye, S. Yoon, H. Aliah, A. Tsukazaki, M. Kawasaki, and Y. Iwasa, *J. Amer. Chem. Soc.*, **132**, 18402–18407 (2010).
- 7 H. Yuan, H. Shimotani, A. Tsukazaki, A. Ohtomo, M. Kawasaki, and Y. Iwasa, *Adv. Funct. Mater.*, **19**, 1046–1053 (2009).
- 8 E. Pomjakushina, K. Conder, V. Pomjakushin, M. Bendele, and R. Khasanov, *Phys. Rev. B*, **80**, 024517 (2009).
- 9 H. Lei, D. Graf, R. Hu, H. Ryu, E. S. Choi, S. W. Tozer, and C. Petrovic, *Phys. Rev. B*, **85**, 094515 (2012).
- 10 M. D. Watson, T. Yamashita, S. Kasahara, W. Knafo, M. Nardone, J. Béard, F. Hardy, A. McCollam, A. Narayanan, S. F. Blake, T. Wolf, A. A. Haghighirad, C. Meingast, A. J. Schofield, H. v. Löhneysen, Y. Matsuda, A. I. Coldea, and T. Shibauchi, *Phys. Rev. Lett.*, **115**, 027006 (2015).
- 11 Y. Mizuguchi, F. Tomioka, S. Tsuda, T. Yamaguchi, and Y. Takano, *Appl. Phys. Lett.*, **93**, 152505 (2008).
- 12 S. Medvedev, T. M. McQueen, I. A. Troyan, T. Palasyuk, M. I. Eremets, R. J. Cava, S. Naghavi, F. Casper, V. Ksenofontov, G. Wortmann, and C. Felser, *Nat. Mater.*, **8**, 630–633 (2009).

- 13 T. M. McQueen, Q. Huang, V. Ksenofontov, C. Felser, Q. Xu, H. Zandbergen, Y. S. Hor, J. Allred, A. J. Williams, D. Qu, J. Checkelsky, N. P. Ong, and R. J. Cava, *Phys. Rev. B*, **79**, 014522 (2009).
- 14 R. Schneider, A. G. Zaitsev, D. Fuchs, and R. Fromknecht, *Supercond. Sci. Technol.*, **26**, 055014 (2013).
- 15 Y. Han, W. Y. Li, L. X. Cao, S. Zhang, B. Xu, and B. R. Zhao, *J. Phys.: Condens. Matter.*, **21**, 235702 (2009).
- 16 Y. F. Nie, E. Brahim, J. I. Budnick, W. A. Hines, M. Jain, and B. O. Wells, *Appl. Phys. Lett.*, **94**, 242505 (2009).
- 17 M. J. Wang, J. Y. Luo, T. W. Huang, H. H. Chang, T. K. Chen, F. C. Hsu, C. T. Wu, P. M. Wu, A. M. Chang, and M. K. Wu, *Phys. Rev. Lett.*, **103**, 117002 (2009).
- 18 Z. Li, J. Ju, J. Tang, K. Sato, M. Watahiki, and K. Tanigaki, *J. Phys. Chem. Solids*, **71**, 495–498 (2010).
- 19 P. A. Ivanov, M. G. Mynbaeva, and S. E. Sadow, *Semicond. Sci. Technol.*, **19**, 319–322 (2004).
- 20 D. C. Look, Z. Q. Fang, S. Soloviev, T. S. Sudarshan, and J. J. Boeckl, *Phys. Rev. B*, **69**, 195205 (2004).
- 21 D. C. Look, Z. Q. Fang, A. Krtschil, and A. Krost, *phys. stat. sol. (c)*, **2**, 1039–1046 (2005).

Table 5-I. Summary of the growth rates, structure parameters, and chemical compositions.

| Sample | Thickness (nm) | Growth rate (Å/min) | Fe/Se atomic ratio | c -axis | a -axis | c/a |
|--------|------------------------|---------------------------|--------------------------|--------------------------|------------------------|-------------------|
| | | | | (Å) | (Å) | |
| #1 | 9.7 | 1.1 | 1.0 | 5.513 | 3.814 | 1.445 |
| #2 | 10 | 1.3 | 1.1 | 5.448 | 3.838 | 1.419 |
| #3 | 8.3 | 1.4 | 1.1 | 5.479 | 3.815 | 1.436 |
| | Poisson's ratio (%) | D_c (Å) | D_a (Å) | $\Delta\omega$ (deg.) | $\Delta\phi$ (deg.) | R_{rms} (nm) |
| #1 | 18 | 85±5 | 159 | 0.013 | 0.8 | 1.0 |
| #2 | 80 | 112±7 | 173 | 0.009 | 0.5 | 0.7 |
| #3 | 73 | 80±7 | 154 | 0.009 | 0.9 | 1.0 |

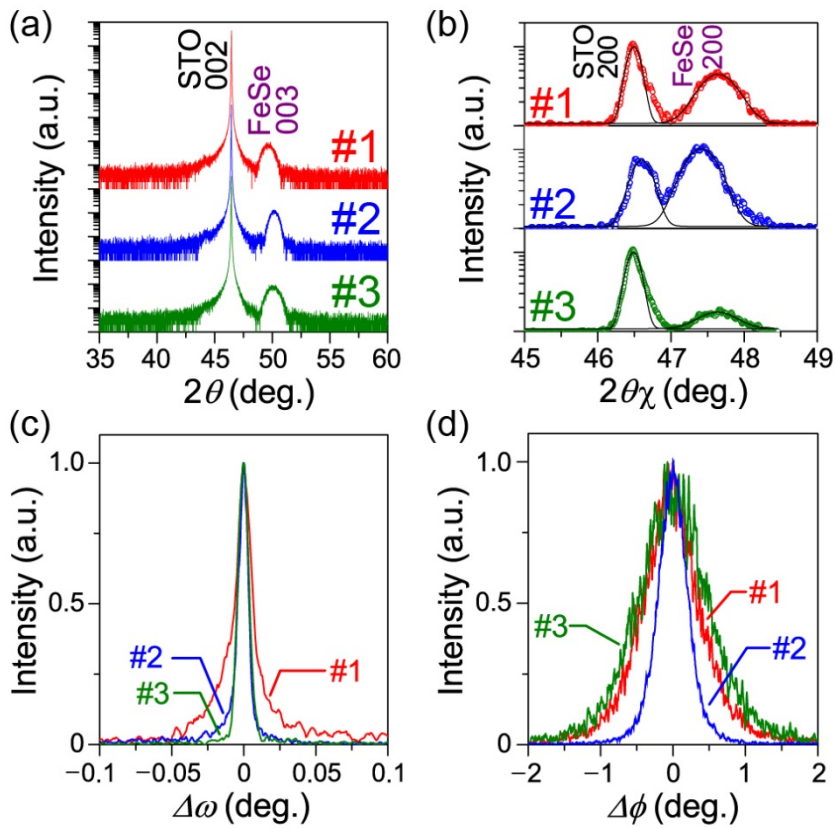


Figure 5-1. Structural and transport properties of ≈ 10 -nm-thick FeSe films grown at three different growth rates. The growth rates of samples #1, #2 and #3 are 1.0, 1.3, and 1.4 $\text{\AA}/\text{min}$, respectively. (a) Out-of-plane and (b) in-plane XRD patterns. Solid curves in (b) indicate peak deconvolution results to calculate a -axis lengths of the films. (c, d) Normalized rocking curves for the out-of-plane FeSe 001 (c) and in-plane 200 (d) diffractions.

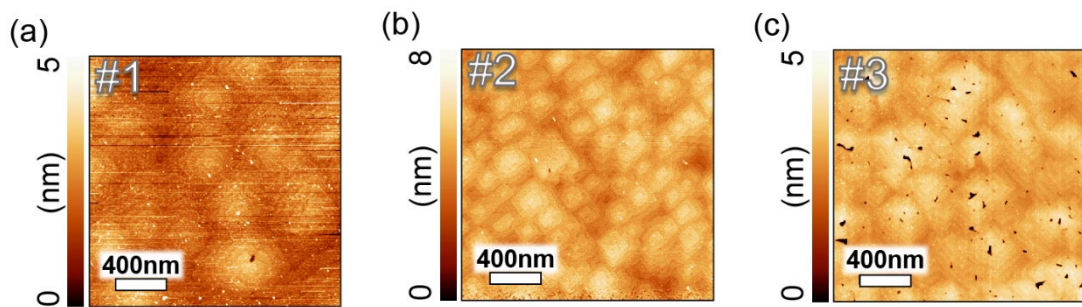


Figure 5-2. Surface morphology of the FeSe films for (a) #1, (b) #2, and (c) #3, respectively. The vertical bars are the height color scales for each image.

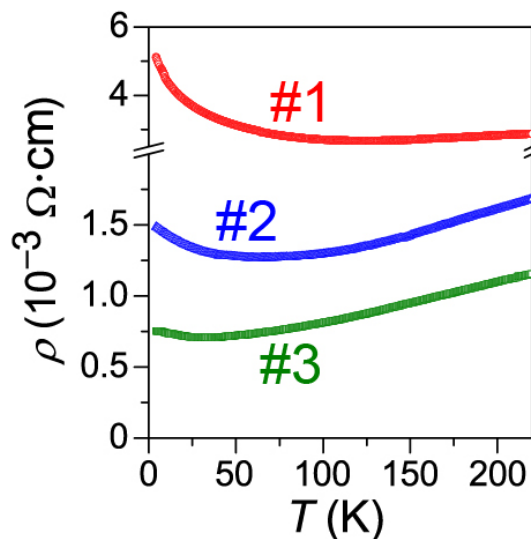


Figure 5-3. Temperature dependences of resistivity of each FeSe film.

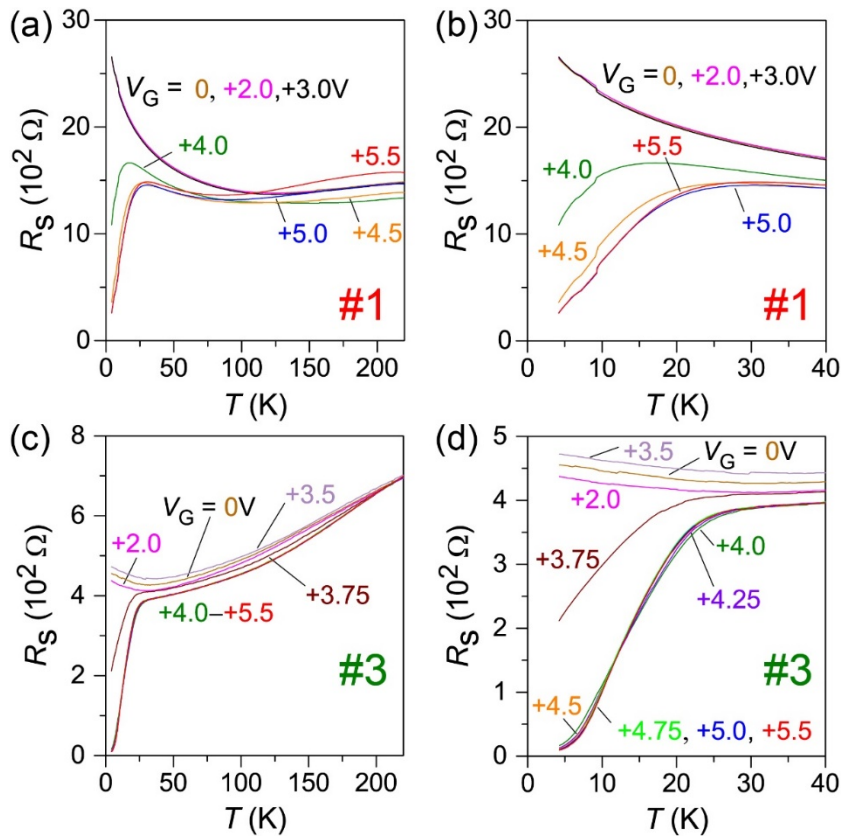


Figure 5-4. Temperature dependences of sheet resistance (R_s) for EDLTs under V_G up to +5.5 V. (a) and (c) correspond to EDLTs fabricated using samples #1 and #3, respectively. (b) and (d) are enlarged images around superconducting transition for (a) and (c), respectively.

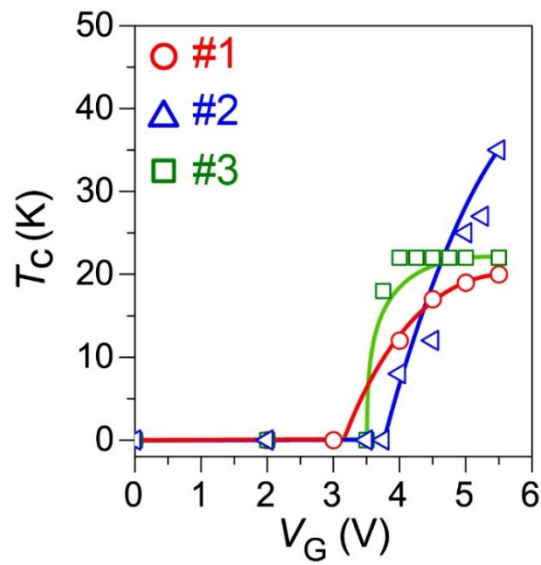


Figure 5-5. Onset T_c of three kinds of the EDLTs as a function of applied V_G .

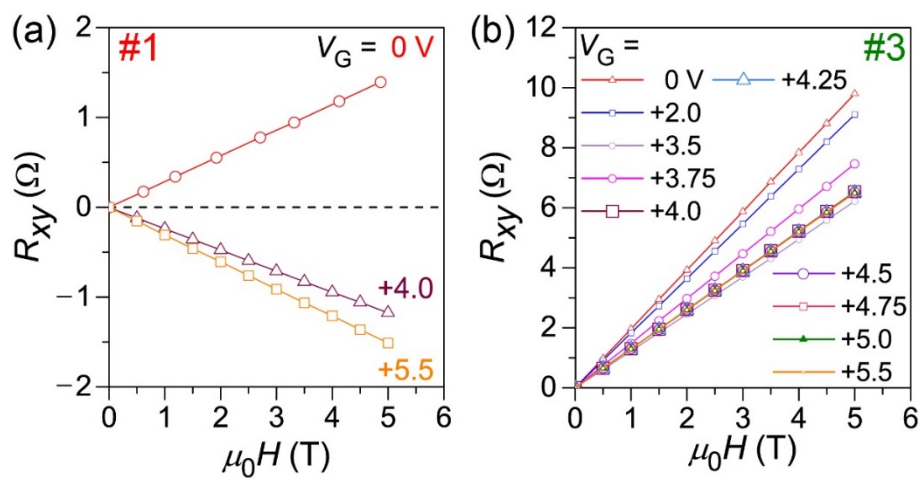


Figure 5-6. External magnetic field (H) dependence of Hall resistance (R_{xy}) at 40 K under $V_G = 0$ – $+5.5$ V for EDLTs fabricated using samples #1 (a) and #3 (b).

Chapter 6. Fabrication of Metastable Tetragonal FeS Heteroepitaxial Thin Film and the EDLT

6.1. Tetragonal FeS

In previous **Chapters**, it was demonstrated that the T_c of FeSe was raised up to 35 K through extremely high-density electron accumulation using electric-double layer transistor (EDLT) structures for FeSe epitaxial thin film exhibiting an insulator-like electric transport property stimulated by the epitaxial strain [1, 2]. This kind of carrier-induced high- T_c superconductivity in FeSe was also reported in refs. 3–6 and observed for monolayer-thick FeSe [7, 8]. As a next step, the strategy, which is carrier doping of Fe-based parent phase with strong electron correlation, is extended to the other Fe-based compound, tetragonal FeS (t -FeS).

Although t -FeS has the same crystal structure as that of FeSe that is displayed in **Fig. 6-1a**, it was previously believed that t -FeS is not a superconductor but exhibits metallic or semiconductor-like behavior [9, 10]. However, recent report showed that t -FeS exhibits superconductivity with $T_c = 5$ K [11]. Thus, it is expected that phenomena observed for FeSe, such as enhancement of electron correlation by application of strain, may also appear in t -FeS. To examine this possibility, an epitaxial thin film is the most promising platform because it is possible to introduce both tensile and compressive stresses as well as to controllably dope of the film with a high density of carriers using EDLT structures.

It should be noted that t -FeS cannot be synthesized by conventional techniques such as a simple solid-state reaction between elemental Fe and S, from which only hexagonal phases (h -FeS; see **Fig. 6-1b**) are generated because they are thermodynamically much more stable than t -FeS in the Fe–S binary phase diagram [12]. Only unconventional methods such as de-

intercalation of alkali metal (A) from $A_x\text{Fe}_{2-y}\text{S}_2$ [13] are effective to obtain t -FeS. They indicate that t -FeS is a thermodynamically metastable phase.

Therefore, in this study, the non-equilibrium process, pulsed laser deposition (PLD), is utilized to stabilize t -FeS. Even though epitaxial $\text{FeSe}_{1-x}\text{S}_x$ solid solution films [14], polycrystalline [15], and monolayer-thick t -FeS films [16] have been fabricated, a pure t -FeS epitaxial thin film has not been reported. It is presumed that stabilization of t -FeS is quite sensitive to the thermal environment because it is a metastable phase, even though thermal assistance is necessary for crystallization and epitaxial growth of precursors. In this **Chapter**, by considering the influences of thermal, kinetic, and reaction paths, it is attempted to stabilize t -FeS phase and fabricate its epitaxial growth on a CaF_2 substrate. Then high-density electron doping of the t -FeS thin films is performed by constructing an EDLT structure.

6.2. Experimental Procedure

6.2.1. Synthesis of polycrystalline hexagonal FeS bulk targets

Polycrystalline bulk samples with nominal chemical compositions of FeS_{1+x} ($x = 0, 0.1, 0.2, \text{ and } 0.4$) were synthesized for use as PLD targets via a solid-state reaction between elemental Fe (99.9%) and S (99.9999%). In an Ar-filled glove box, Fe and S powders were mixed with the appropriate mass ratio, sealed in evacuated silica-glass tubes, and then heated at 900 °C for 24 h. Then, the preheated Fe+S powders were pressed into pellets with a diameter of 7 mm and thickness of ~6 mm, sealed in evacuated silica-glass tubes, and heated at 900 °C for 36 h. The roughly estimated bulk density of the $x = 0$ sample was ~80%.

6.2.2. PLD growth of tetragonal FeS epitaxial films

FeS thin films with a thickness of ~30 nm were grown by PLD in a vacuum growth chamber with a base pressure of $<5 \times 10^{-5}$ Pa, which is different with a growth chamber utilized in **Chapter 2–5**. A KrF excimer laser with a wavelength of 248 nm and repetition

rate of 10 Hz was used as an ablation source. The growth rate (r_g) was controlled between 3.3 and 7.5 nm/min by varying the laser fluence. Six kinds of (001)-oriented single crystals with dimensions of $10 \times 10 \times 0.5$ mm were used as substrates: Y-stabilized ZrO_2 (YSZ), CaF_2 , $(\text{LaAlO}_3)_{0.3}(\text{Sr}_2\text{AlTaO}_6)_{0.7}$ (LSAT), SrTiO_3 (STO), GaAs, and MgO. YSZ, LSAT, and MgO were thermally annealed at 1350, 800, and 1100 °C in air, respectively, before use. STO was annealed at 1050 °C after wet etching with buffered HF solution [17] before use, whereas CaF_2 and GaAs were used without any preliminary treatment (i.e., used as-received from suppliers). During film growth, the substrates were heated at a substrate temperature (T_s) between room temperature (RT) and 400 °C from the back side of a substrate carrier made of Inconel alloy with a halogen lamp. The substrate heating was stopped just after film deposition, and then the films were rapidly cooled in the growth chamber.

6.2.3. Analyses of structure and chemical composition

Crystalline phases and structures of polycrystalline bulk targets and obtained films were evaluated by X-ray diffraction (XRD) using Cu $K\alpha$ radiation. The amounts of *h*-FeS and impurity phases in the bulk samples were estimated by Rietveld analysis. A parallel-beam X-ray, which was monochromated by a two-bounce Ge (220) crystal, was used to measure rocking curves and asymmetric ϕ scans. The thickness of the films was precisely determined by X-ray reflectivity analysis using the parallel-beam geometry. Chemical compositions of the films were quantified from wavelength-dispersive X-ray fluorescence (XRF) analysis. The chemical composition of the film on CaF_2 was precisely determined by wavelength-dispersive electron probe microanalysis. The surface morphology of the films was observed by tapping-mode atomic force microscopy (AFM).

6.2.4. STEM measurements of tetragonal FeS epitaxial film

The cross-sectional microstructure of a *t*-FeS film on CaF_2 was observed with a scanning transmission electron microscope (STEM) using high-angle annular dark field (HAADF)

mode. During observation, selected-area electron diffraction (SAED) measurements in the *t*-FeS film regions and point composition analysis around the interface between *t*-FeS and CaF₂ were also performed by energy-dispersive X-ray (EDX) spectroscopy.

6.2.4. Electronic transport measurements of epitaxial tetragonal FeS and the EDLT

Electrical resistivities (ρ) of the *t*-FeS films were measured by a four-probe technique. Au films deposited with a direct-current sputtering system were used as contact electrodes. The measurement temperature (T) was varied from 2 to 300 K. For carrier doping of the *t*-FeS phase, an EDLT structure was constructed using a *t*-FeS film on CaF₂ as a channel layer through *ex-situ* process (i.e., with air exposure). Gate voltages (V_G) of 0 to +5 V were applied through a Pt electrode at 220 K. Details of the measurement procedure and device configuration are the same as those in **Chapters 4** and **5**. Transfer curves (i.e., drain current I_D and gate leak current I_G at a constant drain voltage V_D of +0.1 V as a function of V_G) at 220 K and the dependence of the sheet resistance (R_s) of the channel on T in the range of 2–220 K were measured for the EDLT structure.

6.3. Results and Discussion

6.3.1. Stabilization of metastable tetragonal FeS phase via thin film growth process

To stabilize metastable *t*-FeS thin films, PLD was used as a non-equilibrium growth process. Through experimental trials, it was found that there are three critical factors affecting the formation of *t*-FeS—temperature, kinetics, and chemical composition of PLD targets.

First, because *t*-FeS is a metastable phase, the influence of temperature was carefully investigated on the grown crystalline phases. **Figure 6-2a** depicts the dependence of crystalline phases grown using a stoichiometric FeS target (i.e., nominal $x = 0$) on T_s . At high

T_s (400 °C), only thermally stable h -FeS phases (space group: $P62c$ (No. 190) and/or $P6_3/mmc$ (No. 194)) were detected; i.e., t -FeS was not generated. In contrast, at T_s between RT and 300 °C, t -FeS formed with preferential orientation along the c -axis for the out-of-plane direction (i.e., diffractions perpendicular to the film plane). This result indicates that T_s needs to be lower than 400 °C for stabilization of t -FeS. Then a t -FeS film grown at $T_s = 300$ °C was thermally annealed in a vacuum growth chamber for 3 h immediately after finishing the deposition. **Figure 6-2b** compares the XRD pattern of the as-grown t -FeS film with the annealed one. Although only the t -FeS phase was observed before annealing, h -FeS phases appeared after annealing. This structural phase transition induced by thermal annealing has also been reported for a t -FeS powder [18], indicating that thermal quenching just after deposition is also necessary to protect the generated t -FeS phase after deposition and prevent conversion to stable h -FeS phases.

Next, effect of r_g was examined at $T_s = 300$ °C on the obtained crystalline phases because kinetics is also another general factor to overcome thermal equilibrium and stabilize metastable phases. **Figure 6-2c** shows the films grown at different r_g . When r_g was too low (3.3 nm/min) or too high (7.5 nm/min), h -FeS phases emerged. In contrast, the pure t -FeS phase was observed at moderate r_g (6.8 nm/min). These results indicate that the optimum r_g is ~ 7 nm/min, which is another critical parameter to effectively nucleate and stabilize t -FeS. Therefore, it was tentatively concluded that the optimum stabilization conditions of t -FeS are $T_s = \sim 300$ °C followed by quenching and $r_g = \sim 7$ nm/min. However, subsequent XRF analysis indicated that the obtained t -FeS contained large amounts of excess Fe; i.e., the [Fe]/[S] atomic ratio was ~ 1.1 .

According to the above XRF result, I then tried to tune the [Fe]/[S] ratio to reach stoichiometry by adding excess S to the PLD bulk targets. The nominal compositions of PLD targets were FeS_{1+x} ($x = 0, 0.1, 0.2, \text{ and } 0.4$). Other parameters were all fixed; i.e., $T_s =$

~ 300 °C followed by quenching and $r_g = \sim 7$ nm/min. **Figure 6-3a** presents XRD patterns of FeS_{1.2} (top) and stoichiometric FeS (bottom) bulk targets. In the case of the stoichiometric FeS target, *h*-FeS (space group: *P62c*) and a small amount of Fe (volume fractions of 98.4 and 1.6 wt%, respectively) were observed. The FeS_{1.2} target is composed of three phases, Fe₇S₈ (70.6 wt%), *h*-FeS (22.5 wt%), and FeS₂ (6.9 wt%). **Figure 6-3b** shows the XRD patterns of FeS films grown using the four different targets with nominal $x = 0-0.4$. While the stoichiometric FeS target led to formation of pure *t*-FeS, all the other S-rich targets did not generate *t*-FeS at all; only *h*-FeS. This result indicates that the chemical composition of the films cannot be easily controlled by adding large amounts of excess S to the PLD target. In addition, the crystalline phase of the target is also probably very important for the formation of *t*-FeS as the phase transition from phases such as FeS₂ and Fe₇S₈ to *t*-FeS would be more difficult than that from *h*- to *t*-FeS because of the higher activation energy of the former transitions. Thus, it was concluded that the most important factors to stabilize the *t*-FeS phase grown via PLD are $T_s = 300$ °C followed by thermal quenching, $r_g = \sim 7$ nm/min, and the chemical composition of bulk target should be pure *h*-FeS.

6.3.2. Fabrication of tetragonal epitaxial FeS thin film

Even though the *t*-FeS phase was successfully stabilized on STO and YSZ single-crystal substrates under the optimum growth conditions, the in-plane orientation was random (i.e., preferentially *c*-axis oriented only in the out-of-plane direction); i.e., the *t*-FeS films were not epitaxial. Therefore *t*-FeS was deposited on various kinds of single-crystal substrates with different in-plane lattice mismatches under the optimum growth conditions in an attempt to achieve epitaxial *t*-FeS film growth. **Figure 6-4a** shows the XRD patterns of films grown on six kinds of substrates. On YSZ, CaF₂, LSAT, and STO, single-phase *t*-FeS was obtained; whereas on GaAs and MgO, impurity *h*-FeS phases were segregated. The in-plane orientation of the films was then examined. **Figures 6-4b** and **6-4c** display the results of ϕ -

scans for the *t*-FeS 112 diffractions of the films on STO and LSAT, respectively. In the case of STO, no diffractions were detected, indicating that *t*-FeS grew with preferred orientation only for the *c*-axis (out-of-plane); i.e., random for in-plane. This feature was observed also for the films grown on GaAs and YSZ substrates (data not shown). Conversely, in the case of LSAT, I observed diffractions consistent with the four-fold symmetry of the tetragonal lattice, which can be classified into two groups rotated by 37° with respect to each other. The rotation angle of 37° is relatively close to the 45° usually observed for tetragonal lattices; the difference of 8° is within the angle resolution of the measurements. However, the origin of such a difference is unclear at present. This result indicates that there are two single-crystalline domains in the film. **Figure 6-4d** shows the ϕ -scans for *t*-FeS 111 and CaF₂ 111 diffractions. Because four-fold symmetry originating from a single in-plane domain rotated by 45° with respect to CaF₂ was observed, it was concluded that *t*-FeS grew heteroepitaxially on CaF₂. The epitaxial relationship is [001] *t*-FeS || [001] CaF₂ for the out-of-plane direction and [100] *t*-FeS || [110] CaF₂ for the in-plane direction. This is the first demonstration of epitaxial *t*-FeS thin-film growth. Therefore, another important factor is added to the critical conditions to stabilize epitaxial *t*-FeS thin films; i.e., use of a CaF₂ (001) single crystal as a substrate.

6.3.3. Structure parameters of tetragonal FeS on various substrates

To examine the reason for the observed selective epitaxial growth of *t*-FeS on CaF₂, the structure parameters of the systems are summarized in **Table 6-I**. Here, the in-plane lattice mismatch (Δa) between *t*-FeS ($a_{\text{FeS}} = 3.683 \text{ \AA}$ [13]) and the substrate (a_{sub}) was mainly focused on, which was calculated from $\Delta a = (a_{\text{sub}} - a_{\text{FeS}})/a_{\text{sub}}$. When $\Delta a \geq 7.61\%$, the in-plane symmetry was random. With decreasing Δa , domains with long-range order appeared. Epitaxial growth was realized at $\Delta a < \sim 6.72\%$. For the system with YSZ, a_{sub} had two kinds of lattice parameters; primitive (5.139 Å) and 1/√2 times the lattice parameter (3.638 Å). In

the case of the latter multiple lattice, the absolute value of Δa is the smallest in **Table 6-I** with expectation of heteroepitaxial growth with 45° rotation. However, despite the small Δa of YSZ, any in-plane orientation was not observed in the t -FeS film grown on YSZ. Therefore, the large $\Delta a = 28.4\%$ for cube-on-cube heteroepitaxy would affect the growth of t -FeS, resulting in random in-plane orientation.

Although substrates with larger a_{sub} values than that of a_{FeS} were used, the c -axis lattice parameter of all the obtained t -FeS films was expanded (e.g., $c = 5.092 \text{ \AA}$ on CaF_2) compared with that of a t -FeS single crystal (5.034 \AA [13]), leading to t -FeS films with compressed in-plane lattice parameters. The a -axis lattice parameters of the films (they can be estimated only for the films on LSAT and CaF_2) were small ($a = 3.668 \text{ \AA}$ on CaF_2) compared with that of a t -FeS single crystal (3.683 \AA [13]). The above strain trend for out-of-plane and in-plane directions is completely opposite to that of $\sim 10 \text{ nm}$ -thick t -FeSe on STO [19]. The exact reason of such unusual lattice variation is unsure; however, the misoriented in-plane lattice, excluding t -FeS on CaF_2 , and an interface layer (see that will be displayed in **Fig. 6-6**) may be possible origins. The chemical composition of all the FeS films was off-stoichiometric; i.e., the $[\text{Fe}]/[\text{S}]$ atomic ratio was > 1.0 except for that on CaF_2 ($[\text{Fe}]/[\text{S}] = 0.9$). To evaluate the crystallinity of the t -FeS films, the full width at half maximum of rocking curves was measured for the out-of-plane t -FeS 001 diffraction ($\Delta\omega$; see **Table 6-I**). $\Delta\omega$ of t -FeS on CaF_2 (2.00°) was the best of the systems, which was attributed to its epitaxial growth. **Figures 6-5a – 6-5f** show the surface morphologies of the t -FeS thin films. Although droplets derived from PLD were observed in the films grown on LSAT and GaAs, all the surfaces were relatively flat; e.g., the root mean square roughness (R_{rms}) of t -FeS on CaF_2 was 1.6 nm .

6.3.4. Microstructure analysis of epitaxial tetragonal FeS on CaF_2

Next, the heteroepitaxial growth of the t -FeS film on CaF_2 was also confirmed by STEM measurements in HAADF mode. **Figure 6-6a** is a wide-view cross-sectional HAADF-

STEM image of the system. Clear stacking along the c -axis, which is consistent with the layered crystal structure of t -FeS (**Fig. 6-1a**), was observed in the entire film region from the substrate–film interface toward film surface. Diffraction spots of the SAED pattern in the film region (inset of **Fig. 6-6a**) are assigned to the t -FeS phase, which supports heteroepitaxial growth of the t -FeS film and is consistent with the XRD results (**Fig. 6-4**). Furthermore, the existence of a 3–3.5-nm-thick interface diffusion layer between the t -FeS film and CaF₂ was unveiled (**Fig. 6-6b**). Similar interface layers have also been observed between t -Fe(Se, Te) and CaF₂ [20, 21]. Point analysis by EDX was then performed to roughly estimate the chemical composition of the film (**Fig. 6-6b**). The results suggested that the t -FeS film bulk region was almost stoichiometric and all of the constituent elements diffused in the interface layer. However, determine the exact structure and composition of this interface layer could not be determined. **Figure 6-6c** shows an atomic-resolution image in the t -FeS film region. All bright positions were assigned to Fe (orange) and S (yellow) in t -FeS. Additionally, dark line-shaped areas were also alternately stacked along the c -axis, which is consistent with the fact that t -FeCh has no insertion layer between the edge-sharing FeCh₄ tetrahedra layers (**Fig. 6-1a**). According to the results of microstructure observation, it was concluded that the film grown on CaF₂ is t -FeS with respect to not only its averaged structure (i.e., XRD results) but also to its local atomic coordination structure.

6.3.5. Electric transport of tetragonal FeS films

The electronic transport properties of the films were then examined. **Figure 6-7** shows the dependence of ρ of the t -FeS films grown under the optimum conditions on five kinds of single-crystal substrates on T . Even though it was reported that t -FeS bulk exhibits superconductivity at 5 K [11], none of the thin films exhibited superconductivity down to 2 K; instead, the films displayed insulator-like behavior as previously suggested [9] and as observed for very thin strained FeSe films [19, 22, 23]. Absolute ρ values of the films

strongly depended on substrate type over the whole T range. One of the possible origins of this behavior should be the crystallinity of the films because the ρ values of samples on GaAs, STO, and YSZ are very high compared with those on the other substrates. According to the results in Table 1, these three samples exhibit only out-of-plane c -axis orientation, mainly because of their large Δa . Conversely, the crystallinity of samples on LSAT and CaF₂, which also exhibited lower ρ , was much higher than that of films on the other substrates. Here it should be noted that the structure of all the t -FeS films obtained was expanded along the c -axis and contracted along the a -axis compared with the corresponding values for a t -FeS single crystal. In a t -FeSe thin film, in-plane lattice variation should affect superconductivity more strongly than out-of-plane lattice variation [24]. Moreover, superconductivity in t -FeS bulk disappears by applying external pressure [25]. Thus, in-plane compressive strain is a possible origin of the lack of superconductivity and insulator-like behavior of the t -FeS films. Another possibility is their off-stoichiometric chemical composition [11]. Therefore, if lattice strain releases and/or chemical composition optimally tunes, the t -FeS films may display superconductivity.

6.3.6. Electric transport of tetragonal FeS-EDLT under electric field

Finally, high-density carrier doping of a t -FeS film was attempted by using an EDLT structure. As a channel layer t -FeS grown heteroepitaxially on CaF₂ was used because superconductivity induced by EDLT strongly depends on the quality of the channel layer, as concluded in **Chapter 5** for a t -FeSe EDLT structure [2]. **Figure 6-8a** presents the transfer curves of the EDLT structure under applied V_G of up to +5.0 V at 220 K. Clear modulation of I_D was induced and was three orders of magnitude larger than that of I_G , even though the on/off ratio was small (~5%). In the cyclic measurements, large hysteresis loops were observed. Furthermore, the initial I_D at $V_G = 0$ V was not the same as that at the end point and decreased from the first cycle to the second, indicating that the resistance of the t -FeS

channel increased during the cyclic measurements. The phase transition of *t*-FeS was then examined by measuring R_s under V_G . **Figure 6-8b** shows the dependence of R_s on T at V_G of 0 to +5 V. Even under a high V_G of +5.0 V, no phase transition was induced. With increasing V_G , R_s also increased, which indicates that carriers were not doped in the channel. However, I_D modulation was observed in the transfer curves (**Fig. 6-8a**). Therefore, carriers are doped in the channel but the channel thickness and/or surface state changed during the measurements. Possible reasons for the changes in the channel during cycling may be electrochemical etching by the ionic liquid [3] and surface degradation, similar to the case for *t*-FeSe [2, 26]. Thus, further improvement of film quality and the fabrication process of the EDLT is necessary to induce superconductivity in *t*-FeS EDLT structures.

6.4. Conclusion

Metastable *t*-FeS was stabilized via the thin-film growth process PLD. The essential factors to stabilize the metastable *t*-FeS phase were determined and included using an optimum growth temperature of $T_s = 300$ °C followed by thermal quenching, optimum r_g of ~ 7 nm/min, and pure *h*-FeS bulk target. At high T_s , competitive *h*-FeS, which is the thermodynamically stable phase, preferentially nucleated, whereas at $T_s < 400$ °C, the *t*-FeS phase was stabilized. Because *t*-FeS is metastable, thermal quenching immediately after deposition was necessary to stabilize the phase and prevent segregation of competitive *h*-FeS. The optimum r_g was ~ 7 nm/min because *h*-FeS was mainly observed at other r_g . Moreover, it was clarified that using a high-purity *h*-FeS (*P62c*) PLD target was important to obtain *t*-FeS. When other PLD targets mainly composed of Fe_7S_8 were used, growth of the *t*-FeS phase was not stabilized. These results suggest that growth of *t*-FeS is very sensitive to growth conditions. It was then revealed that epitaxial growth of *t*-FeS was achieved only on a CaF_2 single-crystal substrate, which was probably related to the small in-

plane lattice mismatch between t -FeS and CaF₂. Therefore, another important factor for t -FeS epitaxial growth is selection of a single-crystal substrate with small in-plane lattice mismatch. This report presented the first demonstration of epitaxial t -FeS thin-film growth. None of the fabricated t -FeS thin films exhibited superconductivity even though superconductivity at 5 K was previously reported for bulk t -FeS. The lack of superconductivity would be attributed to the introduced compressive in-plane and tensile out-of-plane lattice strain, and/or off-stoichiometric chemical composition. In addition, no phase transition was induced in an EDLT structure with t -FeS grown on CaF₂ as a channel layer, which was possibly because of electrochemical etching by the ionic liquid and/or surface degradation due to the *ex-situ* device fabrication. The further researches such as ARPES to examine the electron correlation and characterization of the *in-situ* fabricated EDLT to investigate the intrinsic property are necessary to discuss on lack of the superconductivity of FeS epitaxial films and not activated carrier transport property under electric field.

References

1. K. Hanzawa, H. Sato, H. Hiramatsu, T. Kamiya, and H. Hosono, *Proc. Nat. Acad. Sci. USA.*, **113**, 3986 (2016)
2. K. Hanzawa, H. Sato, H. Hiramatsu, T. Kamiya, and H. Hosono, *IEEE. Trans. Appl. Superconductivity*, **27**, 7500405 (2016).
3. J. Shiogai, Y. Ito, T. Mitsuhashi, T. Nojima, and A. Tsukazaki, *Nat. Phys.*, **12**, 42 (2015).
4. B. Lei, J. H. Cui, Z. J. Xiang, C. Shang, N. Z. Wang, G. J. Ye, X. G. Luo, T. Wu, Z. Sun, and X. H. Chen, *Phys. Rev. Lett.*, **116**, 077002 (2016).
5. W. K. Wang, Y. Liu, J.-Y. Yang, H.-F. Du, W. Ning, L.-S. Ling, W. Tong, Z. Qu, Z.-R. Yang, M.-L. Tian, and Y.-H. Zhang *Chin. Phys. Lett.*, **33**, 057401 (2016).

6. J. Shiogai, T. Miyakawa, Y. Ito, T. Nojima, and A. Tsukazaki *Phys. Rev. B*, **95**, 115101 (2017).
7. For a review see Z. Wang, C. Liu, Y. Liu, and J. Wang, *J. Phys.: Condens. Matter.*, **29**, 153001 (2017).
8. Q.-Y. Wang, Z. Li, W.-H. Zhang, Z.-C. Zhang, J.-S. Zhang, W. Li, H. Ding, Y.-B. Ou, P. Deng, K. Chang, J. Wen, C.-L. Song, K. He, J.-F. Jia, S.-H. Ji, Y.-Y. Wang, L.-L. Wang, X. Chen, X.-X. Ma, and Q.-K. Xue, *Chin. Phys. Lett.*, **29**, 037402 (2012).
9. S. J. Denholme, S. Demura, H. Okazaki, H. Hara, K. Deguchi, M. Fujioka, T. Okazaki, T. Yamaguchi, H. Takeya, and Y. Takano, *Mater. Chem. Phys.*, **147**, 50 (2014).
10. S. J. Denholme, H. Okazaki, S. Demura, K. Deguchi, M. Fujioka, T. Yamaguchi, H. Takeya, M. ElMassalami, H. Fujiwara, and Y. Takano *Sci. Technol. Adv. Mater.*, **15**, 05507 (2014).
11. X. Lai, H. Zhang, Y. Wang, X. Wang, X. Zhang, J. Lin, and F. Huang, *J. Am. Chem. Soc.*, **137**, 10148 (2015).
12. T. B. Massalski, and H. Okamoto, *Binary Alloy Phase Diagrams* 2nd edn (Ohio: ASM International), 1762–1765 (1990).
13. C. H. K. Borg, X. Zhou, C. Eckberg, D. J. Campbell, S. R. Saha, J. Paglione, and E. E. Rodriguez, *Phys. Rev. B*, **93**, 094522 (2016).
14. K. Fujiwara, J. Shiogai, and A. Tsukazaki, *Jpn. J. Appl. Phys.*, **56**, 100308 (2017).
15. H. Nozaki, H. Nakazawa, and K. Sagaguchi, *Mineral. J.*, **8**, 399 (1997).
16. K. Zhao, H.-C. Lin, W.-T. Huang, X.-P. Hu, X. Chen, Q.-K. Xue, and S.-H. Ji, *Chin. Phys. Lett.*, **34**, 087401 (2017).
17. M. Kawasaki, K. Takahashi, T. Maeda, R. Tsuchiya, M. Shinohara, O. Ishiyama, T. Yonezawa, M. Yoshimoto, and H. Koinuma, *Science*, **266**, 1540–1542 (1994).
18. A. R. Lennie, S. A. T. Redfern, P. F. Schofield, and D. J. Vaughan *Miner. Mag.*, **59**, 677 (1995).

19. K. Hanzawa, Y. Yamaguchi, Y. Obata, S. Matsuishi, H. Hiramatsu, T. Kamiya, and H. Hosono, *Phys. Rev. B*, **99**, 035148-1 – 035148-11 (2019).
20. A. Ichinose, F. Nabeshima, I. Tsukada, M. Hanawa, S. Komiya, T. Akiike, Y. Imai, and A. Maeda, *Supercond. Sci. Technol.*, **26**, 075002 (2013).
21. A. Ichinose, I. Tsukada, F. Nabeshima, Y. Imai, A. Maeda, F. Kurth, B. Holzapfel, K. Iida, S. Ueda, and M. Naito, *Appl. Phys. Lett.*, **104**, 122603 (2014).
22. A. Tsukada, K. E. Luna, R. H. Hammond, M. R. Beasley, J. F. Zhao, and S. H. Risbud, *Appl. Phys. A*, **104**, 311 (2011).
23. M. J. Wang, J. Y. Luo, T. W. Huang, H. H. Chang, T. K. Chen, F. C. Hsu, C. T. Wu, P. M. Wu, A. M. Chang, and M. K. Wu, *Phys. Rev. Lett.*, **103**, 117002 (2009).
24. G. N. Phan, K. Nakamura, K. Sugawara, T. Sato, T. Urata, Y. Tanabe, K. Taniguchi, F. Nabeshima, Y. Imai, A. Maeda, and T. Takahashi, *Phys. Rev. B*, **95**, 224507 (2017).
25. S. Holenstein, U. Pachmayr, Z. Guguchia, S. Kamusella, R. Khasanov, A. Amato, C. Baines, H.-H. Klauss, E. Morenzoni, D. Johrendt, and H. Luetkens, *Phys. Rev. B*, **93**, 140506(R) (2016).
26. H. Hiramatsu, K. Hanzawa, T. Kamiya, and H. Hosono, *Journal of Superconductivity and Novel Magnetism*, published online (2019). DOI: 10.1007/s10948-019-5020-9.

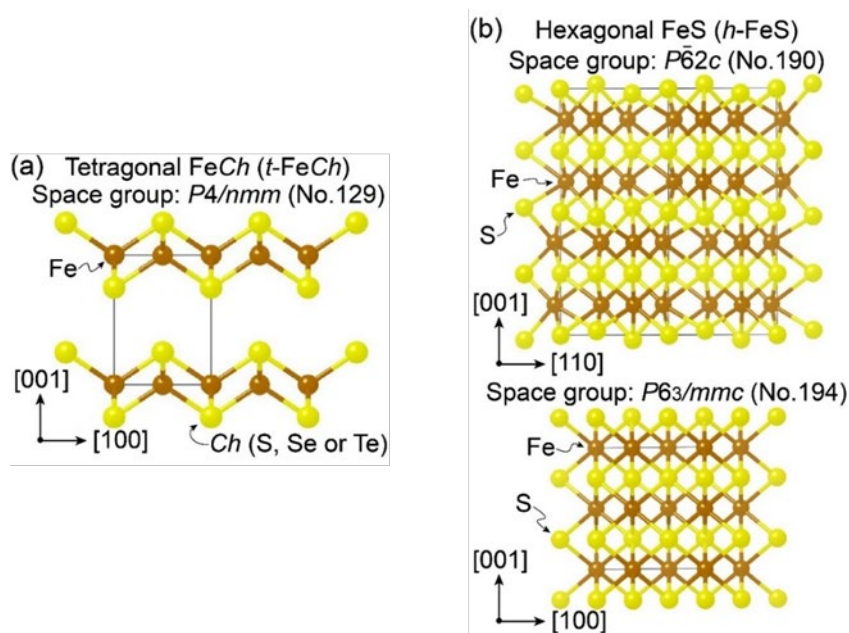


Figure 6-1. Crystal structures of FeS. (a) Tetragonal phase ($t\text{-FeCh}$, $Ch = S, Se, \text{ or } Te$). (b) Two types of hexagonal phases ($h\text{-FeS}$).

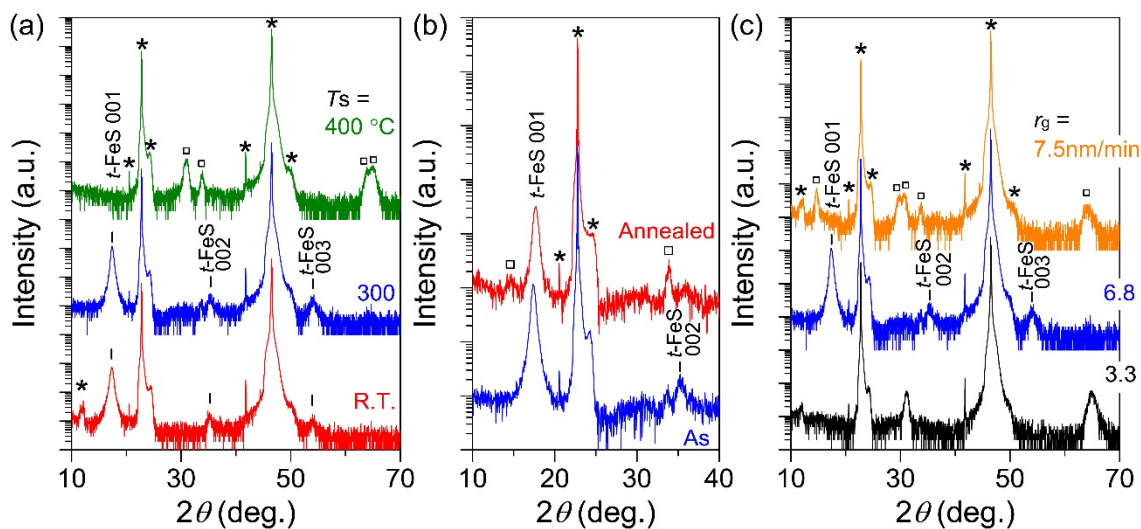


Figure 6-2. Crystalline phase analysis based on out-of-plane XRD patterns of FeS films grown on STO substrates under different conditions. Vertical bars, asterisks, and black squares denote diffraction positions of $t\text{-FeS}$, substrate, and $h\text{-FeS}$, respectively. (a) Films grown at T_s of RT, 300, and 400 °C. (b) Influence of post-deposition thermal annealing under vacuum at 300 °C for 3 h on the phase of a $t\text{-FeS}$ film. Bottom and top patterns are for as-

grown and annealed films, respectively. (c) Films grown at $T_s = 300$ °C and $r_g = 3.3, 6.8,$ and 7.5 nm/min.

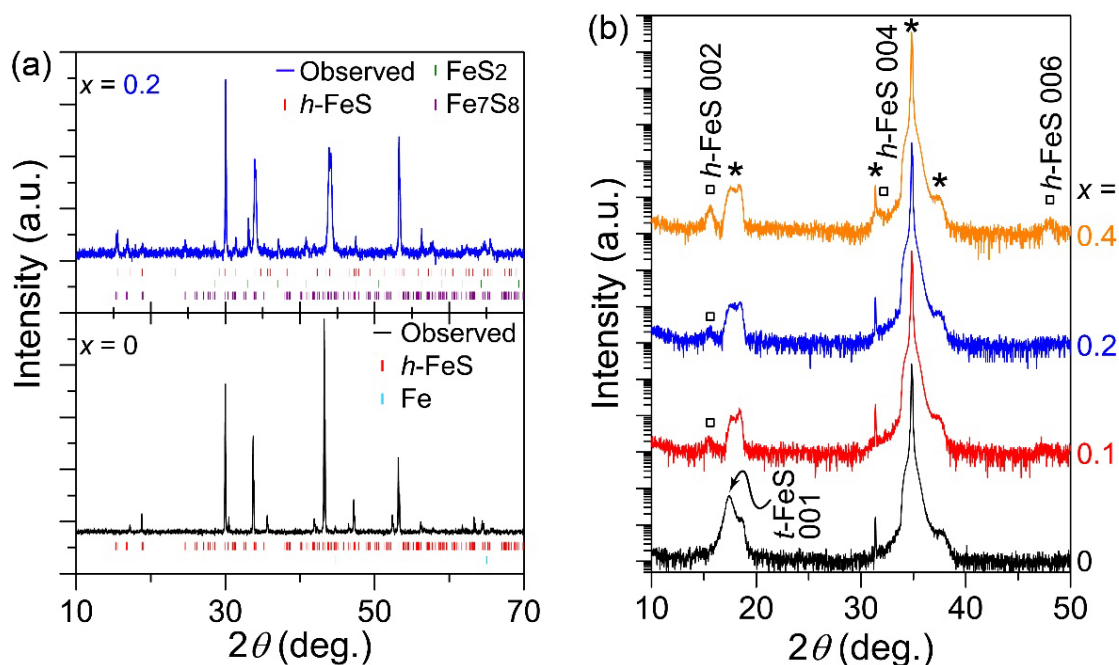


Figure 6-3. Influence of the chemical composition of PLD bulk targets on the formation of crystalline phases via growth at $T_s = 300$ °C and $r_g \approx 7$ nm/min. (a) XRD patterns of polycrystalline targets with nominal chemical compositions of FeS_{1.2} (top) and FeS (bottom). (b) Out-of-plane XRD patterns of FeS films on YSZ grown using four kinds of PLD targets with nominal chemical compositions of FeS_{1+x} ($x = 0, 0.1, 0.2,$ and 0.4). The arrow at $2\theta = 17.6^\circ$ indicates the 001 diffraction of the *t*-FeS phase. Asterisks and black squares denote diffraction positions of the substrate and *h*-FeS, respectively.

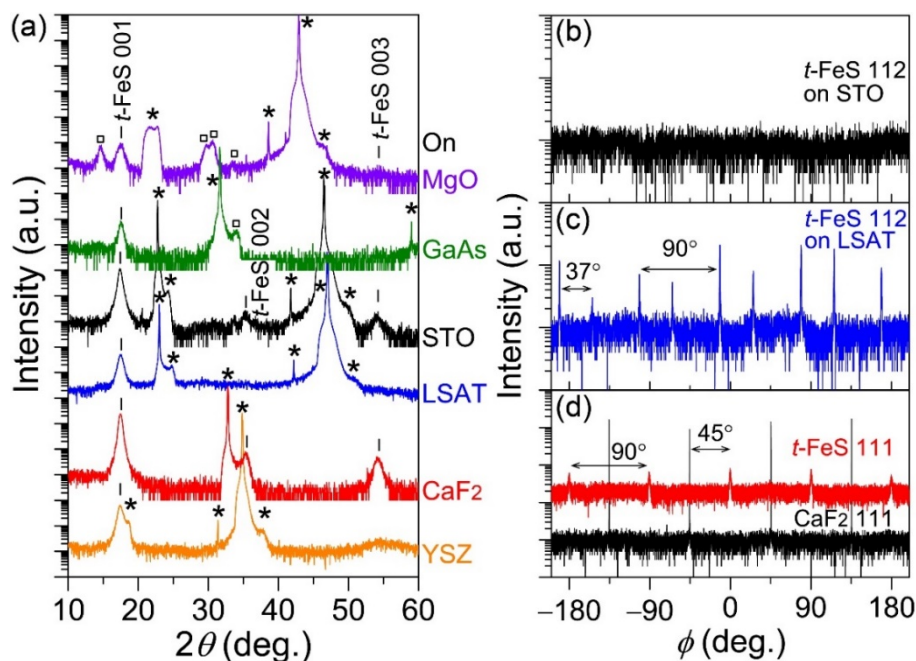


Figure 6-4. Influence of substrate type on FeS thin-film growth. (a) Out-of-plane XRD patterns of the films grown on different substrates. Vertical bars, asterisks, and black squares denote diffraction positions of *t*-FeS, substrate, and *h*-FeS, respectively. In-plane symmetry of *t*-FeS, evaluated by ϕ -scans, grown on (b) STO, (c) LSAT, and (d) CaF₂.

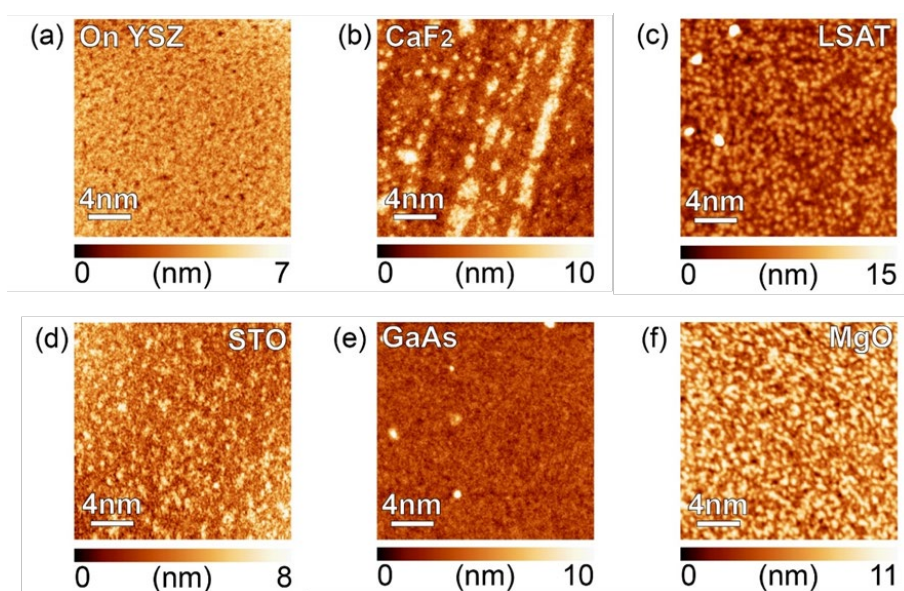


Figure 6-5. Surface morphologies of FeS films deposited on (e) YSZ, (f) CaF₂, (g) LSAT, (h) STO, (i) GaAs, and (j) MgO. Horizontal color bars are height scales.

Table 6-I. Structural parameters and chemical composition of *t*-FeS films. Values in parentheses for YSZ, CaF₂, and GaAs indicate the case of cube-on-cube heteroepitaxy.

| Substrate | a_{sub} | Lattice mismatch | [Fe]/[Se] | a_{film} | c_{film} | $\Delta\omega$ | R_{rms} |
|------------------|------------------|------------------|-----------|-------------------|-------------------|----------------|------------------|
| | (Å) | (%) | | (Å) | (Å) | (deg.) | (nm) |
| MgO | 4.213 | 14.36 | 1.2 | - | 5.070 | - | 1.8 |
| GaAs | 3.998 (5.654) | 7.95 (34.9) | 1.2 | - | 5.050 | - | 0.9 |
| STO | 3.905 | 7.61 | 1.1 | - | 5.070 | 4.35 | 1.2 |
| LSAT | 3.868 | 6.72 | 1.3 | 3.633 3.614 | 5.076 | 5.16 | 2.6 |
| CaF ₂ | 3.862 (5.462) | 6.58 (32.6) | 0.9 | 3.668 | 5.092 | 2.00 | 1.6 |
| YSZ | 3.638 (5.139) | -1.16 (28.4) | 1.2 | - | 5.060 | 3.69 | 0.7 |

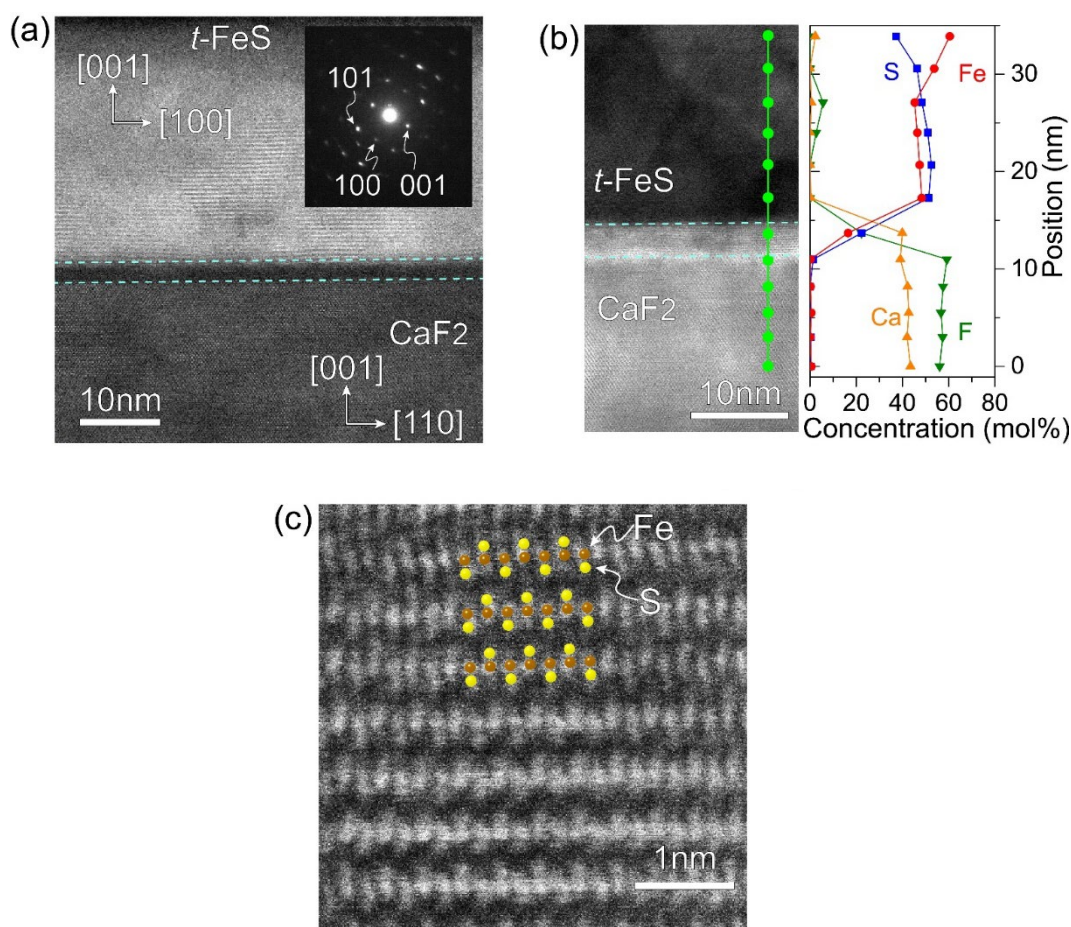


Figure 6-6. Cross-sectional microstructure and chemical composition of a *t*-FeS film on CaF₂ measured by HAADF-STEM. The direction of the incident electron beam was along [010] of the *t*-FeS film. (a) Wide-view cross-sectional HAADF-STEM image. Light blue dashed lines denote the boundaries between *t*-FeS or CaF₂ and an interface diffusion layer. Inset is the SAED pattern taken from the *t*-FeS film area. (b) EDX point analysis (right) at the positions shown by light green circles in the left image. (c) Atomic-resolution image of the *t*-FeS film region. Orange and yellow spheres indicate the positions of Fe and S atoms in *t*-FeS, respectively.

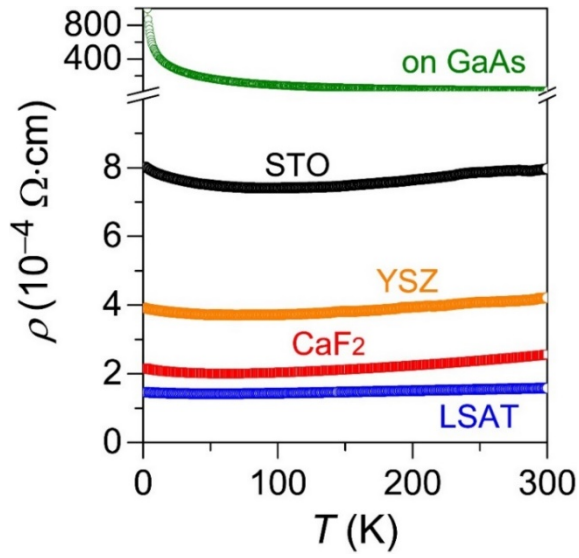


Figure 6-7. ρ - T curves of the t -FeS films grown under the optimum conditions on five kinds of single-crystal substrates.

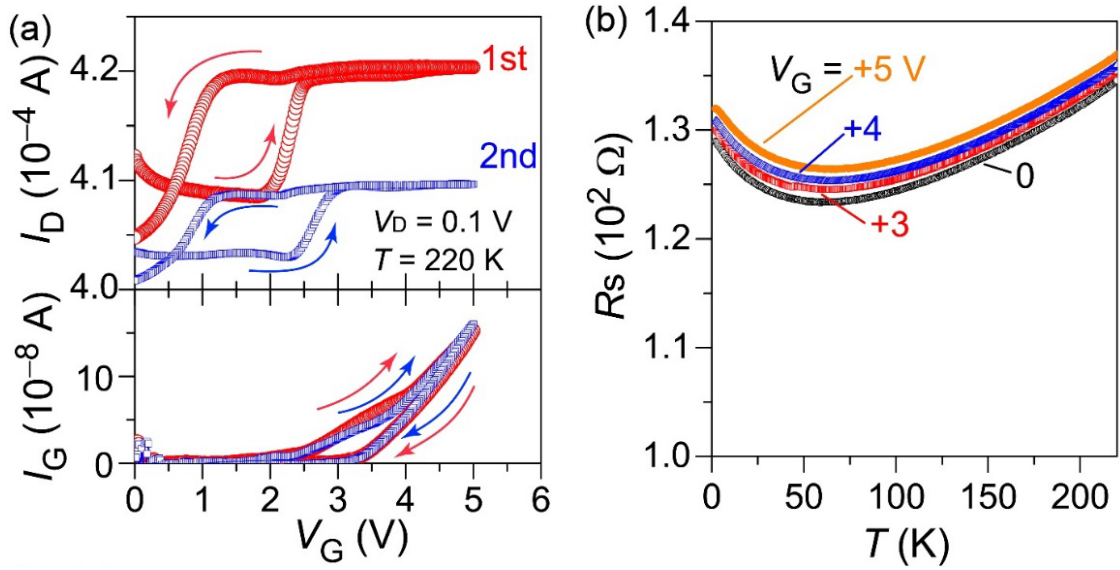


Figure 6-8. Electric transport properties of an EDLT with a t -FeS channel on CaF_2 under V_G .

(a) Transfer curves of first (red, top) and second cycles (blue, top) and leakage currents (bottom) at 220 K. (b) Dependence of R_s on T under V_G of 0 to +5 V.

Chapter 7. Chemical Design of Green Emitting Semiconductors: Perovskite-Type Sulfide SrHfS₃

7.1. Design of Highly Efficient Light-Emitting Semiconductors

As pointed out in **Chapter 1**, a bright green-light source has strong demand to realize next-generation optoelectronic devices [1–3]. Therefore, it is strongly required to explore new semiconductor materials with a high quantum efficiency of the emission in the green wavelength region ($E_g = 2.18\text{--}2.50$ eV, $\lambda = 495\text{--}570$ nm) and *n*- and *p*-type dopability. To meet those requirements, three basic electronic characters of semiconductors are considerable; (i) a deep CBM (large electron affinity) and shallow VBM (small ionization potential) to achieve both of *n*- and *p*-type dopings, respectively, (ii) controllability of electronic conductivity and carrier polarity, and (iii) a direct-allowed band gap to realize highly efficient light emission.

Recently, our research group proposed that early transition metal (*eTM*)-based semiconductors with high symmetry crystal structure can satisfy both the first and second requirements [4–6]. Usually, the empty *d*-orbital of *eTM* and *p*-orbital of anion form a strong antibonding state, so that the conduction band of *eTM*-based compound possesses a too shallow energy level (i.e., too small electron affinity) to dope electron (**Fig. 7-1a**). However, by introducing a deep non-bonding state of *d*-orbital of *eTM*, it was demonstrated that a deep CBM is formed at a specific *k* point, which enables to dope electron and reduce the effective mass. **Figure 7-1b** show an example of the *d*-orbital configuration in cubic perovskite at Γ point ($k = 0$). At the point, the phase of *t*_{2g} orbitals of transition metals (e.g., *eTM* in AeTMX₃, where A and X denote a cation and an anion, respectively) is invariant from one unit cell to the neighbor one. This configuration of *d*-orbital cannot form neither a bonding nor anti-

bonding state with the neighboring *p*-orbitals of anions due to their symmetry constraint. As a result, the deep unoccupied non-bonding state consists of the CBM.

The use of *eTM* has advantages in terms of controllability of electronic conductivity and carrier polarity. The *eTM* cations tend to occupy a high coordination numbers site owing to their large valence states such as Zr⁴⁺, which suppresses the formation of a cation vacancy. Also, the stable valence state inhibits the localization of generated electron at the *eTM* cation site through the change of valence state. These characteristics make a contrast to those of post transition metals cations (*pTM*, e.g., Cu, In, and Sn) which are constituents of conventional oxide semiconductors. Those semiconductors have suffered from the poor doping controllability due to their cation's low and variable valence changes [7–9].

In these regards, *eTM*-based cubic perovskites *AeTMX*₃ seem to be promising candidates in terms of the dopability and controllability of carrier density. A unique feature of the cubic perovskite is that not only their CBM but also their VBM are composed of non-bonding state. **Figure 7-1c** depicts the orbital configuration of fully electron-occupied *p*-orbital of anion X at R point. At the R point of primitive cubic structure, the phase of each orbital in the unit cell is inverted by the primitive translation along *x*, *y*, or *z* direction. This configuration of *p* orbitals cannot form neither a bonding nor anti-bonding state with the neighboring *d*-orbitals of *eTM*. Consequently, this shallow energy level of the non-bonding state pushes up the VBM and makes ease to dope hole carriers.

Although those non-bonding deep *d*- and shallow *p*-orbitals levels are favorable for doping of electron and hole, respectively, the indirect band gap in the cubic perovskite definitely inhibits an efficient light emission (**Fig. 7-1d**). Thus, I introduce another strategy, i.e., band folding, to obtain the direct band gap suitable for light emission. **Figures 7-1e** and **7-1f** show a relationship between size of unit cell in real space and the Brillouin zone (BZ) in reciprocal space [10, 11]. Here it should be considered that how the band structure of one-

dimensional s -orbital chain changes by choosing the unit cell containing one orbital or two orbitals. In the case of one orbital cell with a lattice parameter of a , single s -band appears in the first BZ ranging from $-\pi/a$ to π/a . By doubling the unit cell size $a' = 2a$, the first BZ becomes half. Consequently, bands located outside the first BZ ranging from $-\pi/2a$ to $\pi/2a$ (i.e., located in the second BZ) are folded back to the first BZ and the number of bands becomes double. This relation tells us that the VBM at the R point of cubic perovskite can be transferred to the Γ point by choosing a proper superstructure.

In a perovskite-type structure, superstructure is stabilized by tilting of the $eTMX_6$ octahedra; i.e., structural distortion. Indeed, it is known that the octahedron tilting and the resultant superstructure are well governed by tolerance factor [12], so that a suitable electronic structure with direct-type transition can be designed via applying chemical pressure triggered by choosing constituent elements from a viewpoint of the ionic radius.

In this **Chapter**, highly efficient green-emitting semiconductors are designed by using band folding attributing to construction of superstructure derived from distortion induced by chemical pressure. Then the functionalities are experimentally demonstrated by n - and p -typed dopings of $AE-eTM-S$ system.

7.2. Computational and Experimental Procedures

7.2.1. Theoretical calculations

Electronic structures of $AEEtMS_3$ were calculated by using HSE hybrid-functional with HSE06 vasp code [20]. The mesh sampling in Brillouin zone and cutoff energy were set to $5 \times 4 \times 5$ for all $AEEtMS_3$ and 600 eV, respectively. The DOS of tetragonal ZrOS was also calculated as a normalizer for band alignments of $AEEtMS_3$ with HSE hybrid-functional, where BZ sampling and cutoff energy were set to $6 \times 6 \times 4$ and 600 eV, respectively. The positions of CBM and VBM of $AEEtMS_3$ were normalized by adjusting energy levels of the core S $3s$ -band to that of ZrOS, where the energy levels were determined by estimating the

center of gravity for the DOS peak of S 3s-states. Then all the normalized levels shifted in parallel by adjusting calculated VBM level of ZrOS to experimentally observed one [5]. For SrHfS₃, BaHfS₃ and BaZrS₃, maximally localized Wannier functions as projection functions were constructed from *d*-bands of *AE* and *eTM*, and *p*-bands of S by using Wannier90 code [21]; for CaHfS₃, CaZrS₃ and SrZrS₃, while, they were from *d*-bands of *eTM* and *p*-bands of S. The band structure and DOS shown in **Figs. 7-4a** and **7-4b** respectively were depicted using those Wannier functions. In **Fig. 7-5**, the band structures of *AEeTMS*₃ calculated by vasp code is compared with those by Wannier interpolation.

7.2.2. Polycrystalline sample preparation

Undoped polycrystalline *AEHfS*₃ (*AE* = Sr and Ba) was synthesized by conventional solid-state reaction from mixed precursors of *AES* and HfS₂. The mixtures were pelletized and heated at 1100 °C for 48 hours in Ar-sealed stainless-steel tubes. For electron and hole dopings, La₂S₃ and SrP were employed, respectively. The chemical reaction formulae are as follow; $(1-x)\text{SrS} + 0.5x\text{La}_2\text{S}_3 + \text{HfS}_2 \rightarrow \text{Sr}_{(1-x)}\text{La}_x\text{HfS}_3 + 0.5x\text{S}\uparrow$ and $(1-y)\text{SrS} + y\text{SrP} + \text{HfS}_2 \rightarrow \text{SrHfS}_{(3-y)}\text{P}_y$. All compounds used as precursors and dopants were prepared by myself. *AES* and HfS₂ were synthesized by mixing ~1–2 mm² dendritic pieces of *AE* metal (purity: 99.99%) or Hf metal (99.99%) scraped from metal-rod with sulfur powder (99.9999%) and by heating at 750°C and 950°C, respectively. La₂S₃ was prepared from scraped La metal (99.9 %) and sulfur at 950°C, and SrP was synthesized from Sr metal and phosphorous (99.999%) at 750°C.

7.2.3. Structure analysis

The crystal structure was analyzed from powder X-ray diffraction (XRD) using a Cu-K α radiation source with one-dimensional silicon strip detector. The structure parameters (e.g., lattice parameter) and amounts of impurity phases were evaluated by Rietveld refinement using TOPAS code (Bruker AXS, version 4.2) [22]. The obtained phase was crosschecked

by chemical compositions analysis using electron probe micro analyzer with wave dispersion detector, where AES and HfS₂ were used as standard samples.

7.2.4. Optical properties

Diffuse reflectance spectra were taken in the visible – near-infrared wavelength region at room temperature. Then Kubelka-Munk transformation was performed for the obtained spectra to estimate the optical band gaps. To examine the emission characteristics, photoluminescence (PL) spectra of undoped SrHfS₃ were observed in the temperature range of 30–300 K; whereas for La- and P-doped SrHfS₃, the temperature was set to 300 K. As the excitation source, third-harmonic Nd-doped YAG laser (3ω -Nd:YAG, $\lambda = 355$ nm) was employed, whose pulse width is 7–8 ns. Decay curve was measured for evaluation of the emission lifetime with gate delay between 0–20 ns.

7.2.5. Electronic transport properties

The electrical conductivities were investigated by four and two probe methods for La- and P-doped SrHfS₃, respectively. For ohmic contacts, Au and Pt electrodes were deposited by dc-sputtering on La- and P-doped SrHfS₃. Then thermopower measurements were performed to determine the carrier polarity, where Pt electrode was deposited only on *p*-type SrHfS₃.

7.3. Results

7.3.1. Electronic structures of *AEEtMS*₃

From screening based on the above concepts, *AEEtMS*₃ (*AE* = Alkali earth metal Ca, Sr or Ba, *eTM* = Zr or Hf) was chosen owing to their bandgaps suitable for green light emission. The crystal structure shown in **Fig. 7-2a** forms an orthorhombic perovskite-type structure with a space group of *Pnma*. **Figures 7-2b** and **7-2c** respectively show electron density maps at the CBM and VBM of SrHfS₃ as an example. At the CBM, a *d*-orbital like electron density appears at Hf site, while at the VBM *p*-orbital like population is also visible at S site. The

other orbital contributions are negligibly small both for the CBM and VBM, indicating that the non-bonding state in cubic perovskite is preserved in this orthorhombic structure.

Their lattice constructs a $\sqrt{2} \times 2 \times \sqrt{2}$ superstructure of cubic perovskite-type cell, so that bands at R point of cubic lattice are folded to the Γ point of orthorhombic lattice as explained below in detail. The relationship between formation of the superstructure and the band folding is explained in **Fig. 7-3**. The *Pnma* superstructure has a $\sqrt{2} \times \sqrt{2}$ times larger *ac*-plane and 2 times longer *b*-axis compared with the *Pm $\bar{3}$ m* structure. The structural transformation in *ac*-plane is illustrated in **Fig. 7-3a** and the corresponding reciprocal lattice folding is shown in **7-3b**. In real space, the primitive cubic lattice (black) has a lattice translation vector $\mathbf{T}_{2D} = u_1\mathbf{a} + u_3\mathbf{c}$, where \mathbf{a} and \mathbf{c} are primitive translation vectors, and u_1 and u_3 are integers. Through the change of unit cell size (orange), each primitive translation vector rotates 45° in *ac*-plane and becomes $\sqrt{2}$ times longer. As a result, the lattice translation vector changes to $\mathbf{T}'_{2D} = u'_1\mathbf{a}' + u'_3\mathbf{c}'$, where $\mathbf{a}' = \mathbf{a} + \mathbf{c}$, $\mathbf{c}' = -\mathbf{a} + \mathbf{c}$, and u'_1 and u'_3 are integers. In reciprocal space, reciprocal lattice vector is denoted as $\mathbf{G}_{2D} = v_1\mathbf{x} + v_3\mathbf{z}$, where \mathbf{x} and \mathbf{z} are primitive reciprocal lattice vectors, v_1 and v_3 are integers. Reflecting the unit cell size change in real space, each primitive reciprocal lattice vector also rotates 45° in *ac*-plane and becomes $1/\sqrt{2}$ times shorter (blue). This changes \mathbf{G}_{2D} to $\mathbf{G}'_{2D} = v'_1\mathbf{x}' + v'_3\mathbf{z}'$, where $\mathbf{x}' = (\mathbf{x} + \mathbf{z})/2$, $\mathbf{z}' = (-\mathbf{x} + \mathbf{z})/2$, and v'_1 and v'_3 are integers. Because of the shortening of reciprocal lattice vector, some bands are left outside the first BZ defined by the \mathbf{x} and \mathbf{z} . Consequently, those bands have to be folded along the \mathbf{G}'_{2D} to the first BZ defined by the \mathbf{x}' and \mathbf{z}' , and the number of bands becomes double. This indicates that bands at R point are folded to Y point. This unit cell transformation in real space corresponds to structural transformation from *Pm $\bar{3}$ m* to *P4/mbm*.

Next, the structural transformation to *Pnma* along *b*-axis is considered. In real space, the

b -axis of $Pnma$ is 2 times longer than before the structural transformation as shown in **Fig. 7-3c** (green). The lattice translation vector $\mathbf{T} = u'_1\mathbf{a}' + u_2\mathbf{b} + u'_3\mathbf{c}'$ changes to $\mathbf{T}' = u'_1\mathbf{a}' + u'_2\mathbf{b}' + u'_3\mathbf{c}'$, where \mathbf{b} and \mathbf{b}' are primitive lattice translation vectors before and after the structural transformation ($\mathbf{b}' = 2\mathbf{b}$), and u_2 and u'_2 are integers. The corresponding BZ size becomes half as displayed in **Fig. 7-3d** (red). The reciprocal lattice vector $\mathbf{G} = n'_1\mathbf{x}' + n_2\mathbf{y} + n'_3\mathbf{z}'$ changes to $\mathbf{G}' = n'_1\mathbf{x}' + n'_2\mathbf{y}' + n'_3\mathbf{z}'$, where \mathbf{y} and \mathbf{y}' are primitive lattice translation vectors before and after the structural transformation ($\mathbf{y}' = \mathbf{y}/2$), and n_2 and n'_2 are integers. This represents that bands at Y point are folded to Γ point through translation operation in reciprocal space. In the inset in **Fig. 7-3e**, BZ of $Pm\bar{3}m$ is shown. Here blue and red arrows represent how the VBM at R point transfers to Γ point through the structural transformations in ac -plane and along b -axis. The resultant band folding is shown in **7-3e**. The VBM at R point is folded firstly to Y point, and finally to Γ point.

Figure 7-4a shows the band structure of SrHfS₃. It is obvious that SrHfS₃ has a direct-type band gap at Γ point owing to the band folding as explained above. Band structures of the other $AEEtMS_3$ are displayed in **Fig. 7-5**. To check whether the optical transition from the CBM to VBM is symmetrically allowed or not, corresponding matrix momentum elements were calculated (**Fig. 7-6**). The finite and large value at Γ point indicates that the band-edge transition is allowed. The calculated effective masses of electron in SrHfS₃ are 0.40, 0.26, and 0.43 m_0 for Γ -X, Γ -Y, and Γ -Z, respectively, while those for hole are 0.70, 0.19, and 0.61 m_0 , where m_0 represents effective mass of free electron. For comparison, the calculated effective masses of other $AEEtMS_3$ are summarized in **Table 7-I**. **Figure 7-4b** shows the density of state (DOS) of SrHfS₃. The conduction band (CB) consists of Hf-5d orbitals and the Sr-4d is located at higher energy than the CB of Hf-5d orbitals. Because Sr-4d orbitals do not hybridize with Hf-5d orbitals, almost CBM is determined only by Hf-5d orbitals. The valence bands (VB) are composed mainly of S-3p orbitals. These results

indicate that electronic structure of CBM (i.e., *d* orbitals of an *eTM*) and VBM (i.e., *p* orbitals of an anion) is as expected.

Figure 7-4c summarizes band alignments of *AEeTMS*₃ and other semiconductors exhibiting both *n*- and *p*-type conductivity. The energy levels of CBM and VBM for conventional semiconductors (i.e., Si and GaAs [13, 14]) are located within the typical doping limit region as shown yellow color area [13]. Note that the energy levels of CBM and VBM of *AEeTMS*₃ are both located around boundary or inside of the limit region, suggesting that *n*- and *p*-type dopings should be possible. The calculated band gaps of CaHfS₃, SrHfS₃, and BaHfS₃ are 2.21, 2.18, and 1.90 eV, respectively, while those of CaZrS₃, SrZrS₃, and BaZrS₃ are respectively 1.95, 1.94, and 1.72 eV, which are close to the calculated values reported in ref. [15]. Results of the band gap calculations for other *AEeTMS*₃ are also summarized in **Table 7-I**. Because the band gaps of *AEHfS*₃ are more suitable for a green emission than the Zr-system, the Hf-system was selected and the optoelectronic properties were investigated.

7.3.2. SrHfS₃ with an appropriate band gap for green-light emission

To examine the optical and carrier transport properties of *AEHfS*₃, the undoped polycrystalline samples were firstly prepared. *AEHfS*₃ was previously prepared via a direct sulfurization of mixture of *AECO*₃ and HfO₂ [16]. However a conventional solid-state reaction using binary sulfide precursors was employed to obtain high-density bulks (the relative density > 80 %), which are advantageous especially for reliable carrier transport property measurements. **Figures 7-7a** and **7-7b** show X-ray diffraction (XRD) patterns of SrHfS₃ and BaHfS₃. They indicate that SrHfS₃ and BaHfS₃ were successfully synthesized, which was crosschecked by the chemical composition analysis using electron micro-probe analyzer. For synthesis of *AE* = Ca, however, CaHfS₃ phase could not be obtained at all by the same method. From the Rietveld analysis on the XRD patterns it was found that major

parts of obtained bulks consist of SrHfS₃ (the purity = 94.0 mol%) and BaHfS₃ (79.1 mol%), and the minor impurities were HfO₂ and AES for both samples. Insets in **Figs. 7-7a** and **7-7b** show photographs of SrHfS₃ and BaHfS₃ polycrystalline bulks. The sample colors are vivid yellow and deep orange for SrHfS₃ and BaHfS₃, respectively. Note that both polycrystalline bulk samples are quite stable in ambient air atmosphere in spite of sulfides.

Then the diffuse reflectance was measured at room temperature in visible – near-infrared wavelength region to examine the optical band gap. The raw spectra of the diffuse reflectance and the Kubelka-Munk plots were displayed in **Figs. 7-8a** and **7-8b**. **Figure 7-9** summarizes calculated and observed optical band gaps of AEHfS₃. Even though calculated band gaps were slightly underestimated, they reproduce well the observed optical band gaps. The observed gaps of SrHfS₃ and BaHfS₃ are respectively 2.32 ($\lambda = 534$ nm) and 2.06 eV ($\lambda = 602$ nm), consistent with the sample colors as shown in inset photographs of **Figs. 7-7a** and **7-7b**. Because the band gaps of SrHfS₃ and BaHfS₃ respectively correspond to green- and orange-light emission wavelengths, hereafter SrHfS₃ is focused on.

7.3.3. *n*- and *p*-type carrier conduction of SrHfS₃

Next electron and hole dopings of SrHfS₃ were performed to examine the carrier controllability (i.e., control of carrier polarity and concentration). Among several candidates of appropriate dopant, La³⁺ (1.16 Å [17]) acting as a donor at Sr²⁺ (1.26 Å [17])-site and P³⁻ (2.12 Å [18]) as acceptor at S²⁻ (1.84 Å [18])-site were chosen due to their close ionic radii with each other. The nominal concentrations of La were set to 0.5, 1, 2, 3, 4, and 6%, while those of P-substitution were 1, 2, 2.5, 3, 4 and 4.5%. Hereafter the doping concentrations are defined as the nominal concentrations.

Before carrier transport property measurements, replacement of La and P with Sr- and S-sites was confirmed by XRD. **Figure 7-10a** shows the doping concentration dependence of the lattice volume (V). Change in each lattice parameter is summarized in **Figs. 7-11a** for *a*-

7-11b for *b*- and 7-11c for *c*-axes. In the case of La substitution, the *V* gradually decreases from 461.43 (undoped) to 461.09 Å³ (6 % La-doped) due to the smaller ionic radius of La than that of Sr. On the other hand in P substitution, the *V* expands up to 461.79 Å³ (4.5 % P-doped) because of the larger ionic radius of P than that of S. This fashion of structure variation suggests that La and P continuously occupy Sr- and S-sites with increase in the doping concentrations, respectively.

Figure 7-10b shows the electrical conductivities at room temperature as a function of each doping concentration. Before the measurements, the ohmic contacts using Au electrodes were confirmed for La- and undoped SrHfS₃, and Pt electrodes for P-doped ones. Although undoped SrHfS₃ exhibited a very low conductivity of $6 \times 10^{-7} \text{ S} \cdot \text{cm}^{-1}$, the conductivities sharply increase via both of La- and P-substitutions. In the La case, the conductivity reaches $7 \times 10^{-1} \text{ S} \cdot \text{cm}^{-1}$ at La 6%; while in the case of P, it does $2 \times 10^{-4} \text{ S} \cdot \text{cm}^{-1}$ at P 4%.

The carrier polarity was checked by thermopower measurements for both La- and P-doped SrHfS₃. The raw data, i.e., detected thermoelectromotive forces (ΔV) as a function of difference in temperature (ΔT), are shown in **Fig. 7-12**. Due probably to the high electrical resistance, the clear linear relation could be not obtained for 1 and 2% P-doped SrHfS₃. **Figure 7-10c** shows Seebeck coefficients obtained from the slopes in **Figs. 7-12**. In whole La- and P-concentrations, negative and positive Seebeck coefficients were observed, respectively, indicating that La- and P-substitutions effectively supply electron and hole into SrHfS₃. The negative Seebeck coefficients vary from -450 up to $-230 \mu\text{V/K}$ with increase in La concentration from 0.5 to 6 %, while the positive ones do from $+880$ to $+60 \mu\text{V/K}$ with P concentration from 2.5 to 4.5 %, implying that carrier concentration would increase with increase in doping levels. The above results of electrical conductivity and Seebeck coefficients represent that carriers are continuously and widely activated along with change

in the cell volumes and the doping concentrations. These electronic transport properties demonstrate the good controllability of the carrier polarity as well as the concentrations in SrHfS₃ by intentional impurity doping.

7.3.4. Intense green luminescence of SrHfS₃

Finally photoluminescence (PL) measurements were performed to examine the optical properties. **Figure 7-13a** shows PL spectra of undoped SrHfS₃ at 30 – 300 K. SrHfS₃ exhibited intense green emissions (peaking at $E = 2.37$ eV, $\lambda = 523$ nm at 300 K) at entire temperatures measured, where no other emission peaks were detected. It was confirmed that the emission photon energy at 300 K agrees well with band gap energy estimated from diffuse reflectance (2.32 eV, see **Figs. 7-8** and **7-9**). The full width at half maxima were 0.18 and 0.25 eV at 30 and 300 K, respectively. Note that the green emission could be seen by human eyes even at room temperature (i.e., 300 K) as shown in an inset picture of **Fig. 7-13a**, suggesting that the quantum efficiency of emission should be high. To elucidate the origin of the emission, the variation in the peak energy was investigated at different temperature and constructed the decay curve. **Figure 7-13b** shows the temperature dependence of the emission peak energy. The energy increases from 2.37 at 300 to 2.40 eV at 30 K; i.e., a blue shift clearly is observed and the shift is well reproduced using an empirical model for band edge [19]. From the decay curves the emission lifetime was estimated to be 7.6 at 300 K and 3.7 ns. at 30 K (see **Fig. 7-14**), which were comparable or shorter than a detection limit of PL measurement system used (i.e., pulse width of the excitation laser is 7–8 ns.). This result indicates that the actual life time of the emission is shorter than 7 ns. These results strongly support that this intense emission originates from a band-to-band transition and/or an exciton. Indeed, *eTM*-based compounds are more ionic than *pTM*-based ones due to their lower electron negativity of *eTM* than *pTM*. Also, the electron effective mass of *d*-orbital in *eTM* is usually heavier than that of *s*-orbital in *pTM*.

These intrinsic nature of *eTM*-based semiconductors would be related to the efficient and bright emission, because both the ionicity and heavy electron effective mass are essence to enhance the exciton binding energy. Furthermore any other emissions in band gap (e.g., donor-acceptor pair emission) were not detected, suggesting that amount of defects should be very low even in polycrystalline sample owing probably to the stable valence state of *eTM* as expected. This result is consistent with the quite low electrical conductivity ($6 \times 10^{-7} \text{ S} \cdot \text{cm}^{-1}$) of the undoped SrHfS₃ (**Fig. 7-10b**).

PL behaviors of doped samples were then investigated to clarify the potential for electroluminescence materials. **Figure 7-13c** summarizes room temperature PL spectra of doped (6 % for La and 4 % for P) and undoped SrHfS₃. In both of La- and P-doped SrHfS₃, only the band-edge and/or exciton emissions, similar to the undoped SrHfS₃, were observed even at the high doping concentrations. Also at other doping concentrations, similar emission spectra were observed as shown in **Figs. 7-15a** (La-doping) and **7-15b** (P-doping). Moreover in all doped samples, the green emissions were detected by human eyes at room temperature. It is noteworthy that highly doped carriers of electron or hole do not quench the emission. These features denote that SrHfS₃ can effectively emit green light even under the carrier-doped states.

7.4. Conclusion

I explored candidate compounds for green-emitting electron- and hole-dopable semiconductors. In order to achieve good carrier dopability and controllability, *eTM*-based cubic perovskites were firstly focused on, in which the high and stable valence state of *eTM* cation makes the carrier controllability easy, and the deep non-bonding *d*-orbitals of *eTM* and shallow *p*-orbitals of anion enable electron- and hole-doping, respectively. To obtain the direct band gap in the perovskites, the band folding scheme was applied to fold bands at zone boundary to zone center. An appropriate superstructure was constructed by introduction

distortion in the perovskites derived from chemical pressure (i.e., selection of constituents), leading to stimulation of the band folding. From the screening using the first-principles calculations, it was identified that AEHfS₃ has an optimum, allowed band gap for green emission and appropriate band alignment to *n*- and *p*-type dopings. The experimentally estimated optical band gaps of synthesized SrHfS₃ and BaHfS₃ were 2.3 eV ($\lambda = 534$ nm) and 2.1 eV, corresponding to green and orange colors, respectively. The electrical conductivities of SrHfS₃ were sharply and widely changed from 6×10^{-7} S·cm⁻¹ at 0 % to 7×10^{-1} S·cm⁻¹ at La³⁺ 6 % doping and 2×10^{-4} S·cm⁻¹ at P³⁻ 4 %. The Seebeck effect measurements confirmed that the substituting La³⁺ for Sr²⁺-site successfully introduced *n*-type carriers, while the P³⁻ substitution for S²⁻-site exhibit *p*-type conductivity. From the PL measurements, SrHfS₃ exhibited the intense green PL at all observed temperatures (30–300 K), which originates from band-to-band transition and/or an exciton. The PL could be seen by human eyes even at room temperature and under carrier-doped states. Furthermore other emissions could not be detected other than the green emission even under doped conditions, suggesting that SrHfS₃ should be strong against defects. These electronic and optical properties reveal that SrHfS₃ is a promising candidate for novel green light-emitting semiconductor.

References

1. J. Y. Tsao, M. H. Crawford, M. E. Coltrin, A. J. Fischer, D. D. Koleske, G. S. Subramania, G. T. Wang, J. J. Wierer, and R. F. Karlicek Jr, *Adv. Opt. Mater.*, **2**, 809–836 (2014).
2. K. P. O'Donnell, M. Auf der Maur, A. Di Carlo, K. Lorenz, and the SORBET consortium. *Phys. Status Solidi-Rapid Res. Lett.*, **6**, 49–52 (2012).
3. M. Auf der Maur, A. Pecchia, G. Penazzi, W. Rodrigues, and A. Di Carlo, *Phys. Rev.*

- Lett.*, **116**, 027401 (2016).
4. H. Mizoguchi, T. Kamiya, S. Matsuishi, and H. Hosono, *Nat. Commun.*, **2**, 470 (2011).
 5. T. Arai, S. Iimura, J. Kim, Y. Toda, S. Ueda, and H. Hosono, *J. Am. Chem. Soc.*, **139**, 17175–17180 (2017).
 6. T. Arai, S. Iimura, and H. Hosono, *Chem. Mater.*, **30**, 597–601 (2018).
 7. A. Togo, F. Oba, I. Tanaka, and K. Tatsumi, *Phys. Rev. B*, **74**, 195128 (2006).
 8. H. Raebiger, S. Lany, and A. Zunger, *Phys. Rev. B*, **76**, 045209 (2007).
 9. J. Pohl, and K. Albe, *Phys. Rev. B*, **87**, 245203 (2013).
 10. R. A. Hoffmann, *Rev. Mod. Phys.*, **60**, 601 (1988).
 11. J. K. Burdett, *Prog. Solid State Chem.*, **15**, 173–255 (1984).
 12. V. M. Goldschmidt, *Naturwissenschaften*, **14**, 477–485 (1926).
 13. H. Hosono, *Jpn. J. Appl. Phys.*, **52**, 090001 (2013).
 14. W. Mönch, *Semiconductor Surfaces and Interfaces*. Springer, Berlin (2001).
 15. Y. Y. Sun, M. L. Agiorgousis, P. Zhang, and S. Zhang, *Nano Lett.*, **15**, 581–585 (2015).
 16. R. Lelieveld, and D. J. W. IJdo, *Acta Cryst. B*, **36**, 2223–2226 (1980).
 17. R. D. Shannon, *Acta Cryst. A*, **32**, 751–767 (1976).
 18. L. Pauling, *The Nature of the Chemical Bond*, 3rd Edn. Cornell University Press, N. Y. (1960).
 19. Y. P. Varshni, *Physica*, **34**, 149–154 (1967).
 20. J. Heyd, G. E. Scuseria, and M. Ernzerhof, *J. Chem. Phys.*, **118**, 8207 (2003).
 21. A. A. Mostofi, J. Yates, Y. S. Lee, I. Souza, D. Vanderbilt, and N. Marzari, *Comput. Phys. Commun.*, **178**, 685–699 (2008).
 22. Bruker AXS. TOPAS version 4.2: General profile and structure analysis software for powder diffraction data. (Bruker AXS, Karlsruhe, Germany, 2009).

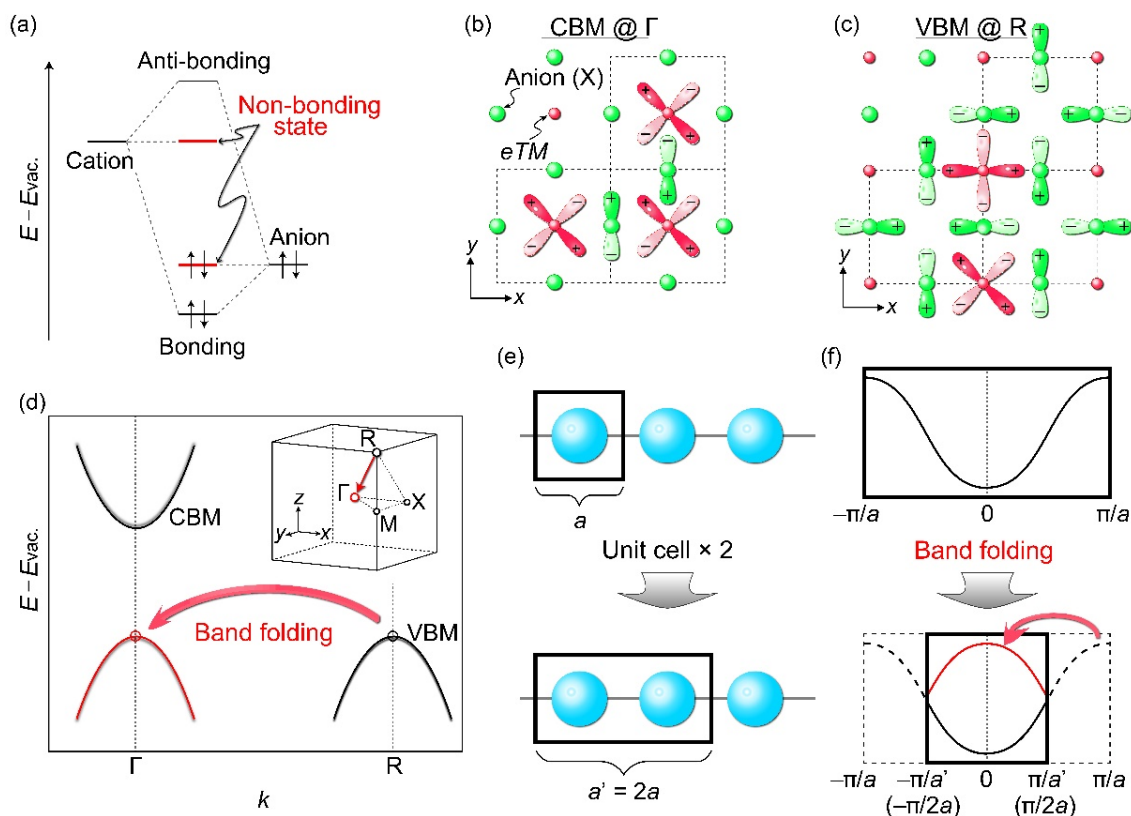


Figure 7-1. Design of n - and p -type dopable semiconductors with direct band gaps in eTM -based perovskite-type compounds. (a) Schematic energy diagram of diatomic molecule. The configurations of non-bonding (b) d -orbitals at Γ point and (c) p -orbitals at R point in cubic perovskite-type structure. The former constitutes CBM, while the later does VBM. Red clover-leaves and green dumbbells represent d -orbitals of eTM and p -orbitals of X (anion), respectively. (d) A schematic band structure of cubic perovskite-type compounds. Black solid curves denote their bands at CBM and VBM. Red one at Γ point is a band transferred from R point after band folding. The inset illustrates the BZ of primitive cubic cell. (e) Two different unit cells in one-dimensional s -orbital chain containing one orbital (top) and two orbitals (bottom). (f) The band structures of one-orbital unit cell (top) and two-orbital unit cell (bottom). For the two-orbital model, bands in the second BZ are folded back to the first BZ of one-orbital model.

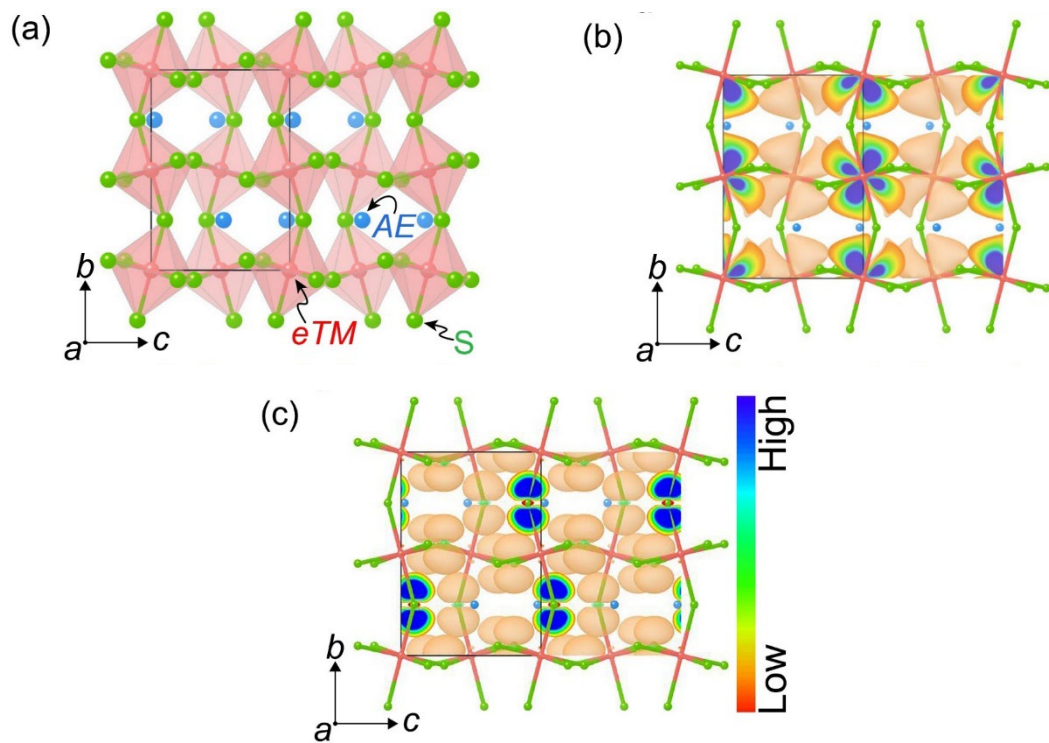


Figure 7-2. Electronic structures of AEEtMS_3 . (a) Crystal structure of orthorhombic perovskite-type sulfide AEEtMS_3 . Blue, red, and green spheres correspond to AE , eTM , and sulfur ions, respectively. Charge density maps at (b) CBM and (c) VBM of SrHfS_3 calculated using HSE hybrid-functional. Vertical color scale bar indicates an intensity of the charge density.

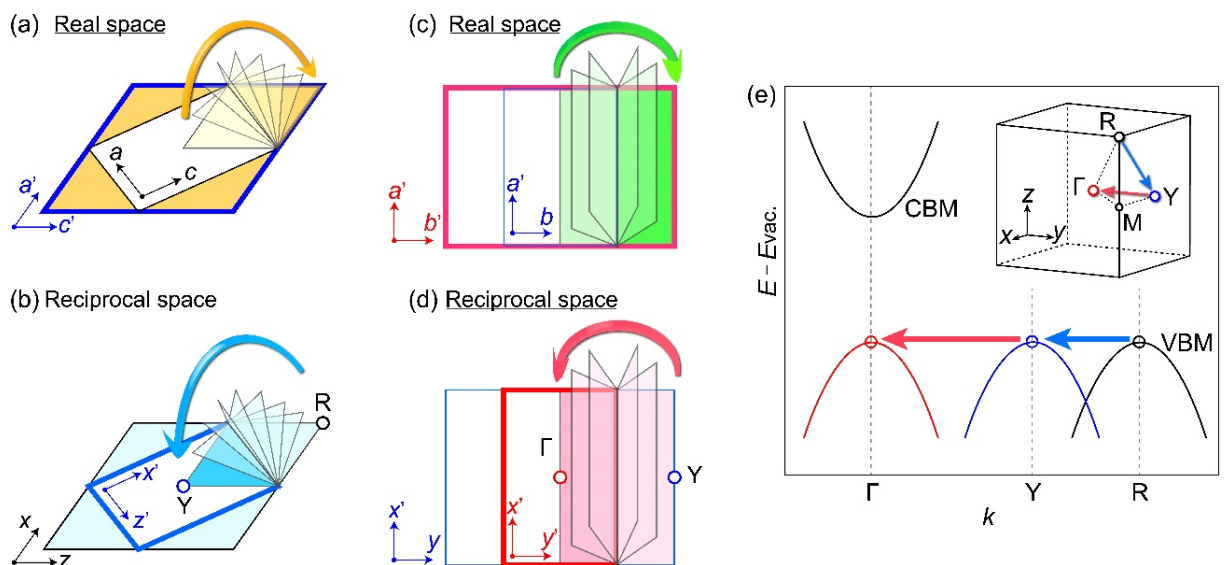


Figure 7-3. Band folding via structural transformation in perovskite from cubic $Pm\bar{3}m$ to orthorhombic $Pnma$. (a) Construction of $\sqrt{2} \times \sqrt{2}$ superstructure for ac -plane in real space and (b) the corresponding reciprocal lattice folding. (c) Unit cell doubling along b -axis and (d) folded BZ. (e) Band folding attributed to structure transformation in (a) and (c).

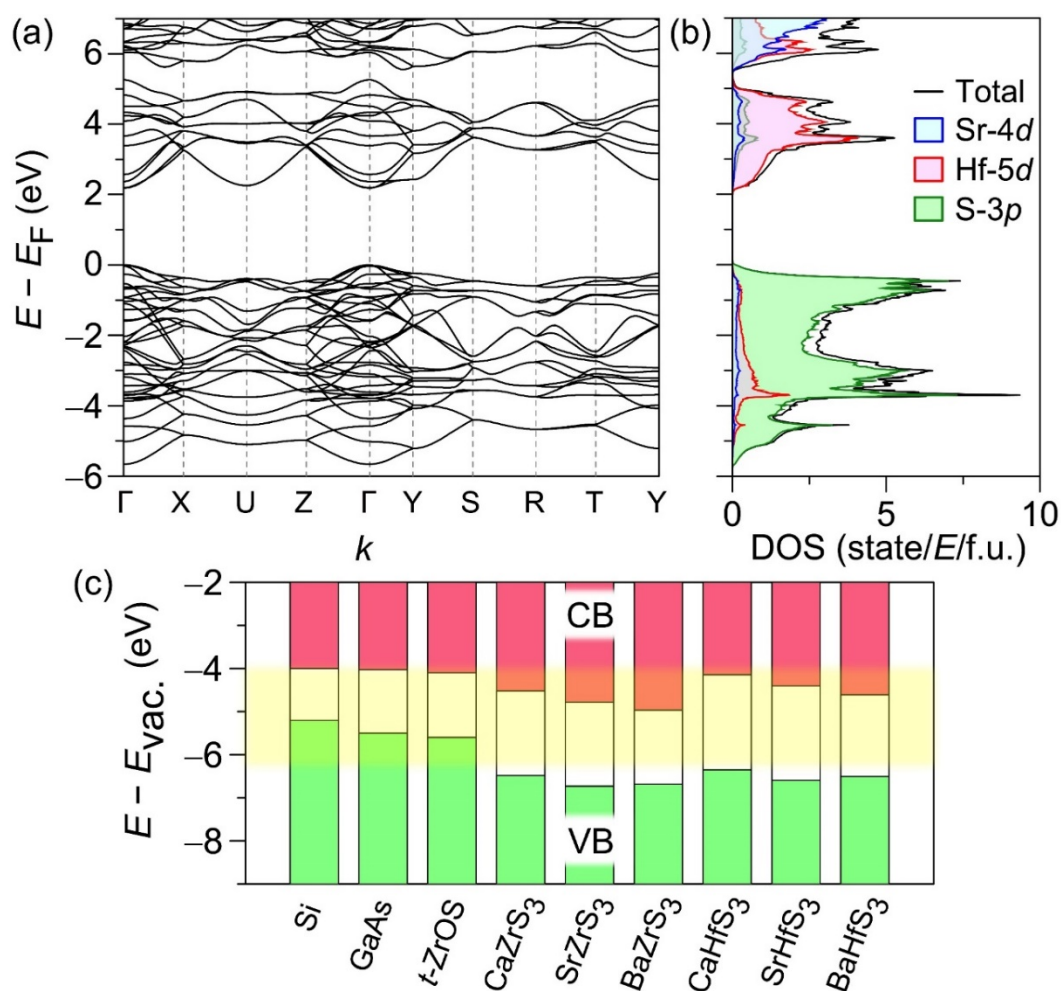


Figure 7-4. (a) A band structure of SrHfS₃ projected by maximally localized Wannier functions. (b) The density of states (DOS). Black, blue, red, and green lines correspond to total DOS and contributions from Sr 4d-, Hf 5d-, S 3p-orbitals, respectively. (c) Band alignment of $AEEtMS_3$ and three n - and p -type dopable semiconductors. Except $AEEtMS_3$, all data are experimental results taken from [5, 13, 14]. The yellow color area denotes a conventional carrier dopable range located from ~ -4 to -6 eV with respect to E_{vac} . [13].

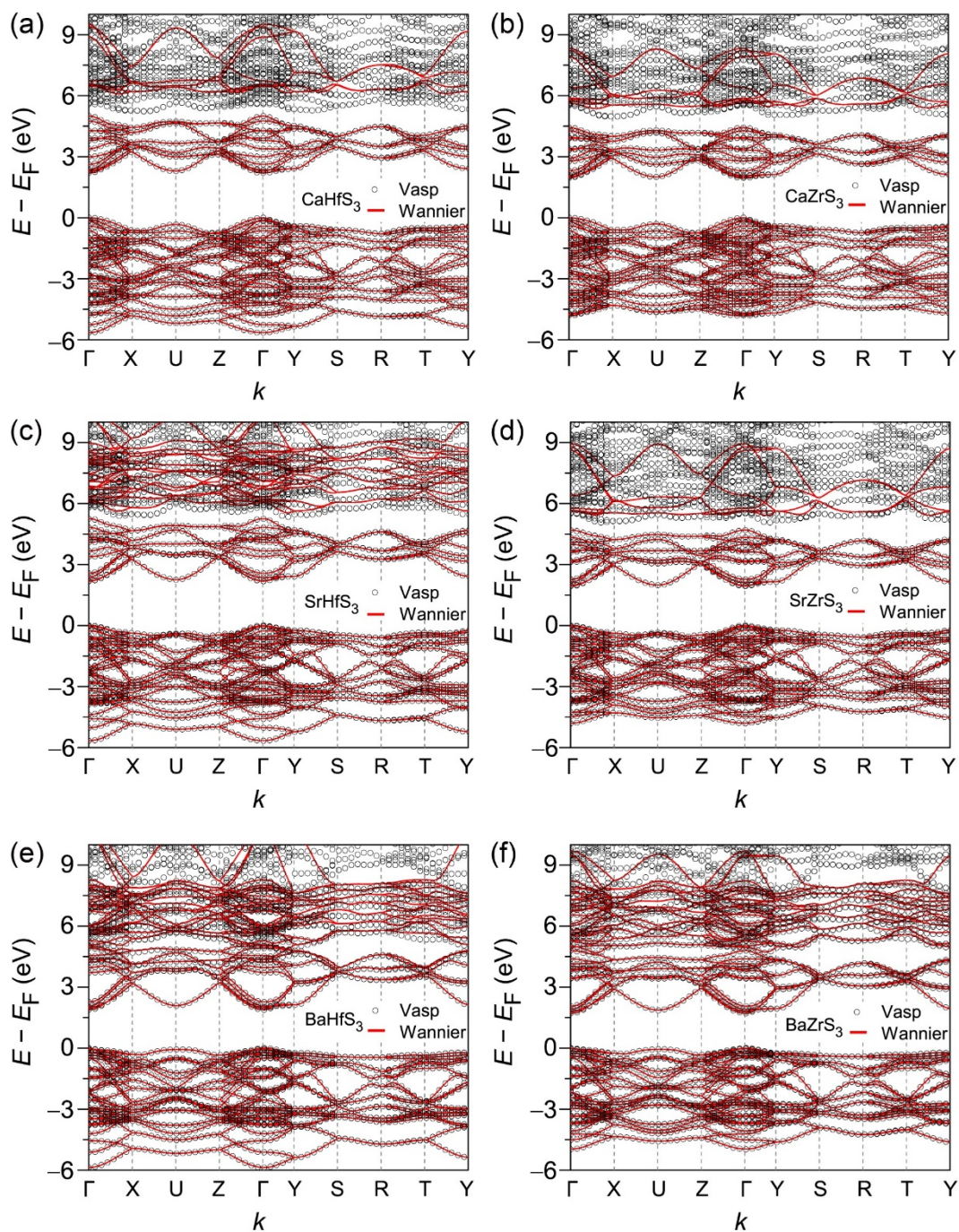


Figure 7-5. Band structures of $AEEtMS_3$. **7-5a**, **7-5c** and **7-5e** denote those of $AHfS_3$, where $AE = Ca, Sr$ and Ba , respectively; whereas **7-5b**, **7-5d** and **7-5f** correspond to $AZrS_3$ ($AE = Ca, Sr$ and Ba , respectively). Black circles are results of band structure calculations of $AEEtMS_3$ using vasp code, while red lines are computed using Wannier interpolation.

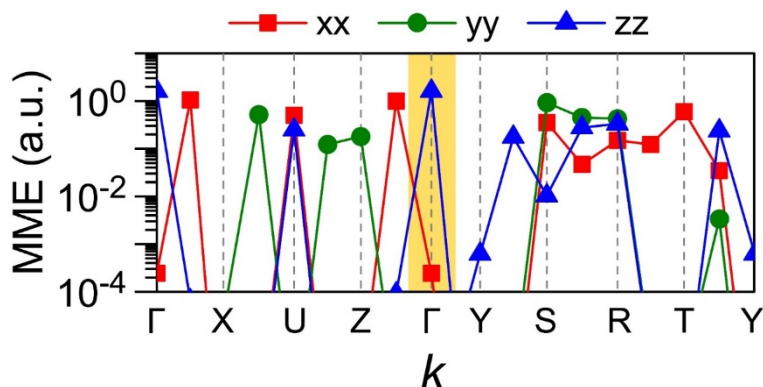


Figure 7-6. Calculated momentum matrix elements (MME) from the valence band edge to conduction band edge of SrHfS₃ at each k point.

Table 7-I. Calculated effective masses and band gaps of $AEeTMS_3$.

| | $m_e^*(m_0)$ | | | $m_h^*(m_0)$ | | | E_g (eV) |
|--------------------|--------------|------------|------------|--------------|------------|------------|------------|
| | $\Gamma-X$ | $\Gamma-Y$ | $\Gamma-Z$ | $\Gamma-X$ | $\Gamma-Y$ | $\Gamma-Z$ | |
| CaHfS ₃ | 0.30 | 0.51 | 0.46 | 0.78 | 0.18 | 0.62 | 2.21 |
| SrHfS ₃ | 0.40 | 0.26 | 0.43 | 0.70 | 0.19 | 0.61 | 2.18 |
| BaHfS ₃ | 0.31 | 0.19 | 0.39 | 0.19 | 0.69 | 0.56 | 1.90 |
| CaZrS ₃ | 0.31 | 0.60 | 0.48 | 0.85 | 0.18 | 0.61 | 1.95 |
| SrZrS ₃ | 0.41 | 0.26 | 0.44 | 0.75 | 0.19 | 0.61 | 1.94 |
| BaZrS ₃ | 0.33 | 0.20 | 0.41 | 0.19 | 0.70 | 0.52 | 1.72 |

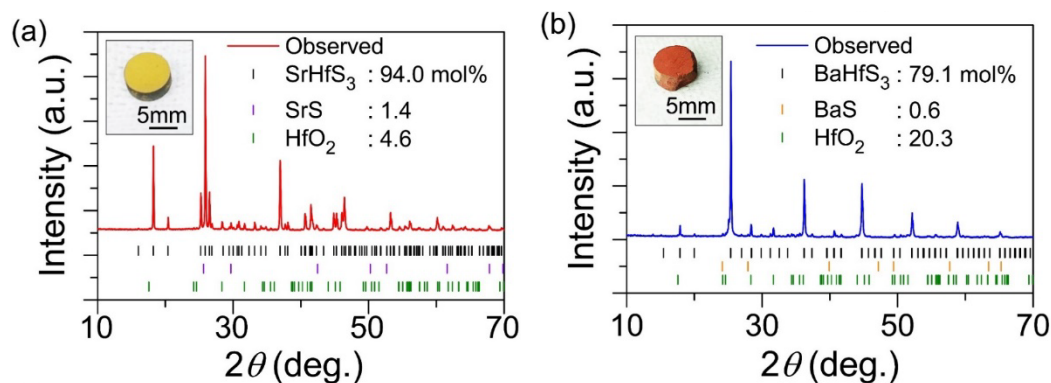


Figure 7-7. XRD patterns of (a) SrHfS₃ and (b) BaHfS₃. Each inset is a photo of the polycrystalline bulk.

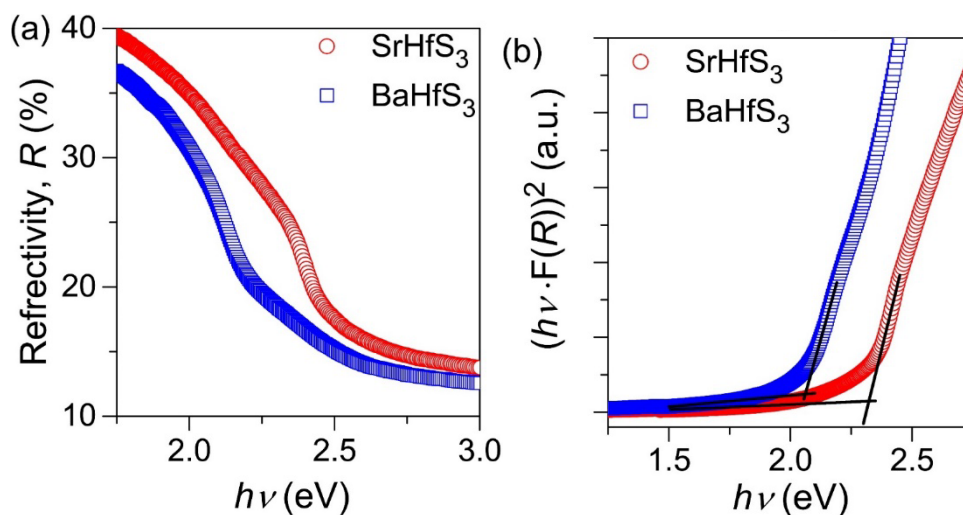


Figure 7-8. (a) Diffuse reflectance spectra and (b) the Kubelka-Munk plot of SrHfS₃ (red circles) and BaHfS₃ (blue squares). A transformation was performed by using an equation; $F(R) = (1-R)^2/2R = K/S$, where K and S indicate optical absorption and scattering coefficients, respectively. Linear lines in (b) are results of the least-square fittings.

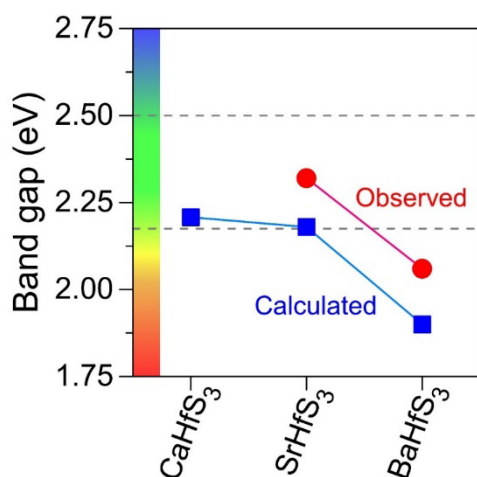


Figure 7-9. Optical band gaps of AEHfS_3 . Red circles and blue squares represent observed optical and calculated band gaps, respectively. Vertical color bar represents colors of the absorbed light. The raw diffuse reflectance spectra were shown in **Fig. 7-8**. The dashed lines indicate green light region, which is the main target of this study.

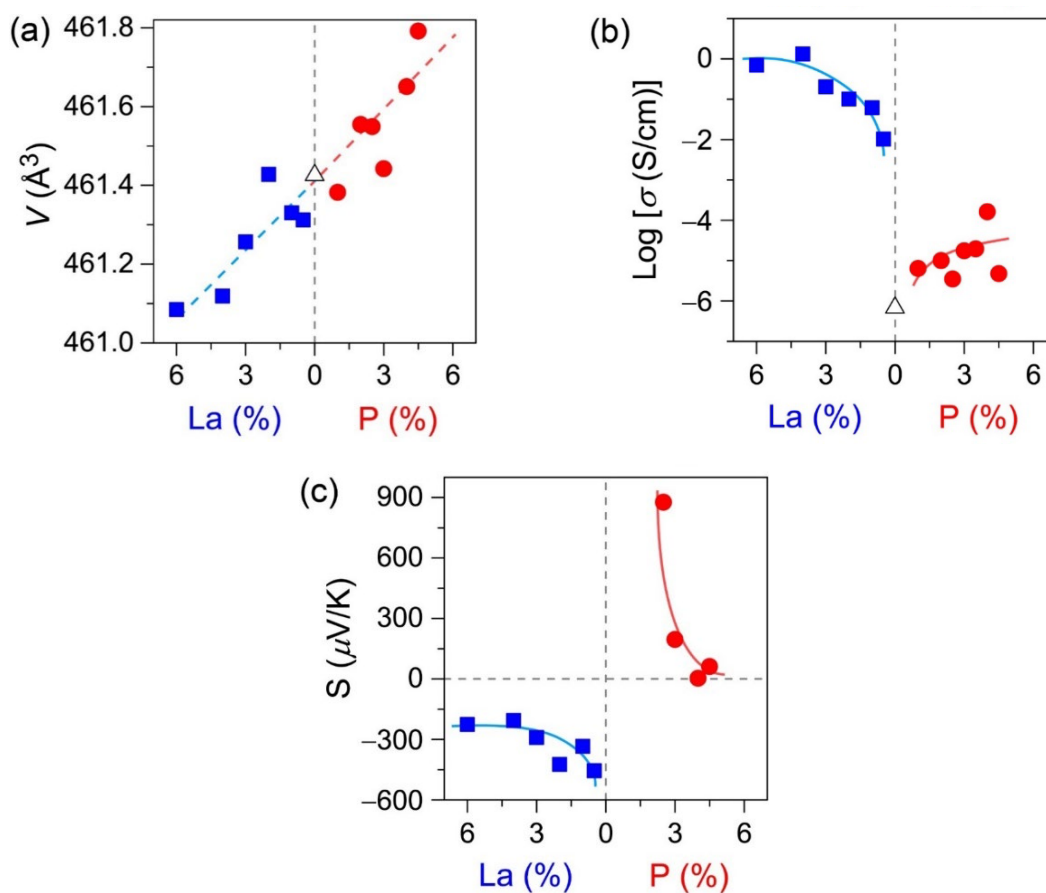


Figure 7-10. Electron- and hole-doping effects on SrHfS₃. (a) Lattice volume (V), (b) electric conductivity (σ), and (c) Seebeck coefficients (S) of La- (blue squares), P- (red circles), and undoped (black triangle) SrHfS₃. Horizontal axis represents nominal doping concentrations of La and P. All these measurements were performed at room temperature. The V was calculated from each axis lattice parameter shown in **Fig. 7-11**.

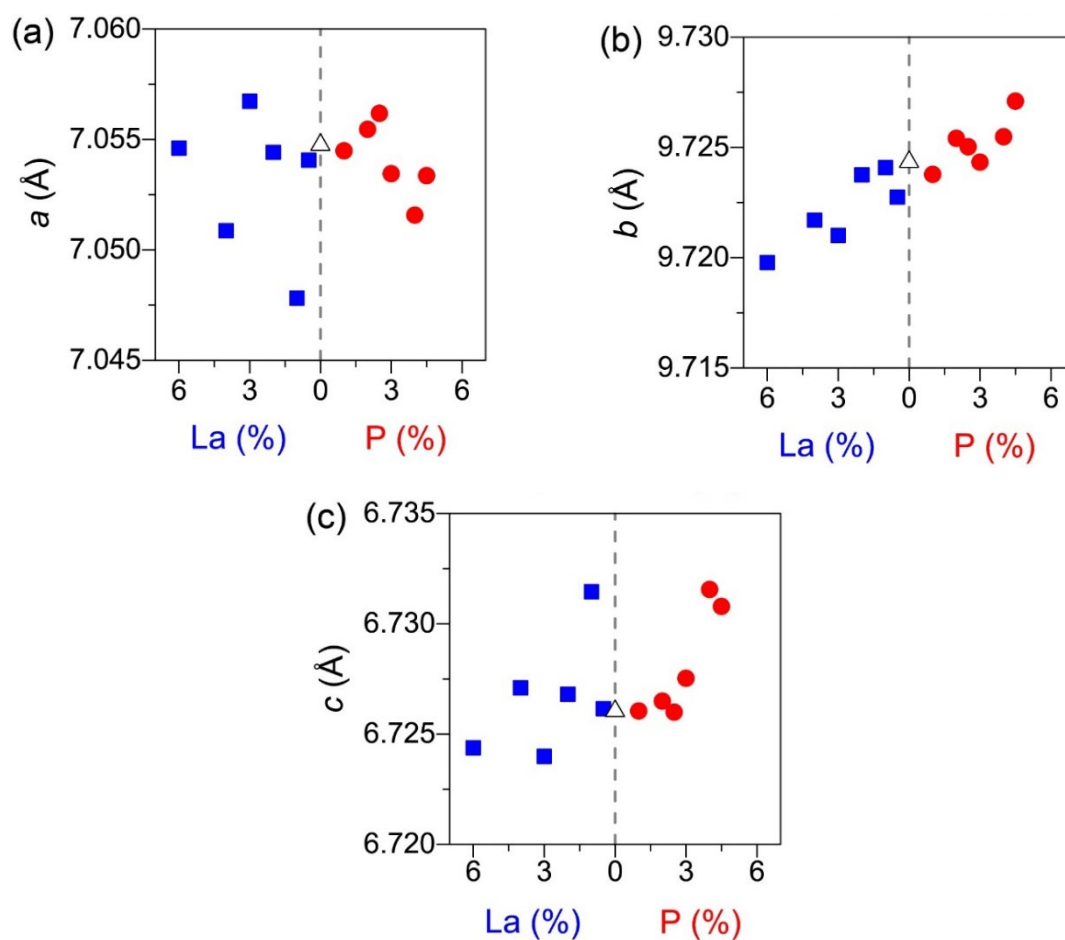


Figure 7-11. (a) a -, (b) b - and (c) c -axes lattice parameter variations in SrHfS₃ via La- (blue squares) and P-dopings (red circles). The horizontal axis denotes nominal La- and P-doping concentrations.

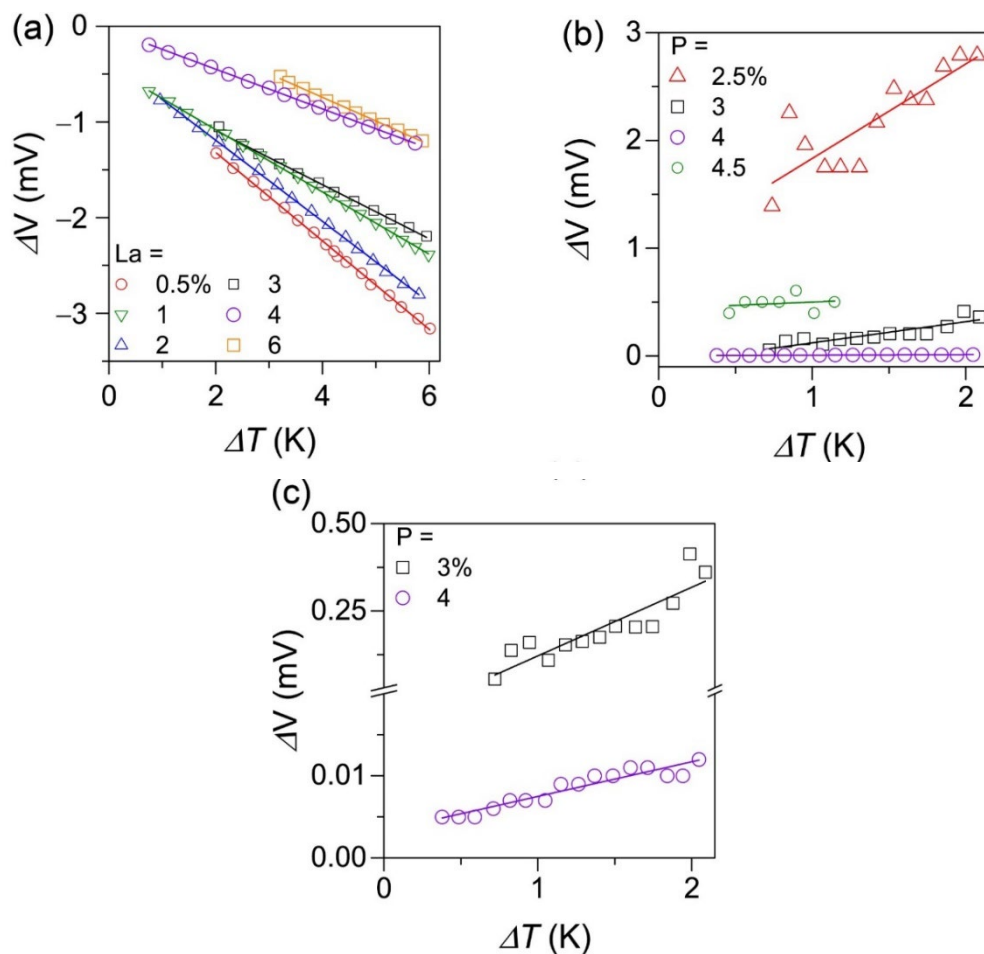


Figure 7-12. Thermopower measurement of (a) La- and (b) P-doped SrHfS₃ as a function of nominal doping concentrations. (c) The enlarged plots of for 3 and 4 % P-doped samples shown in (b). The least-square fitting results are delineated as straight lines.

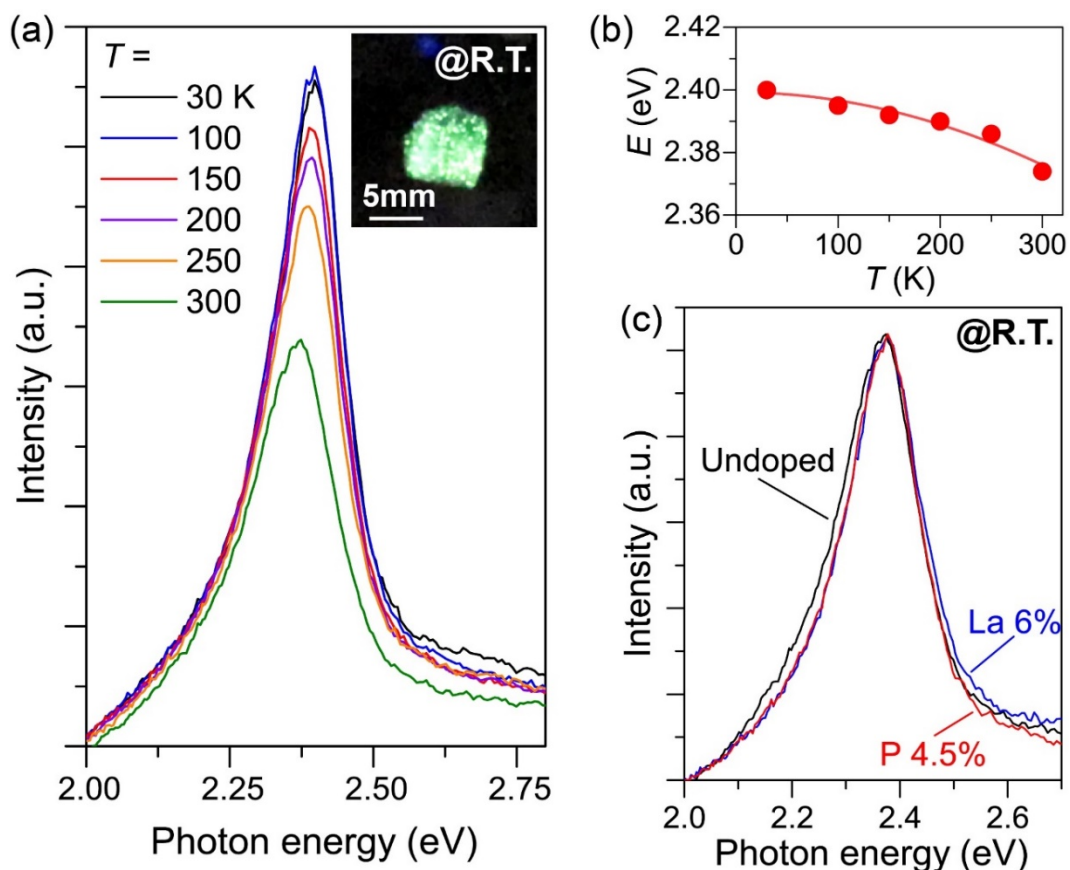


Figure 7-13. Optical emission properties of doped and undoped SrHfS₃. (a) Photoluminescence (PL) spectra of undoped SrHfS₃ observed at 30–300 K. The inset is a picture of undoped SrHfS₃ excited at room temperature. (b) The temperature dependence of emission peak top energies. Red line is a fitting result using following equation; $E_g = E_0 - \alpha T^2 / (T + \beta)$, where E_0 is an E_g at 0 K and α and β denote material constants [19]. (c) PL spectra of La 6%- (blue), P 4.5%- (red), and undoped (black) SrHfS₃ at 300 K.

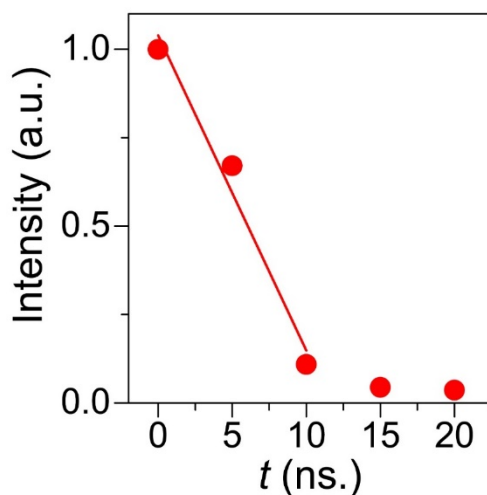


Figure 7-14. Decay curve of undoped SrHfS₃ at 30 K. Red line is a result of the least-square fitting for single-decay model emission lifetime.

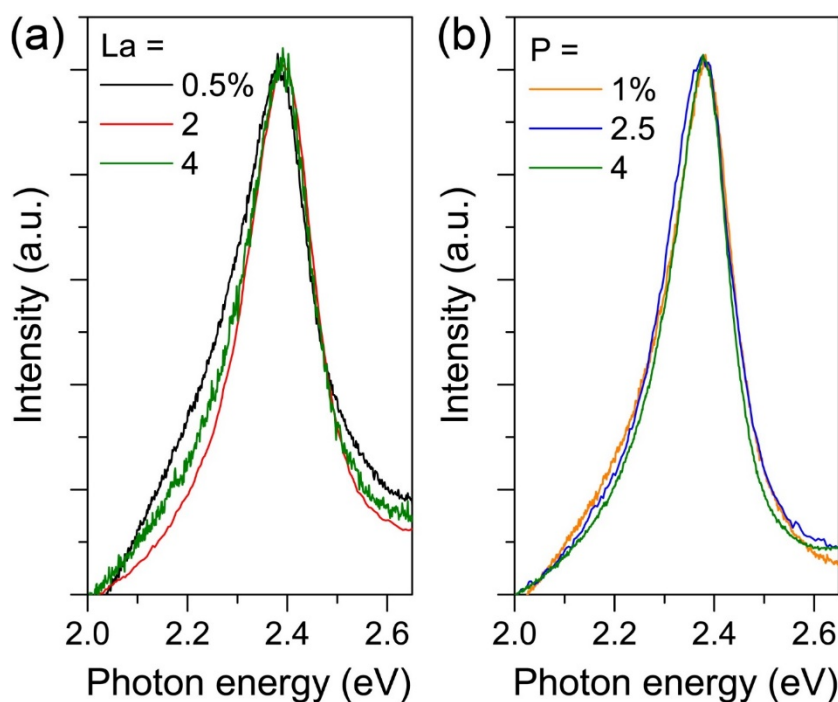


Figure 7-15. Photoluminescence (PL) spectra of (a) La- and (b) P-doped SrHfS₃ taken at 300 K. Black, red and green lines in (a) correspond to PL spectra at La-doping concentrations of 0.5, 2 and 4 %, respectively. Orange, blue and green lines denote PL spectra of 1, 2.5, and 4 % P-doped SrHfS₃.

Chapter 8. Heteroepitaxial Growth of Perovskite-Sulfide Semiconductor $AEHfS_3$ ($AE = Sr$ and Ba)

8.1. Motivation for Fabrication of $AEHfS_3$ Epitaxial Thin Film

In Chapter 7, a materials design concept for n - and p -type dopable light-emitting semiconductors was proposed to overcome a serious “green gap problem,” in which the quantum efficiency of a green emission in GaN- and GaAs-based light emitting diodes (LED) drastically drops ($\sim 15\%$) irrespective of the highly efficient blue and red emissions [1, 2]. The concept contains three strategies about: (i) the suppression of defect formation [3, 4], (ii) the formation of an appropriate band alignment for both n - and p -type dopings [3–5], and (iii) the realization of a direct band gap [6, 7]. Through a materials exploration based on the concept, eTM -based perovskite-sulfide $AEeTMS_3$ ($AE =$ alkali earth metal, $eTM = Zr$ and Hf) was selected as the candidates. Then, the expected optical and electrical properties were experimentally validated in polycrystalline $SrHfS_3$ [8].

For further evaluation of the optoelectronic properties, a single crystalline sample is necessary because the grain boundary in the polycrystalline bulk hinders the intrinsic characteristics due to e.g., trapping conducting carrier and quenching the luminescence. Even though the epitaxial thin film is apparently like the single crystal, they have an advantage in electronic characterization; i.e., the ability to fabricate an optoelectronic device. Semiconductor thin films are essential for current optoelectronic devices; e.g., thin film transistors, LEDs, laser diodes, and solar cells. Almost all these devices are constructed by stacking multilayered semiconductors and the post microfabrication. For example, LEDs and laser diodes are basically composed of pn -junction [9] or $p-i-n$ -junction [10], leading to an observation of the electroluminescence.

Therefore, in this **Chapter**, epitaxial thin films of $AEHfS_3$ ($AE = Sr$ and Ba) are fabricated by one of the thin films growth processes, the pulsed laser deposition (PLD) technique, and the optical properties are characterized as an initial stage for the fabrication of the multilayer devices.

8.2. Experimental Procedure

8.2.1. PLD growth of $AEHfS_3$ epitaxial thin films

PLD, in a combination vacuum chamber of PLD and molecular beam epitaxy, was used to fabricate ~ 25 nm-thick $AEHfS_3$ thin films. The base pressure is $< 1 \times 10^{-7}$ Pa. 10 Hz KrF excimer laser (wavelength = 248 nm) was utilized to ablate PLD targets composed of polycrystalline dense $AEHfS_3$ disc (relative density is > 80 %). S was evaporated from a cracking effusion-cell to maintain a high-S partial pressure during the thin film growth. The growth rate (R_g) varied from 0.4 to 13 nm/min. Four kinds of (001)-oriented single crystalline substrates were employed as substrates: Y-stabilized ZrO_2 (YSZ), $(LaAlO_3)_{0.3}(Sr_2AlTaO_6)_{0.7}$ (LSAT), $SrTiO_3$ (STO), and $LaAlO_3$ (LAO). To obtain an atomically flat surface, YSZ and LSAT were preliminarily annealed at 1350, 800 °C in air. For STO, wet etching with buffered HF solution [11] was performed. Then, STO was thermally annealed at 1050 °C in air. In contrast, LAO was used without any preliminary treatment. The substrates were heated by an infrared laser during the deposition and the temperature (T_s) was set from 450 to 1150 °C. After the deposition, the S-molecular beam was supplied until the T_s reached ~ 100 °C.

8.2.2. Structure parameter analysis

Crystal structure and segregated impurity phase were characterized by X-ray diffraction (XRD, source: $Cu K\alpha$ radiation) with Bragg-Brentano geometry. High-resolution XRD monochromated through a two-bounds Ge crystal was utilized to determine the lattice parameters precisely. The thicknesses of the obtained films were determined by X-ray

reflectivity analysis. The chemical composition of the thin film was evaluated by X-ray fluorescence analysis.

8.2.3. Optical measurements

Photoluminescence (PL) measurement was performed for bulk $BaHfS_3$ with third harmonic Nd-doped YAG laser as an excitation source ($\lambda = 355$ nm). To examine the origin of the PL, temperature dependence of the PL spectra was measured between 30K and room temperature. The transmittance spectra of the obtained $AEHfS_3$ thin film were taken to determine the band gaps between 10 K and room temperature precisely. The measured wavelength ranges were set from 200 to 800 nm.

8.2.4. Auger electron spectroscopy

Auger electron spectroscopy (AES) was employed to investigate O contamination in the obtained $AEHfS_3$ films. Due to the high resistance of the thin films, Ar ion neutralizer was used during measurements. The depth profiles were taken through excavating the thin film by Ar milling.

8.3. Results and Discussion

8.3.1. Epitaxial growth of $SrHfS_3$ thin film

Prior to the fabrication of epitaxial $SrHfS_3$ thin films, the effectiveness of the employed S source in the PLD growth was validated, because a lack of an additional anion source sometime causes formation of anion vacancy in a compound semiconductor thin film. In the case of oxide, precisely controlled oxygen gas [12–14], RF-oxygen plasma [15, 16], or ozone gas [17, 18] is generally introduced into a vacuum growth chamber during the thin film growth to avoid the formation of oxygen vacancy. Also, during the thin film growth of sulfide, H_2S is generally introduced to supply additional S. [19–21]. However, referring to a paper about the calculation of thin film growth condition of $AETMS_3$ [22], it was claimed that very low total pressure is essential to obtain a pure $SrHfS_3$ thin film; otherwise an impurity SrS

appears. Although H_2S gas is effective in increasing the chemical pressure of S owing to the reactivity of the decomposed S^{2-} , it is hard to actualize very low total pressure. Thus, a S-molecular beam supplied from a cracking effusion cell was selected in this study due to the controllability of the evaporated flux and narrow spatial expansion of the beam, resulting in a higher vacuum level of $< 1 \times 10^{-5}$ Pa during the thin film growth.

First, the effectiveness of the S beam was examined through the comparison of $SrHfS_3$ thin films fabricated with or without the S source. $SrHfS_3$ thin film deposited without any S-source colors black and the electric conduction was confirmed, which should originate from a S-vacancy (**Fig. 8-1**). In contrast, the film deposited under the S-beam exhibited a transparent yellow color and insulating electric transport property. Moreover, it was found that the amount of S in the film deposited under the additional S source is 10 % higher than that without a S source. These results briefly prove that the S-molecular beam effectively supplied S into $SrHfS_3$ and filled in the vacancy during the thin film growth. Hereafter, all films were fabricated under S-molecular beam.

Even though a polycrystalline $AEHfS_3$ bulk is synthesized via a conventional solid-state reaction [8], the reaction temperature is relatively severe; the $SrHfS_3$ cannot form when the synthesis temperature is lower than 1000 °C, irrespective of the optimum synthesis temperature of 1100 °C. Thus, the influence of the substrate temperature (T_s) was investigated on the LAO substrate, where R_g was set to 8 nm/min. **Figure 8-2** shows XRD patterns as a function of T_s . In a case of $T_s \leq 700$ °C, any crystalline phase was not detected; while $T_s \geq 1150$ °C, SrS, HfS_2 , HfS, and unidentified impurities were segregated. At $T_s \approx 1000$ °C, *b*-axis oriented $SrHfS_3$ successfully grew. Hence, it was concluded that optimum T_s is around 1000 °C for $SrHfS_3$. Although the crystalline $SrHfS_3$ is obtained, many segregated impurities were confirmed, even at the optimum T_s . The minor impurities were still unidentified; whereas the major impurities were SrS and HfS_x , which are the same as

the precursors of the polycrystalline bulk synthesis.

Since these remaining components suggest that R_g is not optimum, $SrHfS_3$ thin films were fabricated at different R_g tuned by changing the ablation laser fluence at the optimized T_s . **Figure 8-3** summarizes the XRD patterns of $SrHfS_3$ thin films grown at various R_g . At R_g higher than 13 nm/min, $SrHfS_3$ phase did not nucleate at all, and SrS and HfS_x phases appeared with tiny unidentified impurity phases. On the other hand, too low R_g contributed to the formation of a pure SrS . $SrHfS_3$ phase was obtained at R_g between 5 and 8 nm/min. Accordingly, an optimum growth condition is provisionally concluded as $R_g = \sim 5$ nm/min and $T_s = 1050$ °C. The growth window of $SrHfS_3$ is depicted in **Fig. 8-4**. It is obvious that an area, in which $SrHfS_3$ can nucleate, is very small for both T_s and R_g . Furthermore, the single phase was not obtained, implying that other thin film growth techniques, such as molecular beam epitaxy, would be inevitable to obtain the pure single phase.

Even though $SrHfS_3$ film grown at the optimum condition contained impurity phases, the detailed structure analysis was performed. **Figure 8-5** summarizes the in-plane XRD measurements. a -, b -, and c -axes lattice parameters of bulk $SrHfS_3$ are 7.0582, 9.7241, 6.7241 Å, respectively; while that of LAO is 5.360 Å and 45°-rotated LAO lattice is 3.790 Å, indicating that $SrHfS_3$ should grow on LAO with 45° in-plane rotation. **Figure 8-5a** shows the result of $2\theta_\chi/\phi$ scan along LAO [100] and LAO [110] planes. It was confirmed that $SrHfS_3$ [101] and [202] planes are parallel to LAO [100], representing that $SrHfS_3$ grew with in-plane 45°-rotation with respect to the unit cell of LAO. **Figure 8-5b** is an enlarged image of **Fig. 8-5a** from $2\theta = 20$ to 35° . Here, it should be noted that $SrHfS_3$ 200 and 002 diffractions apparently located at the same 2θ angle, indicating that the lattice parameters were almost the same, irrespective of the orthorhombic structure. **Figure 8-5c** shows ϕ -scan at the $SrHfS_3$ 202, $SrHfS_3$ 200, and LAO 110 diffractions. Although bulk $SrHfS_3$ have two-fold symmetry at these diffractions due to orthorhombic structure, four-fold symmetry was

observed in the thin film. The estimated lattice parameters are 6.906 Å for a - and c -axes, and 9.7244 Å for b -axis.

There are two possible explanations for the contradictory single peak in **Fig. 8-5b** and four-fold symmetry. The first possibility is the appearance of two SrHfS_3 domains with the strained lattice. Even though the individual domain has a two-fold symmetry, if one domain rotates 90° in-plane with respect to another, the four-fold symmetry appears. Furthermore, in a case of largely introduced lattice strain, the lattice parameters of a - and c -axes become close. This can lead to the single peak and four-fold symmetry. The other possibility is that of a structure phase transition from orthorhombic to e.g., tetragonal structure. Due to the received strain from substrate and/or non-equilibrium thin film growth, a structure with higher symmetry may be stabilized; the space group relationship of simple perovskite structures is seen in **Chapter 1**. Although there are two possibilities, the obvious conclusion has not been obtained yet. However, it should be noted that, irrespective of the contamination of impurities, SrHfS_3 epitaxially grew on the LAO substrate.

8.3.2. Intense orange PL of bulk BaHfS_3

Next, the research target compound changed from SrHfS_3 to BaHfS_3 . Before fabrication of the thin film, the veiled luminescence property was characterized. **Figure 8-6a** is PL spectra of a polycrystalline bulk BaHfS_3 , as a function of observed temperature. The intense orange emission was detected at all measured temperatures. The peak top energy was 2.08 eV at 300 K, which is consistent with the direct band gap ($E_g = 2.06$ eV) determined by diffuse reflectance and sample color, as seen in the previous **Chapter**. Like SrHfS_3 , defect-related emissions, such as donor-accepter pairs, were not observed at all; this was also true of BaHfS_3 . This result indicates that the polycrystalline BaHfS_3 should also have a high defect tolerance and a low defect concentration due to the component of Hf. An inset in **Fig. 8-6a** is a photograph of an excited polycrystalline BaHfS_3 at room temperature. The orange

PL can be seen by the human eye at room temperature, suggesting that the quantum efficiency would be high.

Figure 8-6b shows the temperature dependence of the PL peak top energy. With a decrease in measurement temperature, the PL peak position shifted to higher energy (i.e., clear blue shift). Thus, it was concluded that the intense orange PL of $BaHfS_3$ originates from band to band transition. These properties support the proposition that $BaHfS_3$ is also a promising candidate for a light-emitting semiconductor, even though the emission color is not green.

8.3.3. Epitaxial growth of single phase $BaHfS_3$ thin film

$BaHfS_3$ thin films were fabricated on LAO substrates at same growth condition as the optimum one of $SrHfS_3$. Then, the R_g dependence of segregated phases were examined and displayed in **Fig. 8-7**. It was clarified that the optimum growth condition of $BaHfS_3$ is almost the same as that of $SrHfS_3$, suggesting that the small growth window seems to be a common feature in this system. At the optimum R_g , peaks originating only from the b -axis oriented $BaHfS_3$ were detected. This indicates that a single phase of $BaHfS_3$ was successfully grown. At higher R_g , Ba_2HfS_4 was segregated; whereas at lower R_g , $BaHfS_3$ disappeared and unidentified impurities appeared.

Figure 8-8 shows the in-plane XRD patterns of $BaHfS_3$ thin film deposited at the optimum condition. $BaHfS_3$ also grew on LAO with 45° in-plane rotation like $SrHfS_3$. From four-fold symmetry of ϕ -scan at $BaHfS_3$ 200 diffraction due to the very close a - and c -axes lattice parameters ($a = 7.002 \text{ \AA}$ and $c = 6.995 \text{ \AA}$, i.e., 200 and 002 diffractions cannot be separated in the angle resolution of a used apparatus), it was confirmed that epitaxial $BaHfS_3$ was grown on LAO. The resultant crystal lattice shrank along a - and c -axes (6.882 \AA) and expanded along b -axis (10.04 \AA) from bulk $BaHfS_3$ ($a = 7.002 \text{ \AA}$, $b = 9.915 \text{ \AA}$, $c = 6.995 \text{ \AA}$).

Next, **Fig. 8-9** shows the transmittance spectra of $BaHfS_3$ epitaxial thin film taken at

various temperature from 10 K to room temperature. Although low temperature measurements were performed, a sharp transition observed in the direct allowed gap semiconductors could not be detected. This feature suggests that the sample quality was too poor, or that the electronic structure changed to an indirect type. Because a discussion begins with the hypothesis that the hindered sharp transition originates from an indirect gap, it was considered that it is possible to actualize the indirect band gap with respect to the epitaxial strain and oxygen contamination. The direct band gap of $AEHfS_3$ attributes to the $Pnma$ structure owing to band folding [6, 7]. In the case of an occurrence of a structure phase transition from the orthorhombic to a higher symmetry phase, such as a tetragonal phase, the direct band structure would also change to an indirect one, where the possible driving force of the phase transition would be introduced epitaxial strain and/or oxygen contamination; for instance, when oxygen occupies a sulfur-site, the tolerance factor varies, which would lead to structure phase transition. Here, it should be remembered that the polycrystalline bulks of $SrHfS_3$ and $BaHfS_3$ contain the oxide impurity of HfO_2 . In the PLD process, oxygen would easily contaminate this sulfide system because the impurity is also ablated simultaneously and oxygen is much more active than sulfur. The existence of oxygen in the thin films was examined by using AES because other methods of observation, such as the use of a scanning electron microscopy and an electron probe microanalyzer, cannot completely ignore oxygen in the oxide substrate, and the penetration depth of AES is very shallow. **Figure 8-10** shows the depth profile of $BaHfS_3$ epitaxial thin film along out-of-plane. As a result, a large amount of oxygen was detected, although the quantitative accuracy is not high. It is not clear that the incorporated oxygen prevents effective optical absorption and emission; however, the intrinsic high optical properties may appear in $AEHfS_3$ by suppression of the oxygen contamination.

8.4. Conclusion

Epitaxial $AEHfS_3$ ($AE = Sr$ and Ba) thin films were fabricated by PLD. During the thin film growth process, an unusual S-supplement process utilizing S-beam flux evaporated from a cracking cell was employed to prevent the formation of S deficiency. The S-molecular beam worked effectively to fill in the vacancies. By controlling R_g and T_s , epitaxial $SrHfS_3$ was successfully obtained, even though it was found that the growth window of $SrHfS_3$ is very small and the impurity phase cannot completely vanish, where stable SrS impurity phase mainly prevented to form single phase of $SrHfS_3$.

For $BaHfS_3$, the PL was first evaluated in the polycrystalline bulk form to preliminarily confirm the potential for an optical semiconductor. $BaHfS_3$ exhibited intense orange PL peaking at 2.08 eV, originating from the band to band transition. Moreover, the orange PL could be seen by human eyes like $SrHfS_3$, and emissions other than the PL were not detected. These properties support that $BaHfS_3$ is also a promising candidate for light-emitting semiconductor. Although the band gap and emission wavelength are not suitable for green emission, a thin film of $BaHfS_3$ was fabricated. In contrast to $SrHfS_3$, a single phase epitaxial $BaHfS_3$ was successfully obtained and then the optical transmittance measurements were performed. However, the absorption was not as sharp as that of a direct semiconductor. To unveil the origin of broad absorption, oxygen contamination was examined, because oxygen should easily replace the sulfur-site and the PLD target included the oxide impurity of HfS_2 . As a result of AES measurement, it was clarified that a large amount of oxygen existed in the $BaHfS_3$ film, suggesting that if the oxygen contamination is effectively suppressed, an intense luminescence coming from the direct band gap would appear.

References

1. K. P. O'Donnell, M. Auf der Maur, A. Di Carlo, K. Lorenz, and the SORBET consortium. *Phys. Status Solidi-Rapid Res. Lett.*, **6**, 49–52 (2012).
2. M. Auf der Maur, A. Pecchia, G. Penazzi, W. Rodrigues, and A. Di Carlo, *Phys. Rev. Lett.*, **116**, 027401 (2016).
3. T. Arai, S. Iimura, J. Kim, Y. Toda, S. Ueda, and H. Hosono, *J. Am. Chem. Soc.*, **139**, 17175–17180 (2017).
4. T. Arai, S. Iimura, and H. Hosono, *Chem. Mater.*, **30**, 597–601 (2018).
5. H. Mizoguchi, T. Kamiya, S. Matsuishi, and H. Hosono, *Nat. Commun.*, **2**, 470 (2011).
6. R. A. Hoffmann, *Rev. Mod. Phys.*, **60**, 601 (1988).
7. J. K. Burdett, *Prog. Solid State Chem.*, **15**, 173–255 (1984).
8. K. Hanzawa, S. Iimura, H. Hiramatsu, and H. Hosono, “Materials Design of Green Emitting Semiconductors: Perovskite-Type Sulfide SrHfS_3 ”, *J. Am. Chem. Soc.*, published online (2019). DOI: 10.1021/jacs.8b13622
9. S. Nakamura, T. Mukai M, and Senoh, *Jpn. J. Appl. Phys.*, **30**, L1998 (1991).
10. S. Nakamura, M. Senoh, S. Nagahama, N. Iwasa, T. Yamada, T. Matsushita, H. Kiyoku, and Y. Sugimoto, *Jpn. J. Appl. Phys.*, **35**, L74 (1996).
11. M. Kawasaki, K. Takahashi, T. Maeda, R. Tsuchiya, M. Shinohara, O. Ishiyama, T. Yonezawa, M. Yoshimoto, and H. Koinuma, *Science*, **266**, 1540–1542 (1994).
12. A. Tsukazaki, H. Saito, K. Tamura, M. Ohtani, and H. Koinuma, *Appl. Phys. Lett.*, **81**, 235 (2002).
13. A. Tsukazaki, A. Ohtomo, S. Yoshida, and M. Kawasaki, *Appl. Phys. Lett.*, **83**, 2784 (2003).
14. A. Tsukazaki, A. Ohtomo, and M. Kawasaki, *Appl. Phys. Lett.*, **84**, 3858 (2004).

15. Y. Nishimoto, K. Nakahara, D. Takamizu, A. Sasaki, K. Tamura, S. Akasaka, Y. Yuji, T. Fujii, T. Tanabe, H. Takasu, A. Tsukazaki, A. Ohtomo, T. Onuma, S. F. Chichibu, and M. Kawasaki, *Appl. Phys. Express*, **1**, 091202 (2008).
16. A. Tsukazaki, H. Yuji, S. Akasaka, K. Tamura, K. Nakahara, T. Tanabe, H. Takasu, A. Ohtomo, and M. Kawasaki, *Appl. Phys. Express*, **1**, 055004 (2008).
17. J. Falson, Y. Kozuka, M. Uchida, J. H. Smet, T. Arima, A. Tsukazaki, and M. Kawasaki, *Sci. Rep.*, **6**, 26598 (2016).
18. Y. Matsubara, K. S. Takahashi, M. S. Bahramy, Y. Kozuka, D. Maryenko, J. Falson, A. Tsukazaki, Y. Tokura, and M. Kawasaki, *Nat. Commun.*, **7**, 11631 (2016).
19. H. Hiramatsu, K. Ueda, H. Ohta, M. Orita, M. Hirano, and H. Hosono, *Appl. Phys. Lett.*, **81**, 598 (2002).
20. H. Hiramatsu, H. Ohta, M. Hirano, and H. Hosono, *Solid State Commun.*, **124**, 411–415 (2002).
21. F. Y. Ran, Z. Xiao, H. Hiramatsu, H. Hosono, and T. Kamiya, *Appl. Phys. Lett.*, **104**, 072106 (2014).
22. S. A. Filippone, Y.-Y. Sun, and R. Jaramilo, *MRS Commun.*, **8**, 145–151 (2018).

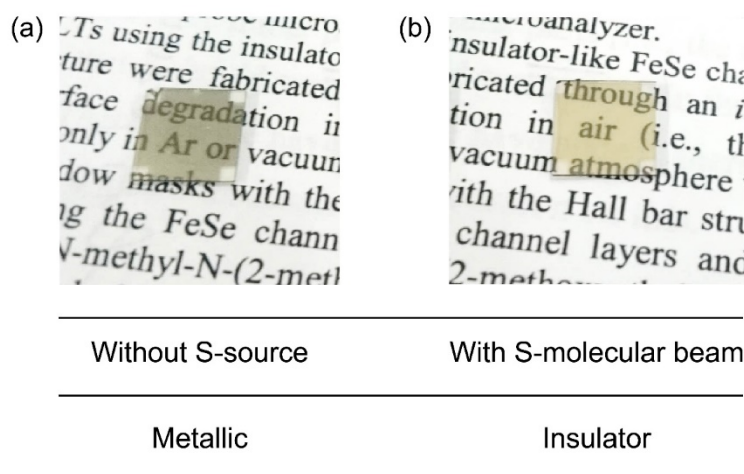


Figure 8-1. Photographs of $SrHfS_3$ thin films deposited (a) without any S-source and (b) with S-molecular beam.

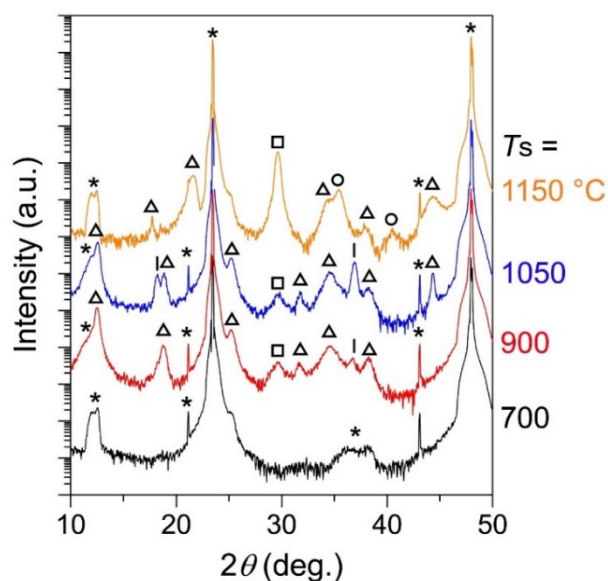


Figure 8-2. XRD patterns of $SrHfS_3$ deposited at $T_s = 1150$ (orange), 1050 (blue), 900 (red), and 700 °C (black). Bars, circles, squares, triangles, and asterisks denote diffractions of $SrHfS_3$ 020, HfS_x , SrS 020, unidentified impurities, and LAO substrate, respectively.

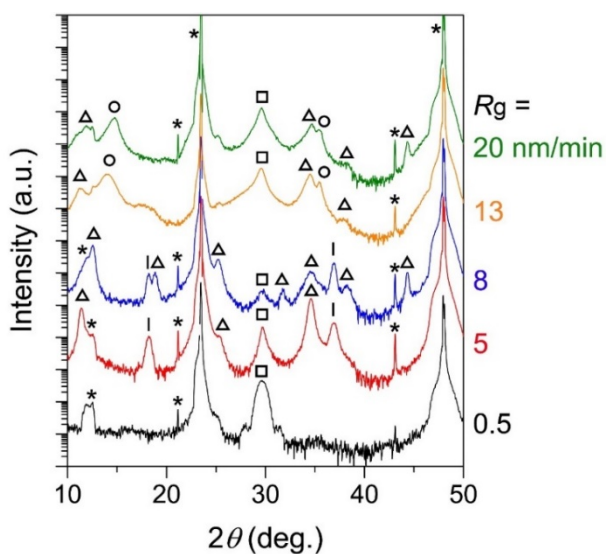


Figure 8-3. XRD patterns $SrHfS_3$ grown at 20 (green), 13 (orange), 8 (blue), 5 (red), and 0.5 nm/min (black). Bars, circles, squares, triangles, and asterisks denote diffractions of $SrHfS_3$ 020, HfS_x , SrS 020, unidentified impurities, and LAO, respectively.

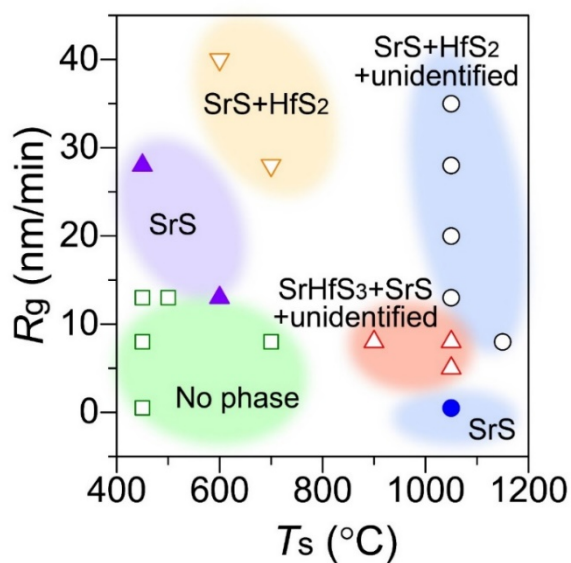


Figure 8-4. Relationship between R_g and T_s in terms of segregated crystal phases.

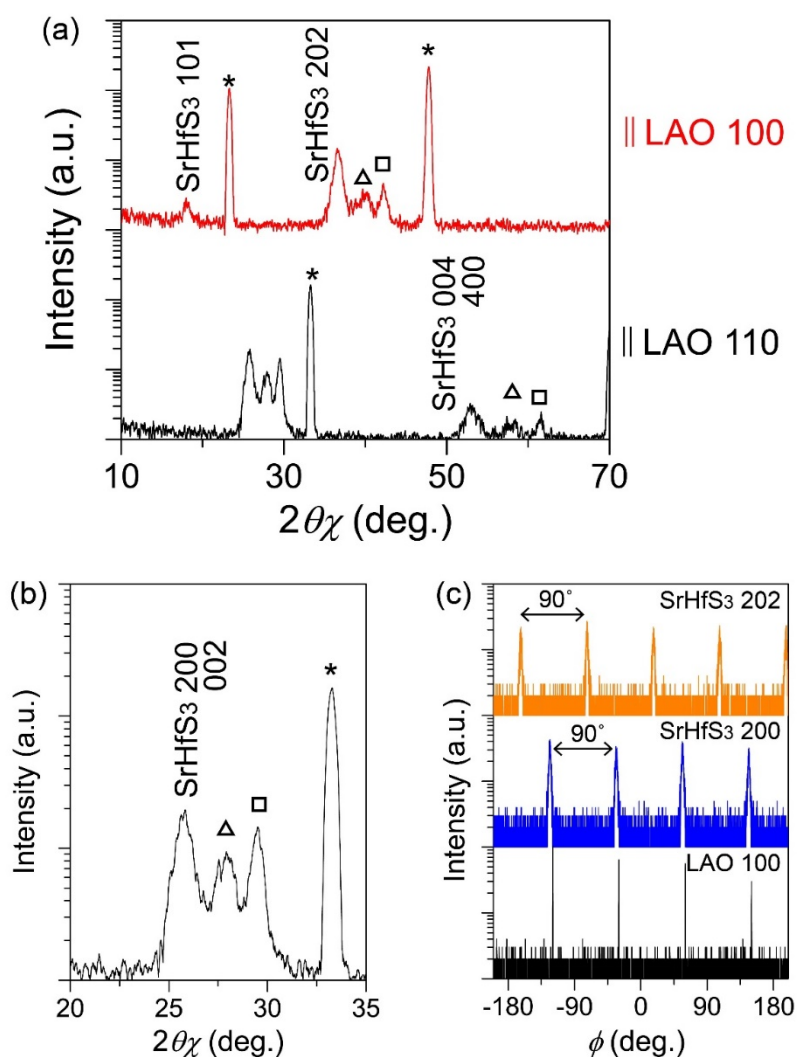


Figure 8-5. In-plane XRD of SrHfS₃. (a) In-plane $2\theta_\chi/\phi$ scan along LAO 100 (red) and LAO 110. Asterisks, triangles, and squares denote diffractions of LAO, unidentified impurity, and SrS. (b) Enlarged image of (a). (c) ϕ -scan at SrHfS₃ 202 (orange), 200 (blue), and LAO 100 (black) diffractions.

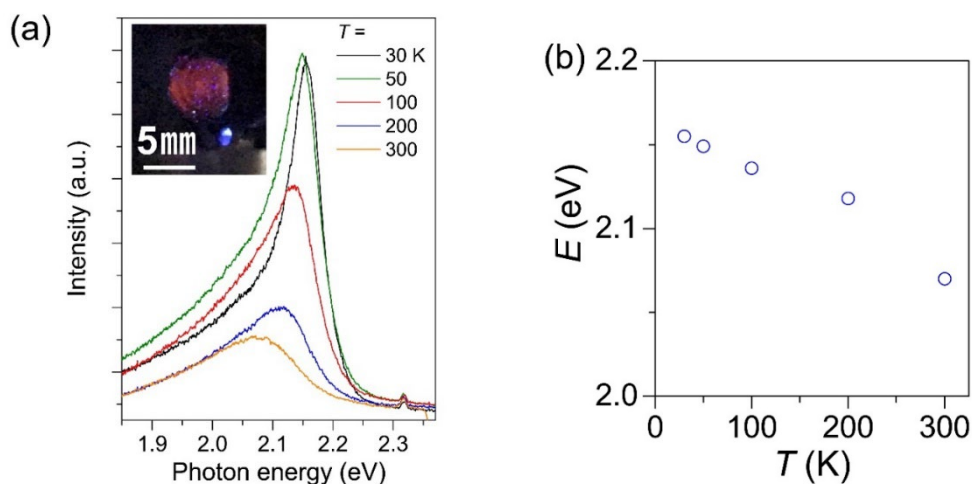


Figure 8-6. (a) PL spectra of bulk $BaHfS_3$ at various temperatures from 30 K to 300 K. An inset is a picture of excited polycrystalline $BaHfS_3$ at room temperature. (b) Temperature dependence of PL peak top energy.

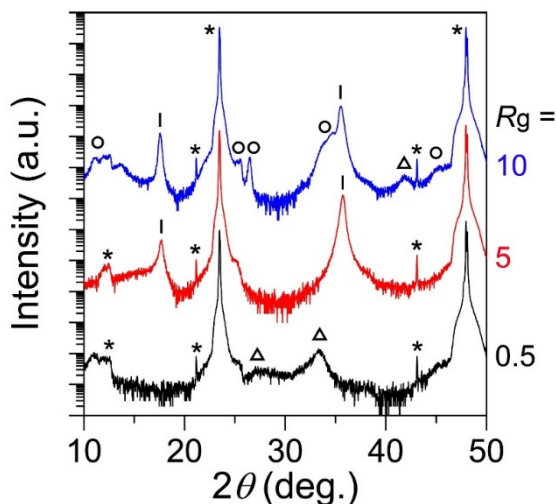


Figure 8-7. XRD patterns of $BaHfS_3$ thin films grown at 10 (blue), 5 (red), and 0.5 nm/min (black). Bars, circles, triangles, asterisks denote diffractions of $SrHfS_3$, Ba_2HfS_4 , unidentified impurity, and LAO.

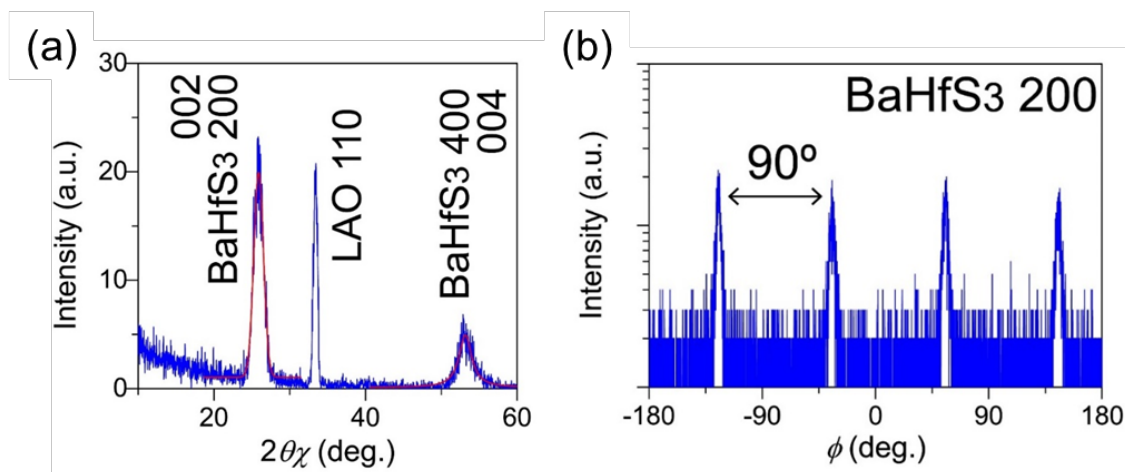


Figure 8-8. In-plane XRD patterns of BaHfS_3 epitaxial thin films. (a) In-plane $2\theta\chi/\phi$ scan along LAO [110]. Red lines are fitting results to determine lattice parameter. (b) ϕ -scan at BaHfS_3 200 diffraction.

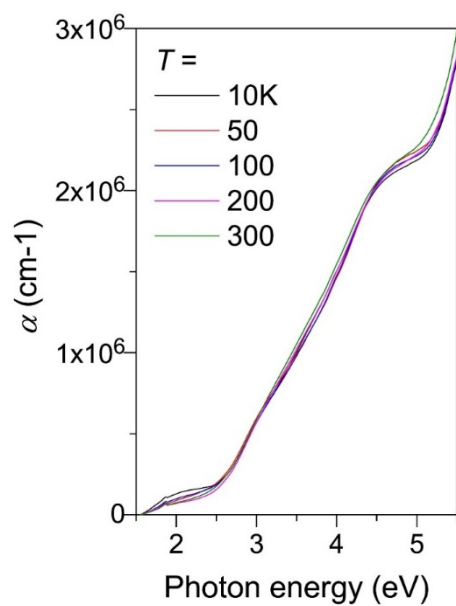


Figure 8-9. Absorption coefficient of BaHfS_3 epitaxial thin films. The spectra were taken from 10 K to 300 K.

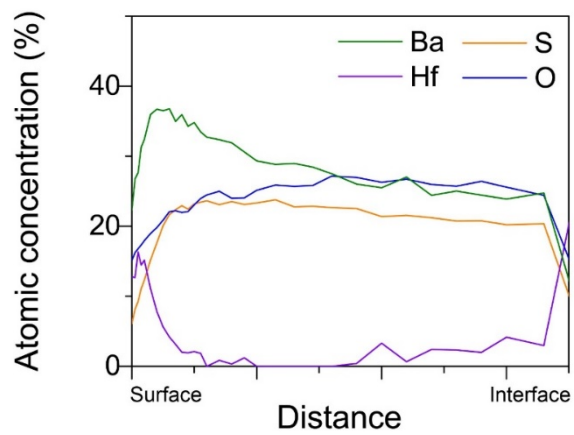


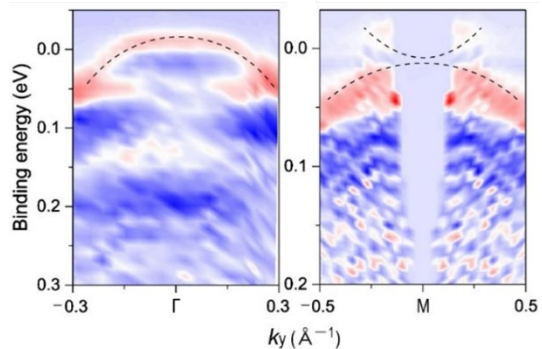
Figure 8-10. Depth profile of AES measurement for $BaHfS_3$ epitaxial thin film. Left edge and right edge correspond to the surface of $BaHfS_3$ thin film and interface between $BaHfS_3$ and LAO substrate.

Chapter 9. General Conclusion

Electronic conductive functionalities in *TM*-based chalcogenides were designed by tuning the electronic structures through the application of structural distortions and were experimentally validated by doping. **Chapters 2–6** designed high- T_c superconductivity in *FeCh* by enhancing the electron correlation of the parent phase derived from epitaxial in-plane tensile strain introduced by the fabrication of the high quality epitaxial thin film and observed at $T_c = 35$ K by extremely high-density electrons doping into the strongly electron-correlated FeSe. **Chapters 7–8** designed light-emitting semiconductors with a direct band gap along with *n*- and *p*-type carrier dopabilities in *eTM*-based perovskite sulfide by band folding of the VBM composed of nonbonding state of S *3p*-orbitals through construction of the superstructure derived from chemical pressure originating in the selection of constituent atoms, and effective green emissions, as well as *n*- and *p*-type conductions by donor and acceptor dopings were demonstrated at room temperature in SrHfS₃.

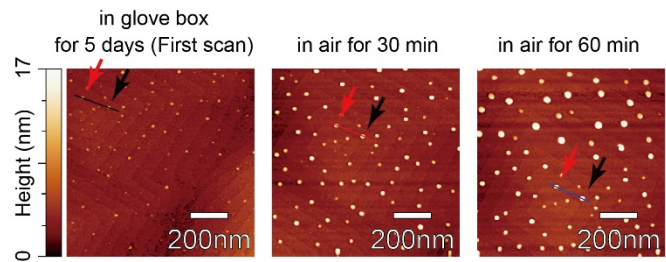
The present study is summarized as follows;

Chapter 2 investigated the origin of the insulator-like behavior of strained FeSe epitaxial thin film fabricated by molecular beam epitaxy on SrTiO₃ single crystal. The electric transport measurement supported that FeSe thin film receiving in-plane tensile strain exhibits insulator-like behavior. On the other hand, an ARPES measurement supported that the electronic structure was metallic because Fermi level intersects of both electron and hole bands.

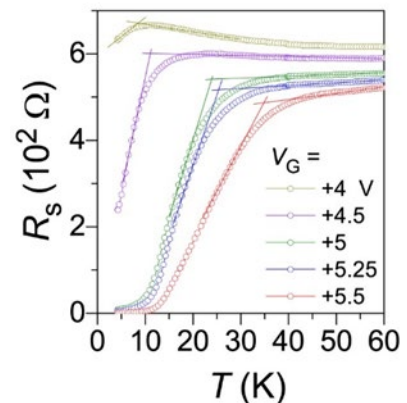
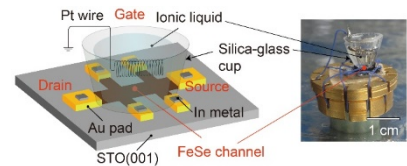


It also clarified that the electron correlation of strained FeSe was enhanced compared to single crystalline FeSe from the estimation of the renormalization factor. From the ARPES and Hall effect measurements, it was concluded that the origin of the insulator-like behavior was not only an enhancement of the electron correlation, but also the formation of a potential barrier for scattering conducting electrons.

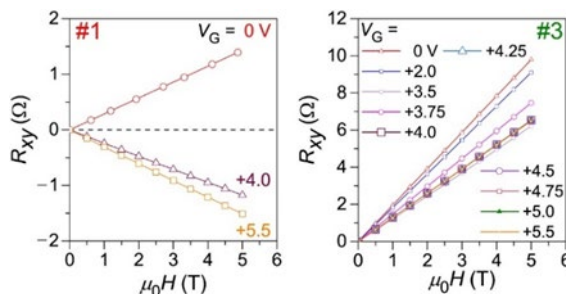
Chapter 3 examined the surface degradation of FeSe against air exposure and the influence of degradation on an electric-field induced carrier accumulation. Bulk FeSe is an air stable compound, however auger electron spectroscopy found that the surface was rapidly degenerated by light elements such as C, H, and O. Moreover, it was unveiled that the nucleated particles prevented the field-induced carrier accumulation using the EDLT structure, indicating that the *in-situ* device fabrication process is necessary.



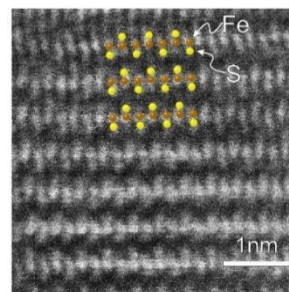
In **Chapter 4**, EDLT was *in-situ* constructed by employing high quality insulator-like strained FeSe epitaxial thin film as a channel layer. The FeSe-EDLT exhibited high- T_c superconductor transition under electric field. The maximum T_c reached 35 K at $V_G = +5.5$ V, which is approximately four times higher than that of a single crystal FeSe ($T_c = 8$ K). The Hall effect measurements unveiled that high-density electrostatic electron doping occurred under the electric field without any chemical reaction and degradation. It was concluded that this high T_c was due to the enhanced electron correlation by epitaxial strain and high-density accumulated electron.



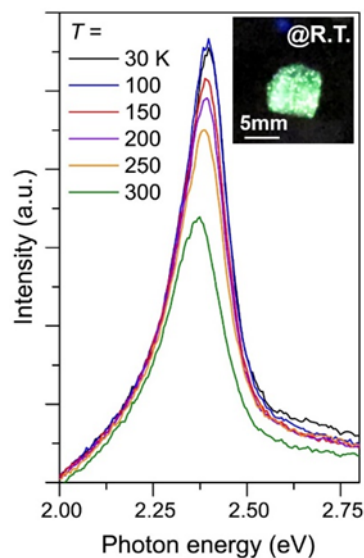
In **Chapter 5**, the essence of the high- T_c superconductivity in the FeSe-EDLT was investigated by preparing and comparing three EDLTs using differently grown insulator-like FeSe. The Hall effect measurements clarified that a key factor to achieve the highest T_c of 35 K is optimally highly accumulated electron density. Moreover, poorer quality FeSe contributed to the difficulty of carrier-density control in the EDLT.



In **Chapter 6**, tetragonal FeS epitaxial thin films were fabricated. Because the stable phase of FeS is hexagonal, the tetragonal phase is metastable. By utilizing a non-equilibrium PLD process, the tetragonal phase was successfully stabilized. It was also found that the thermal effect, optimum growth rate, pure target, and small mismatch substrate are essential to grow the metastable epitaxial film. This is a first demonstration of fabricating the metastable FeS epitaxial film as proved by STEM. Due probably to the introduced compressive in-plane strain to FeS films, the films did not exhibit superconductivity even under an electric field applied by using the EDLT structure.

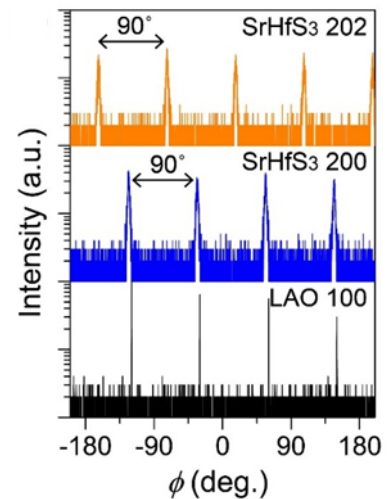


In **Chapter 7**, a novel green light-emitting semiconductor together with n - and p -type carrier controllabilities were designed in eTM -based perovskite sulfide based on chemical bonding of nonbonding state and band folding stimulated by construction of superstructure originating from distortion. A preliminary first-principles calculation suggested that perovskite sulfide $AEeTMS_3$ (AE = Alkali earth metal, eTM = Zr and Hf) with orthorhombic structure was the promising candidate. $SrHfS_3$, with a band gap of ~ 2.3 eV, exhibited



remarkable optical and electrical characteristics; e.g., a visible intense green emission at room temperature, an absence of donor-acceptor pair emission, and great n - and p -type carrier controllabilities by chemical dopings.

In **Chapter 8**, epitaxial thin films of the novel semiconductors $AE\text{HfS}_3$ ($AE = \text{Sr}$ and Ba) were fabricated by PLD on LaAlO_3 . For the fabrication, S-source was supplied not from H_2S gas, but from a S-molecular beam that could maintain high vacuum level during the growth and effectively eliminated S vacancy. In the case of $AE = \text{Sr}$, even though epitaxial SrHfS_3 films were successfully obtained, the segregation of impurity phases, such as SrS , were unavoidable. Whereas in a Ba case, the fabrication of single phase BaHfS_3 epitaxial films were successful.



Acknowledgments

This study was carried out in *Hosono, Kamiya, & Hiramatsu Laboratory*, at the Tokyo Institute of Technology, from April 2014 to March 2019. Numerous people have contributed to this study.

First, I would like to express my gratitude to my supervisors, Associate Prof. **Hidenori Hiramatsu** and Prof. **Hideo Hosono**, for their precise advice and continuous encouragement. I learned a lot from them, such as a sense of materials research.

Also, I would like to express my sincere thanks to Prof. **Toshio Kamiya** and Associate Prof. **Satoru Matsuishi** for their kind guidance, discussions, and important suggestions.

I am indebted to Prof. **Satoru Fujitsu**, Prof. **Hideya Kumomi**, Prof. **Toshiharu Yokoyama**, Associate Prof. **Takayoshi Katase**, Associate Prof. **Silvia Haindl**, Associate Prof. **Masaaki Kitano**, Associate Prof. **Tomofumi Tada**, Associate Prof. **Hiroshi Mizoguchi**, Associate Prof. **Masato Sasase**, Lecturer **Yoshitake Toda** (currently at AGC Inc.), Assistant Prof. **Kosuke Matsuzaki**, Assistant Prof. **Fuji Funabiki**, Assistant Prof. **Soshi Iimura**, Assistant Prof. **Keisuke Ide**, Assistant Prof. **Junghwan Kim**, Dr. **Junjie Wang** (currently Professor at Northwestern Polytechnical University), Dr. **Yoshinori Muraba**, Dr. **Joonho Ban**, Dr. **Tianping Ying**, Dr. **Yangfan Lu**, Dr. **Jiazhen Wu**, Dr. **Christian Niedermeier**, Dr. **Nobuhiro Nakamura** (AGC Inc.), Dr. **Yukiko Obata** (currently at KEK), Dr. **Takeshi Arai**, Dr. **Junichi Ishida** for their kind help and suggestions.

I am especially grateful to Dr. **Hikaru Sato** (currently at General Electric Company) and Dr. **Taku Hanna** (currently at ULVAC, Inc.) for their experimental instruction and suggestions.

I would also like to thank Mr. **Norihiko Miyokawa**, Mr. **Takeshi Inoue**, Mr. **Kyohei Ishikawa**, Mr. **Sang Won Park**, Mr. **Taehwan Jun**, Mr. **Taisuke Hayakeyama**, Mr. **Ryo Igarashi**, Mr. **Hiroshi Okanishi**, Mr. **Ryo Nishimura**, Mr. **Kyosuke Yamagata**, Mr. **Mitsuho**

Kikuchi, Mr. *Takumi Sekiya*, Dr. *Hao-Chun Tang*, Mr. *Takuya Nakao*, Mr. *Naoto Watanabe*, Mr. *Yutaro Kobayashi*, Mr. *Hiroyuki Kinjo*, Mr. *Yuta Yamaguchi*, Mr. *Takashi Sasaki*, Mr. *Shu Kanno*, Ms. *Ayaka Kanai*, and other members of the *Hosono, Kamiya, Hiramatsu & Matsuishi Laboratory*.

Further, I am indebted to Mr. *Yuji Kondo* Mr. *Shizuo Hayashi*, Mr. *Kenji Ariga*, and Ms. *Michiko Sato* for their technical support.

I would like to acknowledge the secretaries, Ms. *Kanako Ochiai*, Ms. *Mayumi Nakano*, and Ms. *Hanae Murayama* for their assistance as well as for their kindness.

Finally, I express my sincere appreciation to my family and friends.

March 2019

Kota Hanzawa

Publication List

Papers included in this thesis

1. **K. Hanzawa**, H. Sato, H. Hiramatsu, T. Kamiya, and H. Hosono
“Electric field-induced superconducting transition of insulating FeSe thin film at 35 K”
Proceedings of the National Academy of Sciences of the United States of America, vol. 113, pp. 3986 – 3990 (2016).
2. **K. Hanzawa**, H. Sato, H. Hiramatsu, T. Kamiya, and H. Hosono
“Key Factors for Insulator-Superconductor Transition in FeSe Thin Films by Electric Field”
IEEE Transactions on Applied Superconductivity, vol. 27, pp. 7500405-1 – 7500405-5 (2017).
3. **K. Hanzawa**, Y. Yamaguchi, Y. Obata, S. Matsuishi, H. Hiramatsu, T. Kamiya, and H. Hosono
“Insulator-like behavior coexisting with metallic electronic structure in strained FeSe thin films grown by molecular beam epitaxy”
Physical Review B, vol. 99, pp. 035148-1 – 035148-11 (2019).
4. **K. Hanzawa**, M. Sasase, H. Hiramatsu, and H. Hosono
“Stabilization and heteroepitaxial growth of metastable tetragonal FeS thin films by pulsed laser deposition”
Superconductor Science and Technology, vol. 32, p. 054002 (2019).
5. **K. Hanzawa**, S. Iimura, H. Hiramatsu, and H. Hosono
“Materials Design of Green Emitting Semiconductors: Perovskite-Type Sulfide SrHfS₃”
Journal of the American Chemical Society, published online (2019).
DOI: 10.1021/jacs.8b13622
6. **K. Hanzawa**, S. Iimura, H. Hiramatsu, and H. Hosono

“Heteroepitaxial growth of $AEHfS_3$ ($AE=Sr$ and Ba) and the optoelectronic properties”
To be submitted (in preparation).

7. H. Hiramatsu, **K. Hanzawa**, T. Kamiya, and H. Hosono

“Particulate Generation on Surface of Iron Selenide Films by Air Exposure”

Journal of Superconductivity and Novel Magnetism, published online (2019).

DOI: 10.1007/s10948-019-5020-9

Other papers

1. Y. Yamaguchi, **K. Hanzawa**, T. Hanna, Y. Toda, S. Matsuishi, H. Hiramatsu, and H. Hosono

“Difference in Electronic Structures of Superconducting and Insulator-Like FeSe Epitaxial Films”

AMTC Letters: International Journal of Advanced Microscopy and Theoretical Calculations, vol. 5, pp. 216 – 217 (2016).

2. **K. Hanzawa**, H. Sato, H. Hiramatsu, T. Kamiya and H. Hosono

“Relationship Between Surface Degradation and Electric Field-Induced Superconductivity for Insulator-Like FeSe Epitaxial Films”

AMTC Letters: International Journal of Advanced Microscopy and Theoretical Calculations, vol. 5, pp. 214 – 215 (2016).

3. S. Haindl, **K. Hanzawa**, H. Sato, H. Hiramatsu, and H. Hosono

“*In-situ* growth of superconducting $SmO_{1-x}F_xFeAs$ thin films by pulsed laser deposition”

Scientific Reports, vol. 6, pp. 35797-1 – 35797-6 (2016).

4. J. Wang, **K. Hanzawa**, H. Hiramatsu, J. Kim, N. Umezawa, K. Iwanaka, T. Tada, and H. Hosono

“Exploration of Stable Strontium Phosphide-Based Electrides: Theoretical Structure Prediction and Experimental Validation”

Journal of the American Chemical Society, vol. 139, pp. 15668 – 15680 (2017).

5. J. T. Kim, D. S. Hyeon, **K. Hanzawa**, A. Kanai, S. Y. Kim, Y. J. Lee, H. Hosono, J. Bang, and K. Lee

“Role of fluorine in two-dimensional dichalcogenide of SnSe₂”

Scientific Reports, vol. 8, pp. 1645-1 – 1645- 8 (2018).

6. S. Haindl, H. Kinjo, **K. Hanzawa**, H. Hiramatsu, and H. Hosono

“Pulsed laser deposition of SmFeAsO_{1-δ} on MgO(100) substrates”

Applied Surface Science, vol. 437, pp. 418 – 428 (2018).

7. M. Tsuji, **K. Hanzawa**, H. Kinjo, H. Hiramatsu, and H. Hosono

“Heteroepitaxial growth of CaZn₂N₂ films by molecular beam epitaxy with active nitrogen plasma source”

To be submitted (in preparation).

8. J. Matsumoto, **K. Hanzawa**, S. Haindl, T. Katase, H. Hiramatsu, and H. Hosono

“Superconductivity at 45 K of highly hydrogen-doped SmFeAsO epitaxial films grown by pulsed laser deposition followed by post-deposition thermal annealing”

To be submitted (in preparation).

Presentation List

International Presentations

1. **K. Hanzawa**, H. Sato, H. Hiramatsu, T. Kamiya, and H. Hosono (**Oral**)

“Molecular beam epitaxy growth of FeSe thin films”

- The 9th International Conference on the Science and Technology for Advanced Ceramics (STAC-9)*, Oct. 19 – 21, Ibaraki, **Japan**, (2015).
2. **K. Hanzawa**, H. Sato, H. Hiramatsu, T. Kamiya, and H. Hosono (**Poster**)
 “Relationship Between Surface Degradation and Electric Field-Induced Superconductivity for Insulator-Like FeSe Epitaxial Films”
The 5th International Symposium on Advanced Microscopy and Theoretical Calculations (AMTC5), May 11 – 13, Aichi, Japan (2016).
3. **K. Hanzawa**, H. Sato, H. Hiramatsu, T. Kamiya, and H. Hosono (**Poster**)
 “Molecular beam epitaxy growth of insulator-like FeSe thin films for direct induction of insulator-superconductor transition by electric field”
Applied Superconductivity Conference 2016 (ASC 2016), Sep. 4 – 9, CO, USA, (2016).
4. **K. Hanzawa**, H. Hiramatsu, T. Kamiya and H. Hosono (**Oral**)
 “Tetragonal FeCh ($Ch = S$ and Se) Epitaxial Thin Films Grown by Non-Equilibrium Process and Their Electric Double-Layer Transistors”
The 15th International Conference on Advanced Materials (IUMRS-ICAM2017), Aug. 27 – Sep. 1st, Kyoto, **Japan**, (2017).
5. **K. Hanzawa**, H. Hiramatsu, T. Kamiya, and H. Hosono (**Oral**)
 “Metastable Iron-Chalcogenide Thin Films and Their Electrical Transport Properties”
The 10th International Conference on the Science and Technology for Advanced Ceramics (STAC-10), Aug. 1 – 3, Kanagawa, **Japan**, (2017).
6. **K. Hanzawa**, S. Iimura, H. Hiramatsu, and H. Hosono (**Poster**)
 “Opto-electronic Properties in Perovskite Sulfide $SrHfS_3$ ”
Solid-state Chemistry and Ionics workshop (The 5th SCI workshop), Sep. 10 – 13, Fukuoka, **Japan**, (2018).
7. **K. Hanzawa**, S. Iimura, H. Hiramatsu, and H. Hosono (**Oral**)

“Exploration of semiconductors exhibiting green emission and *n*- & *p*-type conductivity”
The 3rd Workshop for Defect Functionalized Sustainable Energy Materials: From Design to Devices Application, Workshop on ‘Semiconductor Materials’, Nov. 12 – 13, Kanagawa, Japan (2018).

8. **K. Hanzawa**, S. Iimura, H. Hiramatsu, and H. Hosono (**Oral**)

“A new perovskite-type sulfide semiconductor, SrHfS₃, exhibiting intense green emission at room temperature”

2018 Materials Research Society Fall Meeting & Exhibit (MRS Fall 2018), Nov. 25 – 30, Boston, MA, USA, (2018).

9. **K. Hanzawa**, M. Sasase, H. Hiramatsu, T. Kamiya, and H. Hosono (**Poster**)

“Electrical Transport Properties of Iron-Chalcogenide Epitaxial Thin Films Grown via Non-Equilibrium Process under Electric Field”

The 31st International Symposium on Superconductivity (ISS2018), Dec. 12 – 14, Ibaraki, Japan, (2018).

10. **K. Hanzawa**, S. Iimura, H. Hiramatsu, and H. Hosono (**Oral**)

“Optical and electronic properties of perovskite-type sulfide semiconductors, AEHfS₃ (AE = Sr and Ba)”

The First Annual Symposium of the TokyoTech-UCL-McGill core-to-core collaboration: Defect Functionalized Sustainable Energy Materials: From Design to Devices Application, Feb. 18 – 19, London, UK (2019).

Domestic Presentations

1. **半沢 幸太**, 佐藤 光, 平松 秀典, 神谷 利夫, 細野 秀雄 (**ポスター**)

「分子線エピタキシー法による鉄系超伝導体 FeSe のヘテロエピタキシャル成長」

『新学術領域第3回若手の会』, 北海道, 2015年7月

2. **半沢 幸太**, 佐藤 光, 平松 秀典, 神谷 利夫, 細野 秀雄 (**口頭**)

- 「FeSe エピタキシャル薄膜の分子線エピタキシー成長と電界誘起超伝導」
『第 54 回セラミックス基礎科学討論会』, 佐賀, 2016 年 1 月
3. **半沢 幸太**, 佐藤 光, 平松 秀典, 神谷 利夫, 細野 秀雄 (口頭)
「絶縁性 FeSe 極薄膜における電界誘起超伝導」
『第 63 回応用物理学会春季学術講演会』, 東京, 2016 年 3 月
4. **半沢 幸太**, 佐藤 光, 平松 秀典, 神谷 利夫, 細野 秀雄 (ポスター)
「FeSe 極薄膜を用いた電界誘起超伝導」
『新学術領域第 4 回若手の会』, 茨城, 2016 年 7 月
5. **半沢 幸太**, 平松 秀典, 神谷 利夫, 細野 秀雄 (口頭)
「異なるチャネル成長条件で作製した絶縁性 FeSe を用いた電気二重層トランジスタ」
『第 55 回セラミックス基礎科学討論会』, 岡山, 2017 年 1 月
6. **半沢 幸太**, 平松 秀典, 神谷 利夫, 細野 秀雄 (口頭)
「絶縁性 FeSe 薄膜における電界誘起超伝導に関するチャネル層の影響」
『第 64 回応用物理学会春季学術講演会』, 神奈川, 2017 年 3 月
7. **半沢 幸太**, 平松 秀典, 神谷 利夫, 細野 秀雄 (ポスター)
「FeSe 薄膜における電界誘起超伝導転移の起源」
『新学術領域第 5 回若手の会』, 東京, 2017 年 7 月
8. **半沢 幸太**, 飯村 壮史, 平松 秀典, 細野 秀雄 (口頭)
「ペロブスカイト硫化物 SrHfS₃ の室温緑色発光」
『第 79 回応用物理学会秋季学術講演会』, 愛知, 2018 年 9 月
9. **半沢 幸太**, 飯村 壮史, 平松 秀典, 細野 秀雄 (口頭)
「High opto-electronic functionality of a new perovskite-type sulfide semiconductor, AeHfS₃ (Ae = Sr, Ba)」 (国際セッション)
『第 57 回セラミックス基礎科学討論会』, 宮城, 2019 年 1 月

Awards

1. 新学術領域第3回若手の会 ポスター賞銅賞 (2015年7月)
2. 学問のすすめ賞：材料物理科学専攻 最優秀修士論文発表賞 (2016年2月)
3. Best Presentation Award (最優秀発表賞), 第57回セラミックス基礎科学討論会：国際セッション (2019年1月)

Biography

Date of birth: 4th January 1991.

Education

Mar. 2014: Bachelor from Department of Applied Physics, Tokyo University of Agriculture and Technology, Japan.

Mar. 2016: Master from Department of Materials Science and Engineering, Tokyo Institute of Technology, Japan